TOPICS IN ORGANOMETALLIC CHEMISTRY

29

Volume Editor Alistair J. Lees

Photophysics of Organometallics

Springer

29

Topics in Organometallic Chemistry

Topics in Organometallic Chemistry

Recently Published and Forthcoming Volumes

Molecular Organometallic Materials for Optics
Volume Editors: H. Le Bozec, V. Guerchais
Vol. 28, 2010

Conducting and Magnetic Organometallic Molecular Materials
Volume Editors: M. Fourmigue´, L. Ouahab
Vol. 27, 2009

Metal Catalysts in Olefin Polymerization
Volume Editor: Z. Guan
Vol. 26, 2009

Bio-inspired Catalysts
Volume Editor: T. R. Ward
Vol. 25, 2009

Directed Metallation
Volume Editor: N. Chatani
Vol. 24, 2007

Regulated Systems for Multiphase Catalysis
Volume Editors: W. Leitner, M. Hölscher
Vol. 23, 2008

Organometallic Oxidation Catalysis
Volume Editors: F. Meyer, C. Limberg
Vol. 22, 2007

N-Heterocyclic Carbenes in Transition Metal Catalysis
Volume Editor: F. Glorius
Vol. 21, 2006

Dendrimer Catalysis
Volume Editor: L. H. Gade
Vol. 20, 2006

Metal Catalyzed Cascade Reactions
Volume Editor: T. J. J. Müller
Vol. 19, 2006

Catalytic Carbonylation Reactions
Volume Editor: M. Beller
Vol. 18, 2006

Bioorganometallic Chemistry
Volume Editor: G. Simonneaux
Vol. 17, 2006

Surface and Interfacial Organometallic Chemistry and Catalysis
Volume Editors: C. Copéret, B. Chaudret
Vol. 16, 2005

Chiral Diazaligands for Asymmetric Synthesis
Volume Editors: M. Lemaire, P. Mangeney
Vol. 15, 2005

Palladium in Organic Synthesis
Volume Editor: J. Tsuji
Vol. 14, 2005

Metal Carbenes in Organic Synthesis
Volume Editor: K. H. Dötz
Vol. 13, 2004

Theoretical Aspects of Transition Metal Catalysis
Volume Editor: G. Frenking
Vol. 12, 2005

Ruthenium Catalysts and Fine Chemistry
Volume Editors: C. Bruneau, P. H. Dixneuf
Vol. 11, 2004

New Aspects of Zirconium Containing Organic Compounds
Volume Editor: I. Marek
Vol. 10, 2004

Precursor Chemistry of Advanced Materials
CVD, ALD and Nanoparticles
Volume Editor: R. Fischer
Vol. 9, 2005

Metallocenes in Stereoselective Synthesis
Volume Editor: T. Takahashi
Vol. 8, 2004

Photophysics of Organometallics

Volume Editor: Alistair J. Lees

With Contributions by

Felix N. Castellano · Herbert H. H. Homeier · Arvind Kumar · Kenneth Kam-Wing Lo · Alistair J. Lees · Conor Long · Maria L. Muro · Aaron A. Rachford · Andreas F. Rausch · Shih-Sheng Sun · Xianghuai Wang · Antonín Vlček Jr · Hartmut Yersin

Editor
Prof. Dr. Alistair J. Lees
Department of Chemistry
Binghamton University
Binghamton
NY 13902-6016, USA
alees@binghamton.edu

ISSN 1436-6002 e-ISSN 1616-8534
ISBN 978-3-642-04728-2 e-ISBN 978-3-642-04729-9
DOI 10.1007/978-3-642-04729-9
Springer Heidelberg Dordrecht London New York

Library of Congress Control Number: 2009940923

Cover design: KünkelLopka GmbH; volume cover: SPi Publisher Services

Printed on acid-free paper

Springer is part of Springer Science+Business Media (www.springer.com)

Volume Editor

Prof. Alistair J. Lees

Department of Chemistry
Binghamton University
Binghamton
NY 13902-6016, USA
alees@binghamton.edu

Editorial Board

Topics in Organometallic Chemistry Also Available Electronically

Topics in Organometallic Chemistry is included in Springer's eBook package *Chemistry and Materials Science*. If a library does not opt for the whole package the book series may be bought on a subscription basis. Also, all back volumes are available electronically.

For all customers who have a standing order to the print version of *Topics in Organometallic Chemistry*, we offer the electronic version via SpringerLink free of charge.

If you do not have access, you can still view the table of contents of each volume and the abstract of each article by going to the SpringerLink homepage, clicking on "Chemistry and Materials Science," under Subject Collection, then "Book Series," under Content Type and finally by selecting *Topics in Organometallic Chemistry.*

You will find information about the

- Editorial Board
- Aims and Scope
- Instructions for Authors
- Sample Contribution

at springer.com using the search function by typing in *Topics in Organometallic Chemistry*.
Color figures are published in full color in the electronic version on SpringerLink.

Aims and Scope

The series *Topics in Organometallic Chemistry* presents critical overviews of research results in organometallic chemistry. As our understanding of organometallic structures, properties and mechanisms grows, new paths are opened for the design of organometallic compounds and reactions tailored to the needs of such diverse areas as organic synthesis, medical research, biology and materials science. Thus the scope of coverage includes a broad range of topics of pure and applied organometallic chemistry, where new breakthroughs are being made that are of significance to a larger scientific audience.

The individual volumes of *Topics in Organometallic Chemistry* are thematic. Review articles are generally invited by the volume editors.

In references *Topics in Organometallic Chemistry* is abbreviated Top Organomet Chem and is cited as a journal.

Preface

It is a pleasure to compile and edit this volume on the *Photophysics of Organometallics* with my intention to present some of the most interesting current research in this area and also hopefully to bring it in a concise form to a wider audience. This field has changed so much over the past 30 years and it is truly unrecognizable from initial studies carried out in the late 1970s and early 1980s. Although the photochemistry of organometallic complexes, rightly considered as a distinct part of inorganic photochemistry, has been investigated for around half a century now, it was initially thought that organometallic systems were just too prone to photochemical dissociation to have sufficiently long lived electronically excited states to be able to study their characteristics and their subsequent photophysical mechanisms. The determination of luminescence from such complexes, in some cases even long lived emission in fluid solution, changed all that and made it feasible to investigate the excited states of organometallic systems in considerable detail. Hence, a new field was born.

Initially, photophysical studies of organometallic complexes were undertaken with the objective to learn about the fundamental nature of the excited states and mechanisms arising from them. The electronic characteristics of the excited state, its lifetime, its solvent and temperature dependence, the mechanism of its return to the ground state via thermal processes (including energy transfer and electron transfer pathways) and, most importantly, identification of the excited state responsible for the molecular photochemistry were all investigated for each newly found luminescent organometallic system. During this period, thoughts of practical applications were secondary to uncovering the basic nature of the excited states in these compounds, which seemed to have everything – both organic components (ligands) and inorganic components (metal centers). Thus, these molecules provided a complicated puzzle of participating excited states in the photophysics and the photochemistry. Unraveling all this information has most definitely been a challenge to the researchers in this field. However, since these fundamental studies, the area has developed to such an extent that it now reveals a wide range of important applications, for instance, in catalysis, probes, sensors, optical switches, non-linear optical materials, radiopharmaceuticals, photocleavage of DNA and organic light emitting diodes (OLEDs).

This volume is both a snapshot of current research in the field and an introduction to the various components that are of importance to it. The chapters are representative of some of the most significant experimental and theoretical research

currently being carried out, and they are written by leading scientists in the area. It is the intention to inform the reader on the many facets of the excited states in organometallic complexes and their photophysical processes. In every instance, we have made an effort to provide an introductory overview with a clear interpretation of the current research, and also to indicate any emerging applications, where appropriate. The credit for this goes to the authors of the individual chapters and I am most grateful to them for their expertise and their great efforts. The net result is a succinct representation of their research areas at this present time. Consequently, I hope that this volume is useful not only to the researchers and students already in this field, but it can help attract new people who may have an interest in it. If this field changes as much in the next 30 years as it did in the last 30 years, it will be an extraordinary one to participate in.

Binghamton Alistair J. Lees

Contents

Photophysics and Photochemistry of Organometallic Rhenium Diimine Complexes 1
Arvind Kumar, Shih-Sheng Sun, and Alistair J. Lees

Photophysics of CO Loss from Simple Metal Carbonyl Complexes 37
Conor Long

Ultrafast Excited-State Processes in Re(I) Carbonyl-Diimine Complexes: From Excitation to Photochemistry 73
Antonín Vlček Jr

Exploitation of Luminescent Organometallic Rhenium(I) and Iridium(III) Complexes in Biological Studies 115
Kenneth Kam-Wing Lo

Platinum^{II} Acetylide Photophysics 159
Maria L. Muro, Aaron A. Rachford, Xianghuai Wang, and Felix N. Castellano

Organometallic Pt(II) and Ir(III) Triplet Emitters for OLED Applications and the Role of Spin–Orbit Coupling: A Study Based on High-Resolution Optical Spectroscopy 193
Andreas F. Rausch, Herbert H. H. Homeier, and Hartmut Yersin

Index 237

Top Organomet Chem (2010) 29: 1–35
DOI: 10.1007/3418_2009_2

Published online: 13 June 2009

Photophysics and Photochemistry of Organometallic Rhenium Diimine Complexes

Arvind Kumar, Shih-Sheng Sun, and Alistair J. Lees

Abstract This review describes the photophysics and photochemistry of various diimine rhenium(I) tricarbonyl complexes. The exceptionally diverse photophysical behavior of these complexes is largely dependent on the nature of their lowest excited states. These excited states and the excited-state characteristics can be easily changed by varying the substituents on either the diimine ligands or the ancillary ligands. The prolificacy of the photophysical and photochemical properties of diimine rhenium(I) tricarbonyl complexes allows for a range of important applications such as light-emitting devices, sensors, probes for photo-polymerization, optical switches, nonlinear optical materials, radiopharmaceuticals, carbon dioxide reduction and supramolecular chemistry. We have covered the studies that best characterize the state of the field as far as the most significant fundamental photochemical advances, and the applications of the photochemistry of rhenium complexes.

Keywords Chromophores • Luminescence • Organometallics • Photochromism • Photophysics • Rhenium • Self-assembly, Sensors • Supramolecular chemistry

Contents

1 Introduction and Scope 2
2 Photophysical Properties of Rhenium Carbonyl Diimine Complexes 3
2.1 Complexes with Lowest MLCT Excited States 4
2.2 Complexes with Lowest LLCT Excited States 7
2.3 Complexes with Lowest IL Excited States 10

A. Kumar and S.-S. Sun (✉)
Institute of Chemistry, Academia Sinica, 128 Academia Road, Section 2, Nankang, Taipei, 115, Taiwan, ROC
e-mail: sssun@chem.sinica.edu.tw

A.J. Lees (✉)
Department of Chemistry, State University of New York at Binghamton, Binghamton, NY, 13902-6016, USA
e-mail: alees@binghamton.edu

3 Photoinduced Transformations and Chemical Reactions 11
3.1 Photochemical Ligand Substitution Reactions 11
3.2 Photoinduced cis-trans Isomerization Reactions 13
4 Metal-Directed Macrocyclic Complexes Incorporating Diimine Rhenium Tricarbonyl Moieties 18
4.1 Photophysical Properties 18
5 Sensors 25
6 Light-Emitting Devices 29
References 31

1 Introduction and Scope

Photophysical and photochemical phenomena are quintessential to the survival of life on our planet. The vital role played by light in biological and materials science needs no further emphasis as the value of solar energy has never been more evident than now. The recent interest in the photophysics and photochemistry of molecules with relatively long-lived highly excited electronic states has been prompted by advances in optoelectronics and by the development of molecular logic devices [1, 2]. Photochemically stable molecules with relatively long-lived fluorescent states could act as excitation wavelength-sensitive electron or electronic energy donors/acceptors when incorporated into larger supramolecular or polymeric systems [3, 4]. The potential value of incorporating such species into molecular devices increases with their increased stability and excited-state lifetime.

Organometallic rhenium complexes occupy a prominent position in the photophysics and photochemistry of transition-metal complexes. Since the first systematic studies of the photophysical and photochemical properties of the remarkably stable complexes, *fac*-$Re^{I}X(CO)_3(L)$ (where L is a bidentate–diimine ligand or two monodentate pyridyl ligands, and X is a halogen, an alkyl group, or a pyridyl ligand), in the 1970s by Wrighton and coworkers, polypyridyl complexes of rhenium(I) have played an important role in contributing to an understanding of the photophysical and light-induced electron-transfer (ET) and electronic energy-transfer (ENT) processes [5–9]. A number of investigations have appeared in the literature, based on complexes incorporating the $Re^{I}X(CO)_3$(bpy) chromophore (bpy = 2,2′-bipyridine or its derivatives). These have elegantly demonstrated medium effects [10, 11], fundamental photophysical properties of *metal-to-ligand charge transfer* (MLCT) excited states [12, 13], and physical and/or chemical processes facilitated by covalently linked chromophore-quencher systems [14, 15]. The rhenium(I)-based compounds offer several advantages for elucidating the various excited-state properties of organometallic complexes. As pointed out by Vogler and Kunkley, the photophysics and photochemistry of rhenium complexes is rich, spanning eight oxidation states from formal rhenium(0) (for example, $Re_2(CO)_{10}$) to formal rhenium(VII) (for example $MeReO_3$) [13].

The convenient and easy synthesis of *fac*–$Re^{I}(CO)_3$(diimine) complexes and the modification of the diimine ligands themselves makes systematic tuning of the

electronic properties easier for these complexes [16–18]. Altering the excited-state properties provides insight into the role of the acceptor diimine ligand in determining spectroscopic and photophysical features. Moreover, the lifetimes of the lowest excited states in these *fac*–$Re^{I}(CO)_3$(diimine)-based complexes are usually sufficiently long enough to permit energy- or electron-transfer processes to nearby components when suitable energetic and electronic conditions are satisfied [14].

In general, the excited-state properties of diimine rhenium(I) tricarbonyl complexes primarily occur through their lowest triplet excited states, due to rapid vibrational relaxation and intersystem crossing from the upper vibrational energy levels [6, 7]. Thus, the nature of the lowest-energy-acceptor ligands (either diimine ligands or bridging ligands) plays a decisive role in determining the ultimate photophysical and/or photochemical properties. Various excited states are generated, depending on the relative energy levels of the metal and ligand orbitals, as well as the extent of interaction between them. Many mononuclear diimine rhenium(I) tricarbonyl complexes are highly emissive (Φ_{em} = 0.001–0.1) and feature relatively long emission lifetimes (10 ns to 1 μs) in solution, due to the existence of lowest energy triplet-centered MLCT excited states [6, 19]. In these cases, the decay of the lowest-lying MLCT-emitting states is often primarily determined by an energy gap law effect [20]. Another prominent feature of these complexes is the large hypsochromic shift of their emission maxima on going from a fluid environment to a rigid medium and this is described as "*luminescence rigidochromism*." Here, the long-lived triplet MLCT excited state is apparently raised in energy compared to the ground-state molecule, due to the restricted ability of the solvent molecules to reorient and stabilize the excited-state dipole moment [5, 10, 12].

Understandably, there is an enormous richness in the photophysical and photochemical behavior of the excited states present in diimine rhenium(I) tricarbonyl complexes. Indeed, this plethora of molecular photophysical characteristics has led to a wide range of interesting and important applications, including their use as catalysts [21–25], sensors [26–33], probes for photo-polymerization [10, 34, 35], optical switches [36–45], light-emitting materials [46–52], nonlinear optical materials [53–56], binding or photocleavage of DNA [57–61], and radiopharmaceuticals [62–66]. Under the purview of this article our focus will be to cover photophysical and photochemical properties and hence other aspects, such as synthetic, catalytic, pharmaceutical, etc., will not be discussed.

2 Photophysical Properties of Rhenium Carbonyl Diimine Complexes

Several transitions are possible in diimine rhenium(I) tricarbonyl complexes, such as *ligand field* (LF), *metal-to-ligand charge transfer*, *ligand-to-ligand charge transfer* (LLCT), *σ-bond-to-ligand charge transfer* (σ→π*), and *intraligand* (IL) excited states. Recently, density functional theory (DFT) and time-dependent density functional theory (TD-DFT) have provided new insights into the appropriateness of

these models [67–73]. For the "parent complexes," [Re(bpy)$(CO)_3$Cl] and [Re(bpy)$(CO)_3$(py)]$^+$, the *highest occupied molecular orbital* (HOMO) contained 50% or greater Re_d character along with ~20% contributions each from CO and Cl for [Re(bpy)$(CO)_3$Cl] and ~20% contributions from CO for [Re(bpy)$(CO)_3$(py)]$^+$. The *lowest unoccupied molecular orbital* (LUMO) consists of 80% or greater diimine ligand π* character in both cases. Thus, the lowest energy optical transition was assigned as *a metal-ligand-to-ligand charge transfer transition* (MLLCT) [67].

Similarly the HOMOs of [Re(diimine)$(CO)_3$(RNC)]$^+$ complexes contained 45% or greater Re_d character and 27% or greater RNC character in general, where RNC is 6-dimethylphenylisocyanide and diimine is phenanthroline derivatized with electron-donor groups or electron-withdrawing groups, whereas the LUMOs contained >81% diimine π character [68, 69]. Hence, the lowest optical transition was assigned as MLLCT. The HOMOs of complexes of the type [Re(bpy)$(CO)_3(ER)_2$], where ER = NHPh, N(4-CH_3Ph), PPh_3, were located on the amido and phosphido ligands and the LUMOs were located on the π(bpy) levels. Thus, the lowest energy transition was assigned as LLCT and emission as ^{3}LLCT for these complexes [70].

2.1 Complexes with Lowest MLCT Excited States

The MLCT absorption band of the rhenium carbonyl complexes often lies at lower energy on the shoulder of the π–π* diimine *ligand-centered* transition (LC); hence, both the ^{1}MLCT and ^{1}LC levels are often populated simultaneously. Further, the ^{3}MLCT and ^{3}LC vary in energy relative to one another. Consequently, emission spectra are often found to occur in the 500 nm region with strong vibronic character consistent with a large ^{3}LC contribution; in other cases the spectra occur near 600 nm which are structureless and assignable to a ^{3}MLCT state. However, as the emission envelope of the coordinated diimine ligand is red-shifted from that of the free ligand, a combination of ^{3}LC and ^{3}MLCT states is often employed to account for the emission behavior (see Fig. 1).

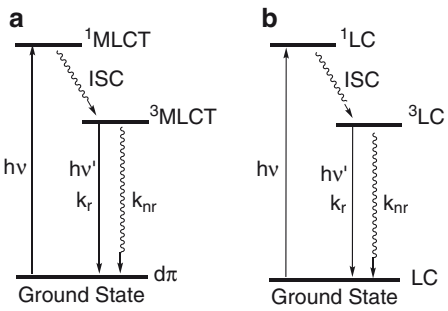

Fig. 1 Jablonski diagram for [Re(diimine)$(CO)_3$L] complexes: (**a**) MLCT model, (**b**) ligand-centered model. The k_r and k_{nr} are the radiative and nonradiative decay constants from the excited state to the ground state

These bands show negative *solvatochromism* as revealed by band shifts to lower energy in less polar solvents [5, 7, 8, 12]. The direction of the solvent dependence is associated with a reduced (and reversed) molecular dipole in their MLCT excited states. Emissions from these complexes are typically broad and structureless, and they also often exhibit a *rigidochromic effect* [7–12]. Tables 1 and 2 summarize the luminescence characteristics and environmental effects on absorption and emission maxima for rhenium(I) tricarbonyl diimine complexes.

Both the emission quantum yields and lifetimes are significantly increased on cooling the solution to 77 K, implying that the radiative decay pathways are favored in the more rigid environment; the emission lifetimes are typically governed by the *energy gap law* [17, 20, 74, 75]. Table 3 summarizes the excited-state decay parameters for the MLCT excited states of *fac*–[ClRe^{I}(4, 4′–$(X)_2$–bpy)$(CO)_3$] complexes (where 4,4′–$(X)_2$-bpy is 4,4′-disubstituted-2,2′-bipyridine).

These complexes also usually exhibit substantial photostability under visible light irradiation and, due to their relatively long-lived triplet excited-state characteristics, the emission lifetimes are easily quenched by bimolecular electron- and/or energy-transfer processes in solution [6, 76]. The electronic structures of MLCT excited molecules of diimine rhenium(I) tricarbonyl complexes can be viewed as a charge-separated species, [LRe^{II}$(CO)_3$(diimine$^{\bullet-}$)]*, with an essentially oxidized

Table 1 Luminescence characteristics for various [LRe(CNx)$(CO)_3$](PF_6) complexes (CNx = 2, 6-dimethylphenylisocyanide) in EtOH:MeOH (4:1, v/v) (data taken from [68])

	λ_{em} (10^3 cm^{-1})		τ_{em}(μs)	τ_{em}(μs)	Φ_{em}
L	77 K	298 K	77 K	298 K	298 K
1,10-Phenanthroline	21.8	19.7	65	8.6	0.77
	20.4				
	19.1				
	17.7				
5-Chloro-1,10-phenanthroline	21.1	19.1	171	1.5	0.78
	19.7				
	18.3				
	17.1				
5-Nitro-1,10-phenanthroline	20.4		322		
	19.0				
	17.8				
5-Methyl-1,10-phenanthroline	21.6	19.6	231	20.2	0.83
	19.3				
	18.8				
	17.5				
5,6-Dimethyl-1,10-phenanthroline	20.7	20.3	229	30.9	0.56
	20.4	19.3			
	18.0				
	16.6				
1,10-Phenanthrolinopyrrole	20.4	18.5	268	6.2	0.11
	18.6				
	17.3				
	16.0				

Table 2 Environmental effects on absorption and emission maxima of $[ClRe(CO)_3L]$ (data taken from [6])

L	Environment (*T*, K)	First λ_{abs} (10^3 cm^{-1})	λ_{em} (10^3 cm^{-1}) (Φ_{em}, ±15%)	τ (μs)
Phen	CH_2Cl_2 (298)	26.3	17.33 (0.36)	0.3
	Polyester resin (298)		18.52	3.67
	EPA (77)		18.94 (0.33)	9.6
5-Cl–phen	CH_2Cl_2 (298)	25.91	17.12	
	Pure solid (298)		17.99	
	EPA (77)		18.69	6.25
5-Br–phen	Benzene (298)	25.32	17.15	≤0.65
	CH_2Cl_2 (298)	25.84	17.12 (0.20)	
	MeOH (298)	26.88	17.04	
	Pure solid (298)		17.83	
	Polyester resin (298)		18.32	2.2
	EPA (77)		18.69 (0.20)	7.6
5-Me–phen	Benzene (298)	25.65	17.00	≤0.65
	CH_2Cl_2 (298)	26.32	17.01 (0.30)	
	MeOH (298)	27.05	17.00	
	Pure solid (298)		18.42	
	Polyester resin (298)		18.48	3.5
	EPA (77)		18.83 (0.33)	5.0

Table 3 Excited-state decay parameters for the MLCT excited states of *fac*-$[ClRe^{I}(4,4'\text{-}X_2\text{-bpy})(CO)_3]$ in THF (data taken from [17])

X	λ_{em} (nm) 77 K	λ_{em} (nm) 295 K	Φ_{em}	τ (μs) 77 K	τ (ns) 295 K	10^4k_r, s^{-1} (295 K)	10^6k_{nr}, s^{-1} (295 K)
NEt_2	501	575	0.033	12.5	412	7.9	2.4
NH_2	502	573	0.020	11.0	262	7.8	3.7
$NHCOCH_3$	535	620	0.0073	4.60	65	11.0	15.0
OCH_3	525	630	0.0028	3.66	26	10.0	37.0
CH_3	530	626	0.0057	3.45	49	12.0	20.0
H	540	642	0.0031	3.12	39	8.0	26.0
Ph	560	647	0.0084	4.36	56	15.0	18.0
Cl	580	700	0.0006	1.15	9	6.7	110.0
CO_2Et	598	715	0.0014	2.93	15	9.3	67.0
NO_2	670	780	<0.0001	0.86	<6	1.7	167.0

metal center and reduced diimine ligand. The MLCT excited state experiences a decrease in the extent of Re-CO π-back bonding, and this effect can be easily monitored by time-resolved IR spectroscopy and time-resolved resonance Raman spectroscopy [77, 78]. Indeed, the nanosecond time-resolved IR spectrum of $ClRe(CO)_3(bpy)$ shows an average shift to higher energy by 55 cm^{-1} in the three ν(CO) bands and the transient infrared spectrum of $[(4\text{-Me-py})Re(phen)(CO)_3)]^+$ shows an average shift to higher energy by 46 cm^{-1} in the three ν(CO) bands [79, 80]. Thus, time-resolved IR spectroscopy has been able to differentiate the lowest excited state between MLCT or IL levels in $ClRe(bpy)(CO)_3$ containing phenyle-

neethynylene oligomers [81]. Transient resonance Raman spectroscopy also provides evidence, based on the resonance enhancement of the ν(CO) Raman peaks, for identifying the lowest excited states and possible excited-state intermediates [82, 83]. In such cases, intense excited-state Raman lines have been observed that are associated with the radical anion of the diimine ligand.

2.2 Complexes with Lowest LLCT Excited States

In complexes with both reducing- and oxidizing-type ligands, excited states can arise that are the result of charge transfer from one ligand (donor) to another ligand (acceptor). Several rhenium tricarbonyl-based chromophore-quencher complexes are known to have lowest excited states featuring LLCT character [16, 84]. Owing to the very weak electronic interaction between the donor and the acceptor components, the extinction coefficients for such LLCT bands are usually very low. For example, the extinction coefficient of the LLCT band for complex $[(py–ptz)Re^{I}(CO)_3(bpy)]^+$ is only 2.4 M^{-1} cm^{-1} [85]. Nevertheless, the LLCT state can be indirectly populated by MLCT excitation followed by an intramolecular electron-transfer process. For example, in the case of the chromophore-quencher complex $[(py–ptz)Re^{I}(CO)_3(bpy)]^+$, optical excitation into the dπ(Re) to π*(bpy) MLCT transition generates the excited-state species, $[(py–ptz)Re^{II}(CO)_3(bpy^{\bullet-})]^+$ [86]. Thereafter, rapid electron transfer from py-ptz to Re^{II} takes place, with a determined rate constant higher than 4.8×10^9 s^{-1}. The species subsequently formed is $[(py–PTZ^{+\bullet})Re^{I}(CO)_3(bpy^{\bullet-})]^+$, which can be considered as a py–PTZ to bpy charge transfer (LLCT) excited state (see Fig. 2). Direct evidence for the formation of this charge-separated species has been provided from time-resolved resonance Raman and absorption spectroscopies, revealing that the complex has both the characteristics of the reduced $bpy^{\bullet-}$ and oxidized $PTZ^{+\bullet}$ moieties [84, 87, 88]. The LLCT excited state decays to the ground state via back electron transfer from bpy to ptz with a rate constant of 1.1×10^7 s^{-1} [87]. Typically, the nonradiative decay parameters of the LLCT excited states in such complexes with similar bipyridyl derivatives follow the *energy gap law*. Figure 2 below shows the electron-transfer processes taking place in such systems.

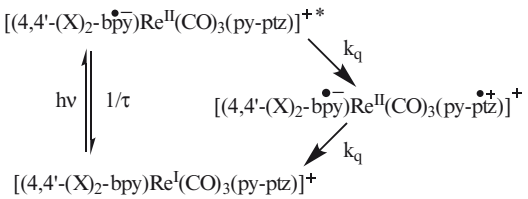

Fig. 2 Excited state dynamics of $[(py\text{-}PTZ)Re^{I}(CO)_3(bpy)]^+$ (reproduced with permission from [87])

In another typical case, the complex $[Re^{I}(MQ^{+})(CO)_3(dmb)]^{2+}$, (where MQ^{+} = *N*-methyl-4,4′–bipyridinium and dmb = 4,4′-dimethyl-2,2′–bipyridine) the optical excitation (400 or 355 nm) of the complex populates a Re→dmb ^{3}MLCT excited state $*[Re^{II}(MQ^{+})(CO)_3(dmb^{\bullet-})]^{2+}$. A picosecond $dmb^{\bullet-}\rightarrow MQ^{+}$ interligand electron transfer (ILET) follows, producing a Re→MQ^{+} MLCT excited state $*[Re^{II}(MQ^{\bullet})(CO)_3(dmb)]^{2+}$. The ILET rate (8–18 ps, depending on solvent) being accelerated by a combination of large electronic coupling through Re^{II} and vibrational excitation of the ^{3}MLCT (dmb) precursor state (see Fig. 3) [89].

Because of the generally nonemissive nature of LLCT states, their excited-state properties can be studied only by transient spectroscopy, or indirectly analyzed by their effect on the MLCT excited-state lifetimes of the emissive chromophores. However, if the electron-donor ligand is not stable toward oxidation, then subsequent photochemical reactions may occur. Thus, these irreversible photochemical reactions can be monitored to quantitatively determine the photophysical parameters

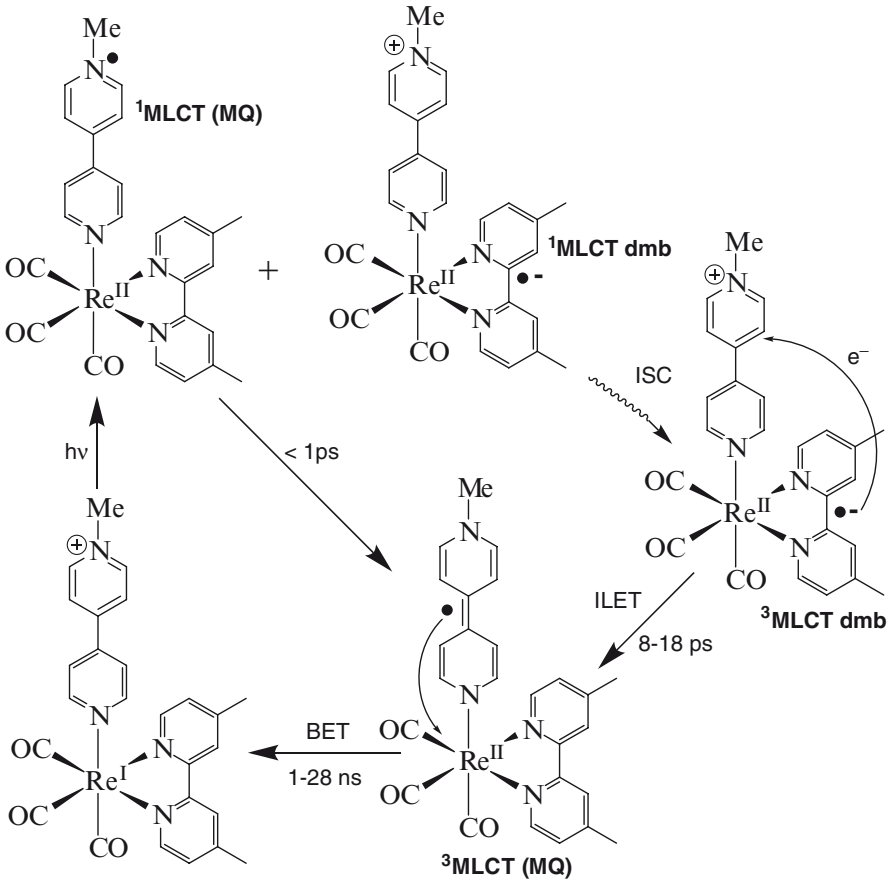

Fig. 3 Excited state dynamics of $[Re^{I}(MQ^{+})(CO)_3(dmb)]^{2+}$ (reproduced with permission from [89])

of LLCT states [90–95]. Figure 4 depicts the excited-state processes of a typical example, involving the rhenium chromophore coordinated to a 1, 2-diamine donor ligand [95]. Initial photoexcitation produces the relaxed dπ(Re)→π*(bpy) MLCT excited state.

The MLCT state relaxes via radiative and nonradiative decays to the ground state (k_d path) or by forward intraligand electron transfer (ET) from the diimine donor to the photoexcited Re(I) center (k_{FET}) path. Forward ET reaches the LLCT state, which can relax either by back ET (k_{BET} path) from $bpy^{\bullet-}$ to the diimine radical cation or by C-C bond fragmentation of the diimine radical cation (k_{BF} path). From the luminescence and transient absorption studies, it is clear that the forward ET from the MLCT state is very fast; the MLCT emission decays with $k_{FET} = 2 \times 10^9 s^{-1}$, which is nearly 10^3-times faster than the normal MLCT decay rate ($k_d \approx 4.8 \times 10^6\ s^{-1}$). The dynamics of triplet→singlet intersystem crossing in the LLCT state may play a role in determining the rate of back ET because it is formed by forward ET from ^{3}MLCT (e.g., ^{3}MLCT→^{3}LLCT). Since the product of back ET has singlet spin multiplicity, intersystem crossing must precede decay of ^{3}LLCT via back ET. It was found that the bond fragmentation competes very effectively with back ET. The rate for bond-fragmentation and back electron transfer are $5 \times 10^5\ s^{-1}$ and $8.3 \times 10^7\ s^{-1}$, respectively [95].

Another important type of LLCT state arising in diimine rhenium(I) tricarbonyl complexes is found in $IRe^I(CO)_3$(diimine) complexes. When I^- replaces Cl^- or Br^-, the lowest excited state changes from being MLCT in nature to that of XLCT (*halide-to-ligand charge transfer*) in character (see Fig. 5) [18, 96]. For the case of $IRe^I(CO)_3$(bpy), a broad but distinct low-energy band appears around 780 nm. In contrast to the above-mentioned LLCT (L to diimine) transitions, which are weak due to the very small electronic coupling between the donor and acceptor, the halide p_y and π*(diimine) orbitals are now directly coupled by either sharing the

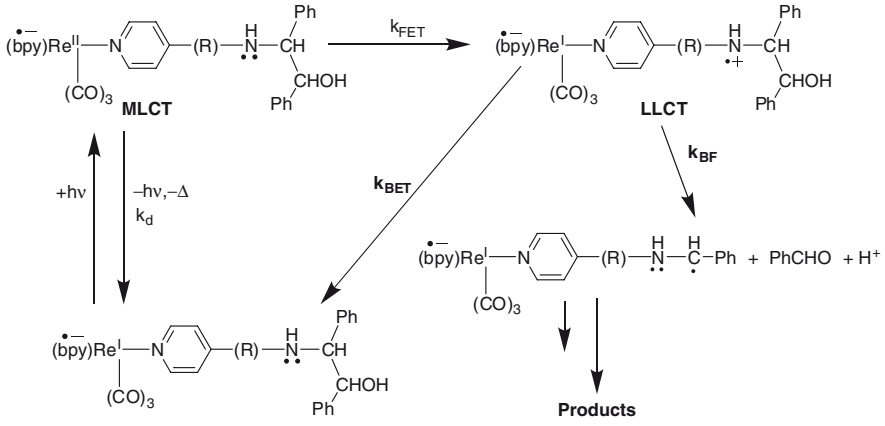

Fig. 4 Excited state dynamics of C–C bond fragmentation (reproduced with permission from [95])

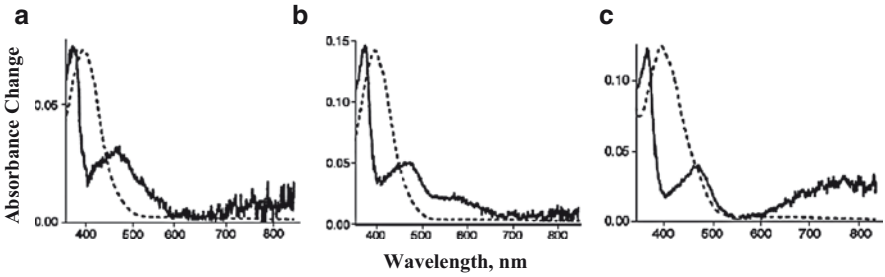

Fig. 5 Ground state (*broken line*) and transient absorption (*solid line*) spectra of $Re(X)(CO)_3(bpy)$ in THF measured 10 ns after laser excitation at 460 nm. (**a**) X=Cl, (**b**) X=Br, (**c**) X=I (reproduced with permission from [96])

metal d_{yz} orbital or by through-space p_y–π* interactions. Thus, XLCT transitions exhibit comparable or slightly weaker intensities compared to MLCT transitions. The XLCT state is a better luminophore because of the higher emission quantum yields and has a longer lifetime compared to the MLCT excited state due to lower nonradiative decay to the ground state. The lifetime of the excited state depends on the diimine ligand which affects both emission and nonradiative decay constant. The MLCT state is more sensitive to the changes of diimine than the XLCT state.

2.3 Complexes with Lowest IL Excited States

Lowest IL states usually occur in complexes containing extended conjugation of the ligands, where the electron is excited predominantly from the ligand-based n- or π-orbitals. Typical characteristics of ^{3}IL emissions are structured profiles and longer emission lifetimes, compared to ^{3}MLCT transitions [97–102]. The emission lifetime is sometimes greatly influenced by temperature or medium effects, though, due to the presence of close-lying ^{3}MLCT states [103]. An early report by Wrighton and coworkers revealed that the complex $ClRe(CO)_3$(3-benzoylpyridine) exhibits typical ^{3}MLCT emission in benzene solution at room temperature [97]. However, in a 77-K EPA glass, the rigidochromic effect shifts the ^{3}MLCT state to higher energy and, thus, multiple emissions from both ^{3}MLCT and ^{3}IL (n–π*) excited states can be observed. Here, the ^{3}MLCT and ^{3}n–π* states are clearly not thermally equilibrated in this glassy environment at low temperature [97]. Many $LRe^I(CO)_3$(X–phen) complexes, where L is a Lewis base and X–phen is phenanthroline or its derivatives, exhibit overlapping emissions from both ^{3}MLCT and ^{3}IL ($\pi \rightarrow \pi^*$) excited states at room temperature. By varying L, X–phen, and temperature, the emitting states can be tuned from ^{3}MLCT to $^3\pi \rightarrow \pi^*$ in nature. More structured emissions were observed at 77 K, as well as in complexes with higher ^{3}MLCT excited states [68, 69, 98]. The excited-state decays are also more complicated at low temperature and feature bi- or multiexponential kinetics [99]. Meyer and

coworkers revealed that the observed ^{3}MLCT emission in a system with close-lying ^{3}MLCT and ^{3}IL states does not necessarily prove that the lowest excited state is ^{3}MLCT in character [104]. In the case of *fac*-[ClRe(CO)$_3$(dppz)] (dppz is dipyrido[3,2-a:2′,3′-c]phenazine), the lowest excited state was determined to be the $^3\pi$ –π^* excited state by time-resolved resonance Raman spectroscopy, although the emission apparently originates from the ^{3}MLCT excited state. The above chloro complex is a MLCT emitter at room temperature but $\pi\pi^*$ emitter at 77 K. Replacing Cl by PPh$_3$ yields emission originating from the $^3\pi$ –π^* state, which is also confirmed by time-resolved resonance Raman spectroscopy [104].

3 Photoinduced Transformations and Chemical Reactions

3.1 Photochemical Ligand Substitution Reactions

Photochemical ligand substitution (PLS) reactions of many transition-metal complexes are known to proceed via a ^{3}LF excited state that is thermally accessible from a ^{3}MLCT state, especially when the photosubstitution involves dissociative mechanisms [105]. The temperature dependence of the emission yield and lifetime of photosubstitution reactions renders an activated process proceeding from ^{3}MLCT to ^{3}LF states, as shown in Fig. 6a. The constants k_{d1} and k_{d2} are nonradiative decay rate constants for the ^{3}MLCT and ^{3}LF states to ground state, respectively. The rate constants k_{th} and k_{-th} are the forward and backward internal conversion rates between the ^{3}MLCT state and the photoexcited state thermally accessible from the ^{3}MLCT state. The thermodynamic analysis of the data unambiguously supports that the photoexcited state is ^{3}LF (see Fig. 6a). There are three possible relaxation pathways

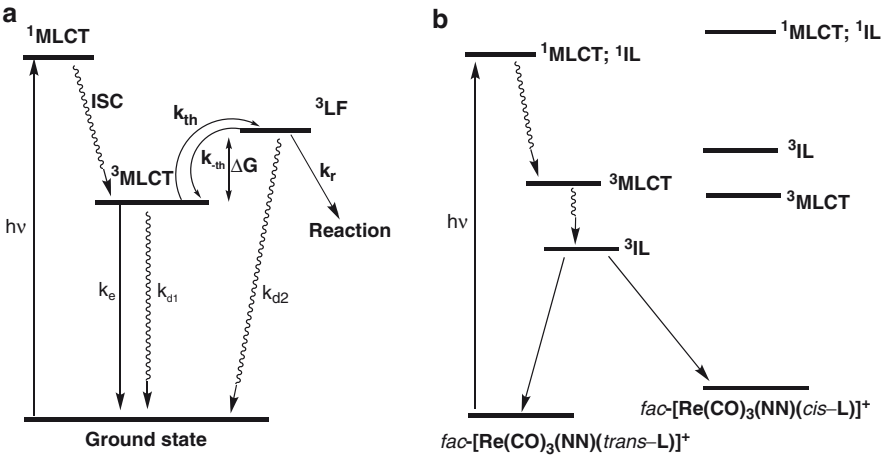

Fig. 6 Simplified energy diagram describing the mechanism of the (**a**) PLS reaction of *fac*-[Re^I(bpy)(CO)$_3$(PR$_3$)]$^+$ and (**b**) *trans-cis* isomerization of *fac*-[Re^I(NN)(CO)$_3$(L)]$^+$

through the ^{3}LF state: (1) photodissociation that gives reaction products, (2) photodissociation and successive recombination, and (3) direct nonradiative decay to the ground state. Both the nonradiative decay and reaction pathways from the ^{3}LF state are extremely fast with rate constants > 10^{14} s^{-1}, and this suggests that the ^{3}LF excited states of the complexes have repulsive potential curves and that the temperature-dependent nonradiative decay processes proceed via CO ligand dissociation and successive recombination of the produced species in rhenium(I) diimine complexes of the type $[Re(X_2bpy)(CO)_2(PR_3)]^+$ [106].

Many complexes of the type $Re(bpy)(CO)_3L$, where L is a weak field ligand like pyridine or halide, are photostable to irradiation into the MLCT manifold. Efficient photochemical ligand substitution is found for *fac*–$[Re(X_2bpy)(CO)_3(PR_3)]^+$ to yield substitution *trans* to the axial PR_3 group by CO loss (X_2bpy is 4,4′-X_2 −2,2′-bpy, where X is H, CF_3, OEt or Ph, and PR_3 is a tertiary phosphine or phosphite) and the biscarbonylrhenium(I) diimine complexes, *cis-trans*-$[Re(X_2bpy)(CO)_2(PR_3)L]^{n+}$, were formed with chloride, py or CH_3CN as the entering group [107]. The activation energies for photosubstitution were found to be between 3,200 and 4,800 cm^{-1}, and photosubstitution yields were generally in the range of 0.1–0.55. Labeling (^{13}CO) studies demonstrated that the axial CO, which is *trans* to the phosphorus ligand, was indeed labilized, consistent with a dissociative mechanism and an associated excited-state kinetic *trans*-effect [106].

The photostability of *fac*–$[Re(bpy)(CO)_3py]^+$, *fac*–$[Re(bpy)(CO)_3Cl]$, or related bipyridyl-substituted complexes is proposed to be due to the weaker *trans*-labilizing ability of the py or chloride ligand compared to a phosphorus donor, and not because of a larger activation energy being required to reach the ^{3}LF state. For the *fac*–$[Re(bpy)(CO)_3(PEt_3)]^+$ complex, both possible *trans*-axial labilization products are observed in CH_3CN solution, i.e., *trans* to axial-phosphine as well as *trans* to axial-CO labilized substitutions, and $Re(bpy)(CO)_2(PEt_3)(CH_3CN)^+$ and $Re(bpy)(CO)_3(CH_3CN)^+$ are found in a 2:1 ratio. This may indicate that the kinetic *trans*-effect of the triethylphosphine group and CO is comparable [108].

Ishitani et al. reported that the PLS reactions of *fac*–$[Re(4,4'\text{-}X_2\text{-bpy})(CO)_3Cl]$ (X = H, MeO, NH_2, CF_3) are induced by high-energy (UV light) photoexcitation and yielded solvato complexes, *fac*–$[Re(4,4'\text{-}X_2\text{-bpy})(CO)_2(solvent)Cl]$ [109]. The fact that the PLS reaction rate was not affected by the presence of O_2, but the emission was efficiently quenched with a rate constant of 3.6×10^9 M^{-1} s^{-1} by O_2, reveals that the PLS reaction does not occur from the emissive state. Mechanistic studies, including TRIR measurements, clearly reveal that the PLS reaction does not proceed via the lowest ^{3}MLCT state, but instead it occurs via higher vibrational levels of the ^{1}MLCT and/or higher electronic states, such as $^1\pi\rightarrow\pi^*$, and higher-lying Re→bpy and Re→CO ^{1}MLCT states. The TRIR measurements have indicated that the CO ligand dissociates with subpicosecond rates after excitation, leading to vibrationally hot CO-loss photoproducts (with a very broad TRIR band) after 1 ps of excitation and the relaxed photoproduct (with a distinct TRIR band) forms during 50–100 ps after excitation [109].

Photosubstitution of diphosphine-bridged bimetallic complexes utilizes 1,2-*trans*-bis-diphenylphosphinoethylene as the bridging ligand and yields only *trans*-substituted

products with quantum yields as high as 0.35 [110]. This is proposed to be due to self-quenching, i.e., intramolecular energy transfer from the high-energy chromophore that proceeds efficiently to the low-energy photostable ligand-substituted chromophore. In fact, TRIR studies have demonstrated this rapid energy transfer by monitoring the change in the ground and excited-state Re-CO modes.

The homolysis of the metal–alkyl bond for $[Re(R)(CO)_3(diimine)]$ (R = CH_3 and C_2H_5) is also reported [111, 112]. The optical excitation of an CH_3CN solution of $[Re(Et)(CO)_3(dmb)]$, where dmb is 4,4′-dimethyl-2,2′-bipyridine, produces within 2 ps the radicals $Et^{\bullet}$ and $[Re(MeCN)(CO)_3(dmb)]^{\bullet}$ together with an excited state, which undergoes a slower (~90 ps) conversion to the same radicals. The photoactive excited state was identified as ^{3}MLCT with an admixture of ^{3}SBLCT (*sigma bond-to-ligand charge transfer*) character [112]. For the ethyl complex, ^{3}SBLCT is the lowest state, while in the methyl complex, this lies above both the singlet and triplet MLCT states. The excited state decay of $[Re(C_2H_5)(CO)_3(dmb)]$ led only to homolytic cleavage of the Re–C_2H_5 bond, whereas for $[Re(CH_3)(CO)_3(dmb)]$, both homolytic cleavage of the Re–CH_3 bond and decay from the excited state to the ground state occurred in a 1:1 ratio.

3.2 Photoinduced cis-trans Isomerization Reactions

Complexes incorporating a ligand with a lowest nonemissive ^{3}IL excited state that is energetically tunable by a light-induced structural change (such as in stilbene or azobenzene derivatives) have potential applications as light-switching materials. When the olefin or azo groups are in *trans*-conformations, the complexes are weakly or nonemissive due to the presence of lowest nonemissive $^3\pi$ –π^* or ^{3}n–π^* excited states. Excitation into their ^{3}MLCT excited state sensitizes the $^3\pi$ –π^* or ^{3}n–π^* excited states and results in *trans-cis* isomerization of the ligand. The $^3\pi$ –π^* or ^{3}n–π^* excited states in the *cis*-conformer are shifted to a higher energy position compared to the emissive ^{3}MLCT state and, consequently, strong emission is observed [36–38]. Figure 6b depicts the simplified energy diagram of *trans-cis* isomerization. Figure 7 represents the processes involved in the *trans*-to-*cis* isomerization of azo and ethylene linkages associated with complexes of the type

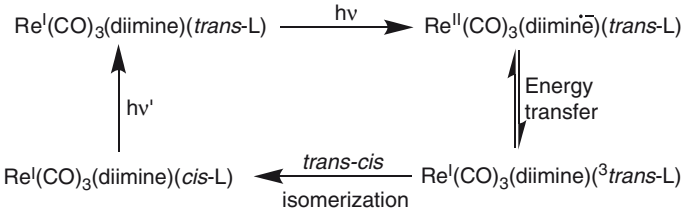

Fig. 7 Photoinduced *cis-trans* isomerization of complexes with olefin or azo linkages

$[Re(diimine)(CO)_3L]^+$, where L is the ligands shown in Fig. 8a. To achieve the reverse process of *cis* to *trans* isomerization, requires exciting the complexes at higher energy than the energy needed to cause *trans*-to-*cis* isomerization [113, 114]. The reversible *trans*-to-*cis* and *cis*-to-*trans* behavior resulting from excitations at differing frequencies was equated to a "*light-controlled photoswitch*." Several reports have taken advantage of this unique property to design a variety of photoswitching systems in recent years [36–43].

Gray et al. reported the *cis-trans* photoisomerization of $[Re(phen)(CO)_3L_1](PF_6)$ [113]. The $[Re(phen)(CO)_3(cis\text{-}L_1)](PF_6)$ complex exhibits yellow luminescence after UV excitation, whereas the *trans*-counterpart, $[Re(phen)(CO)_3(trans\text{-}L_1)](PF_6)$, is nonluminescent. Irradiation at 350 nm causes *trans*-to-*cis* isomerization while the reverse *cis*-to-*trans* isomerization was achieved by irradiating at 250 nm. $[Re(diimine)(L_3)(CO)_3]Cl$ complexes undergo reversible isomerization upon alternate irradiation at 365 nm and 254 nm [114]. The intense absorption band centered ca. 350–380 nm decreases in intensity upon irradiation at ca. 365 nm and recovers upon irradiation at ca. 254 nm. These changes are attributed to the *trans*-to-*cis* isomerization of the –CH=CH– moiety. For the azo-group containing complexes $[Re(diimine)(azo\text{-}L_3)(CO)_3]Cl$, reversible electronic absorption spectral changes were observed in degassed dichloromethane solution upon alternate irradiation at 365 and 450 nm. The spectral changes are suggested to be associated with the *trans-cis* isomerization of the –N=N– moiety.

Coordination of an azobenzene-like ligand to the Re^I center accelerates the singlet→triplet state intersystem crossing from optically prepared Franck-Condon states (for example, $^1\pi\pi^*$, ^{1}MLCT, and $^1n\pi^*$) in femtosecond time domain, thereby switching the *trans-cis* isomerization mechanism to the $^3n\pi^*$ potential energy surface. The Re^I moiety acts as an intramolecular triplet sensitizer. The ^{3}MLCT(bpy) state of *fac*–$[Re(bpy)(CO)_3L_2]^+$ undergoes a 3 ps conversion to the reactive intraligand $^3n\pi^*$ excited state. The isomerization of –N=N– is about 200-times faster than the isomerization of the –C=C– bond from the $^3\pi\pi^*$ state of the analogous Re(I) styrylpyridine complexes [115].

Moore and coworkers reported one particularly interesting proton-induced photoisomerization of the *fac*–$[Re^I(bpy)(L_4)(CO)_3]^+$ chromophore at the stilbene-like bridging ligand, because the intramolecular energy-transfer is feasible after protonation of the azacrown ether [39]. The absorption spectra of the *trans*-conformer *fac*–$[Re^I(bpy)(trans\text{-}L_4)(CO)_3]^+$ feature the $d\pi(Re)\rightarrow\pi^*(bpy)$ MLCT band at ca. 380 nm and an intense ILCT band at ca. 435 nm, localized on the azacrown ligand L_4, in which charge is transferred from azacrown ether nitrogen to the pyridyl N-atom acceptor. The ILCT band is blue shifted to ca. 320 nm in the protonated complex, owing to the protonated azacrown ether at the N-atom inhibiting the charge transfer and raising the energy level of the ILCT excited state. The complex is only weakly emissive at room temperature in both the protonated and nonprotonated forms. Prolonged irradiation of the complex shows no spectral changes, while the protonated complex shows pronounced spectral changes in absorption and enhanced emission intensity (see Fig. 8b). This is consistent with efficient *trans*-to-*cis* photoisomerization at the olefin bond in the protonated form of the complex.

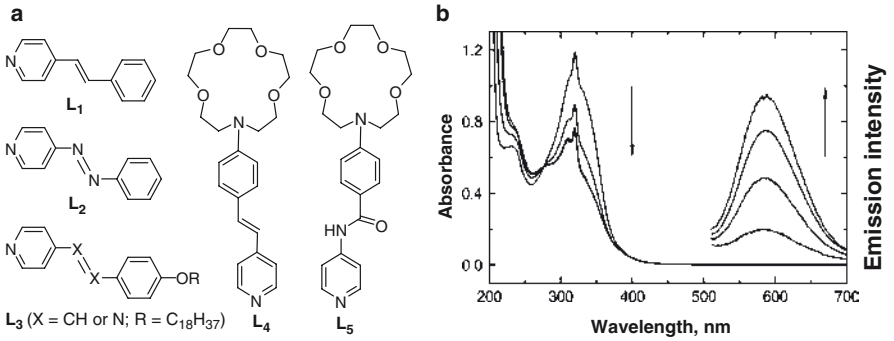

Fig. 8 (**a**) Azo, ethylenic, and crown ligands studied for photoswitch and isomerization and (**b**) absorption spectra of *fac*-$[Re^{I}(CO)_3(bpy)(trans\text{-}L_4)]^+$ in CH_3CN with excess HCl added after irradiation at 406.7 nm for 0, 30, 120, and 180 min, along with corresponding emission obtained on excitation at 380 nm (no distinct emission features were observed at wavelengths lower than 500 nm) (reproduced with permission from [39])

The increase in emission intensity of the protonated species can be attributed to a reduction in the intramolecular energy-transfer decay after isomerization to the *cis*-complex, reflecting the higher energy position of the $^3\pi$ –π^* states compared to the ^{3}MLCT states in the *cis*-styryl pyridine complex [39].

An interesting light-controlled alkali and alkaline earth metal ion switching was observed for the complex $[Re^{I}(CO)_3(bpy)L_5]^+$, where L_5 contains an azacrown ether [116]. It can release the ion in nanoseconds and recapture it in microseconds. The emission from the complex $[Re^{I}(CO)_3(bpy)L_5]^+$ is very weak and has a very short life of $\tau_{em} < 1$ ns, due to rapid quenching of the MLCT state by electron transfer from the LLCT state, with $\tau_{FET} = 500$ ps (see Fig. 9). The complex shows an intense band at 344 nm, which has been assigned to an ILCT transition, in which charge is transferred from the azacrown electron donor to the amidopyridyl electron acceptor. A weak MLCT band at 350 nm appears as a shoulder to this ILCT band. The addition of acid or metal salts results in a blue-shift of the ILCT band, with a large shift occurring on protonation. This is attributed to the interaction of the cation with the azacrown nitrogen atom, increasing its oxidation potential by raising the energy of the ILCT transition. The emission quantum yield and lifetime are increased on forming the $[Re(CO)_3(bpy)L_5]^+$–H^+ and –M^{n+} complexes. Protonation substantially increases the MLCT emission yield and lifetime by raising the energy of the LLCT state so effectively that all of the photophysics occurs via the MLCT state. Photoexcitation to the MLCT state of the metal ion-complexed form, $[Re(CO)_3(bpy)L_5]^+$–M^{n+} ($M^{n+} = Li^+$, Na^+, Ca^{2+}, or Ba^{2+}), results in cation release and, after decay to ground state, $[Re(CO)_3(bpy)L_5]^+$ recaptures the metal cation to restore the starting thermal equilibrium (see Fig. 9).

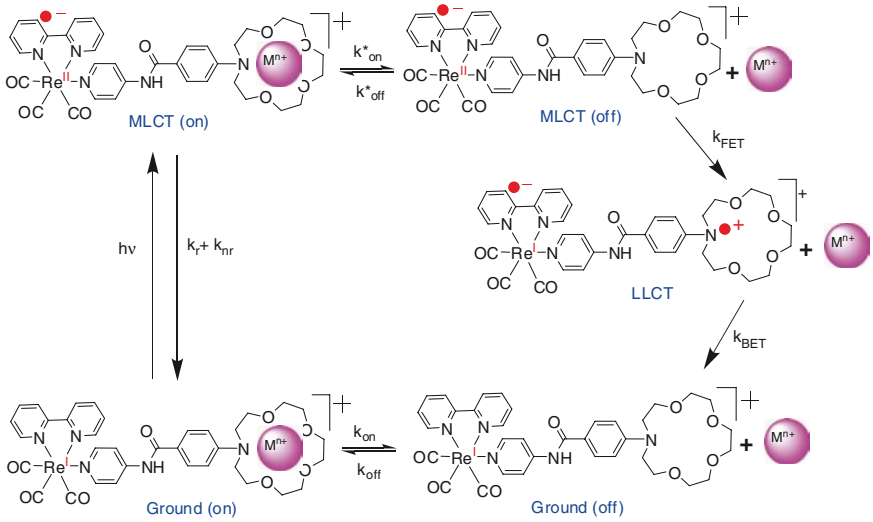

Fig. 9 General mechanism for light-controlled ion switching in the *fac*-[$Re^{I}(CO)_3(bpy)L_5$] complex

Yam's group have studied the photosensitized intramolecular ring-opening [117, 118] and ring closing [119–121] of rhenium complexes containing spirooxazine and diarylethene moieties attached to either pyridine or diimine ligands (see Fig. 10). The ring-closing process of the complexes proceeds initially with formation of the ^{1}MLCT state, which undergoes intersystem crossing to the ^{3}MLCT excited state ($\tau \leq 0.8$ ps). The ^{3}MLCT excited state then undergoes internal conversion or intramolecular energy transfer to produce the ^{3}IL excited state ($\tau \approx 1.8$ ns), which subsequently initiates the formation of the closed form of the complexes ($\tau \approx 7$ ns). In the case of complex **5** (see Fig. 10), excitation into either the IL or MLCT band of the open form in chloroform resulted in light emission with a maximum at 570 nm, which can be assigned as ^{3}MLCT phosphorescence [119]. Upon prolonged excitation at the isosbestic point ($\lambda = 352$ nm) of the complex **5**, photocyclization took place and the emission intensity at ca. 570 nm was found to decrease, indicating photoisomerization. Complex **5** shows an intense IL absorption band at ca. 352 nm and a shoulder at ca. 425 nm, which was ascribed to a MLCT [$d\pi(Re) \rightarrow \pi^*$(ligand)] transition, with some mixing of a metal-perturbed IL ($\pi \rightarrow \pi^*$) transition. Interestingly, upon UV excitation at $\lambda \leq 450$ nm into either the IL or MLCT bands, three absorption bands were generated at ca. 290, 480, and 713 nm (see Fig. 10c). This new set of absorption bands were assigned as metal-perturbed ^{1}IL transitions with mixing of ^{1}MLCT transitions in the longest wavelength absorption band originating from the ring-closed form of the complex **6**. Such a large shift of the absorption band of the cyclized form of complex **6** to the NIR region could be attributed to the planarization of the four heterocyclic rings relative to the open forms.

Thus, contrary to the twisted conformation of the ligand, the coordination of the rhenium(I) metal center forces the 2,2′-linked pyridyl and imidazoyl rings into coplanarity from their twisted conformation, causing an increase in the extent of

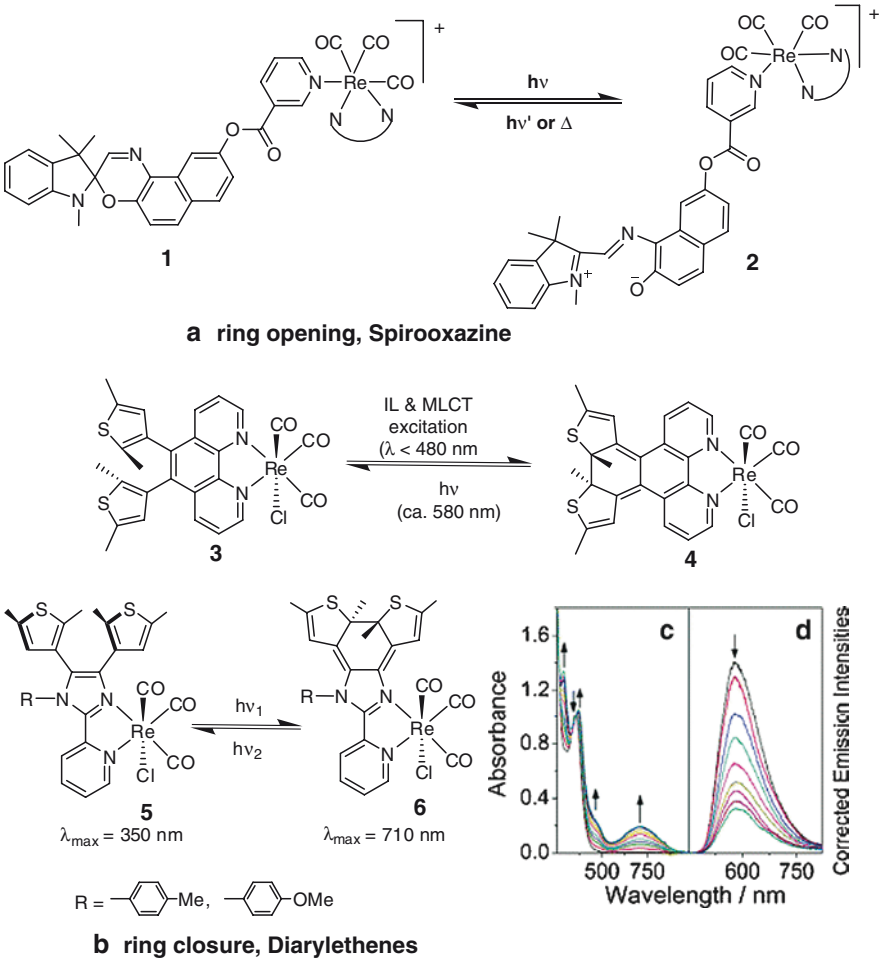

Fig. 10 Photoinduced ring opening (**a**) and ring closing (**b**) mechanisms. *Inset* shows UV–Vis absorption (**c**) and corrected emission spectral changes (**d**) of **5** in chloroform upon MLCT excitation at 410 nm at 298 K (reproduced with permission from [119])

π-conjugation. Upon photocyclization, the extent of π-conjugation in closed forms is further enhanced leading to absorption in the NIR region. In addition, excitation into the MLCT absorption band also triggered photocyclization of the open forms, implying that the photocyclization can occur via MLCT excited-state photosensitization. Upon excitation into the bands of the closed forms of complex **5**, the photochromic backward reaction took place. The quantum yield for photocyclization (ca. $\Phi_{350} = 0.4$) is much higher than the photocycloreversion reaction (ca. $\Phi_{510} = 0.004$) [119].

Unlike most metal complexes containing the *fac*–(diimine)$Re^{I}(CO)_3$ unit, which are typically highly luminescent in solution, trinuclear rhenium carbonyl compounds **7** and **8** (see Fig. 11a) show only weak luminescence ($\Phi_{em} = 0.0015$) in CH_3CN at room temperature [36]. The quenching appears to occur via intramolecular

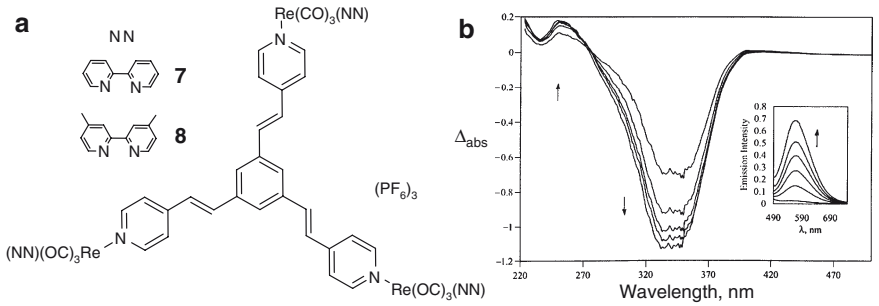

Fig. 11 (**a**) Trinuclear rhenium carbonyl complexes **7** and **8** and (**b**) UV–Vis difference spectra ($\Delta_{abs} = A_t - A_{t=0}$) of compound **7** in CH_3CN at 293 K after irradiation at 366 nm for 0, 1, 2, 3, 4, 6 h, and *inset* shows the emission spectral changes before and after photolysis (reproduced with permission from [39])

sensitization of the π→π* transitions localized on the olefin link of the bridging ligand. Prolonged photolysis into the MLCT band at 366 nm, bleaches the π→π* absorption of the bridging ligand at ca. 280–370 nm with concomitant appearance of new bands at ca. 200–270 nm and an enhancement in the emission intensity (see Fig. 11b). The determined emission quantum yields for complexes **7** and **8** are 18 and 21 times increased after 7 h photolysis at 366 nm, respectively. The UV-Vis spectral changes and large increase in the luminescence intensities for **7** and **8** are consistent with the *trans*-to-*cis* isomerization of the olefinic bond. Therefore, the nonradiative decay of energy is inhibited and highly efficient energy transfer from the ^{3}MLCT to ^{3}LF state occurs, which triggers the *trans*-to-*cis* isomerization at olefinic bonds in the complex.

4 Metal-Directed Macrocyclic Complexes Incorporating Diimine Rhenium Tricarbonyl Moieties

4.1 Photophysical Properties

In general, Re(I) complexes form corners of triangles, squares, and rectangles [27, 122–140], and the squares **14** and **15** contain two Re and two Pd/Pt complexes in opposite corners [132, 133]. Though, the spacers holding the metal centers in place are mostly based on ligands containing pyridine functionalities on opposite ends of an organic linker, diimine bridges [130, 131], alkoxides [122, 123], and hydroxyquinones [125] have also been reported. Bridging ligands containing a metal complex resulting in additional metal centers to the squares **13m**, **14m**, and **19** were also studied [129–131, 135–137]. A cage-like hexanuclear rhenium molecular prism **21** has also been reported [141–143]. Figure 12 lists metal-directed molecular

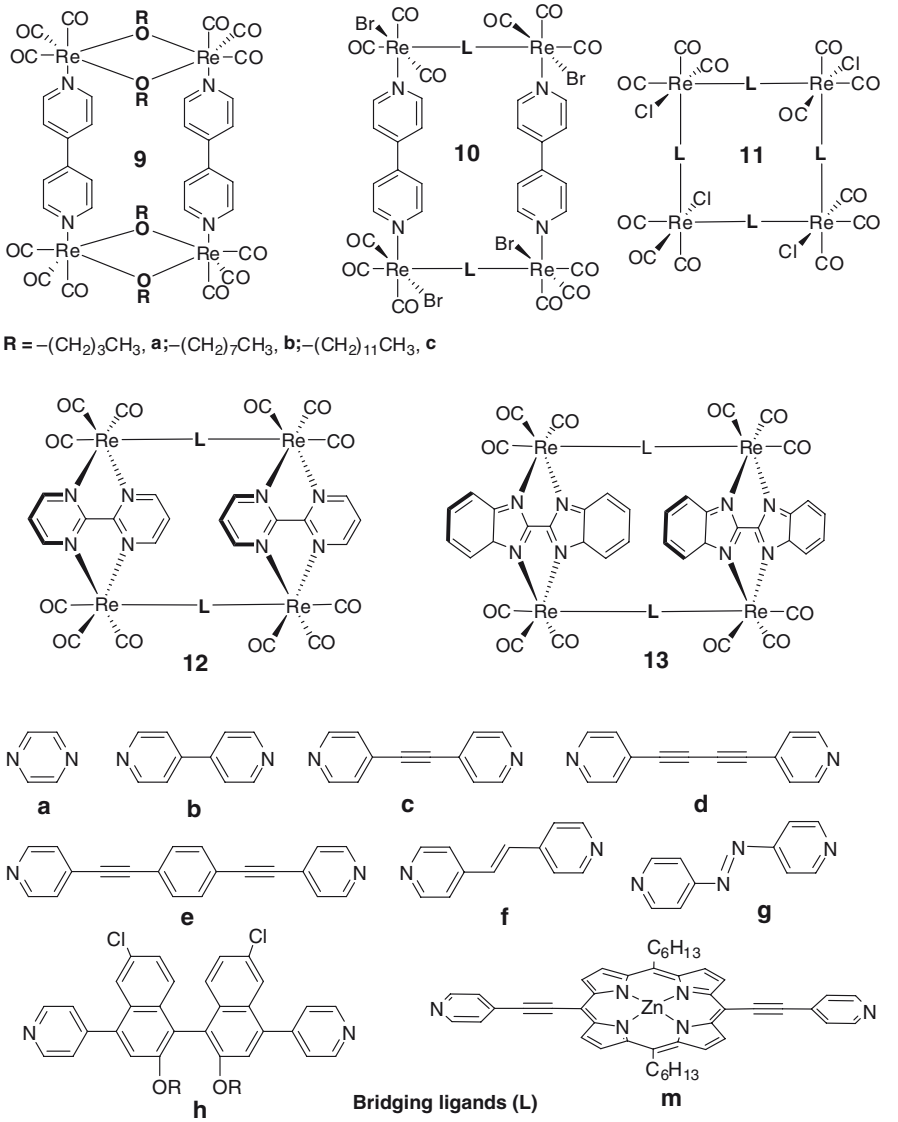

Fig. 12 Supramolecular metallacyclic rhenium(I) tricarbonyl diimine complexes

assemblies of Re(I) diimine complexes in various geometries, such as triangles, squares, rectangles, etc. In general, the absorption spectra of rhenium carbonyl-based metallacycles exhibit two main features that are assigned as bridging-ligand localized $\pi \rightarrow \pi^*$ and MLCT transitions and the emission intensity is significantly diminished to that of the mononuclear rhenium complexes. The diminished luminescence can be attributed to a decrease in the emission lifetime, thought to be quenched by the additional vibronic components.

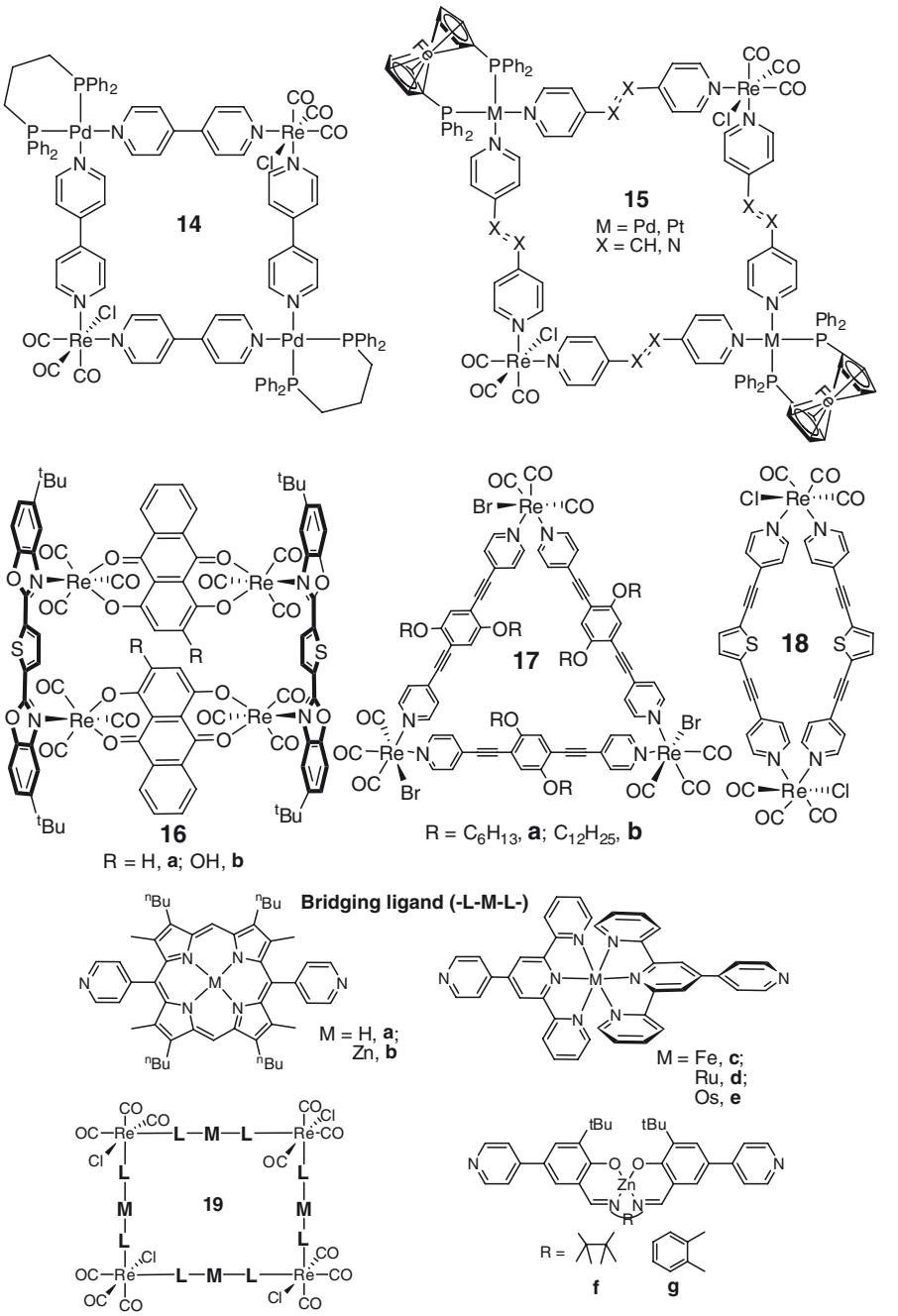

Fig. 12 (continued)

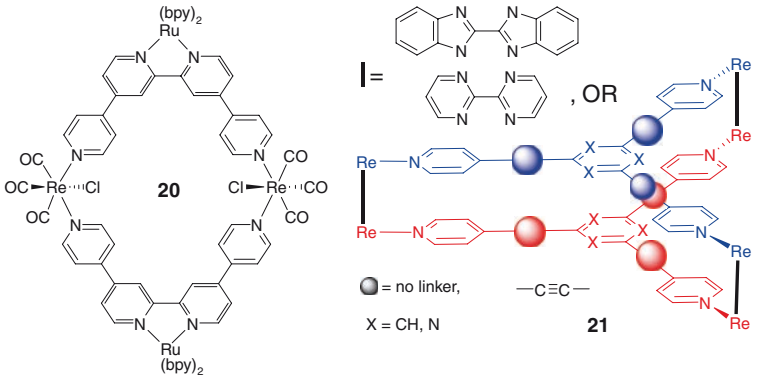

Fig. 12 (continued)

The MLCT band and emission maximum of rectangle **9c** were located near 385 nm and 600 nm, respectively [122]. The emission intensity was dependent on the solvent. The quantum efficiency and lifetime increased from 0.39×10^{-3} and 0.39 ns in CH_3CN to 6.54×10^{-3} and 212 ns in a 1:9 CH_3CN:H_2O mixture, owing to aggregation in the presence of water. Other rectangles **9** having linkers (R = H, CH_3, CH_2CH_2OH) were not emissive in solution at room temperature [122, 123]. The intense absorption maxima at ~350 nm was observed for rectangle **10**, which is ascribed to spin-allowed MLCT from the Re_d orbital to the π* orbital of the ligand, and the high-energy band ca. 260 nm is assigned to the ligand-centered transitions. Emission maxima for rectangle **10** in CH_2Cl_2 were located near 600 nm and the emission lifetimes varied from 86 to 495 ns for **10c**, **10d**, and **10e** [124]. The exceptionally longer lifetime for **10e** is probably due to the involvement of the extended π-system of the bridging ligand.

The electronic absorption of square **11** is contained with two main features of bridging-ligand localized π→π* and MLCT transitions [125–128]. In square **11a**, **11b** the lowest-energy band is solely of MLCT character, while in the other squares **11c-f**, the π→π* and MLCT bands are substantially overlapping. Square **11d** gave the characteristic ^{3}MLCT emission of Re(diimine)$(CO)_3$Cl complexes located at 635 nm with a short emission lifetime of 39 ns and a low emission quantum yield of 8.5×10^{-4} [127, 128]. The MLCT band in square **11d** is bathochromically shifted by 1,385 cm^{-1} to that of its corner complex because of additional conjugation. The shorter lifetime of the square to its corner is attributed to an enhanced nonradiative decay rate of the square, due to the lower energy of the excited state and more effective vibronic coupling [20]. The square **11g** shows an additional low-energy n→π* transition that originates from the *trans*-azp ligand (azp = 4,4′-azobipyridine), which is overlapped by a MLCT transition. Square **11d** exhibits ^{3}MLCT emission at ca. 635 nm, which is independent of excitation wavelength, with an emission lifetime of 39 ns in THF at ambient temperature. In contrast, the square **11g** is nonluminescent owing to effective intramolecular energy transfer from the initially

formed ^{1,3}MLCT excited states to the lowest nonemitting n→π* state [41]. The luminescent metallacycles **11h** exhibit electronic absorption bands at ca. 245, 305, and 360 nm in the UV region originating from the ligand π→π* transitions and additional bands at ca. 325 nm, which are probably due to the MLCT transitions [129]. The square **11h** shows two luminescence peaks ca. 412 and 536 nm in THF when excited at 360 nm. The emission peak at 412 nm can be assigned to a ligand-localized π→π* excited state, while the weaker emission at 536 nm is due to a ^{3}MLCT excited state.

Molecular rectangle **12a** shows a solvatochromic absorption MLCT band at 490, 484, and 450 nm in H_2O, DMSO, and CH_3CN, respectively, due to dπ(Re)→π*(bpm) charge-transfer transitions [130]. These rectangles are not emissive at room temperature, in agreement with results reported for the monomer, [Re(bpm)$(CO)_3$Cl] (bpm = 2,2′-bipyrimidine), which is also nonluminescent [131]. The UV–Vis spectrum of rectangle **13b** shows a band in the high-energy region, which is absent in the dinuclear benzimidazole (biz), $Re_2(CO)_6(biz)_2$ complex. This band is ascribed to the allowed dπ(Re)→π*(bpy) singlet charge transfer [132]. Unlike **12b** or other pyrimidine-edged rectangles, **13b** luminesces in solution at ca. 617 nm in tetrahydrofuran and in the solid state at ca. 572 nm. The emission lifetime varies in the range 26 ns ($CHCl_3$) to 238 ns (THF/MeOH) depending on the solvent. Owing to its long lifetime and large Stokes shift, the emission was attributed to predominantly originating from triplet charge-transfer state(s). The visible region spectra of molecular rectangles **12m** and **13m** are dominated by porphyrin-based B- and Q-bands. In particular the Q-bands for both molecular assemblies are bathochromically shifted ca. 20 and 10 nm to that of porphyrin bridge, respectively [133]. This red shifting is consistent with electron-withdrawing effects due to metal-cation coordination. Both rectangular metallacycles **12m** and **13m** show red-shifted singlet emission maxima compared to the porphyrin bridging complex at ca. 694 and 714 nm, respectively. Interestingly, the emission from the rectangle **13m** occurs from a singlet state, which is ca. 3,000 cm^{-1} higher in energy than the usual MLCT emission of Re^I(diimine)$(CO)_3$ complexes.

The luminescent heterometallasquare (Re/Pd) **14** showed emission from the ^{3}MLCT state with a maximum at ~625 nm and an emission lifetime of 17 ns in deoxygenated acetone [134]. The luminescence intensity was decreased by ca. 25-fold after the square formation. This quenching of luminescence was attributed to the Pd(II) fragment. The square **15**, containing azp as the bridging ligand, shows high-energy bands below 300 nm, which are assigned to azp-localized π→π* transitions and a broad shoulder at ca. 380 nm, which is assigned to dπ(Re)→π*(azp) MLCT [135]. The very weak absorption band that tails into the visible region comprises azp-localized n→π*, Pd-centered LF, and Fe-centered LF absorptions. The 4,4′-ethenylbipyridine (bpe) linked square **15** show bands that are characteristic of both *cis*- and *trans*-bpe. The *trans*-bpe-**15** square exhibits a band at ca. 300 nm that extends into the visible region, while the *cis*-bpe-**15** complex displays a blue-shifted band at ca. 290 nm [135]. No luminescence was observed for square **15** because of the proximity of close-lying Pd- and Fe-localized LF bands to the lowest excited state(s) that provide rapid nonradiative decay to the ground state.

The gondola-shaped molecular rectangle **16** displayed an intense absorption band in the region 230–395 nm and a weak shoulder at ca. 420 nm, which are ascribed to π→π* and MLCT transitions, respectively [136]. It also shows weak intraligand absorptions at ca. 585 and 632 nm, originating from anthraquinone bridging ligands. A set of structured emissions appeared at ca. 438 nm with high quantum yields of 0.719 for **16a** and 0.379 for **16b**. The small Stokes shift and short lifetime of **16a** indicate that the emission originates from a singlet π→π* state. Solid-state emission centered at ca. 448 and 518 nm for **16a** is attributed to the decay of the π→π* excited state of the bridging benzooxazolylthiophene (bzt) ligand and dπ(Re)→π*(bzt) excited state, respectively [136].

The absorption spectrum of triangle **17a** exhibits two broad bands at 329 and 422 nm [127]. The lowest-energy band is assigned to a mixture of MLCT and π→π* excited states. The room-temperature emission spectrum of triangle **17** in $ClCH_2CH_2Cl$ exhibits structured features with maxima at 499 and 476 nm (for **17a**) and 512 and 470 nm (for **17b**). The low-temperature emission spectrum of **17a** displays more distinct structure with bands at 463, 488, 520, and 549 nm (an average spacing of 1,188 cm^{-1}) in 2-methyltetrahydrofuran. These observations illustrate that the dual emission bands are actually a vibronic structure form of the π→π* excited state. A very small blue shift on going from the solution to a rigid glass also supports the assignment that the emission occurs from a ligand-based π→π* excited state [7, 8]. The extremely short lifetime (ca. 360 ps) and relatively high-energy emission from **17a** (Φ_{em} = 0.032) indicate that the emission is apparently ligand-localized ^{1}π→π*. However, the fast radiative decay rate (k_r ~10^8 s^{-1}) from the ^{1}π→π* excited state localized on the corresponding bridging ligand implies that the fluorescence is still able to compete with the other nonradiative decay processes. The folding motions of the hexyloxyl chains in **17a** are believed to be responsible for the rapid vibrational relaxation from the ^{3}MLCT excited state. In fact, except for the vibronic structures observed at high-energy positions, a very weak emission centered at 602 nm with lifetime 163 μs was also observed at 77 K glass. This band is assigned as a ^{3}MLCT transition on the basis of the absence of vibrational structure, although some involvement of ^{3}π→π* character cannot be completely ruled out.

The absorption spectrum of the dinuclear complex **18** features a broad band centered at 383 nm and a shoulder at 422 nm [126]. The low-energy shoulder is assigned to be MLCT in character and the band at 383 nm is assigned to the ligand localized π→π* transitions and no luminescence was observed from **18** in CH_2Cl_2 solution. The square assembly of porphyrins **19a, b** is highly soluble in CH_2Cl_2 but insoluble in water and highly chromophoric in the porphyrin Soret region, ca. 400–420 nm [137]. The square formation induces a bathochromic shift of ca. 6 nm in the Soret region because of rhenium-pyridine coordination. Near-UV fluorescence excitation studies suggest that rhenium corners serve only a structural rather than a direct photophysical role within the square framework. Single photon counting experiments yielded excited-state lifetimes of 3.0 ns for **19a** and 2.4 ns for **19b**. The squares **19c, d, e** display broad and intense visible absorptions in the region 400–600 nm, which are assigned to metal (Fe, Ru, or Os)-to-ligand (pytpy) MLCT

transitions [138]. Square **19e** exhibits an additional weak band at ca. 676 nm which is assigned to an Os^{-3}MLCT band. The bands centered between 279 and 377 nm are assigned to ligand π–π* bands and the Re-based MLCT band. Though, the corresponding corner $Re(CO)_3$(pytpy) (pytpy = 4′-pyridyl-2,2′;6′,2″-terpyridine) exhibits ^{3}MLCT luminescence at ca. 530 nm in CH_3CN with a lifetime of 646 ns, the squares **19c** and **19d** do not have any detectable luminescence at room temperature.

The lack of luminescence from squares **19c** and **19d** is attributed to the existence of metal-centered (MC) states lying in close proximity to the MLCT states [14]. The square **19e** exhibits room-temperature luminescence in deoxygenated CH_3CN solution at ca. 748 nm with a shorter lifetime ca. 42 ns and lower quantum yield 4.2×10^{-4} compared with its bridging unit $Os(pytpy)_2$. The origin of the emission is assigned to Os(II)-based ^{3}MLCT transitions. The stronger ligand field and lower oxidation potential of Os(II), compared with Ru(II) and Fe(II), results in an increased energy gap between the ^{3}MLCT and ^{3}MC states [14]. Further, the excitation of square **19e** at 380 nm, where the Re(I) moiety is the sole chromophore, and the excitation at 490 nm resulted in the same emission maxima. This lack of excitation wavelength dependence implies that the energy transfer from higher-energy state(s) (Re-MLCT or π–π*)-to-lowest Os-^{3}MLCT state(s) is very efficient. The spectral overlap between the absorption band of square **19e** and the emission from its corresponding corner $Re(CO)_3(pytpy)_2Br$ occurs from the red edge of the singlet absorption band to the triplet absorption band. This kind of overlap of absorption bands implies that the intramolecular energy transfer is most likely to be a triplet to triplet process. The incorporation of the Zn-salen complex into molecular squares **19f** and **19g** results in only subtle changes in visible-region characteristics, indicating little contribution from the Re^I charge transfer [139]. The slight blue shift of emission maxima and modest decrease of lifetime for both squares **19f** (λ_{em} = 460 nm, Φ_{em} = 0.039, τ_{em} = 0.50 ns) and **19g** (λ_{em} = 526 nm, Φ_{em} = 0.073, τ_{em} = 0.62 ns) compared to their Zn-salen bridging unit implies that there is enhanced intersystem crossing to nonemissive triplet state(s).

The heterometallacyclic assembly **20** shows high intensity-high energy bands which are consistent with intraligand π→π* transitions. The band at ca. 470 nm is assigned to Ru(dπ)→L(π*) MLCT transitions, while the band centered at ca. 363 nm is attributed to Re(dπ)→L(π*) MLCT transitions [140]. The complex exhibits intense emission centered at ca. 665 nm in aqueous and organic solvents, which is assigned as emission from Ru-MLCT. Interestingly, the emission is independent of the excitation wavelength, implying that the energy transfer within the macrocycle is efficient and that the excitation into any MLCT or π–π* excited state results in relaxation to the lowest lying Ru-MLCT state.

The molecular prism **21**, held with 2,2′-bipyrimidine, features intense bands in the near-UV region and a low-energy band at ca. 470 nm, tailing past 600 nm in CH_3CN. This low-energy band is assigned to the dπ(Re)→π*(bpm) MLCT [140]. It shows no detectable emission in CH_3CN solution at room temperature. The alkoxide-bridged neutral prism **21** shows an extended solvochromic MLCT band at ca. 549 nm in CCl_4, 488 nm in CH_3CN, and 424 nm in DMSO [141]. Hupp et al. studied the redox behavior of the prism **21** bridged with 2,2′-bisbenzimidazole

(biz) [142]. The reduction of **biz-21** to **biz-21**$^-$ state is accompanied by the appearance of absorption bands at 600, 850, and 960 nm. The singly reduced form showed a band at ca. 5,650 cm^{-1}, while this band is not present in the neutral form of **biz-21**.

5 Sensors

[Re(CO)$_3$(5-COOH-bpy)Cl] was found to have potential use as a pH sensor. It is weakly emissive in its protonated form, while it undergoes a 10-fold luminescence increase in its deprotonated form with a pK_a value of 5.39 [117, 144]. A sol–gel-based luminescence pH sensor capable of responding over a wide range of pH 2.3–12 based on the hydrolysis product of [Re(py–pzH)(CO)$_3$(pmat)]$^+$, where py–pzH = 3-(pyridine-2-yl)pyrazole; pmat = 3-*N*-(pyridine-4-methylene) (amino-propyltriethoxysilane) (see Fig. 13a), has been reported. The pH-dependence was related to the protonation/deprotonation of the 3-(pyridine-2-yl)pyrazole ligand. The excited state pK_a* for [Re(py–pzH)(CO)$_3$(py)]$^+$ is 7.05 [145]. The acid–base behavior of both monometallic [Re(bpy)(CO)$_3$(pca)]$^+$ and bimetallic [Re(bpy)(CO)$_3$(pca)Re(bpy)(CO)$_3$]$^{2+}$, pca = 4-pyridinecarboxaldehydeazine, complexes (see Fig. 13a) was opposite to the above examples. Emission increased in the presence of H$^+$ and was attributed to protonation of one of the N atoms of the –C=N–N=C– group of the pca ligand. The excited state pK_a* value for this complex is 2.7 [146].

Beer et al. reported the use of a modified 2,2′-bipyridine ligand bonded to {Re(CO)$_3$Cl} (see Fig. 13b) as the anion sensor [147]. The modified bipyridine ligand contained a macrocyclic NH-cavity capped with a calix[4]arene strapped on its back. An increase in emission was found upon addition of Cl$^-$, OAc$^-$, $H_3PO_4^-$ with a preference for OAc$^-$.

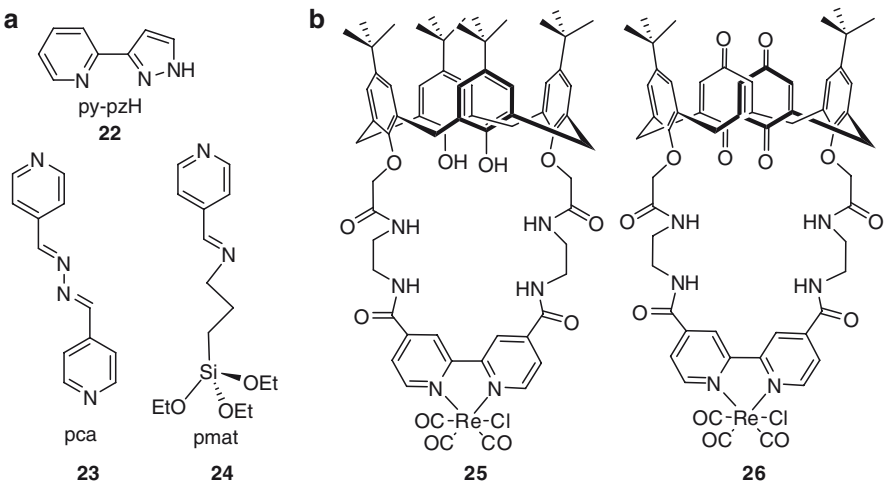

Fig. 13 (**a**) pH sensor ligands and (**b**) calix[4]arene{Re(CO)$_3$Cl}complexes

In a simpler approach, Lees' group reported that rhenium-bpy complexes of the type **27** (see Fig. 14) containing amide-type receptors served as anion binding sites [28, 148]. In this case, emission intensity was quenched in the presence of several anions: CN^-, F^-, Cl^-, Br^-, I^-, OAc^-, $H_2PO_4^-$, NO_3^-, and ClO_4^-. The complex showed strong binding affinity toward halides, cyanide, or acetate anions, while only moderate binding affinity toward dihydrogen phosphate and very weak binding affinity to nitrate or perchlorate anions. The overall order determined for binding affinity is: $CN^- > F^- > I^- > Cl^- \sim Br^- \sim OAc^- \gg H_2PO_4^- > NO_3^- > ClO_4^-$. In fact, a combination of interactions such as electrostatic, hydrogen bonding, and steric effects, apparently influence the binding affinities toward anions in this complex. The red shift of the emission band, however, indicates that the emission quenching is associated with a change in the energy of the excited state and, thus, an enhancement of nonradiative decay. The sensitivity for CN^- and F^- was so high that quenching of 10% was observed at 10^{-8} M ion concentration.

Fletcher et al. reported another interesting neutral dinuclear rhenium complex **28** (see Fig. 15) which interacts strongly with $H_2PO_4^-$, reasonably with Cl^- but only

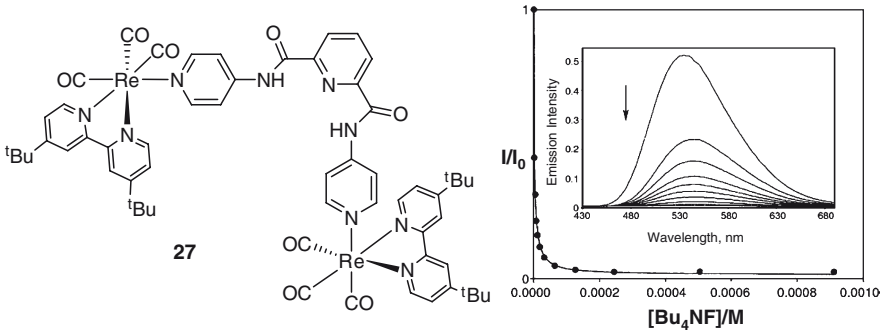

Fig. 14 The molecular structure of complex **27** and a titration plot with the addition of $[^nBu_4N]F$ ion (*right*). *Inset* shows the change in emission intensity of **27** in CH_2Cl_2 on addition of F^- ion (reproduced with permission from [28])

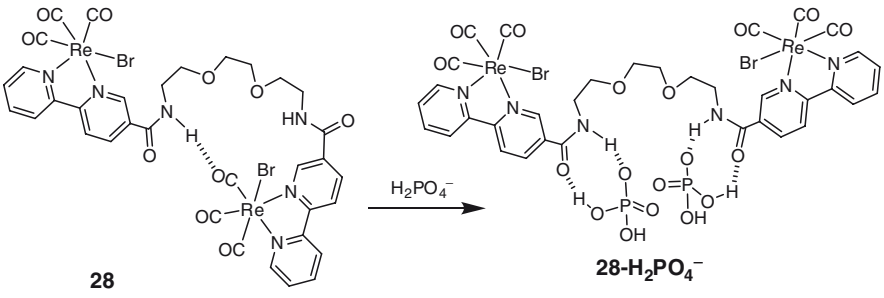

Fig. 15 Proposed mechanism for conformational change upon introduction of $[^nBu_4N]H_2PO_4$ to complex **28**

weakly with Br^-, HSO_4^-, and NO_3^-. Here, the recognition is driven by internal hydrogen bonding between the complex and the added anion [149]. The complex shows very strong affinity for dihydrogenphosphate over chloride (for $H_2PO_4^-$, $\beta_2 = 3.5 \times 10^5\ M^{-1}$; for Cl^-, $\beta_2 = 1.5 \times 10^4\ M^{-1}$). Addition of the $H_2PO_4^-$ anion to the complex gave rise to a large increase in the emission at 632 nm and a concomitant blue shift of 10 nm, related to the energy increase of the MLCT state. The increase in emission was due to the unfolding of the structure as hydrogen bonds are broken between the amide and rhenium carbonyl.

Cation recognition by luminescent rhenium carbonyl diimine complexes has also been reported. Moore and coworkers reported release and recapture of alkali and alkaline earth metal ions for $[Re(CO)_3(bpy)L_4]^+$ (vide supra) [46]. Yam et al. reported a series of interesting rhenium(I) tricarbonyl phenanthroline complexes with crown ether pendants (see Fig. 16) [150]. These complexes showed selective and specific binding properties for various metal cations of different sizes and degrees of hardness and softness by variation of the cavity size and donor atoms of the crown ether. A strong enhancement in the emission intensity was observed upon binding of the metal ions to the complexes. Such an enhancement in the emission intensity is due to blocking of the intramolecular reductive electron-transfer quenching mechanism, since the coordination of metal ions into the crown cavity reduces the ability of the donor atoms in the crown unit to quench the emissive ^{3}MLCT state by photoinduced electron transfer. The slight red shift of the emission maxima was explained by the fact that binding of the cation to the crown would decrease the σ-donating ability and stabilize the π* orbital of the phenanthroline ligand and, hence, decrease the emission intensity.

Lo et al. synthesized a number of luminescent rhenium(I) diimine-biotin complexes of the type, $[Re(N\text{-}N)(CO)_3(py\text{-}biotin)]^+$, where N–N is 1,10-phenanthroline (or derivative) and py-biotin is a pyridyl ligand attached with biotin containing different spacer-arms (see Fig. 17) [151–153]. The complexes show intense high-energy absorption at ca. 248–300 nm that are assigned to spin-allowed ^{1}IL (π→π*) (diimine and py-biotin ligands), while the less intense absorption shoulders at ca. 320–400 nm are assigned to spin-allowed dπ(Re)→π*(diimine) ^{1}MLCT transitions. Upon photoexcitation, each of these complexes exhibited intense and long-lived dπ(Re)→π*(diimine) ^{3}MLCT luminescence in solution at ambient temperature. These complexes show a very large Stokes shift of ca. 7,657 cm^{-1}. The most remarkable observation was that the biotin-incorporated rhenium complexes dis-

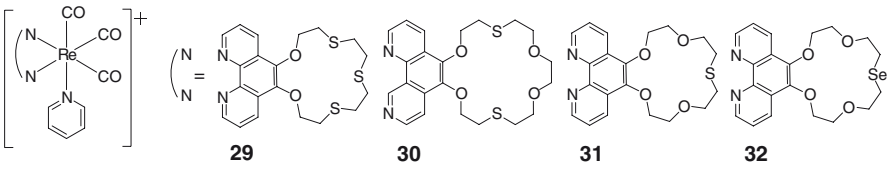

Fig. 16 Rhenium(I) tricarbonyl diimine complexes with crown ether pendants as metal cation sensors

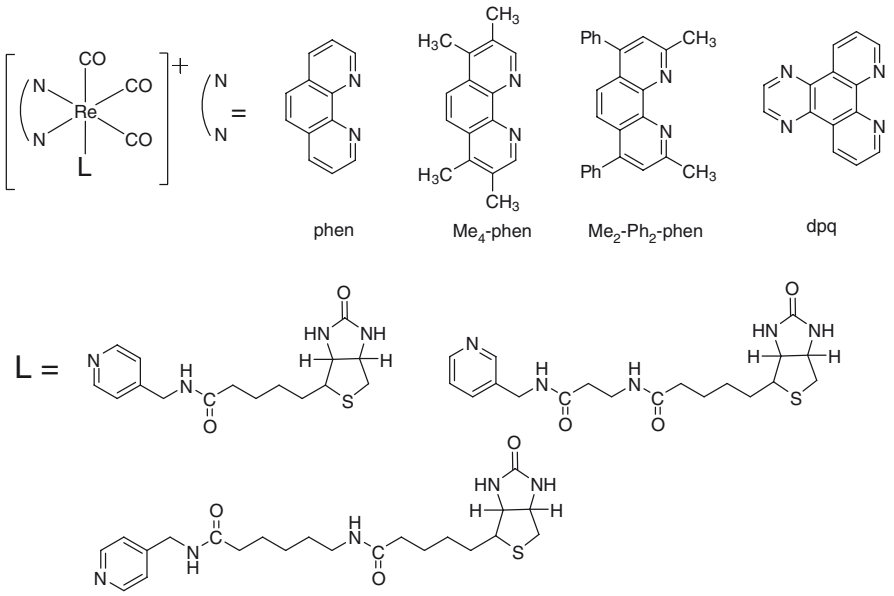

Fig. 17 Luminescent rhenium(I) tricarbonyl diimine-biotin complexes as probes for avidin

play enhanced emission intensities and extended lifetimes upon binding to avidin. Since no similar changes were observed when excess biotin was present, the increase in emission intensities and lifetimes was attributed to a specific binding of the complexes to the biotin-binding site of avidin. These observations are in contrast to most fluorophore–biotin conjugates, which suffer from severe emission quenching upon binding to avidin due to resonance-energy transfer (RET), unless exceptionally long spacers such as poly(ethylene glycol) are present between the fluorophore and biotin unit [154]. The absence of emission quenching in rhenium(I)-biotin complexes is because of the insignificant overlap between their absorption and emission spectra, which disfavors RET quenching.

The enhancement of the emission intensities and lifetimes can be further explained by considering the hydrophobicity associated with the binding pockets of avidin, as the lifetimes of these complexes are sensitive to the hydrophobicity of the environment. Another reason for the enhancement of emission and lifetime is the increased rigidity of the surroundings of the complexes upon binding to avidin, which may lead to lower nonradiative decay, thereby more intense and longer-lived emission. Hence, rhenium(I) polypyridine–biotin complexes offer remarkable advantages over traditional biotin–fluorophores as probes for avidin and can be utilized in homogeneous assays for biotin and biotinylated biomolecules.

Sun's group reported the synthesis, characterization, and photophysical properties of a series of organic receptors and their corresponding Re(I) tricarbonyl complexes as anion probes, featuring bis-sulfonamide as interacting sites attached to highly chromophoric π-conjugated quinoxaline moieties (see Fig. 18) [155].

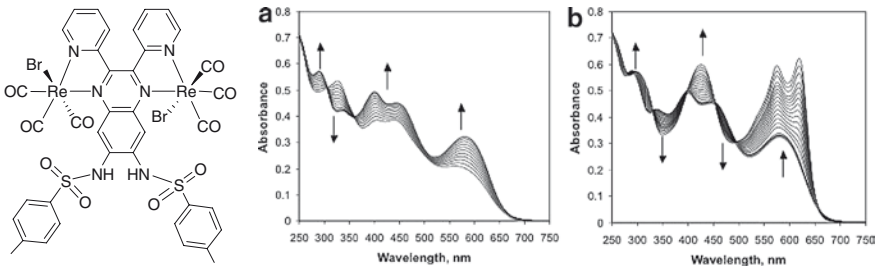

Fig. 18 The structure of rhenium(I) tricarbonyl diimine complex for anion sensing and the absorption spectral changes of this probe molecule (2.5×10^{-5} M) in CH_3CN upon addition of *n*-Bu_4NF, (**a**) $[F^-] = 0 - 2.8 \times 10^{-5}$ M and (**b**) $[F^-] = 2.8 \times 10^{-5} - 1.1 \times 10^{-4}$ M. (reproduced with permission from [155])

The interactions with various anions were extensively investigated. These probe molecules are capable of recognizing F^-, OAc^-, CN^-, and $H_2PO_4^-$ with different sensitivity. The probe-anion interactions can be easily visualized by naked eye colorimetric responses. Moreover, the anion-probe interaction can also be monitored by the metal carbonyl stretching frequencies. The colorimetric responses upon addition of anions were attributed to the direct N-H deprotonation of sulfonamide groups.

6 Light-Emitting Devices

Figure 19 shows the rhenium(I) diimine complexes exploited as dopants in *organic light-emitting diodes* (OLEDs) [46–52]. The trifunctional molecule **33** was synthesized integrating three functions needed for efficient operation of OLEDs. The molecule contains an emissive chromophore (a Re^I polypyridyl complex containing dipyrido[3,2-a-2′,3′-c]phenazine), an electron-transporting 1,3,4-oxadiazole group, and a hole-transporting terthiophene unit. The HOMO and LUMO energies of the complex lie within the band gap of the host polymer, poly(*N*-vinylcarbazole) (PVK), a property suggesting its potential use as an OLED [46]. Electrically neutral rhenium(I) tricarbonyl complexes **34**–**38** were used as emitters for electrophosphorescent devices. Complex **34** was used as an orange-emitting dopant in a 4, 4′-*N*, *N*′-dicarbazole-biphenyl host to fabricate *phosphorescent organic light-emitting diodes* (PhOLEDs). The maximum electroluminescence (EL) efficiency and luminescence of 21.8 cd A^{-1}, and 8,315 cd cm^{-2} at 17.5 V were obtained, respectively, and so far this is the best electroluminescence reported for Re^I-doped PhOLEDs [47]. The improvement in electroluminescent performance could be attributed to the synergistic effects of the two reciprocally repulsive phenyl and methyl groups in the backbone of the 1,10-phenanthroline molecule.

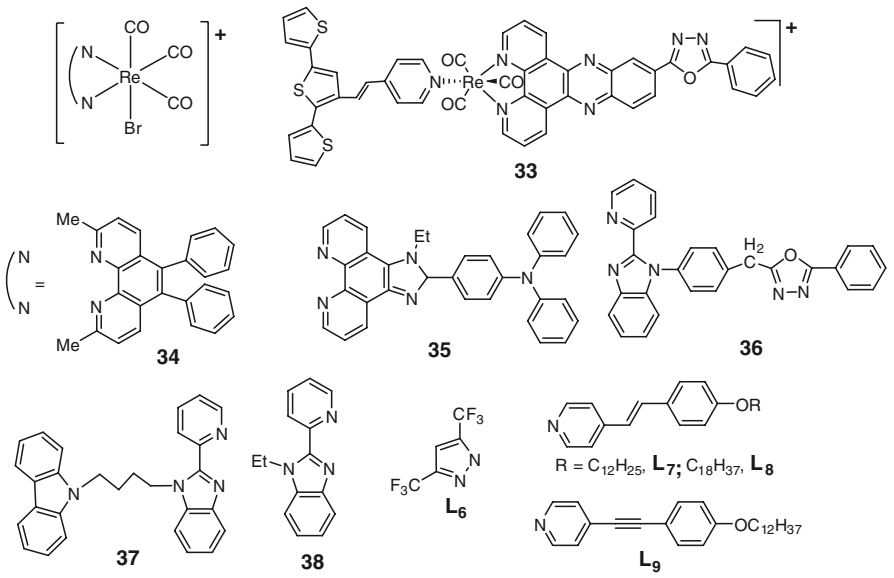

Fig. 19 Rhenium(I) tricarbonyl diimine complexes for LEDs

The OLED devices incorporating complex **35** functionalized by triphenylamine, a hole transport group, emit strong yellow–green light with an emission maximum at 552 nm [48]. A current efficiency up to 17.6 cd A^{-1} corresponding to a power efficiency of 9.2 Im W^{-1} at 6 V and peak brightness as high as 6,500 cd m^{-2} at 16 V were achieved. Complex **36** showed a maximum brightness of 1,174 cd m^{-2} at 17 V, while the devices based on the carbazole-containing (hole transport group) complex **37** showed a maximum brightness of 2,300 cd m^{-2} at 16 V [49]. The devices with a doping concentration of 10 wt% of **36** and **37** showed a maximum efficiency at 230 mA cm^{-2} and still possessed 51% of the maximum efficiency at 4.2 mA cm^{-2} for 36 and 56% of the maximum efficiency at 2.7 mA cm^{-2} for 37, respectively. A two-layer electroluminescent device of a rhenium(I) tricarbonyl complex of 2-(1-ethylbenzimidzol-2-yl)pyridine **38** with a configuration of ITO/TDP/**38**/$Mg_{0.9}Ag_{0.9}$/Ag gave a turn-on voltage as low as 3 V and a maximum luminescence of 113 cd m^{-2} at a bias voltage of 10.5 V [156].

The complexes $[Re(bpy)(CO)_3(\mathbf{L_6})]^+$ and $[Re(phen)(CO)_3(\mathbf{L_6})]^+$ were used as dopants in host materials 4,4′-dicarbazolylbiphenyl (CBP) and 2,2′,2″-(1,3,5-benzenetriyl)-tris[1-phenyl-1H-benzimidazole] (TBPI) and sublimable in the temperature range 150–165°C in vacuum [50]. For $[Re(bpy)(CO)_3(\mathbf{L_6})]^+$, electrophosphorescence occurred at 530 nm at a turn-on voltage of 6 V with a luminescence power of 0.72 Im W^{-1} and luminescence of 2,300 cd m^{-2} at a current density of 100 mA cm^{-2}. Rhenium(I) 2,2′-bipyridine surfactant complexes $[Re(bpy)(CO)_3(\mathbf{L_{7,8,9}})]PF_6$ formed stable Langmuir-Blodgett films that served as the emitting layer in OLEDs. An OLED consisting of 25 layers with ITO glass at the bottom and Al on top took 7 V to turn-on and 18 V to reach 9 cd cm^{-2} [157].

Rhenium(I) tricarbonyl-2,2′-bipyridine moieties were used to cap both ends of a poly fluorine, yielding Re-capped $\{Re(bpy)(CO)_3(py)\text{-}X\text{-}(py)(CO)_3(bpy)Re\}^{2+}$ polymers, where X = polyfluorene [51, 52]. The polymers with and without the Re caps were spin-coated from their solutions in CH_2Cl_2 onto an ITO surface previously modified with a layer of poly(styrene sulfonic acid), doped with poly(ethylenedioxythiophene). The LED (light-emitting device) was then topped with a layer of Ca/Al. The photoluminescence (PL) and electroluminescence seen were consistent with the presence of $[Re(bpy)(CO)_3(py)]^+$ [158].

References

1. Holten D, Bocian DF, Lindsey JS (2002) Acc Chem Res 35:57
2. Remacle F, Levine RD (2001) J Phys Chem B 105:2153
3. Yeow EKL, Steer RP (2003) Phys Chem Chem Phys 5:97
4. Yeow EKL, Steer RP (2003) Chem Phys Lett 377:391
5. Geoffroy GL, Wrighton MS (1979) Organometallic photochemistry. Academic, New York
6. Wrighton M, Morse DL (1974) J Am Chem Soc 96:998
7. Lees AJ (1987) Chem Rev 87:711
8. Lees AJ, Sun SS in McCleverty JA, Meyer TJ (Eds) (2004) Comprehensive coordination chemistry II, Vol 2. Elsevier, Oxford, UK, p 731
9. Kirgan RA, Sullivan BP, Rillema DP in Balzani V, Campagna S (Eds) (2007) Top Curr Chem 281:45
10. Lees AJ (1995) Comments Inorg Chem 17:319
11. Chen P, Meyer TJ (1998) Chem Rev 98:1439
12. Stufkens DJ (1992) Comments Inorg Chem 13:359
13. Vogler A, Kunkely H (2000) Coord Chem Rev 200–202:991
14. Balzani V, Juris A, Venturi M, Campagna S, Serroni S (1996) Chem Rev 96:759
15. Schanze KS, Walters KA (2000) Photoinduced electron transfer in metal-organic dyads. In: Ramamurthy V, Schanze KS (Eds) Organic and Inorganic Photochemistry. Molecular and Supramolecular Photochemistry Series, Vol 2, Chap 3. Marcel Dekker, New York, p 75
16. Schanze KS, MacQueen DB, Perkins TA, Cabana LA (1993) Coord Chem Rev 122:63
17. Worl LA, Duesing R, Chen P, Della Ciana L, Meyer TJ (1991) J Chem Soc Dalton Trans:849
18. Stufkens DJ, Vlček A Jr (1998) Coord Chem Rev 177:127
19. Kalyanasundaram K (1992) Photochemistry of polypyridine and porphyrin complexes, Chap 10. Academic, New York, p 321
20. Caspar JV, Meyer TJ (1983) J Phys Chem 87:952
21. Takeda H, Koike K, Inoue H, Ishitani O (2008) J Am Chem Soc 130:2023
22. Abdel-Shafi AA, Bourdelande JL, Ali SS (2007) Dalton Trans:2510
23. Belliston-Bittner W, Dunn AR, Nguyen YHL, Stuehr DJ, Winkler JR, Gray HB (2005) J Am Chem Soc 127:15907
24. Hayashi Y, Kita S, Brunschwig BS, Fujita E (2003) J Am Chem Soc 125:11976
25. Hwang J-S, Chang J-S, Park S-F, Ikeue K, Anpo M (2005) Top Cat 35:311
26. Kumar A, Sun SS, Lees AJ (2008) Coord Chem Rev 252:922
27. Sun SS, Less AJ (2002) Coord Chem Rev 230:171
28. Sun SS, Lees AJ (2000) Chem Commun:1687
29. Mizuno T, Fukumatsu T, Takeuchi M, Shinkai S (2000) J Chem Soc Perkin Trans 1:407
30. Keefe MH, Sloan RV, Hupp JT, Czaplewski KF, Snurr RQ, Stern CL (2000) Langmuir 16:3964
31. Bakir M, McKenzie JAM (1997) J Chem Soc Dalton Trans:3571

32. De Silva AP, Gunaratne HQN, Gunnlaugsson T, Huxley AJM, McCoy CP, Rademacher JT, Rice TE (1997) Chem Rev 97:1515
33. Demas JN, DeGraff BA (1991) Anal Chem 63:A829
34. Lees AJ (1998) Coord Chem Rev 177:3
35. Lees AJ (2001) Luminescent metal complexes as spectroscopic probes of monomer/polymer environments. In: Ramamurthy V, Schanze KS (Eds) Optical Sensors and Switches. Molecular and Supramolecular Photochemistry Series, Vol 7, Chap 5. Marcel Dekker, New York, p 209
36. Sun SS, Lees AJ (2002) Organometallics 21:39
37. Polo AS, Itokazu MK, Frin KM, Patrocnio AOT, Iha NYM (2006) Coord Chem Rev 250:1669
38. Argazzi R, Bertolasi E, Chiorboli C, Bignozzi CA, Itokazu MK, Iha NYM (2001) Inorg Chem 40:6885
39. Lewis JD, Perutz RN, Moore JN (2000) J Chem Soc Chem Commun:1865
40. Sun SS, Robson E, Dunwoody N, Silva AS, Brinn IM, Lees AJ (2000) J Chem Soc Chem Commun:201
41. Fernandez-Acebes A, Lehn JM (1999) Chem Eur J 5:3285
42. Yam VWW, Lau VCY, Wu LX (1998) J Chem Soc Dalton Trans:1461
43. Schanze KS, Lucia LA, Cooper M, Walters KA, Ji HF, Sabina O (1998) J Phys Chem A 102:5577
44. Beyeler A, Belser P, De Cola L (1997) Angew Chem Int Ed Engl 36:2779
45. Yam VWW, Lau VCY, Cheung KK (1995) J Chem Soc Chem Commun:259
46. Lundin NJ, Blackman AG, Gordon KC, Officer DL (2006) Angew Chem Int Ed 45:2582
47. Li X Zhang D, Li W, Chu B, Han l, Zhu J, Su Z, Bi D, Wang D, Yang D, Chen Y (2008) Appl Phys Lett 92:083302
48. Liu C, Li J, Li B, Hong Z, Zhao F, Liu S, Li W (2006) Appl Phys Lett 89:243511
49. Si z, Li J, Li B, Zhao F, Liu S, Li W (2007) Inorg Chem 46:6155
50. Ranjan S, Lin S-Y, Hwang K-C, Chi Y, Ching W-L, Liu C-S (2003)Inorg Chem 42:1248
51. Zhang Y, Huang z, Zeng W, Cao Y (2008) Polymer 49:1211
52. Lee P-I, Hsu SL-C, Chung C-T (2006) Synth Metals 156:907
53. Zhang J, Chu BW-K, Zhu N, Yam VW-W (2007) Organometallics 26:5423
54. Yam VWW, Yang Y, Yang HP, Cheung KK (1999) Organometallics 18:5252
55. Briel O, Sunkel K, Krossing I, Noth H, Schmalzlin E, Meerholz K, Brauchle C, Beck W (1999) Eur J Inorg Chem:483
56. Bourgault M, Baum K, Le Bozec H, Pucetti G, Ledoux I, Zyss J (1998) New J Chem:517
57. Victor RF, Correia I, Videira M, Marques F, Paulo A, Pessoa JC, Viola G, Martins GG, Santos I (2008)Chem Bio Chem 9:131
58. Ma D-L, Che C-M, Siu F-M, Yang M, Wong K-Y (2007) Inorg Chem 46:740
59. Ruiz GT, Juliarena MP, Lezna RO, Wolcan E, Feliz MR, Ferraudi G (2007) J Chem Soc Dalton Trans:2020
60. Reece SY, Nocera DG (2005) J Am Chem Soc 127:9448
61. Stoeffler HD, Thornton NB, Temkin SL, Schanze KS (1995) J Am Chem Soc 117:7119
62. Fuks L, Gniazdowska E, Meiczkowski J, Sadlej-Sosnowska N (2008) Polyhedron 27:1353
63. Tzanopoulou S, Pirmettis IC, Patsis G, Paaravatou-Petsotas M, Livaniou E, Papadopoulos M, Pelecanou M (2006) J Med Chem 49:5408
64. Dunn AR, Belliston-Bittner W, Winkler JR, Getzoff ED, Stuehr DJ, Gray HB (2005) J Am Chem Soc 127:5169
65. Zhang J, Vittal JJ, Henderson W, Wheaton JR, Hall IH, Hor TSA, Yan YK (2002) J Organomet Chem 650:123
66. Pietzsch H-J, Gupta A, Reisgys M, Drews A, Seifert S, Syhre R, Spies H, Alberto R, Abram U, Schubiger PA, Johannsen B (2000) Bioconjugate Chem 11:414
67. Stoyanov SR, Villegas JM, Cruz AJ, Lockyear LL, Reibenspies JH, Rillema DP (2005) J Chem Theory Comput 1:95
68. Villegas JM, Stoyanov SR, Huang W, Rillema DP (2005) Inorg Chem 44:2297
69. Villegas JM, Stoyanov SR, Huang W, Rillema DP (2005) Dalton Trans:1042

70. Gabrielsson A, Busby M, Matousek P, Towrie M, Hevia E, Cuesta L, Perez J, Zális S, Vlček A Jr (2006) Inorg Chem 45:9789
71. Kirgen R, Simpson M, Moore C, Day J, Bui L, Tanner C, Rillema DP (2007) Inorg Chem 46:6464
72. Zhao G-J, Zhou X, Liu T, Zheng Q-C, Bai F-Q, Zhang H-X (2008) J Mol Struct Theochem 855:52
73. Machura B, Kruszynski R (2007) J Organomet Chem 692:4161
74. Baiano JA, Kessler RJ, Lumpkin RS, Munley MJ, Murphy WR Jr (1995) J Phys Chem 99:17680
75. Hino JK, Della Ciana L, Dressick WJ, Sullivan BP (1992) Inorg Chem 31:1072
76. Kalyanasundaram K (1986) J Chem Soc Faraday Trans 2 82:2401
77. Schoonover JR, Strouse GF (1998) Chem Rev 98:1335
78. Schoonover JR, Bignozzi CA, Meyer TJ (1997) Coord Chem Rev 165:239
79. Schoonover JR, Strouse GF, Dyer RB, Bates WD, Chen P, Meyer TJ (1996) Inorg Chem 35:273
80. George MW, Johnson FPA, Westwell JR, Hodges PM, Turner JJ (1993) J Chem Soc Dalton Trans:2977
81. Walters KA, Dattelbaum DM, Ley KD, Schoonover JR, Meyer TJ, Schanze KS (2001) J Chem Soc Chem Commun:1834
82. Schoonover JR, Chen P, Bates WD, Dyer RB, Meyer TJ (1994) Inorg Chem 33:793
83. Chen P, Curry M, Meyer TJ (1989) Inorg Chem 28:2271
84. Shaver RJ, Perkovic MW, Rillema DP, Woods C (1995) Inorg Chem 34:5446
85. Katz NE, Mecklenburg SL, Graff DK, Chen P, Meyer TJ (1994) J Phys Chem 98:8959
86. Chen P, Westmoreland TD, Danielson E, Schanze KS, Anthon D, Neveux PE Jr, Meyer TJ (1987) Inorg Chem 26:1116
87. Chen P, Duesing R, Graff DK, Meyer TJ (1991) J Phys Chem 95:5850
88. Schoonover JR, Strouse GF, Chen P, Bates WD, Meyer TJ (1993) Inorg Chem 32:2618
89. Vlček A Jr , Busby M (2006) Coord Chem Rev 250:1755
90. Wang Y, Schanze KS (1996) J Phys Chem 100:5408
91. Trammell S, Goodson PA, Sullivan BP (1996) Inorg Chem 35:1421
92. Wang Y, Lucia LA, Schanze KS (1995) J Phys Chem 99:1961
93. Lucia LA, Wang Y, Nafisi K, Netzel TL, Schanze KS (1995) J Phys Chem 99:11801
94. Wang Y, Schanze KS (1993) Chem Phys 176:305
95. Wang Y, Hauser BT, Rooney MM, Burton RD, Schanze KS (1993) J Am Chem Soc 115:5675
96. Rossenaar BD, Stufkens DJ, Vlcek A Jr (1996) Inorg Chem 35:2902
97. Giordano PJ, Fredericks SM, Wrighton MS, Morse DL (1978) J Am Chem Soc 100:2257
98. Wallace L, Rillema DP (1993) Inorg Chem 32:3836
99. Wallace L, Jackman DC, Rillema DP, Merkert JW (1995) Inorg Chem 34:5210
100. Leasure RM, Sacksteder L, Nesselrodt D, Reitz GA, Demas JN, DeGraff BA (1991) Inorg Chem 30:3722
101. Del Guerzo AD, Leroy S, Fages F, Schmehl RH (2002) Inorg Chem 41:359
102. Ziessel R, Juris A, Venturi M (1998) Inorg Chem 37:5061
103. Baba AI, Shaw JR, Simon JA, Thummel RP, Schmehl RH (1998) Coord Chem Rev 171:43
104. Schoonover JR, Bates WD, Meyer TJ (1995) Inorg Chem 34:6421
105. Vlcek A Jr (1998) Coord Chem Rev 177:219
106. Koike K, Okoshi N, Hori H, Takeuchi K, Ishitani O, Clark IP, George MW, Johnson FPA, Turner JJ (2002) J Am Chem Soc 124:11448
107. Koike K, Tanabe J, Toyama S, Tsubaki H, Sakamoto K, Westwell JR, Johnson FPA, Hori H, Saitoh H, Ishitani O (2000) Inorg Chem 39:2777
108. Hightower SE, Corcoran RC, Sullivan BP (2005) Inorg Chem 44:9601
109. Sato S, Sekine A, Ohashi Y, Ishitani O, Blanco-Rodriguez AM, Vlček A Jr, Unno T, Koike K (2007) Inorg Chem 46:3531
110. Del Negro AS, Woessner SM, Sullivan BP, Dattelbaum DM, Schoonover JR (2001) Inorg Chem 40:5056

111. Rossenaar BD, Kleverlaan CJ, Stifkens DJ, Sskam A (1994) J Chem Soc Chem Commun:63
112. Gabrielsson A, Blanco-Rodríguez AM, Matousek P, Towrie M, Vlček A Jr (2006) Organometallics 25:2148
113. Wenger OS, Henling LM, Day MW, Winkler JR, Gray HB (2004) Inorg Chem 43:2043
114. Yam VW-W, Yang Y, Zhang J, Chu BW-K, Zhu N (2001) Organometallics 20:4911
115. Busby M, Matousek P, Towrie M, Vlček A Jr (2007) Inorganica Chimica Acta 360:885
116. Lewis JD, Perutz RN, Moore JN (2004) J Phys Chem A 108:9037
117. Yam VW-W, Ko C-C, Wu L-X, Wong KM-C, Cheung K-K (2000) Organometallics 19:1820
118. Ko C-C, Wu L-X, Wong KM-C, Zhu N, Yam VW-W (2004) Chem Eur J 10:766
119. Lee PH-M, Ko C-C, Zhu N, Yam VW-W, (2007) J Am Chem Soc 129:6058
120. Ko C-C, Kwok W-M, Yam VW-W, Phillips DL (2006) Chem Eur J 12:5840
121. Yam VW-W, Ko C-C, Zhu N (2004) J Am Chem Soc 126:12734
122. Manimaran B, Thanasekaren P, Rajendran T, Lin R-J, Chang I-J,Lee G-H, Peng S-M, Rajagopal S, Lu K-L (2002) Inorg Chem 41:5323
123. Woessner SM, Helms JB, Shen Y, Sullivan BP (1998) Inorg Chem 37:5406
124. Thanasekaren P, Liao R-T, Manimaran B, Liu Y-H, Chou P-T, Rajagopal S, Lu K-L (2006) J Phys Chem A 110:10683
125. Rajendran T, Manimaran B, Liao R-T, Lin R-J, Thanasekaran P, Lee G-H, Peng S-M, Liu Y-H, Chang I-J, Rajgopal S, Lu K-L (2003) Inorg Chem 42:6388
126. Sun S-S, Lees AJ (2000) J Am Chem Soc 122:8956
127. Sun S-S, Lees AJ (1999) Inorg Chem 38:4181
128. Slone RV, Hupp JT, Stern CL, Albrecht-Schmitt TE (1996) Inorg Chem 35:4096
129. Lee SJ, Lin W, (2002) J Am Chem Soc 124:4554
130. Benkstein KD, Hupp JT, Stern CL (1998) J Am Chem Soc 120:12982
131. Vogler A, Kisslinger J (1986) Inorg Chim Acta 115:193
132. Benkstein KD, Hupp JT, Stern CL (2002) Angew Chemie Int Ed Eng 39:2891
133. Benkstein KD, Stern CL, Splan KE, Johnson RC, Walters KA, Vanhelmont FWM, Hupp JT (2002)Eur J Inorg Chem :2818
134. Slone RV, Yoon DI, Calhoun RM, Hupp JT (1995) J Am Chem Soc 117:11813
135. Sun S-S, Anspach JA, Lees AJ (2002) Inorg Chem 41:1862
136. Sathiyendiran M, Liao R-T, Thanasekaran P, Luo T-T, Venkataramanan NS, Lee G-H, Peng S-M, Lu K-L (2006) Inorg Chem 45:10052
137. Slone RV, Hupp JT (1997) Inorg Chem 36:5422
138. Sun S-S, Lees AJ (2001) Inorg Chem 40:3154
139. Splan KE, Massari AM, Morris GA, Sun S-S, Reina E, Nguyen ST, Hupp JT (2003) Eur J Inorg Chem :2348
140. Kumar A, Sun S-S, Lees AJ (2008) Coord Chem Rev 252:922
141. de Wolf P, Heath S, Thomas J (2002) J Chem Soc Chem Commun:2540
142. Sun S-S, Lees AJ (2001) Chem Commun:103
143. Manimaran B, Rajendran T, Lu Y-L, Lee G-H, Peng S-M, Lu K-L (2001) Eur J Inorg Chem:633
144. Amendola V, Bacchilega D, Costa I, Gianelli L, Montalti M, Pallavicini P, Perotti A, Prodi L, Zaccheroni N (2003) J Photochem Photobiol A: Chem 159:249
145. Lam MHW, Lee DYK, Man KW, Lau CSW (2000) J Mater Chem 10:1825
146. Cattaneo M, Fagalde F, Katz NE (2006) Inorg Chem 45:6884
147. Beer PD, Timoshenko V, Maestri M, Passaniti P, Balzani V (1999) J Chem Soc Chem Commun:1755
148. Sun S-S, Lees AJ, Zavalij PY (2003) Inorg Chem 42:3445
149. Pelleteret D, Fletcher NC, Doherty AP (2007) Inorg Chem 46:4386
150. Li, M-J, Ko C-C, Duan G-P, Zhu N, Yam VW-W (2007) Organometallics 26:6091
151. Lo KK-W, Hui W-K (2005) Inorg Chem 44:1992
152. Lo KK-W, Hui W-K (2002) J Am Chem Soc 124:9344

153. Lo KK-W, Hui W-K, Chung C-K, Tsang KH-K, Lee TK-M, Li C-K, Lau JS-Y, Ng DC-M (2006) Coord Chem Rev 250:1724
154. Grubber, HJ Kada HG, Riener CK, Harms GS, Ahrer W, Dax TG, Knaus HG, (2000) Bioconjugate Chem 11:696
155. Lin T-P, Chen C-Y, Wen Y-S, Sun S-S (2007) Inorg Chem 46:9201
156. Wang K, Huang L, Gao L, Jin L, Huang C (2002) Inorg Chem 41:3353
157. Yam VW-W, Li B, Yang Y, Chu BW-K, Wong KM-C, Cheung K-K (2003) Eur J Inorg Chem:4035
158. Dinolfo, PH Coropceanu V, Bredas J-L, Hupp JT, (2006) J Am Chem Soc 128:12592

Top Organomet Chem (2010) 29: 37–71
DOI: 10.1007/3418_2009_5

Published online: 20 May 2009

Photophysics of CO Loss from Simple Metal Carbonyl Complexes

Conor Long

Abstract This work describes the ultrafast processes preceding the photoinduced decarbonylation of the simple metal carbonyl complexes $Cr(CO)_6$, $Fe(CO)_5$, and $Ni(CO)_4$. Models for their electronic structure are presented based on recent ab initio quantum chemical calculations and these models are used to describe initial excited-state dynamics leading to the expulsion of one CO ligand. Experimental support for the proposed excited-state dynamics is presented, as obtained from ultrafast pump-probe experiments using mass-selective detection, ultrafast electron diffraction, and luminescence studies. The results of some steady-state experiments are also presented where they support the proposed dynamic model.

Keywords Carbonyl • Chromium • Decarbonylation • Electronic structure • Excited state dynamics • Iron • Mass selective detection • Nickel • Photophysics • Ultrafast electron diffraction

Content

1 Introduction and Scope 38
2 The Photodecarbonylation of $Cr(CO)_6$ 39
2.1 Ab Initio Calculations on $Cr(CO)_6$ 40
2.2 Excited State Dynamics of $Cr(CO)_6$ 40
2.3 Low-Temperature Matrix Isolation Photochemistry of $Cr(CO)_6$ 46
2.4 Ultrafast Photolysis of $Cr(CO)_6$ with Mass-Selective Detection 47
2.5 The Overall Description of Photoinduced CO Loss from $Cr(CO)_6$ 50
3 The Photodecarbonylation of $Fe(CO)_5$ 52
3.1 The Electronic Structure of $Fe(CO)_5$ 52
3.2 Ultrafast Multiphoton Excitation of $Fe(CO)_5$ 53
3.3 Ultrafast Single-Photon Excitation of $Fe(CO)_5$ with Mass Detection 58
3.4 Ultrafast Electron Diffraction by $Fe(CO)_n$ (n = 5–0) 60
3.5 Concluding Comments 62

C. Long
School of Chemical Sciences, Dublin City University, Dublin 9, Ireland
e-mail: conor.long@dcu.ie

4 The Photodecarbonylation of $Ni(CO)_4$ 63
4.1 Luminescence Following Excitation of $Ni(CO)_4$ 65
4.2 Ultrafast Photodissociation Dynamics of $Ni(CO)_4$ 66
4.3 Concluding Comments 68
References 69

1 Introduction and Scope

Metal carbonyl complexes are amongst the most photochemically active organometallic systems. Early work recognized the importance of photochemical techniques in the synthesis of a wide range of ligand-substituted derivatives which were difficult to access using conventional thermal methods [1]. It was clear from these studies that the CO-loss is an important photochemical process for metal carbonyl compounds [2, 3]. The loss of the two electron donor ligand CO, from an 18 electron metal complex reduces the electron count by two and frequently produces highly reactive metal species with useful synthetic or catalytic properties [4].

In this work the ultrafast photophysical processes associated with photoinduced CO loss will be described with particular regard to the mononuclear homoleptic carbonyls $Cr(CO)_6$, $Fe(CO)_5$, and $Ni(CO)_4$. These complexes were the earliest metal carbonyls to be synthesized, indeed $Fe(CO)_5$ and $Ni(CO)_4$ have been known since the latter part of the nineteenth century. The carbonylation of nickel provided an important route to high purity nickel which was required by many important industrial processes. However, it is only within the last few decades that adequate models have been developed to explain the mechanisms of photoinduced CO loss from metal carbonyl complexes.

Early semiempirical calculations laid the foundations for subsequent ab initio methods which can now not only describe the electronic structure of optically accessible excited states, but also model the wavepacket propagation on the resulting potential energy surfaces. These models are supported by ultrafast studies using femptosecond (fs) pulsed lasers with a variety of detection systems. Many systems use indirect detection of excited-state processes because many excited states are unbound and not amenable to spectroscopic techniques.

The metal carbonyl systems for this work were chosen because they demonstrate a range of interesting features. For instance the photoejection of CO from $Cr(CO)_6$ is one of the fastest photochemical processes possible. The CO is expelled on a timescale similar to a molecular vibration, at the very time-limit of chemistry. Consequently $Cr(CO)_6$ has long been used as a prototypical system to test advances in time-resolution of transient spectroscopic and other ultrafast techniques. $Fe(CO)_5$ also has extensive photochemistry, with both the singlet and triplet species playing important roles. Herein the description is limited to the singlet manifold because intersystem crossing to the triplet state is slow compared to the ultrafast processes observed on the singlet potential energy surface. $Ni(CO)_4$ is unique amongst the mononuclear homoleptic carbonyls as it is the only one to exhibit luminescence at room temperature. All of these features are reviewed in this work which mainly focuses on processes on the fs timescale although in some cases slower processes and indeed steady-state results are presented where they help in the interpretation of the ultrafast experimental data.

2 The Photodecarbonylation of $Cr(CO)_6$

Initial models for the electronic structure of simple homoleptic metal carbonyl complexes were developed using semiempirical methods [5, 6]. These calculations were designed to help in the interpretation of their UV/Vis absorption spectra. For instance, the UV/Vis spectrum of $Cr(CO)_6$ exhibits weak features on the low-energy side of the lowest-energy absorption maximum (Fig. 1). The molecular orbital energy level diagram for $Cr(CO)_6$, derived from these early calculations, is presented in Fig. 2. This model placed the Laporte forbidden $^1A_{1g} \rightarrow {}^1T_{1g}$ absorption

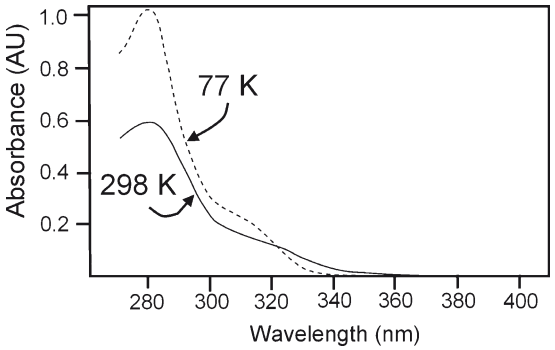

Fig. 1 The UV/Vis spectrum of $Cr(CO)_6$, recorded in a mixture of ether, pentane, and ethylalcohol (EPA) at 298 K or 77 K showing a weak feature on the low-energy side of the absorption maximum

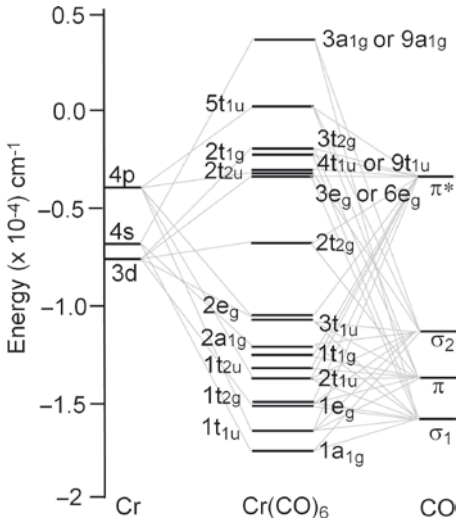

Fig. 2 The molecular orbital energy level diagram derived from semiempirical orbital overlap methods. An alternative numbering system is shown for some orbitals to maintain consistency with later calculations. Adapted from [5]

toward the low-energy side of the intense metal-to-ligand charge transfer (MLCT) bands ($^1A_{1g} \rightarrow a,b^1T_{1u}$). The $^1A_{1g} \rightarrow {}^1T_{1g}$ transition would remove electron density from the orbital set which is involved with the bonding interaction between chromium and the CO ligands and populate orbitals which are strongly antibonding with respect to the same interaction. This would result in a very efficient loss of one CO ligand which is consistent with many experimental results [7–9]. Thus, the explanation for the high quantum efficiency of CO-loss from $Cr(CO)_6$ ($\Phi_{CO} = 0.67$) relies on an efficient population of an excited state which is strongly antibonding with respect to the Cr-CO interaction. However, it is difficult to explain how a Laporte forbidden transition which formally cannot be efficiently populated from the ground state would result in a photochemical process with such a high quantum yield.

2.1 Ab Initio Calculations on $Cr(CO)_6$

With the advent of more sophisticated ab initio methods, the model of the electronic structure for $Cr(CO)_6$ was significantly modified [10]. Using complete active space (CAS) calculations the low intensity features in the UV/Vis spectrum of $Cr(CO)_6$ were reassigned to symmetry forbidden metal-to-ligand charge transfer transitions. The resulting excited states would not be dissociative with respect to CO loss as they correlate with an ion pair. This ion pair is subject to initial Coulomb attraction which would not favor ligand loss. Consequently models that allow the electronic structure of the excited states to develop with time are required to explain the resulting highly efficient CO-loss photochemistry.

The work of Baerends et al. using density functional theory (DFT) methods confirmed that the energies of the orbitally forbidden or spin-forbidden MLCT transitions are lower than the energies of the metal-centered (MC) transitions (Fig. 3, Table 1) and this placed the MC transitions further up the energy scale in the UV/Vis absorption spectrum [10–12]. The MC ($2t_{2g} \rightarrow 6e_g$) transitions move to higher energy for the heavier metals of the triad.

2.2 Excited State Dynamics of $Cr(CO)_6$

Calculations that allow the O_h symmetry of the excited $M(CO)_6$ species to reduce to C_{4v} by allowing one Cr–CO bond to lengthen, demonstrate that some components of these states are repulsive with respect to the M–CO interaction. This dynamic study explains why excitation into MLCT states results in efficient CO loss [12].

More demanding calculations conducted by Daniel et al. using equations-of-motion coupled cluster methods (EOM–CC) provided a better description of the contribution of MLCT and MC transitions to the electronic spectrum of $Cr(CO)_6$ [13]. These calculations confirm that the lowest-energy transition, which is responsible for the shoulder on the low-energy side of the first absorption maximum, corresponds to

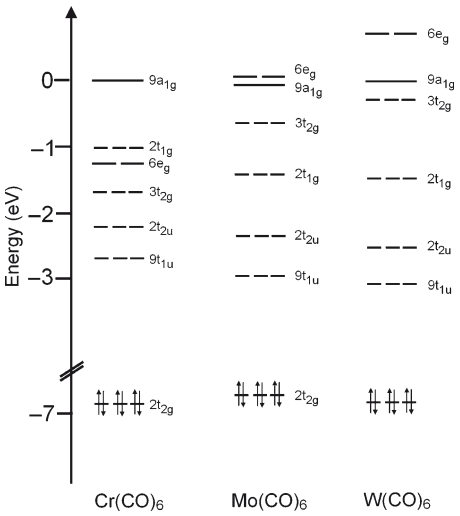

Fig. 3 The energy level scheme for $M(CO)_6$ (M = Cr, Mo, or W). Consistency with the orbital numbering system of $Cr(CO)_6$ requires the 1*s*–2*p* and the 1*s*–2*p*, 4*f* orbitals of Mo and W respectively to be excluded. Adapted from [11]

Table 1 The excitation energies (eV) to the lowest-energy metal-to-ligand charge transfer and ligand field states

State	DFT[a]	CASSCF[b]	CASPT2[b]	STEOM-CCSD[c]	Experiment[d]
			Transition energies (eV)		
MLCT excited states					
$a^1T_{2u}(2t_{2g}\rightarrow 9t_{1u})$	4.0	5.18–5.26	3.70–3.56	3.92	3.9(*sh*)
$a^1E_u(2t_{2g}\rightarrow 9t_{1u})$	4.0	5.11–5.28	3.41–3.59		
$a^1A_{2u}(2t_{2g}\rightarrow 9t_{1u})$	4.2	5.14–5.32	3.58		
$b^1E_u(2t_{2g}\rightarrow 2t_{2u})$	4.5	5.86–6.16	3.97–4.05		
$a^1A_{1u}(2t_{2g}\rightarrow 2t_{2u})$	4.5	5.92–6.29	4.10–4.15		
$b^1T_{2u}(2t_{2g}\rightarrow 2t_{2u})$	5.0	6.21–6.57	4.31–4.43	4.93	
$a^1T_{1u}(2t_{2g}\rightarrow 9t_{1u})$	5.6	5.97–6.15	4.11–4.54	4.37	4.43
$b^1T_{1u}(2t_{2g}\rightarrow 2t_{2u})$	6.5	7.16–7.75	5.07–5.20	5.20	5.53
LF excited states					
$^1T_{1g}(2t_{2g}\rightarrow 6e_g)$	5.2	5.66	4.85	4.37	
$^1T_{2g}(2t_{2g}\rightarrow 6e_g)$	6.3	6.42	5.08	4.67	4.87(*sh*)

[a]From [12]
[b]From [10], energy ranges refer to different choices of active space
[c]From [13]
[d]From [5]

an orbitally forbidden ($a^1A_{1g}\rightarrow a^1T_{2u}$) MLCT transition. Furthermore, the lowest-energy MC transition ($a^1A_{1g}\rightarrow a^1T_{1g}$) occurs close to the first allowed MLCT transition ($a^1A_{1g}\rightarrow a^1T_{1u}$). The results of these calculations are outlined in Table 1 along with the results of CAS and DFT calculations.

These data clearly show that the MC states are too high to be populated following irradiation at ca. 4.0 eV (310 nm). The potential energy curves (PEC) were estimated along the Cr–CO dissociation coordinate from a value of 1.90 to 2.3 Å. The equilibrium distance in $Cr(CO)_6$ is 1.97 Å at this level of theory (Fig. 4). In these calculations it was assumed that the structure of $Cr(CO)_5$ product remains the same as the $Cr(CO)_5$ fragment in $Cr(CO)_6$ [14]. The structure of the $Cr(CO)_5$ fragment was fixed as the Cr–CO distance of the remaining ligand was increased reducing the symmetry from O_h to C_{4v}. This causes the a^1T_{2u} MLCT state to be split into dissociative E and bound B_1 components. The a^1T_{1u} state splits into an A_1 (not shown in Fig. 4) and a bound E component while the a^1T_{1g} and a^1T_{2g} states split into E (unbound) $+A_2$ and E (bound) $+B_2$ components, respectively. At a Cr–CO distance of about 1.92 Å, i.e., a distance shorter but close to the equilibrium Cr–CO distance, the E components of the a^1T_{1g} MC and a^1T_{1u} MLCT states generate an avoided crossing (indicated by the small ellipse in Fig. 4). The associated conical intersection, in the multidimensional description, facilitates fast population of the a^1T_{1g} state once the absorbing a^1T_{1u} state is populated. This process occurs close to the Franck-Condon state and is therefore both fast and efficient [15]. This work provides an elegant explanation for the efficient population of the MC state though the initial and efficient population of a MLCT state. It also describes the early dynamics associated with launching the $Cr(CO)_6$ excited-state species onto an unbound surface which ultimately leads to loss of one CO ligand (Fig. 5).

The subsequent dynamics has been modeled by CAS calculations. In this model, one Cr–CO bond is significantly longer than the others [17]. Further along this surface a saddle point connecting two equivalent dissociation valleys was located. At this saddle point two CO ligands are partially dissociated, and the transition vector corresponds to an asymmetric M–CO stretching mode (Fig. 6). Intrinsic reaction coordinate (IRC) calculations from this saddle point led to the trigonal bipyrimidal (D_{3h}) $Cr(CO)_5$ fragment in both forward and reverse directions. This represents the last portion of the CO dissociation path from the electronically excited $Cr(CO)_6$ to

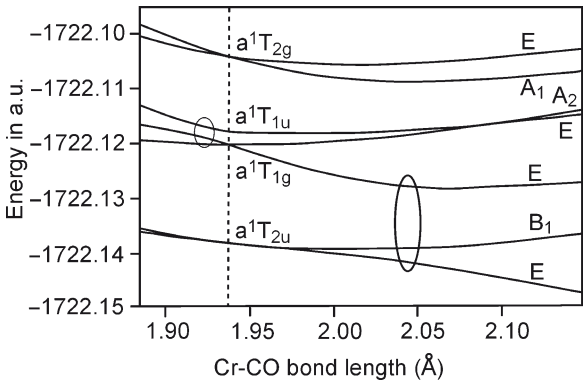

Fig. 4 The EOM-CCSD potential energy curves of $Cr(CO)_6$ along the $Cr–CO_{axial}$ bond elongation. Regions of the avoided crossing of E states are indicated by *ellipses*. Adapted from [13]

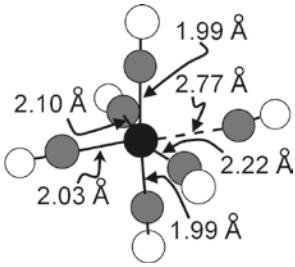

Fig. 5 The starting structure for the excited-state dynamics calculations for the S_1 state of $Cr(CO)_6$. The chromium atom is represented by the *black circle*, the carbons by the *gray*, and the oxygen atoms by the *white circles*. Adapted from [16]

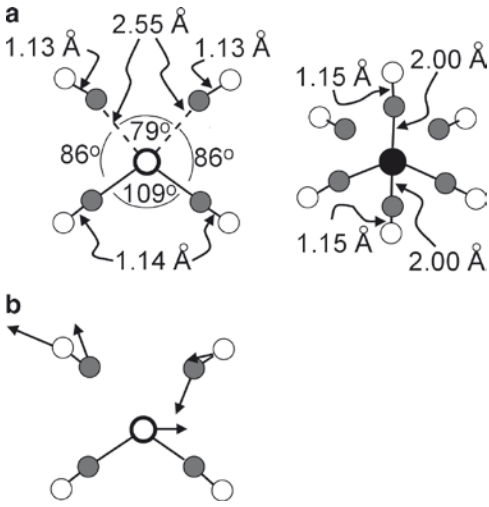

Fig. 6 (**a**) Projections of the CAS(6,8)/LanL2DZ optimized structure of the $Cr(CO)_6$ S_1 transition state with C_{2v} symmetry viewed down a twofold axis showing two *cis* ligands partially dissociated. (**b**) One transition vector leading to the loss of a single CO ligand. The chromium atom is represented by a *black*, the carbons by a *gray*, and the oxygens by *white circles*. Adapted from [16]

the electronically excited (S_1) $Cr(CO)_5$ fragment. Snapshots of the $Cr(CO)_6$ dissociation trajectory where the CO ligand is completely expelled in under 77 fs are presented in Fig. 7.

The resulting $Cr(CO)_5$ fragment is vibrationally excited. The major motion involves a symmetric equatorial bending mode where two CO ligands move to fill the site vacated by the leaving CO [17]. A small fraction of the available energy is also partitioned mainly into the rovibrational degrees of freedom of the expelled CO and the $Cr(CO)_5$ fragment remains electronically excited [18]. As there is no evidence for luminescence following irradiation of $Cr(CO)_6$, it is necessary to provide a mechanism for the deactivation of the $Cr(CO)_5$ excited state.

Calculations show that the ground (S_0) and first excited state (S_1) of the $Cr(CO)_5$ fragment are degenerate at the D_{3h} structure. This is the location of a Jahn-Teller conical intersection of the three equivalent ground-state $Cr(CO)_5$ species belonging to the C_{4v} point group. This intersection provides a funnel for the radiationless deactivation of the S_1 state to the ground S_0 state. At this point the nuclear motion lifts the degeneracy of the electronic state resulting in a featured "moat" around the Jahn-Teller conical intersection which also represents a branching state for the

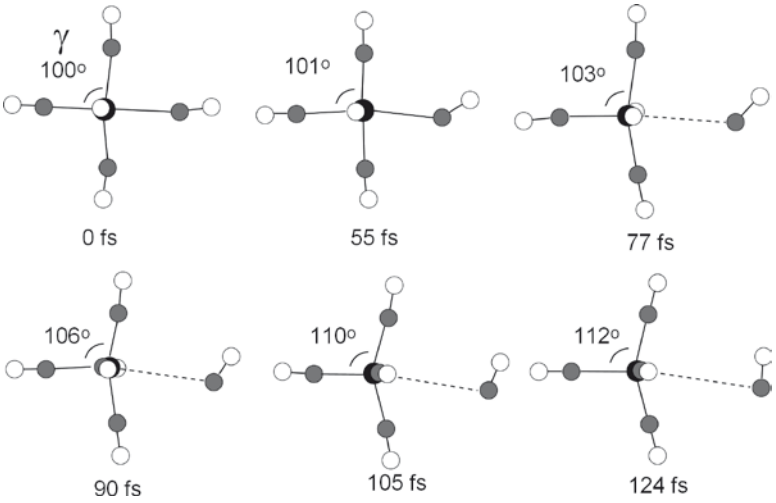

Fig. 7 Snapshots in time along the $Cr(CO)_6$ trajectory to loss of CO projected onto two dimensions. The CO leaves in a rotationally excited state and a large amplitude bending motion is promoted in the $Cr(CO)_5$ fragment. The chromium atom is represented by the *black*, carbon by the *gray*, and oxygen by the *white circles*. Adapted from [16]

$Cr(CO)_5$ trajectory. The coordinates of this branching state are defined by the gradient difference and derivative coupling vectors presented in Fig. 8.

Following surface hopping events which reflects the significant excess vibrational energy in the $Cr(CO)_5$ fragment, the system relaxes on the ground electronic state surface to the three equivalent C_{4v} square pyramidal $Cr(CO)_5$ species which differ only in the orientation of the vacant coordination site. Thermal conversion between the square pyramidal species is achieved through a transition state of C_{2v} symmetry, consistent with the Stanton-McIver rules [19, 20]. The barrier to this conversion is significant (40-50 kJ mol^{-1}) and is surmounted by way of the pseudorotation as indicated in Fig. 9.

Wavepacket dynamics in the moat was modeled using a multiconfiguration time dependent Hartree (MCTDH) method which used a two-mode ($Q1$, $Q2$) three-state model (Fig. 10) [17]. Mapping the wavepacket density onto the adiabatic moat surface provides time-dependent snapshots of the coherent nuclear motion extending to 340 fs after the excitation event. The major motion is the symmetric equatorial bending mode which, as mentioned above, remains highly excited after the expulsion of the CO ligand. It is clear that the $Cr(CO)_5$ fragment retains this excess vibrational energy for some considerable time after the expulsion of the CO ligand and this energy is available for further CO expulsions in the gas phase. Even in condensed phases the transient Raman spectroscopy confirmed that cooling of some vibrational modes, including the C-O stretch, in $Cr(CO)_5$ can take in excess of 150 ps [21].

From these calculations it is clear that the ejection of CO from $Cr(CO)_6$ to form the ground-state $Cr(CO)_5$ fragment occurs within 80 fs of the excitation process.

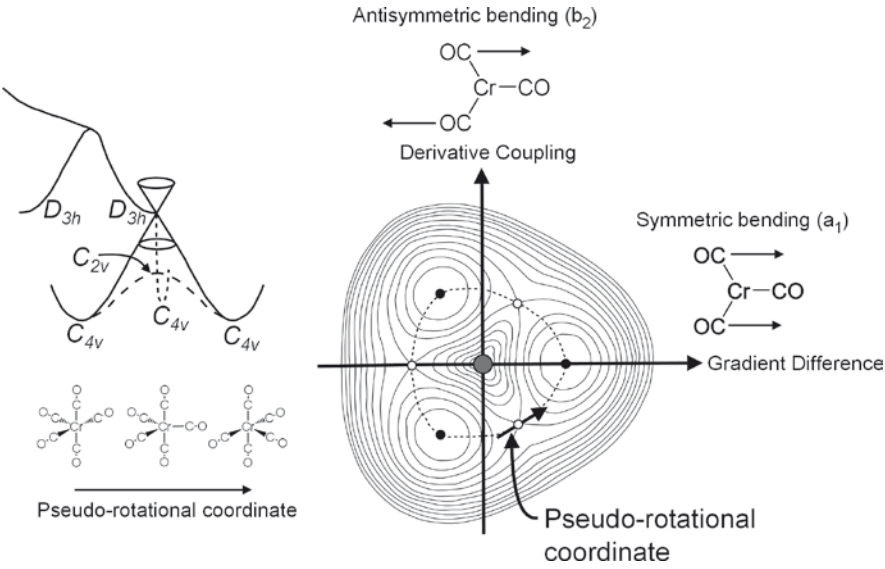

Fig. 8 On the left is the $Cr(CO)_5$ potential energy surface topology traversed after photodissociation of $Cr(CO)_6$ to the conical intersection of the S_1 and S_0 states at D_{3h} symmetry. The *right hand side* shows the branching space at the D_{3h} conical intersection. The pseudorotation coordinate is shown connecting the C_{4v} geometries through a C_{2v} transition structure. The D_{3h} symmetry is indicted by the *gray circle*, the transition states by *open circles* while the three equivalent C_{4v} species are indicated are indicted with *solid circles*. Adapted from [17]

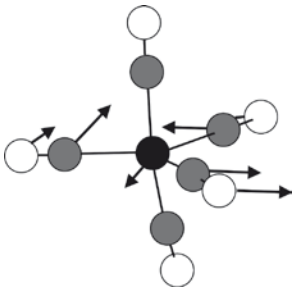

Fig. 9 The transition state vectors applied to the CAS(6,8)/LanL2DZ optimized structure of S_0 $Cr(CO)_5C_{2v}$ transition state. Adapted from [16]

In addition these processes occur through a series of unbound (nonquantized) excited states. These excited states cannot be probed by direct spectroscopic techniques and are known as "dark states."

The predicted quantum yield of CO loss (Φ_{CO}) should be very high perhaps approaching unity because each of the sequential processes is populated by way of barrierless events from the previous state. The measured Φ_{CO} is 0.67 in cyclohexane, considerably less than unity and is further reduced to 0.52 in more viscous media [22, 23]. The branching space at the conical intersection allows the $Cr(CO)_5$ fragment to locate in one of three possible C_{4v} species only one of which has an

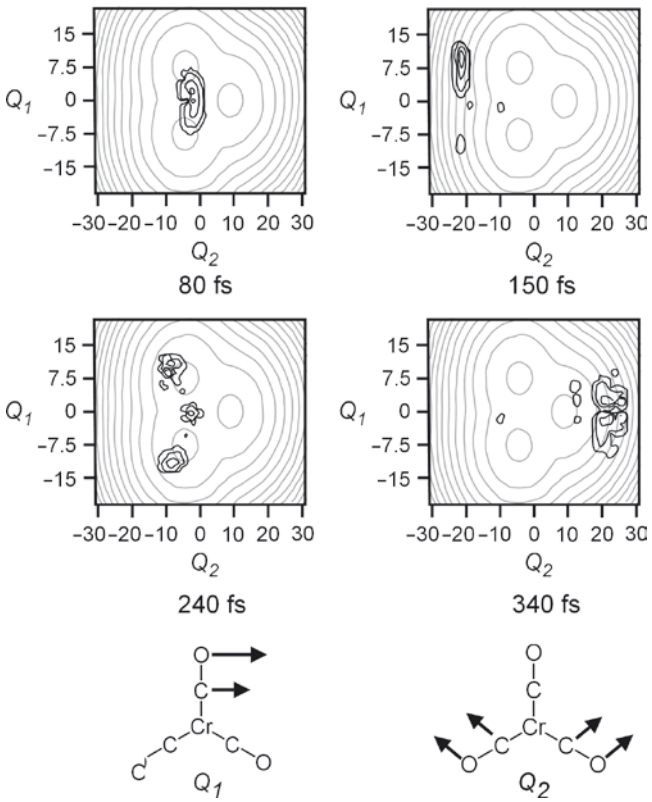

Fig. 10 The time evolution of the adiabatic wavepacket in the space of coordinates $Q1$ and $Q2$ for the 2D three-state model of the relaxation of $Cr(CO)_5$ after formation by photodissociation superimposed on the lower adiabatic potential energy surface. The D_{3h} conical intersection is at (0,0). Adapted from [17]

orientation which facilitates efficient recombination with the photoejected CO within a solvent cage. Thus, the apparent quantum yield for CO loss is reduced by one third in the condensed phase as described in the next section.

2.3 *Low-Temperature Matrix Isolation Photochemistry of $Cr(CO)_6$*

Further insight into the apparent difference between the expected and observed quantum yield for loss of CO from $Cr(CO)_6$ can be gained from a series of elegant experiments in which $Cr(CO)_6$ and $Cr(CO)_5X$ (X = Ar or N_2), were irradiated using plane polarized light [24]. If a nonrotating molecule is photolysed with plane polarized light in a rigid low-temperature matrix, the preferential absorption of the polarizing light by some molecules in specific orientations will lead to the

apparent partial orientation of the remaining unphotolysed material, a phenomenon known as dichroic photodepletion. If there is no reorientation by way of rotation during the photochemical reaction the product will exhibit a preferred orientation (dichroic photoproduction). If, however, the excited molecule undergoes a rotation without accompanying reaction the process involves photoreorientation.

In a series of experiments $Cr(CO)_6$ was photolysed with unpolarized light in various isolating matrixes [24, 25]. Photolysis in a N_2 matrix produced randomly orientated $Cr(CO)_5(N_2)$ which exhibits a λ_{max} at approximately 360 nm (Fig. 11). Subsequent photolysis (λ_{exc} = 367 nm) of this matrix with polarized light produced dichroism in the spectra indicating a photoreorientation. Excitation of $Cr(CO)_5(N_2)$ ejects the N_2 ligand and launches the $Cr(CO)_5$ fragment onto the S_1 surface at a point removed from the Jahn-Teller conical intersection. The $Cr(CO)_5$ species then returns to the ground state and relaxes to the three possible C_{4v} orientations by traversing the branching state with D_{3h} symmetry. Thus, these matrix experiments provide support for the last part of the dynamic model for the photoinduced expulsion of CO from $Cr(CO)_6$.

In order to probe the earlier processes, femptosecond lasers were used to excite and ionize $Cr(CO)_6$ and its photofragments. Mass-selective detectors then monitored progress through the dark states leading to CO-loss.

2.4 *Ultrafast Photolysis of $Cr(CO)_6$ with Mass-Selective Detection*

The electronic excitation of $Cr(CO)_6$ into the accessible UV absorption bands provides sufficient energy to break more than one M–CO bond. While $Cr(CO)_5$ is the dominant photoproduct in the condensed phase, $Cr(CO)_4$, $Cr(CO)_3$, and $Cr(CO)_2$

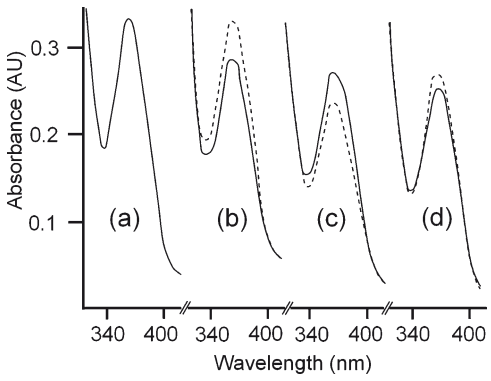

Fig. 11 The effect of polarized photolysis on the near-UV absorption of $Cr(CO)_5N_2$ in pure N_2 (**a**) after 20 min unpolarized photolysis λ = 314 nm and photolysis with λ = 367 nm, (**b**) with vertically polarized photolysis 20 min, (**c**) with horizontally polarized photolysis 30 min, vertically polarized photolysis 15 min: (*solid line*) spectrum polarized vertically, (*broken line*) spectrum polarized horizontally. Adapted from [24]

photofragments are produced in 73%, 14%, and 10% yields respectively following 248 nm excitation in the gas phase [26]. However, Rosenfeld et al. monitored the diffusion of the CO out of the probe laser volume using IR detection and confirmed that only the first CO ejected from $Cr(CO)_6$ contained a nonstatistical excess translational and rotational energy [27]. This suggests a sequential loss of CO ligands from $Cr(CO)_6$ following excitation, but only the first occurs on an accelerating potential energy surface, i.e., from an electronically excited state.

As described above, excitation of $Cr(CO)_6$ into its lowest-energy optically accessible state initiates a cascade of rapid processes through unbound states before reaching the electronic ground state of $Cr(CO)_5$. These unbound states cannot be studied using conventional spectroscopic techniques. However, Trushin and Fuß have probed the early dynamics of this process by using fs weak pump pulses at 267 nm and delayed, intense ionizing probe pulses at 800 nm coupled with time-of-flight detection of the resulting ions [15, 28–30]. This technique is particularly useful in studying the chemical dynamics of processes not amenable to spectroscopic methods [31]. In these experiments, a weak (270 nm; 10 or 30 fs) pulse excites $Cr(CO)_6$ in the gas phase in a single-photon absorption event. At various time intervals a subsequent high-intensity nonresonant pulse, ionizes the excited-state species and products as they move away from the Franck–Condon state along the developing potential energy surfaces. The parent ion $Cr(CO)_6^+$, and all fragment ions produced, exhibit different temporal behavior at different delay times up to several hundred fs after the excitation pulse. Measuring the intensity of the transient ion signal at these time intervals provides information on the dynamics of the decomposition of $Cr(CO)_6$ (Reaction 1).

$$Cr(CO)_6 \xrightarrow{h\nu} Cr(CO)_5 + CO. \qquad \text{(Reaction 1)}$$

The main features of the early kinetics could be reproduced using a five-level rate equation which included convolution with the pump and probe pulse shapes. These levels represent five locations, or time windows (L1–L5), describing five discrete time zones in the evolution of the $Cr(CO)_6$ excited state and ultimate formation of $Cr(CO)_5$ and $Cr(CO)_4$ in the gas phase. These levels are consecutively populated and differ in the nature and ratio of the fragment ions they produce. Their populations are modeled by rate equations providing the lifetimes (τ_i for Li) and the ionization-dissociation cross section ($^n\sigma_i$ for $Cr(CO)_n^+$) for a particular fragment in Li. This five-level model is represented in Fig. 12 and Table 2 contains the optimized

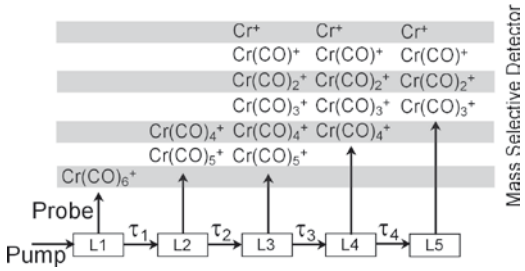

Fig. 12 A schematic representation of the consecutive locations Li on the potential energy surface and the range of fragments detected for each location. Adapted from [15]

lifetimes and ionization dissociation cross sections obtained from the kinetic modeling.

The first level L1 corresponds to the electronically excited $Cr(CO)_6$ (a^1T_{1u}) and L5 is the ground state (S_0) of $Cr(CO)_5$. Each of these levels produces a different range of ionized fragments following application of the probe pulse. The time-of-flight detector can select ions of a particular mass, and the time-dependent behavior of each fragment ion provides information on the length of time taken for the system to traverse each of the five levels.

For instance $Cr(CO)_6^+$ is formed only during L1. The time-dependent behavior of the ion yields of $Cr(CO)_6^+$ is presented in Fig. 13. Deconvolution of the time-dependent ion yield with the instrument function derived from the Xe^+ signal provides a measure of the time constant (τ_1) of 12.5 ± 0.05 fs for the L1 level (Table 2). This represents the time it takes for the excited $Cr(CO)_6$ to cross to the repulsive surface through the conical intersection close to the Franck-Condon state. At the Franck–Condon point with O_h symmetry, the only coordinates with nonzero slope are the totally symmetric a_{1g} M–C stretch or the Jahn–Teller-active vibrations which have e_g or t_{2g} symmetry [32]. The time taken for a wavepacket to travel from any

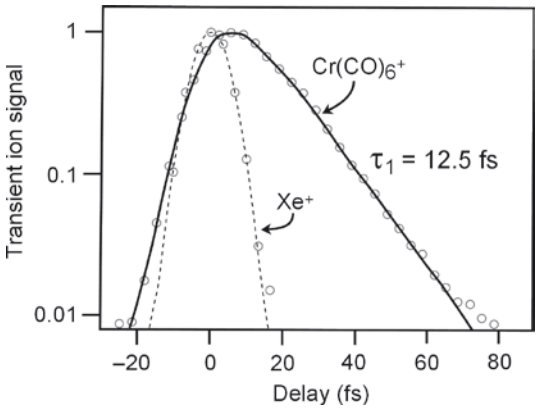

Fig. 13 The measured ion yields of $Cr(CO)_6$ (log scale) using a pump pulse of 270 nm with 10 fs duration. The Xe^+ signal represents the instrumental function. Adapted from [15]

Table 2 The lifetimes τ_i and effective ionization dissociation cross sections ${}^n\sigma_i$ for the various fragment ions following excitation of $Cr(CO)_6$ with λ_{exc} = 270 nm (From [15])

Li	L1	L2	L3	L4	L5
τ_i/fs	12.5 ± 0.5	18 ± 2	40 ± 3	930 ± 100	∞
$Cr(CO)_6^+$	1	0	0	0	0
$Cr(CO)_5^+$	0	1.0	0.082	0	0
$Cr(CO)_4^+$	0	1.0	0.440	0.002	0
$Cr(CwO)_3^+$	0	0	1.0	0.063	0.013

point on a potential energy surface to the minimum, or a conical intersection close to the minimum, is approximately one quarter of a period. For the a_{1g} vibration (400 cm^{-1}) this would take about 20 fs. For the e_g mode the curvature corresponds to a wavenumber of 360 cm^{-1}, which would take 23 fs to reach the minimum. Both of these are larger than the measured time constant of 12.5 fs. However, the t_{2g} bending mode (measured at 532 cm^{-1} in the ground state Fig. 14) is a more likely candidate with a quarter period of 15 fs. Consequently this mode contributes to the initial acceleration to the conical intersection and transition to the repulsive surface aT_{1g} (Fig. 4). During this time the nuclei are not accelerated appreciably and the $Cr(CO)_6$ excited state does not obtain sufficient excess vibrational energy to expel further CO ligands following the ionization process. This explains why $Cr(CO)_6$ is the only fragment that is produced in L1.

The remaining time constants τ_2 to τ_4 are extracted by sequential curve fitting procedures and are presented in Table 2. After crossing to the aT_{1g} state the M–C bond length extends, passing through a second conical intersection, with ultimate dissociation of one CO ligand within L2 (18 fs). This forms the electronically and vibrationally excited (S_1) C_{4v} $Cr(CO)_5$ fragment. The steepness of the repulsive surfaces transfers a significant part of the potential energy to the kinetic energy of the nuclei. This promotes further fragmentation following the nonresonant ionization process. Ionization in the time periods of L2–L5 therefore produces the smaller fragment ions. In addition the smaller fragments exhibit coherent oscillations in the ion yield (Fig. 15). The origin of these oscillations is twofold. First the high frequency mode (350 cm^{-1}) corresponds to a totally symmetric M–C stretch which persists down to the S_0 state of $Cr(CO)_5$. Second the low frequency mode (96 cm^{-1}) characterizes the nuclear motion in the moat surrounding the conical intersection of S_1 and S_0 states of $Cr(CO)_5$.

Thus, it is clear that when the $Cr(CO)_5$ species reaches the ground-state (S_0) it retains excess vibrational energy. This is used to expel a further CO loss producing $Cr(CO)_4$ in L4 (930 ± 100 fs). It is important to note that the timescale at which $Cr(CO)_4$ is produced is slow compared to solvent-induced vibrational relaxation processes. Thus, $Cr(CO)_4$ is formed only in the gas phase while photoinduced decarbonylation of $Cr(CO)_6$ stops at $Cr(CO)_5$ in the condensed phase.

2.5 *The Overall Description of Photoinduced CO Loss from $Cr(CO)_6$*

The photoinduced CO loss from $Cr(CO)_6$ occurs following a symmetry and spin-allowed transition to produce the a^1T_{1u} MLCT excited state. A Jahn-Teller active (t_{2g} bending) mode promotes motion to a conical intersection close to the Frank-Condon state. This provides an efficient barrierless transition to the *E* component derived from the a^1T_{1g} state. This process takes approximately 12.5 fs. The *E* component is unbound with respect to the M-CO interaction. As the M-CO bond lengthens a further conical intersection with the *E* component derived from the a^1T_{2u} state,

Fig. 14 A representation of the t_{2g} bending mode for $Cr(CO)_6$ with O_h symmetry

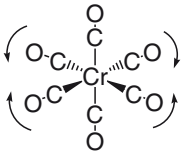

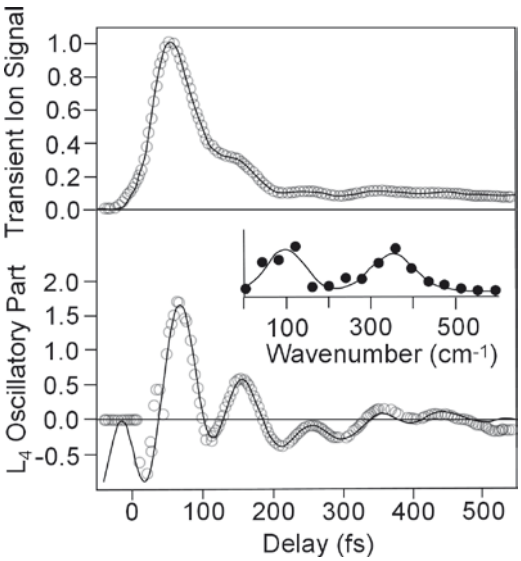

Fig. 15 The ion yield of $Cr(CO)_3^+$ obtained using a 270 nm pulse of 30 fs duration showing the periodic functions and a Fourier transform of these functions in the inset showing coherent oscillations at 96 and 350 cm^{-1}. Adapted from [15]

accelerates the breaking of the M-CO bond which occurs within 18 fs, equivalent to one quarter of the period of a M-CO stretching vibration. The CO ligand leaves in a rotationally excited state but the electronically excited (S_1) $Cr(CO)_5$ fragment retains considerable excess vibrational energy as the steep surface leads to two equivalent $Cr(CO)_5$ species with D_{3h} symmetry. The conical intersection at the D_{3h} symmetry provides an efficient and barrierless transition to the S_0 $Cr(CO)_5$ surface but also represents a branching space to the three equivalent $Cr(CO)_5$ fragments with C_{4v} symmetry. Thus, the $Cr(CO)_5$ appears in its ground electronic state some 70 fs after the initial excitation.

As the wavepacket develops in the moat around the D_{3h} symmetry, the $Cr(CO)_5$ fragment can recombine with the ejected CO. This process is likely to be more efficient in the condensed phase where the measured quantum yield for CO loss from $Cr(CO)_6$ shows solvent dependency [22, 33]. In the gas phase the excess vibrational energy is available for the expulsion of a further CO ligand. These processes are summarized in Fig. 16.

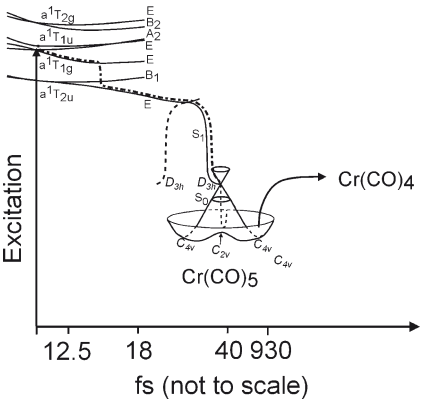

Fig. 16 A schematic representation of the photoinduced loss of CO from $Cr(CO)_6$ following excitation into the a^1T_{1u} states, showing the cascade of processes (*dash dot line*) leading to three equivalent ground-state $Cr(CO)_5$ fragments and the subsequent ejection of a further CO

3 The Photodecarbonylation of $Fe(CO)_5$

The photoinduced decarbonylation of $Cr(CO)_6$ described in the previous section demonstrates the complexities of ultrafast processes leading ultimately to the photoinduced expulsion of a single CO ligand. While there is no evidence for the involvement of triplet species in the photochemistry of $Cr(CO)_6$, triplet species play a significant role in the photochemistry of $Fe(CO)_5$ particularly for processes occurring on the ns timescale or slower [34]. In addition photoinduced decarbonylation of $Cr(CO)_6$ stops at $Cr(CO)_5$ in the condensed phase while photoinduced decarbonylyation of $Fe(CO)_5$ produced both $Fe(CO)_4L$ and $Fe(CO)_3L_2$ (L = PMe_3) even in solution [35, 36]. A triplet $^3Fe(CO)_4L$ intermediate was implicated in this process which undergoes thermal decarbonylation ultimately yielding the singlet $Fe(CO)_3L_2$ product.

In the gas phase, photolysis at 193, 248, or 251 nm, using ns pulsed lasers and IR detection, produced a range of products $Fe(CO)_n$ (n = 4, 3, 2, 1) depending on the excitation wavelength [37–41]. These observations seemed to support a concerted multiple ligand loss from a single excited state of $Fe(CO)_5$. However, the results of ultra-fast studies were more consistent with the expulsion of a single CO following optical excitation of $Fe(CO)_5$.

3.1 The Electronic Structure of $Fe(CO)_5$

The UV spectrum of $Fe(CO)_5$ is given in Fig. 17 [42]. This spectrum exhibits two weak shoulders at 333 nm (30,000 cm^{-1}), 280 nm (35,700 cm^{-1}), a more intense shoulder at 240 nm (41,600 cm^{-1}) and an intense absorption centered at 200 nm

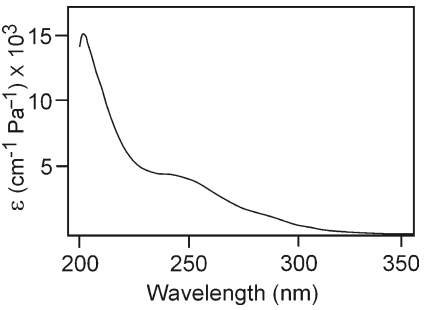

Fig. 17 The UV spectrum of $Fe(CO)_5$ in the gas phase. Adapted from [42]

(50,000 cm^{-1}). Semiempirical calculations based on structural parameters obtained from IR measurements [43] suggested that the lower-energy absorptions are metal-centered in nature [42]. The electronic ground state ($^1A'_1$) of $Fe(CO)_5$ has a configuration represented by

$$(\pi_{CO})^2(\pi_{CO})^2(3d_\sigma)^4(3d_\pi)^4(3d_{x^2})^0,$$

where $3d_\sigma$ denotes the set of $3d_{yz}$, $3d_{y^2-z^2}$ e' orbitals and the $3d_\pi$ denotes the set of $3d_{xy}$ and $3d_{xz}$ e'' orbitals. For the low-lying excited states, $3d_\sigma$, $3d\pi \rightarrow 3d_{x^2}$ are MC while $3d\pi^*_{CO}$, $3d\pi \rightarrow \pi^*_{CO}$ are MLCT states. Averaged CASSCF calculations were used as references for multireference contracted configuration interaction (MR-CCI) calculations in order to obtain accurate excitation energies to low-lying singlet states [44]. The results of these calculations are presented in Table 3 along with some results of second-order perturbation theory CASPT2 [45] and earlier CCI calculations [46].

The results in Table 3 indicate that there are three allowed transitions at 26,900-27,450 (370-365 nm; = 0.003), 37,900 (263 nm; $f = 0.01$), and 38,930-40,850 cm^{-1} (256-244 nm; $f = 0.006$). The lowest-energy transition can be characterized as MC and the other two are MLCT in nature. Also presented in Table 3 are the transition energies of the two lowest spin-forbidden ($^1A'_1 \rightarrow a^3E'$ and $^1A'_1 \rightarrow a^3E''$) transitions.

3.2 Ultrafast Multiphoton Excitation of $Fe(CO)_5$

First attempts to investigate the photodissociation dynamics of $Fe(CO)_5$ used molecular beam technology coupled with high intensity femptosecond lasers [47, 48]. It is important to note that these experiments relied on multiphoton absorption to populate the electronic excited states of $Fe(CO)_5$. This work built on the results of earlier experiments using nanosecond pulsed lasers which provided information on the photoproduct distribution and their energies [37–40, 49–56]. The energies of the various dissociation processes for $Fe(CO)_5$ are presented in Fig. 18 for comparison with the excitation photon energies and the absorption profile of $Fe(CO)_5$.

Table 3 Excitation energies (in cm^{-1}) to low-lying states of $Fe(CO)_5$ and associated oscillator strengths *f*

State	One electron excitation in the principal configuration	CASSCF[a]	MR-CCI[a]	With averaged coupled pair functional[a]	CASPT2[b]	CASSCF/CCI[c]
$^1A'_1 \rightarrow a^1E'$	$3d_\sigma \rightarrow 3d_{x^2}$	32,100	26,670	26,940	35,360	33,360
		32,620	28,690	27,450		
		$f = 0.003$				
$^1A'_1 \rightarrow {}^1A''_1$	$3d_\sigma \rightarrow \pi^*_{CO}$	34,980	33,280	35,700		
$^1A'_1 \rightarrow a^1E''$	$3d_\pi \rightarrow 3d_{x^2}$	35,600	36,730	35,520	42,160	34,150
		35,360	36,790	36,820		
$^1A'_1 \rightarrow b^1E''$	$3d_\sigma \rightarrow \pi^*_{CO}$	36,600	35,550	37,400		
		35,360	35,530	37,350		
$^1A'_1 \rightarrow {}^1A''_2$	$3d_\sigma \rightarrow \pi^*_{CO}$	39,240	37,030	37,900		
		$f = 0.01$				
$^1A'_1 \rightarrow {}^1A'_2$	$3d_\sigma \rightarrow \pi^*_{CO}$	37,900	38,050	39,530		
$^1A'_1 \rightarrow b^1E'$	$3d_\sigma \rightarrow \pi^*_{CO}$	38,900	39,350	38,930	39,520	
		38,300	39,310	40,850		
		$f = 0.006$				
$^1A'_1 \rightarrow c^1E''$	$3d_\sigma \rightarrow \pi^*_{CO}$	41,360	42,640	42,350		
		41,900	42,660	42,410		
$^1A'_1 \rightarrow {}^1A'_1$	$3d_\sigma \rightarrow \pi^*_{CO}$	43,900	45,030	44,630		
$^1A'_1 \rightarrow a^3E'$	$3d_\sigma \rightarrow 3d_{x^2}$	22,088	17,760	17,510		22,370
		22,083	18,160	16,400	28,240	
$^1A'_1 \rightarrow a^3E''$	$3d_\sigma \rightarrow 3d_{x^2}$	26,920	23,090	22,170		24,350
		26,925	23,000	22,580	34,560	

[a]From [44]
[b]from [45]
[c]from [46]

The earlier nanosecond work suggested that the expulsion of multiple CO ligands occurs following photoexcitation of $Fe(CO)_5$ and also that the distribution of $Fe(CO)_n$ (n = 4-0) fragments was dependent on the excitation wavelength. Table 4 contains the relative yields of $Fe(CO)_n$ fragments obtained following photolysis with low-intensity Nd/YAG or excimer laser radiation (353, 248, or 193 nm) with 8-10 ns pulse durations [50]. In these experiments the fragments were trapped using PF_3. Even using the highest-energy photons (193 nm), FeCO only comprises a small fraction of the total fragment yield and the $Fe(CO)_2$ fragment predominates. This result should be contrasted with the pump-probe methods and time-of-flight detection [48]. Figure 19(a) contains the ion-signal obtained following 337 nm excitation of $Fe(CO)_5$ using a 3 ns (1 mJ per pulse) laser. The pump-probe experiments rely on multiphoton absorption first to induce the photochemical change and then to ionize the fragments for detection in the mass spectrometer. The only fragment observed following ns pulse photolysis is that of the fully decarbonylated Fe^+.

Reducing the excitation pulse duration to 80 fs and using 400 nm photons produced all fragment ions as well as the parent ion and these signals are presented in Fig. 19. Indeed the product ion distribution was found to be sensitive to

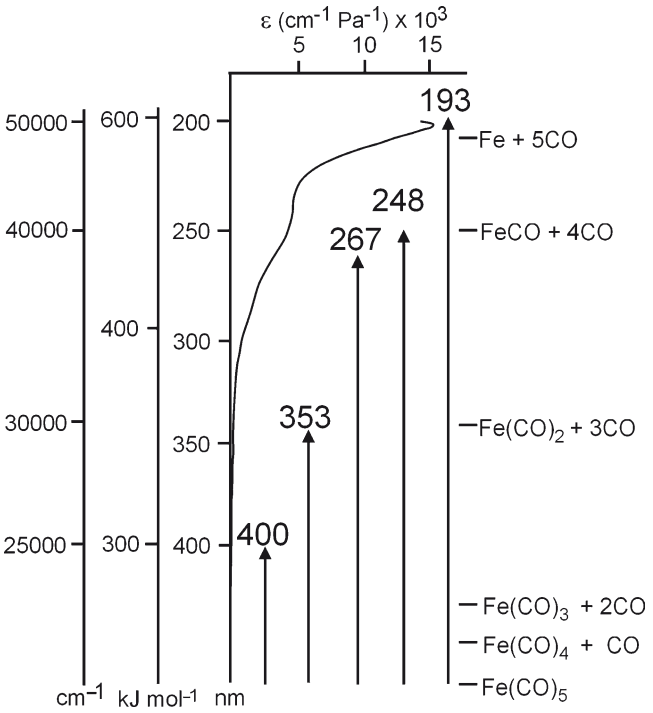

Fig. 18 Representations of the photon energies used and their relation to the UV absorption spectrum and dissociation energies of $Fe(CO)_5$. Adapted from [51]

Table 4 Excitation conditions and relative yields for photodissociation of $Fe(CO)_5$ to give $Fe(CO)_n$ (n = 4–1) From [51]

Laser	Nd/YAG (3rd harmonic)	KrF	ArF
λ (nm)	353	248	193
E (kJ/Einstein)	339.4	482.0	619.5
σ (cm^2)[a]	1.3×10^{-18}	2.7×10^{-17}	2.4×10^{-16}
E/A (mJ cm^2)[b]	7–14	0.1–10	5–15
Φ[c]		1.1	>0.6
Relative yields			
FeCO			0.012[d]
$Fe(CO)_2$	0.31	0.55	0.81
$Fe(CO)_3$	0.46	0.35	0.09
$Fe(CO)_4$	0.23	0.10	0.09

[a]Absorption cross section
[b]Laser energy per unit area
[c]Sum of quantum yields for all fragments
[d]Upper limit of yield

the pulse duration at a given excitation wavelength. Figure 20 shows how the product ion distribution changes with pulse duration at 800 nm. Multiphoton absorption by $Fe(CO)_5$ is required at this excitation wavelength. For laser pulses

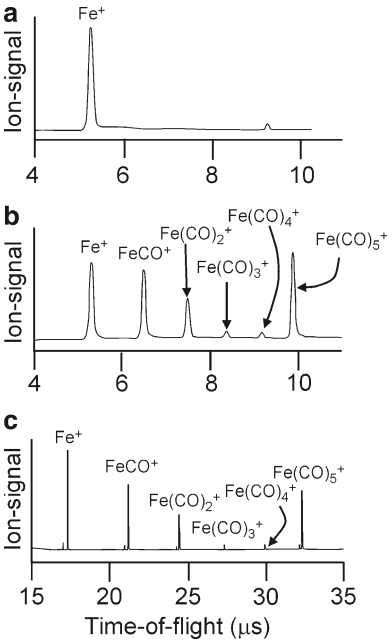

Fig. 19 The time-of-flight spectra obtained following irradiation of $Fe(CO)_5$ with (**a**) ns and (**b**, **c**) fs laser pulses at 400 nm; spectra were obtained using a linear (**a**, **b**) and high-resolution reflectron (**c**) mass detectors. Adapted from [48]

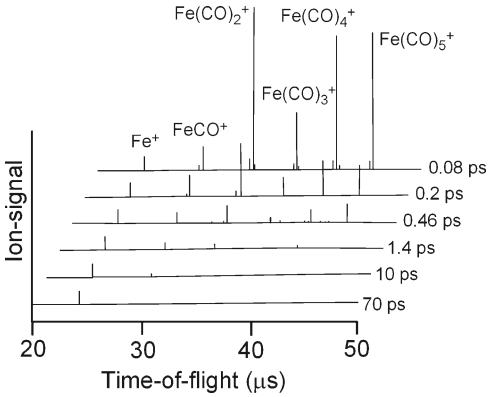

Fig. 20 Reflectron TOF spectra obtained after excitation using 800 nm variable pulse widths between 80 fs and 70 ps. All the traces have been normalized to have the same Fe^+ mass peak intensity. Adapted from [48]

with widths of more than 70 ps, only Fe^+ is observed in the mass spectrum. This suggests that the leading edge of the laser pulse induces the excitation to a low-lying electronic excited state which in turn absorbs further photons from the trailing edge of the pulse producing a highly excited species. Using two color experiments (400 nm two photon pump and 800 nm probe pulse) it is possible to obtain time-resolved information on the fragment formation by delaying the probe pulse relative to the pump pulse.

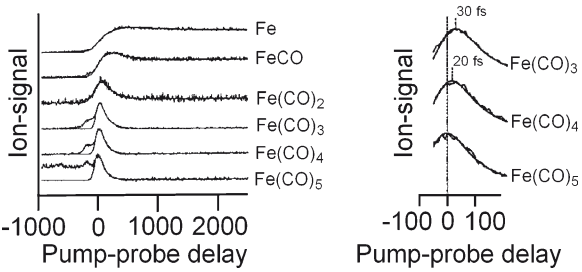

Fig. 21 The temporal behavior of the ion signals for the fragments $Fe(CO)_n$ (n = 5–0). The expanded region shows the transients around time delay zero for the parent molecule and the $Fe(CO)_4$ and $Fe(CO)_3$ fragments. Adapted from [48]

Table 5 Rise and decay times for the transient signals corresponding to the parent $Fe(CO)_5$ and all its fragments from [48]

Species	τ_{decay} (fs)	τ_{rise} (fs)	Time shift (fs)
$Fe(CO)_5$	100 ± 5		
$Fe(CO)_4$	105 ± 5		20 ± 5
$Fe(CO)_3$	115 ± 5		30 ± 5
$Fe(CO)_2$	150 ± 20		60 ± 15
FeCO	230 ± 20	120 ± 20	
Fe	490 ± 50	260 ± 20	

The temporal behavior of the various fragments is presented in Fig. 21 and the rise and decay times obtained by either single or multiple exponential curve fitting procedures are presented in Table 5. These results can be summarized as follows:

- The same decay times were observed for $Fe(CO)_n$ (n =5–2) and none of these species had detectable rise times
- The signals for $Fe(CO)_n$ (n =4–2) are time-shifted with respect to $Fe(CO)_5$ with increasing time differences as n reduces
- Only the signals of FeCO and Fe show rise times and the FeCO rise time is similar to the decay of $Fe(CO)_5$

A rather controversial proposal of a concerted CO loss from a $Fe(CO)_5$ excited state ($Fe(CO)_5$*) was used to explain these observations. In this description $Fe(CO)_5$*, formed following the absorption of two 400 nm photons, is launched onto a steep unbound surface and loses four CO's within the time scale of the vibrational period of a Fe–CO bond (100 fs). The time shift in the signals for the $Fe(CO)_n$ (n = 4–2) is explained by the time taken for the fragments to move away from their force field attraction.

The difficulty with this proposal is that it cannot explain the observed photochemistry of $Fe(CO)_5$ in the condensed phase. If the photoinduced CO loss from $Fe(CO)_5$ was concerted, then it should be observed in solution or in low-temperature

matrixes because it would occur on a timescale faster than any solvent-solute deactivation process [34, 37, 38, 53, 55, 57-62]. However, there are no reports of such a concerted CO loss in the condensed phase. An alternative explanation for the temporal behavior of the signals in the pump-probe experiments is required. One possible explanation is discussed in the next section.

3.3 *Ultrafast Single-Photon Excitation of $Fe(CO)_5$ with Mass Detection*

Pump-probe experiments using single photon (λ_{pump} =267 nm) coupled with nonresonant photoionization probing (λ_{probe} =800 nm) produced ions of all fragments $Fe(CO)_n^+$ (n =4–0) along with the parent ion [63]. In these experiments the pump pulse intensity was 10^{-2} to 10^{-4} times those used in the multiphoton experiments described in Sect. 3.2 (10^9 compared to 10^{11}–10^{13} W cm^{-2}).

At early times (<300 fs) all fragments exhibit different temporal behavior (Fig. 25). These signals were modeled using kinetic equations in a manner similar to that described in Sect. 2.4. In this case a six-level model was required each level being sequentially produced from the previous with its own unique rate. The parameters in this model are the rate constant (τ_i) for the decay of a particular level i to level j, and the probabilities of forming a particular ion ($Fe(CO)_n$) from level i ($^n\sigma_i$). These parameters are presented in Table 6. The first level (L1) is the excited state of $Fe(CO)_5$ close to the Franck–Condon region and L6 is the final product of the photodecomposition.

Probing of these levels was achieved by nonresonant photoionization using a 800 nm pulse. The parent ion is produced close to the Franck–Condon region as indicated by the $^5\sigma_1$ value of 1.000 in Table 6 where little of the excitation energy has been converted into nuclear motion, while smaller fragments are produced as the neutral photoproduct arrives at its ground state.

The parent ion $Fe(CO)_5^+$ and the other heavy ions, $Fe(CO)_4^+$ and $Fe(CO)_3^+$ exhibit different time behaviors (Fig. 22), which require four different precursor levels (L1–L4). In each successive level, an ever-increasing fraction of the pump

Table 6 Lifetimes ($\tau_{i,j}$) and effective ionization–dissociation cross sections ($^n\sigma_i$) used in the six-level model for the photochemical decomposition of $Fe(CO)_5$. From [63]

Level Li	L1	L2	L3	L4	L5	L6
τ_i (fs)	21 ± 2	15 ± 5	30 ± 3	47 ± 5	3,300 ± 300	∞
$Fe(CO)_5^+$	1.000	0	0	0	0	0
$Fe(CO)_4^+$	0	0.924	0.076	0	0	0
$Fe(CO)_3^+$	0	0.517	0.452	0.032	0	0
$Fe(CO)_2^+$	0	0	0.677	0.252	0.038	0.032
$FeCO^+$	0	0	0.124	0.604	0.131	0.142
Fe^+	0	0	0.125	0.500	0.170	0.210

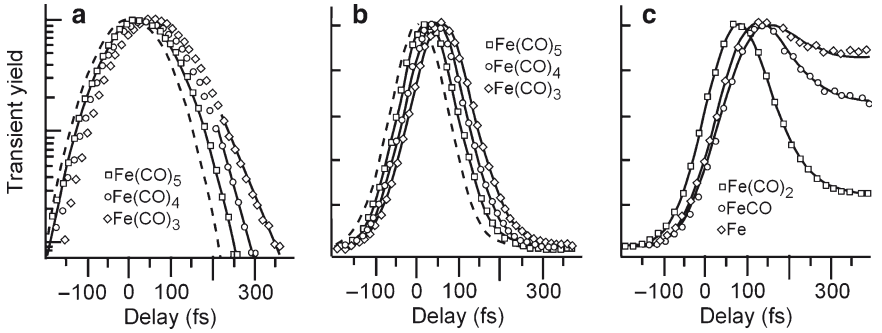

Fig. 22 Transient ion signals following excitation of $Fe(CO)_5$ at 267 nm. The *vertical scale* is logarithmic in (**a**) and *linear* in (**b**) and (**c**). The *dashed curve* in (**a**) and (**b**) represents the instrument response function and the *solid lines* in (**a**) correspond to the single exponential functions from which the time constants for $Fe(CO)_4$ and $Fe(CO)_3$ were obtained. Adapted from [63]

energy is converted into vibrational energy, which promotes progressively greater fragmentation after ionization. This means that upon excitation the $Fe(CO)_5$ is launched onto a steep potential energy surface which within a fraction of a Fe-CO vibrational period (21 fs) leaves the Franck-Condon region.

The pump wavelength of 267 nm (4.65 eV; 37,453 cm^{-1}) is close to the region of the $^1A'_1 \rightarrow {}^1A''_2$ and $^1A'_1 \rightarrow b^1E'$ MLCT transitions but far removed from the weak $^1A'_1 \rightarrow a^1E'$ MC transition (Table 3). It is likely that the initially produced excited state has MLCT character and would not be expected to be repulsive along the Fe–CO coordinate. For the totally symmetric $^1A'_1$ state, the slope of the PE surface must be zero along any Fe–CO coordinate because only symmetric vibrations are possible in this state. Consequently population of such a state is unlikely to result in a rapid departure from the Franck–Condon region.

The b^1E' state is degenerate but this degeneracy is lifted by Jahn-Teller distortion along any e' coordinate. For $Fe(CO)_5$ (D_{3h}) there are four coordinates of e' symmetry, two involving Fe–C and C–O stretch of the equatorial bonds and two involving C–Fe–C bending of the equatorial and axial bonds. So in the absence of more detailed information on the shape of the potential energy surfaces along specific reaction coordinates, Jahn–Teller splitting of the degenerate b^1E' state provides a plausible explanation for the rapid exit from the Franck–Condon region along either bending or stretching coordinates (Fig. 26). At some point along the Jahn–Teller coordinate it may cross the lower energy $^1A''_2$ surface at a conical intersection and the population may divert into the $^1A''_2$ state but can leave again by displacement along the orthogonal e'' coordinate (see inset in Fig. 26) by passage around the circumference of the conical intersection. The population then rejoins the direct reaction path from b^1E'. The lower-lying MC a^1E' state will also be subject to Jahn-Teller splitting and at some point the surfaces derived from the b^1E' and a^1E' states will approach generating a conical intersection at an avoided crossing and providing a barrierless path to the a^1E' repulsive state.

Since $Fe(CO)_4^+$ is observed in the L3 window it is likely that it arises from $Fe(CO)_5$, suggesting that $Fe(CO)_5$ survives intact until reaching this window. This indicates that photoinduced CO loss occurs around 66 fs after excitation while the population moves along a reaction coordinate involving the lengthening of one Fe-CO bond. $Fe(CO)_4$ has C_{4v} symmetry and its lowest-energy singlet state (S_0) is nondegenerate ($^1A_1$) [66, 67]. Consequently this state can only correlate with the ground state of $Fe(CO)_5$. The lowest excited state of $Fe(CO)_5$ must therefore correlate with the lowest singlet state of $Fe(CO)_4$ (S_1, $^1B_2$). This means that the $Fe(CO)_4$ formed photochemically must be launched onto its first excited-state surface ($^1B_2$).

As there is no evidence for luminescence in this system a route for the efficient conversion to the ground singlet state (S_0) must exist. Such a deactivation of the $^1B_2$ state would require a degenerate state where Jahn–Teller distortion will lead to correlation with both S_1 and S_0 with C_{2v} symmetry namely A_1 and B_2 states. At tetrahedral symmetry $Fe(CO)_4$ gives rise to three states A_1, E, and T_2. Coordinates of symmetry e and t_2 are Jahn-Teller active, and distortion along e leads to states A_1, B_2, and B_1 of which only A_1 and B_2 are required. Thus, conversion from $^1B_2$ to $^1A_1$ can proceed via a Jahn-Teller induced conical intersection at T_d symmetry joining the S_1 to the S_0 state. The model for deactivation to the lowest-energy singlet state is similar to that proposed for $Cr(CO)_5$, except that in the case of $Fe(CO)_4$ the lowest-energy singlet state is not the ground state [28].

Interconversion between species of C_{2v} symmetry can be achieved through a low-energy nonBerry pseudorotation similar to that proposed to explain the IR-induced intramolecular ligand exchange reaction in matrix isolated $Fe(CO)_4$ in the triplet state [61, 68]. Thus, the $Fe(CO)_4$ arrives at the lowest-energy singlet state in a moat around the Jahn-Teller induced conical intersection. The $Fe(CO)_4$ will contain sufficient excess vibrational energy to thermally eject a second CO ligand, on the ps timescale in L5. In the case of $Cr(CO)_5$ coherent oscillations in the ion yield signal were observed for the lighter fragments [28]. No such oscillations were detected for the $Fe(CO)_5$ system presumably because the S_0–S_1 energy gap is small compared to the probe photon energy (1.55 eV) and resonance between the S_0 and S_1 states is not possible following the absorption of the ionizing pulse.

The ultrafast processes leading to loss of one CO in the condensed phase and two CO's in the gas phase can be adequately described by processes on the singlet manifold. The observation of the triplet $Fe(CO)_4$ at longer timescales indicates that intersystem crossing to the triplet manifold occurs on timescales longer than 3 ps. Indeed the ultrafast electron diffraction studies outlined in the following section confirm that $Fe(CO)_4$ persists in the singlet state for up to 200 ps following excitation [69].

3.4 *Ultrafast Electron Diffraction by $Fe(CO)_n$ (n = 5–0)*

Two ultrafast electron diffraction studies on the $Fe(CO)_5$ system have been published [69, 70]. In these experiments fs pump pulses excite $Fe(CO)_5$ in the gas phase in a free expansion jet. Two photon excitation was used in these experiments

(λ_{pump} =310 nm). Following excitation the structure of photofragments were probed using a 10 ps electron pulse. The experimental time resolution in these experiments was of the order of 12 ps. Two-dimensional electron diffraction images were recorded at various time delays. These data provide information on the internuclear separations expressed as a radial distribution curve. Figure 23 presents the radial distribution function ($f(r)$) for $Fe(CO)_5$ obtained prior to irradiation, along with the changes in function ($\Delta f(r)$) for various time delays after excitation. These results confirm that the photochemistry is complete within 10 ps, which is consistent with the fs data outlined above.

Information on the product distribution can also be obtained from the electron diffraction data. This indicates that the photoproducts detected after 10 ps are $Fe(CO)_2$, FeCO, and Fe in the ratio 2:5:5 (Fig. 24). Structural parameters for these fragments were obtained from computational [66] and experimental results [71, 72]. A photon with a wavelength of 310 nm would have insufficient energy to remove four CO ligands from $Fe(CO)_5$. The formation of FeCO and Fe in the electron diffraction study means that at least two 310 nm photons were absorbed in the pump process.

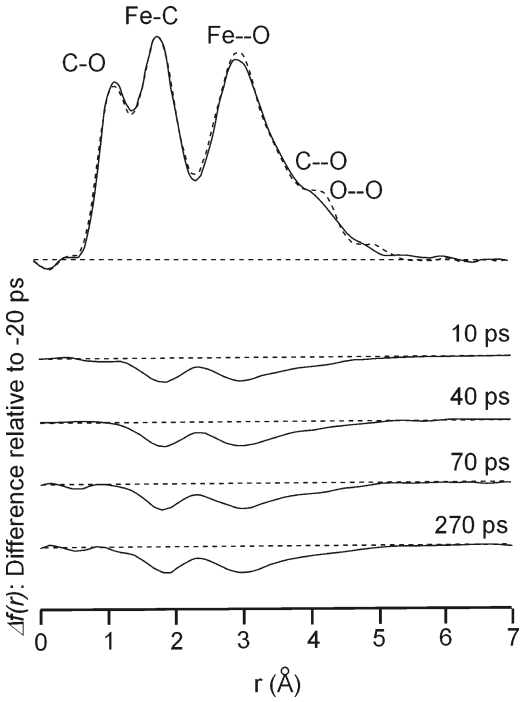

Fig. 23 The ultrafast electron diffraction radial distribution curves obtained using 10 ps electron pulses prior to excitation with a 310 nm fs pulse (top) and the difference signals ($"f(r)$) obtained at 10, 40, 70, and 270 ps delay times. No significant change to the $"f(r)$ function was observed after 10 ps. Adapted from [70]

By increasing the pump wavelength to 620 nm, $Fe(CO)_4$ emerges as the predominant photofragment following absorption of a least two photons [69]. The structure of the $Fe(CO)_4$ fragment obtained in the ultrafast electron diffraction study is consistent with the singlet $^1A_1$ state rather than the lower energy $^3B_2$ state (Fig. 24). Thus, intersystem crossing to the triplet is slow (>200 ps), and this confirms that the photoinduced fragmentation observed in the ultrafast experiments occurs from the manifold of singlet states.

3.5 Concluding Comments

The quantum chemical calculations on $Fe(CO)_5$ indicate that the lowest-energy accessible excited state is MC in character. The oscillator strength for the ground state to MC transition is small and most ultrafast experiments use either single or multiphoton excitation to MLCT states. The difference in product distribution depending on the excitation pulse duration points to an enhanced absorption cross section for the $Fe(CO)_5$ excited state over the ground-state species to both pump and probe pulses. This tends to complicate the apparent photochemistry. Consequently the use of short-pulse single-photon excitation provides a better picture of the excited-state dynamics.

The experiments using mass detection techniques suggest that CO-loss occurs at about 66 fs following excitation and $Fe(CO)_4$ arrives at the S_1 state after approximately 110 fs. This species can then either expel a further CO (possibly by absorbing a probe photon) or undergo intersystem crossing to the triplet $Fe(CO)_4$ ground state. The scheme of potential energy curves and pathways are presented in Fig. 25.

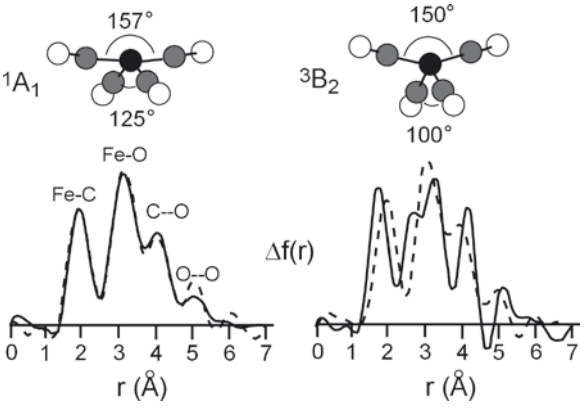

Fig. 24 Ultrafast electron diffraction radial distribution functions (*solid lines* -calculated; *broken lines*- experimental) showing excelling agreement for the $^1A_1$ $Fe(CO)_4$ (*left*) compared to the $^3B_2$ structure (*right*). Bonds represented by broken lines correspond to nonbonding distances. Adapted from [69]

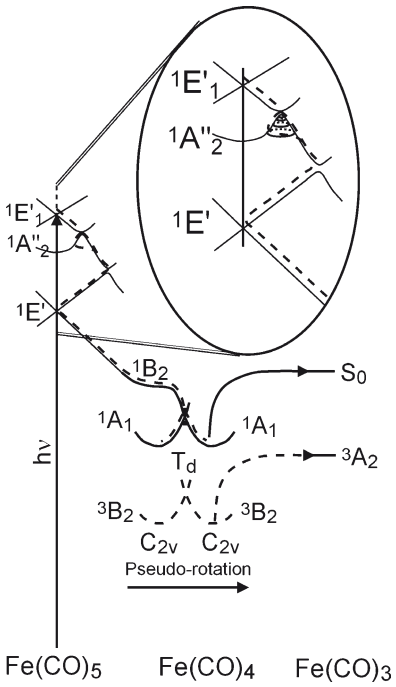

Fig. 25 Proposed scheme of potential energy curves and pathways leading to photoinduced loss of CO from $Fe(CO)_5$. The inset indicates the diversion to the $^1A''_2$ state and the passage around the circumference of the conical intersection. Adapted from [63]

4 The Photodecarbonylation of $Ni(CO)_4$

The UV/Vis spectrum of $Ni(CO)_4$ in the gas phase is presented in Fig. 26 [42]. The spectrum has also been recorded in solution [73], and in low temperature matrixes [74]. In the gas phase the absorption maximum occurs at 207 nm (6.02 eV) and two shoulders can be observed at 230 nm (5.52 eV) and 270 nm (5.24 eV). These features have been attributed to four bands, the two lowest-energy bands have been assigned to $9t_2 \rightarrow 12t_2$ and $9t_2 \rightarrow 4e$ orbital transitions producing a^1T_2 and b^1T_2 states respectively. These calculations used symmetry adapted cluster expansion (SAC) methods [64]. The nature of the other two bands remains controversial [65], although the SAC methods suggest that the c^1T_2 state corresponds to MC ($d \rightarrow s$) transitions which may have a similar role to the $d \rightarrow d$ MC transitions in $Cr(CO)_6$ and $Fe(CO)_5$ systems.

Table 7 contains the experimental and calculated excitation energies and assignments for $Ni(CO)_4$ [10, 42, 64, 73, 74]. Difficulties with the choice of the active space reduces the accuracy of the CAS calculations but both TDDFT and SAC methods predict four dipole allowed excited states in the 4.0–6.5 eV range which is in agreement with the experimental results. All low-lying singlet excitation energies for TDDFT and SAC-CI calculations are presented in Table 8.

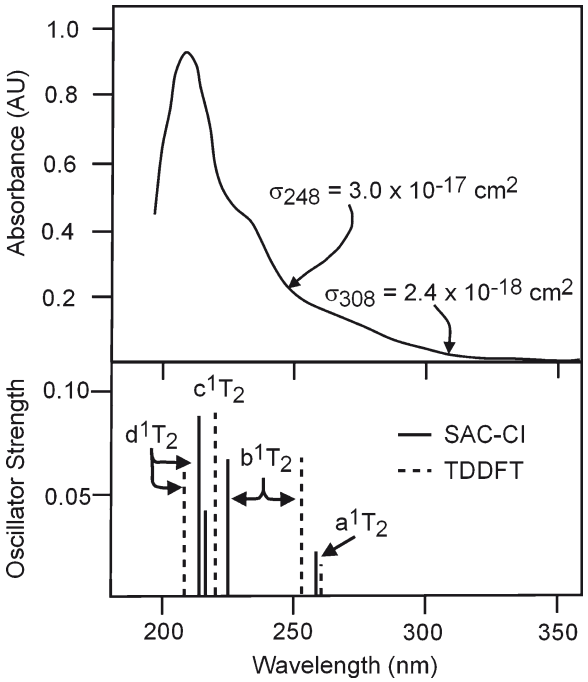

Fig. 26 A comparison of the experimental gas phase (5 Pa) spectrum of $Ni(CO)_4$ with calculated one electron transition energies, SAC-CI data from [64] and TDDFT results from [65]

Table 7 The experimental and calculated excitation energies and assignments for $Ni(CO)_4$

Method/ property	Band I	Band II	Band III	Band IV	Band V
Solution[a]					
Energy (eV)		5.24	5.52	6.02	
Matrix[b]					
Energy (eV)	4.54	5.17			
Gas[c]					
Energy (eV)	4.5	5.4		6.0	
CASSCF[d]					
Energy (eV)	7.34	7.49	7.57	7.67	8.16
Assignment	$9t_2 \rightarrow 10t_2$ 92%	$9t_2 \rightarrow 3e$ 92%	$2e \rightarrow 10t_2$ 94%	$9t_2 \rightarrow 2t_1$ 93%	$2e \rightarrow 2t_1$ 88%
CASPT2[d]					
Energy (eV)	4.34	5.22	5.57	6.28	6.97
Osc Str.	0.29	0.38	0.29	0.47	0.83
SAC-CI[e]					
Energy (eV)	4.79	5.51	5.72	5.76	
Assignment	$9t_2 \rightarrow 12t_2$ 54% $9t_2 \rightarrow 4e$ 8%	$9t_2 \rightarrow 4e$ 48% $9t_2 \rightarrow 9a_1$ 20% $2e \rightarrow 12t_2$ 18%	$9t_2 \rightarrow 9a_1$ 69% $9t_2 \rightarrow 10a_1$ 20% $9t_2 \rightarrow 3e$ 10%	$2e \rightarrow 12t_2$ 42% $9t_2 \rightarrow 3t_1$ 19%	
Osc Str.	0.0023	0.0067	0.0043	0.0089	
TDDFT[f]					
Energy (eV)	4.70	4.82	5.37	5.84	6.74
Assignment	$9t_2 \rightarrow 10t_2$ 56% $9t_2 \rightarrow 3e$ 35%	$9t_2 \rightarrow 3e$ 49% $9t_2 \rightarrow 10t_2$ 23%	$9t_2 \rightarrow 2t_1$ 52% $2e \rightarrow 10t_2$ 19%	$2e \rightarrow 10t_2$ 51% $2e \rightarrow 2t_1$ 37%	$2e \rightarrow 2t_1$ 47% $2e \rightarrow 10t_2$ 9%
Osc Str.	0.006	0.099	0.123	0.086	1.002

[a]From [73]
[b]from [74]
[c]from [42]
[d]from [10]
[e]from [64]
[f]from [65]

Table 8 The low-lying singlet excitation energies of $Ni(CO)_4$

State	TDDFT[a]	SAC-CI[b]
a^1T_1	4.36	4.53
a^1E	4.60	4.52
b^1T_1	4.62	4.97
a^1T_2	4.70	4.79
b^1T_2	4.82	5.51
a^1A_2	4.95	6.07
b^1A_1	4.99	5.41
c^1T_1	4.99	5.25
b^1E	5.06	6.28
c^1T_2	5.37	5.72
d^1T_1	5.45	
b^1A_2	5.60	
d^1T_2	5.84	5.76
c^1E	6.02	
e^1T_1	6.04	
e^1T_2	6.74	
f^1T_2	6.99	

[a]From [65]
[b]from [64]

4.1 Luminescence Following Excitation of $Ni(CO)_4$

Luminescence from homoleptic metal carbonyl compounds is very rare and is usually only observed at low temperatures [75, 76]. However, photolysis of $Ni(CO)_4$ produces emission even at room temperature [77, 78]. The emission spectrum obtained from $Ni(CO)_4$ in the gas phase shows a maximum at 13,700 cm^{-1} (730 nm) following excitation at 351 nm (Fig. 27). This emission spectrum also exhibits vibronic structure with a spacing of 400 ± 10 cm^{-1} (see inset in Fig. 27). The emission has a lifetime of approximately 200 ± 100 ns at high pressures of buffer gas (4.53×10^4 Pa) [77], while this increases to greater than 10 μs when low-pressure (0.6 Pa) collision-free conditions are used [78]. The luminescence has been assigned to a photofragment of $Ni(CO)_4$ rather than an excited state of $Ni(CO)_4$. This is because of the very large separation between the E_{00} band of the emission at approximately 18,500 cm^{-1} and the "tail" of the absorption spectrum (approximately 26,500 cm^{-1}) suggesting that the absorption and emission spectra relate to two distinct species. In addition the vibronic separation at 400 cm^{-1} is too large to be associated with the symmetric stretch of $Ni(CO)_4$ (369 cm^{-1}) and is more likely to be associated with $Ni(CO)_3$ [79]. In the case of $Cr(CO)_5$ and $Fe(CO)_4$, no luminescence was observed because of the facile deactivation of the S_1 states by way of Jahn-Teller induced conical intersections. No such deactivation mechanism is available in the nickel system (Reaction 2). The variation of emission lifetime with buffer gas pressure suggests that at high pressures the emission involves a $S_1 \rightarrow S_0$ transition (fluorescence). Intersystem crossing to the triplet is slow in the collision-free

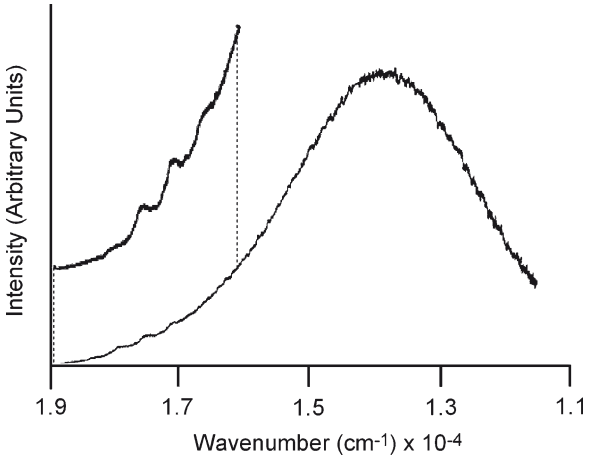

Fig. 27 Emission spectrum obtained by exciting $Ni(CO)_4$ (2×10^4 Pa) at 351 nm. The scale expanded region shows vibronic features. Adapted from [77]

conditions of low pressure facilitating the build up of the triplet population which results in phosphorescence ($T_1 \rightarrow S_0$).

The initial formation of an electronically excited $Ni(CO)_3$ species was confirmed by state-resolved photofragmentation studies using ultraviolet laser-induced fluorescence in supersonic molecular beams. These experiments showed that the $Ni(CO)_3$ fragment stored a significant proportion of its internal energy in a form which is not available for further fragmentation [80]. This means that most of the excitation energy is retained as electronic energy following expulsion of the first CO ligand.

$$\begin{array}{l} Ni(CO)_4 \xrightarrow{h\nu} Ni(CO)_3{}^{*} + CO \\ \qquad\qquad\quad \downarrow \\ \qquad\qquad\quad Ni(CO)_3 + h\nu^{*} \end{array} \qquad \text{(Reaction 2)}$$

4.2 Ultrafast Photodissociation Dynamics of $Ni(CO)_4$

Ultrafast experiments using single-photon pump (267 nm, 4.65 eV) and nonresonant multiphoton probe (800 nm, 1.55 eV) techniques coupled to time-of-flight mass detection were conducted by Fuß et al. [81]. Using this pump wavelength the first allowed excited state will be populated (a^1T_2; see Table 8). The five ion signals $Ni(CO)_n^+$ ($n = 4$–0) differed in their temporal behavior which could be modeled using five time constants (τ_1–τ_5) and six observation windows or locations on the potential energy surfaces of the parent molecule of its neutral photoproducts (L1–L6). The time-resolved signals obtained from these experiments are presented in Fig. 28.

The time constants and relative ionization cross sections derived from the kinetic analysis of the time-dependent signals are presented in Table 9.

As mentioned above, excitation of $Ni(CO)_4$ using 267 nm radiation populates the a^1T_2 state in an allowed transition from the ground state. However, there are other lower-lying excited states, a^1T_1 and a^1E according to the SAC-CI method [64], and an additional b^1T_1 according to TDDFT calculations [65], which are coupled to the ground state only by symmetry forbidden transitions. However, these may play a role in the excited-state dynamics following population of the a^1T_2 state.

Some features are worth noting from Table 9. The signals for the $Ni(CO)_3^+$ fragment are produced up to L6. This confirms that the $Ni(CO)_3$ fragment must be produced in a long-lived electronically excited state because the excess energy carried over to a ground-state $Ni(CO)_3$ species (approximately 3.5 eV) would be sufficient to promote two further decarbonylation reactions in the ionization process. Consequently only $NiCO^+$ and Ni^+ would be detected from a ground-state $Ni(CO)_3$ fragment. Table 10 contains bond dissociation energies for

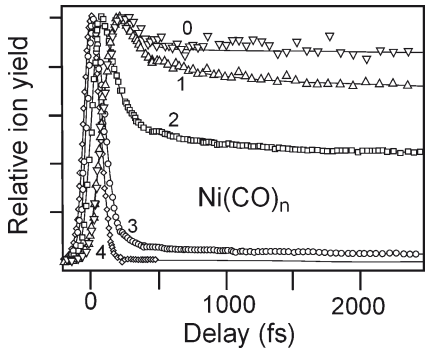

Fig. 28 Time-resolved normalized signals for $Ni(CO)_n^+$. Adapted from [81]

Table 9 The time constants to pass and leave location Li and the relative ionization cross sections ${}_n\sigma_i$ to generate ion $Ni(CO)_n^+$ from location Li

Li	L1	L2	L3	L4	L5	L6
τ_i/fs	22 ± 2	50 ± 10	60 ± 10	70 ± 10	600 ± 100	$55 \times 10^3 \pm 10\%$
				${}^n\sigma_i$		
$Ni(CO)_4^+$	1	0	0	0	0	0
$Ni(CO)_3^+$	1	0.732	0.00242	0.022	0.0212	0.0128
$Ni(CO)_2^+$	0	1	0.993	0.518	0.403	0.328
$NiCO^+$	0	0	0.10	1	0.43	0.365
Ni^+	0	0	0	1	0.434	0.434

Table 10 Bond dissociation energies in (eV) for $Ni(CO)_n$ and $Ni(CO)_n^+$ species[a]

n	4	3	2	1
$Ni(CO)_{n-1}$–CO	1.1 ± 0.1	0.8 ± 0.3	2.3 ± 0.7	1.3 ± 0.7
$Ni(CO)_{n-1}$–CO^+	0.54	1.32	1.96	2.28

[a]From [81] and references therein

$Ni(CO)_n$ and $Ni(CO)_n^+$ species. In fact $Ni(CO)_2^+$ is the strongest ion signal at all delay times in these experiments. If L6 corresponds to a long-lived excited state of $Ni(CO)_3$, then τ_5 must measure the rate of formation of this excited state (600 ± 100 fs). This is significantly slower than the time taken to expel CO from either $Cr(CO)_6$ or $Fe(CO)_5$ and implies the presence of a small thermal barrier to the decarbonylation process.

If the preceding assignments are correct, the time constants τ_1 to τ_5 represent processes in the intact $Ni(CO)_4$ species. It would seem reasonable to assign these time constants to the times taken to travel from the initially populated a^1T_2 state, through the lower-energy excited states before finally emerging through the a^1E state and over a small barrier to the S_1 state of $Ni(CO)_3$. A detailed description of these processes is presented in reference [81] but this must remain speculative until more accurate determinations of the relative energies of the various accessible excited states of $Ni(CO)_4$ become available.

However it is clear that the a^1E state of $Ni(CO)_4$ is the only state that correlates with the S_1 state of $Ni(CO)_3$. The barrier on this trajectory responsible for the slow CO-loss, is formed by an avoided crossing with a higher energy surface, possibly originating from the MC ($d \rightarrow s$) state mentioned earlier. This state is higher in energy than the MC states in $Cr(CO)_6$ or $Fe(CO)_5$ which produces a higher barrier on the $Ni(CO)_3$–CO lengthening coordinate and a slower expulsion of CO.

In the case of the $Cr(CO)_5$ or $Fe(CO)_4$ fragments a Jahn–Teller induced surface intersection between the S_1 and S_0 states explains the rapid transition to the S_0 state following excitation of the parent. However for the $Ni(CO)_3$ fragment the ground state is the $^1A'_1$ state and this has a planar structure (D_{3h}). The first excited state S_1 is the degenerate $^1E''$ state which splits by planar distortion producing $^1B_1$ and $^1A_2$ states but not an A_1 state at the C_{2v} limit. Consequently such a distortion does not provide a deactivation route to the S_0 surface of $Ni(CO)_3$. The $Ni(CO)_3$ fragment remains in its S_1 state which explains the luminescence observed in this system.

4.3 Concluding Comments

The electronic structure of $Ni(CO)_4$ is not as well defined as those of either $Cr(CO)_6$ or $Fe(CO)_5$. This makes the assignment of processes in the early development of the excited-state dynamics somewhat speculative. However there are a number of unique features to the photophysics of CO-loss from $Ni(CO)_4$. Firstly, the CO loss is very slow compared to the other two systems outlined herein taking approximately 600 fs. In addition the $Ni(CO)_3$ fragment is produced in its S_1 state and this state persists because there is no facile deactivation process available based on molecular motions. Deactivation can be achieved only by further CO loss or by radiative processes of either fluorescence or phosphorescence. The overall scheme of potential energy curves and pathways for photoinduced loss of CO from $Ni(CO)_4$ is represented in Fig. 29.

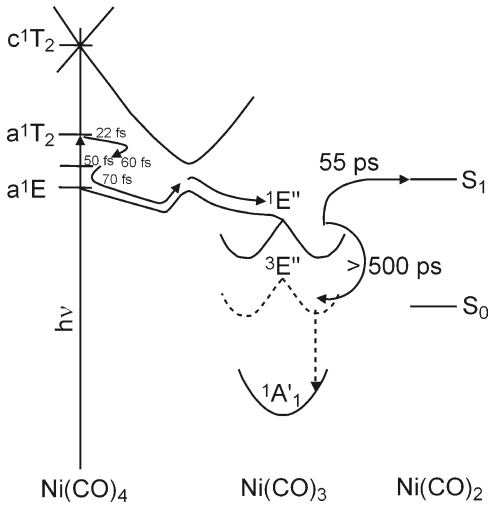

Fig. 29 Suggested outline of the potential energy surfaces, pathways, and time constants for the $Ni(CO)_4$ system. More definitive details of the initial processes close to the Franck–Condon region must await better estimates of excited-state energies. Adapted from [81]

While the CO loss from $Ni(CO)_4$ is slow compared to either $Cr(CO)_6$ or $Fe(CO)_5$ there are examples of even slower photoinduced expulsion of CO ligands from heteroleptic systems. For example photoinduced CO loss from $(\eta^6\text{-}C_6H_6)Cr(CO)_3$ takes over 150 ps [82] while CO loss from [Ru(X)(X′)(CO)(2)(*N*,*N*′-diisopropyl-1, 4-diazabutadiene)] (X = X′ = Cl or I; X = Me, X′ = I; X = SnPh3, X′ = Cl) occurs on the ns timescale [83].

References

1. Strohmeier W (1964) Angew Chem Int Ed 3:730
2. Geoffroy GL, Wrighton MS (1979) Organometallic photochemistry. Academic, New York
3. Wrighton M (1974) Chem Rev 74:401–430
4. McQuillin FJ, Parker DG, Stephenson GR (1991) Transition metal organometallics for organic synthesis. Cambridge University Press, Cambridge, UK
5. Beach NA, Gray HB (1968) J Am Chem Soc 90:5713
6. Gray HB, Beach NA (1963) J Am Chem Soc 85:2922
7. Simon JD, Xie XL (1989) J Phys Chem 93:291–293
8. Simon JD, Xie XL (1987) J Phys Chem 91:5538–5540
9. Simon JD, Xie XL (1986) J Phys Chem 90:6751–6753
10. Pierloot K, Tsokos E, Vanquickenborne LG (1996) J Phys Chem 100:16545–16550
11. Rosa A, Baerends EJ, van Gisbergen SJA, van Lenthe E, Groeneveld JA, Snijders JG (1999) J Am Chem Soc 121:10356–10365
12. Pollak C, Rosa A, Baerends EJ (1997) J Am Chem Soc 119:7324–7329
13. Villaume S, Strich A, Daniel C, Perera SA, Bartlett RJ (2007) Phys Chem Chem Phys 9: 6115–6122

14. Rosa A, Ehlers AW, Baerends EJ, Snijders JG, Velde GT (1996) J Phys Chem 100:5690–5696
15. Trushin SA, Kosma K, Fuss W, Schmid WE (2008) Chem Phys 347:309–323
16. Paterson MJ, Hunt PA, Robb MA, Takahashi O (2002) J Phys Chem A 106:10494–10504
17. Worth GA, Welch G, Paterson MJ (2006) Mol Phys 104:1095–1105
18. Holland JP, Rosenfeld RN (1988) J Chem Phys 89:7217–7225
19. McIver JW, Stanton RE (1972) J Am Chem Soc 94:8618–8620
20. Stanton RE, McIver JW (1975) J Am Chem Soc 97:3632–3646
21. Yu SC, Xu XB, Lingle R, Hopkins JB (1990) J Am Chem Soc 112:3668–3669
22. Nasielski J, Colas A (1978) Inorg Chem 17:237–240
23. Nasielski J, Colas A (1975) J Organomet Chem 101:215-219
24. Burdett JK, Grzybowski JM, Perutz RN, Poliakoff M, Turner JJ, Turner RF (1978) Inorg Chem 17:147–154
25. Perutz RN, Turner JJ (1975) J Am Chem Soc 97:4791–4800
26. Tumas W, Gitlin B, Rosan AM, Yardley JT (1982) J Am Chem Soc 104:55–59
27. Fletcher TR, Rosenfeld RN (1985) J Am Chem Soc 107:2203–2212
28. Trushin SA, Fuss W, Schmid WE (2000) Chem Phys 259:313–330
29. Trushin SA, Fuss W, Schmid WE, Kompa KL (1998) J Phys Chem A 102:4129–4137
30. Boesl U (1991) J Phys Chem 95:2949–2962
31. Trushin SA, Fuss W, Schikarski T, Schmid WE, Kompa KL (1997) J Chem Phys 106:9386–9389
32. Adelman D, Gerrity DP (1990) J Phys Chem 94:4055–4060
33. Nayak SK, Burkey TJ (1991) Organometallics 10:3745–3750
34. Poliakoff M, Weitz E (1987) Acc Chem Res 20:408–414
35. Nayak SK, Burkey TJ (1992) Inorg Chem 31:1125–1127
36. Nayak SK, Farrell GJ, Burkey TJ (1994) Inorg Chem 33:2236–2242
37. Ryther RJ, Weitz E (1991) J Phys Chem 95:9841-9852
38. Seder TA, Ouderkirk AJ, Weitz E (1986) J Chem Phys 85:1977–1986
39. Weitz E (1987) J Phys Chem 91:3945–3953
40. Weitz E (1994) J Phys Chem 98:11256–11264
41. Venkataraman BK, Bandukwalla G, Zhang ZJ, Vernon M (1989) J Chem Phys 90:5510–5526
42. Kotzian M, Rosch N, Schroder H, Zerner MC (1989) J Am Chem Soc 111:7687–7696
43. Jones LH, McDowell RS, Goldblat.M, Swanson BI (1972) J Chem Phys 57:2050–2064
44. Rubner O, Engel V, Hachey MR, Daniel C (1999) Chem Phys Lett 302:489–494
45. Persson BJ, Roos BO, Pierloot K (1994) J Chem Phys 101:6810–6821
46. Veillard A, Strich A, Daniel C, Siegbahn PEM (1987) Chem Phys Lett 141:329–333
47. Banares L, Baumert T, Bergt M, Kiefer B, Gerber G (1997) Chem Phys Lett 267:141–148
48. Banares L, Baumert T, Bergt M, Kiefer B, Gerber G (1998) J Chem Phys 108:5799–5811
49. Duncan MA, Dietz TG, Smalley RE (1979) Chem Phys 44:415–419
50. Nathanson G, Gitlin B, Rosan AM, Yardley JT (1981) J Chem Phys 74:361–369
51. Yardley JT, Gitlin B, Nathanson G, Rosan AM (1981) J Chem Phys 74:370–378
52. Dixon AJ, Gravelle SJ, Vandeburgt LJ, Poliakoff M, Turner JJ, Weitz E. (1987) J Chem Soc Chem Commun:1023–1025
53. Ouderkirk AJ, Seder TA, Weitz E (1984) Proc Soc Photo-Opt Instrum Eng 458:148–153
54. Ouderkirk AJ, Weitz E (1983) J Chem Phys 79:1089–1091
55. Ouderkirk AJ, Wermer P, Schultz NL, Weitz E (1983) J Am Chem Soc 105:3354–3355
56. Waller IM, Hepburn JW (1988) J Chem Phys 88:6658–6669
57. Burdett JK, Grzybowski JM, Poliakoff M, Turner JJ (1976) J Am Chem Soc 98:5728–5729
58. Cooper AI, Poliakoff M (1993) Chem Phys Lett 212:611–616
59. Davies B, McNeish A, Poliakoff M, Turner JJ (1977) J Am Chem Soc 99:7573–7579
60. Poliakoff M (1987) Spectrochim Acta A Mol Biomol Spectrosc 43:217–222
61. Poliakoff M, Ceulemans A (1984) J Am Chem Soc 106:50–54
62. Poliakoff M, Turner JJ (2001) Angew Chem Int Ed 40:2809–2812

63. Trushin SA, Fuss W, Kompa KL, Schmid WE (2000) J Phys Chem A 104:1997–2006
64. Hada M, Imai Y, Hidaka M, Nakatsuji H (1995) J Chem Phys 103:6993–6998
65. van Gisbergen SJA, Groeneveld JA, Rosa A, Snijders JG, Baerends EJ (1999) J Phys Chem A 103:6835–6844
66. Barnes LA, Rosi M, Bauschlicher CW (1991) J Chem Phys 94:2031–2039
67. Li J, Schreckenbach G, Ziegler T (1995) J Am Chem Soc 117:486–494
68. Berry RS (1960) J Chem Phys 32:933–938
69. Ihee H, Cao JM, Zewail AH (2001) Angew Chem Int Ed 40:1532–1536
70. Ihee H, Cao J, Zewail AH (1997) Chem Phys Lett 281:10–19
71. Poliakoff M, Turner JJ. (1974) J Chem Soc Dalton Trans:2276–2285
72. Peden CHF, Parker SF, Barrett PH, Pearson RG (1983) J Phys Chem 87:2329–2336
73. Schreiner AF, Brown TL (1968) J Am Chem Soc 90:3366–3374
74. Lever ABP, Ozin GA, Hanlan AJL, Power WJ, Gray HB (1979) Inorg Chem 18:2088–2090
75. McHugh TM, Narayanaswamy R, Rest AJ, Salisbury K. (1979) J Chem Soc Chem Commun:208–210
76. Wrighton M, Hammond GS, Gray HB (1971) J Am Chem Soc 93:4336–4337
77. Preston DM, Zink JI (1987) J Phys Chem 91:5003–5005
78. Rosch N, Kotzian M, Jorg H, Schroder H, Rager B, Metev S (1986) J Am Chem Soc 108:4238–4239
79. Dekock RL (1971) Inorg Chem 10:1205–1211
80. Schlenker FJ, Bouchard F, Waller IM, Hepburn JW (1990) J Chem Phys 93:7110–7118
81. Fuss W, Schmid WE, Trushin SA (2001) J Phys Chem A 105:333–339
82. Alamiry MAH, Boyle NM, Brookes CC, George MW, Long C, Portius P, Pryce MT, Sun XZ, Towrie M, Ronayne KL, Vuong KQ. (2009) Oranometallics 28:1461–1468
83. Gabrielsson A, Towrie M, Zalis S, Vlcek A (2008) Inorg Chem 47:4236–4242

Top Organomet Chem (2010) 29: 73–114
DOI: 10.1007/3418_2009_4

Published online: 20 May 2009

Ultrafast Excited-State Processes in Re(I) Carbonyl-Diimine Complexes: From Excitation to Photochemistry

Antonín Vlček Jr

Abstract Rhenium(I) carbonyl-diimines are chemically robust and synthetically flexible photo- and redox active compounds that can be incorporated into supramolecular systems, polymers or biomolecules. They can be used as efficient and fast photosensitizers. In this chapter, we will follow excited-state evolution of Re^{I} complexes from the instant of photon absorption through intersystem crossing, relaxation of "hot" triplet states, to their decay either to the ground state or to photoproducts. Out of many decay pathways, we concentrate on nonradiative decay following the energy gap law, excited-state electron- and energy transfer and ligand isomerization. Characterization of the lowest excited state by ultrafast IR spectroscopy and DFT calculations are discussed in detail. It is shown that excited-state properties are much influenced by mixing of $Re(CO)_3$→diimine, L→diimine CT and intraligand ππ* excitations.

Keywords rhenium • carbonyl • diimine • photophysics • excited state • electron transfer • charge transfer • relaxation • intersystem crossing • DFT • time-resolved IR spectroscopy

Contents

1 Introduction 75
2 Optical Excitation 78
3 Dynamics of Singlet Excited States and Intersystem Crossing 81
4 Nature of Triplet Excited States 84
4.1 Overview of the Character and Emission of Triplet Excited States 84
4.2 Excited-State DFT and TD-DFT Calculations 86
4.3 Excited-State Infrared Spectra 87
4.4 Character Mixing in the Lowest Excited States 90
5 Relaxation of Triplet Excited States 94
6 Decay of the Lowest Triplet Excited State 98

A. Vlček Jr (✉)
School of Biological and Chemical Sciences, Queen Mary, University of London,
Mile End Road, London E1 4NS, UK
e-mail: a.vlcek@qmul.ac.uk and
J. Heyrovský Institute of Physical Chemistry, Academy of Sciences of the Czech Republic,
Dolejškova 3, Prague, Czech Republic

7 Photochemistry 102
7.1 Rhenium-Ligand Bond Splitting 102
7.2 Intramolecular Energy Transfer: Sensitization of Axial Ligand Isomerization 103
7.3 Electron Transfer 105
References 110

Abbreviations

* In front of a formula denotes electronic excitation

bpy	2,2′-Bipyridine
CT	Charge-transfer transition, excitation or excited state. Detailed character (herein MLCT, XLCT, or LLCT) not specified
DFT	Density functional theory
dmb	4,4′-Me_2–2,2′-bpy
dppz	Dipyrido[3,2-*a*:2′,3′-*c*]phenazine
EFFF	Energy factored force field
ET	Electron transfer
EnT	Energy transfer
Etpy	4-Ethyl-pyridine
IL	Intraligand, localization on a particular ligand may be specified in brackets: IL(N,N) or IL(L)
ILCT	Intraligand charge transfer
im	Imidazole
L	Axial ligand
LLCT	Ligand-to-ligand charge transfer, herein L→N,N
MLCT	Metal-to-ligand charge transfer
MLLCT	Metal–ligand-to-ligand charge transfer, herein $Re(L)(CO)_3$→N,N. A general abbreviation replacing MLCT/LLCT and MLCT/XLCT
MQ^+	*N*-methyl-4,4′-bipyridinium
ν(CO)	C≡O stretching vibration of a carbonyl ligand
N,N	α-Diimine or polypyridine ligand
phen	1,10-Phenanthroline
PTZ	Phenothiazine, an electron donor
py	Pyridine
SBLCT	Sigma bond-to-metal charge transfer
TD-DFT	Time-dependent DFT
TR^2	Transient resonance Raman
TR^3	Time-resolved resonance Raman
TRIR	Time-resolved IR absorption
2D-TRIR	Two-Dimensional TRIR
trp	Tryptophan
tyr	Tyrosine
UKS	Unrestricted Kohn–Sham approach
X	Halide axial ligand
XLCT	X→N,N charge transfer, a kind of LLCT for L= halide
ZFS	Zero-field splitting

1 Introduction

Rhenium (I) complexes of the type *fac*-[Re(L)$(CO)_3$(N,N)]^n (see Fig. 1 and Charts 1, 2) show exceptionally rich excited-state behavior [1–4] and redox [5–9] chemistry. They are thermally and photochemically robust and highly flexible synthetically. Broad structural variations of the N,N ligand as well as the axial ligand L are possible, allowing us to incorporate these chromophores into a range of media, attach them to proteins, intercalate into DNA, or make them parts of supramolecules designed to perform specific functions. The same structural and medium variations affect the nature and energetic order of low-lying excited states and, thus, the spectroscopy, photophysics, photochemistry, and electrochemistry of the Re chromophore. This opens the way to applications of [Re(L)$(CO)_3$(N,N)]^n complexes as sensors, probes, and emissive labels for imaging biomolecules, which are summarized in Chap. 2 of this book. Herein, we will focus on dynamic aspects of the processes triggered by electronic excitation and follow the evolution of excited Re chromophores from the photon absorption until the ground state is recovered or a photochemical product formed (Fig. 2). Additionally, we will discuss the structures and characters of the excited states involved, as documented by time-resolved IR spectra and DFT calculations. The currently emerging understanding of their excited states and photophysics allows us to use rhenium (I) carbonyl diimines for the testing and development of new theoretical and mechanistic models and to open up paths to new applications.

Before discussing the dynamics and conversions between various excited states in [Re(L)$(CO)_3$(N,N)]^n, it is necessary to review some general aspects of their electronic structures, Fig. 3, and low-lying excited states, Fig. 4 [1, 10–17]. The highest set of occupied molecular orbitals of [Re(L)$(CO)_3$(N,N)]^n consists of three 5dπ(Re) orbitals that mix with π*(CO) orbitals, giving rise to Re→CO π back bonding. In the case that L is an electron-rich ligand (halide, pseudohalide, aromatic isonitrile) with a donor atom X, its two *p*π orbitals mix with two of the *d*π orbitals, resulting in two fully occupied pairs of Re–X π-bonding and antibonding

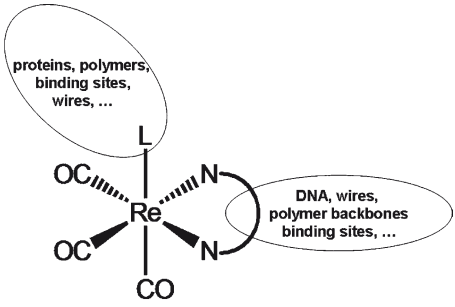

Fig. 1 Schematic formula of complexes *fac*-[Re(L)$(CO)_3$(N,N)]^n. The *ellipses* show how these chromophores can be incorporated in more complex and organized media. The prefix *fac*- will be hereafter omitted. An approximate C_s symmetry of the complex molecules is assumed throughout this article

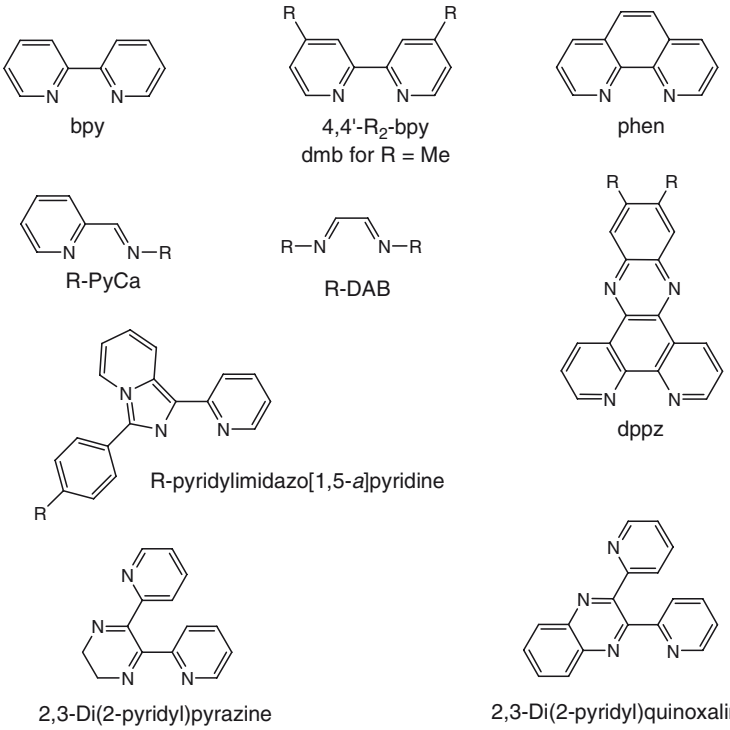

Chart 1 Structures of N,N ligands in $[Re(L)(CO)_3(N,N)]^n$. The same names and abbreviations are used in the text and the chart

orbitals, Fig. 3 – right. An N,N-localized occupied π orbital also occurs within the set of the highest occupied orbitals, energetically close to the *d*π orbitals. The lowest unoccupied orbital is almost always a π*(N,N) orbital, which interacts with the *d*π HOMO-1. The possible characters of low-lying excited states clearly ensue from this simple MO picture. Figure 4 shows schematically the limiting cases of Re→N,N MLCT(N,N), L→N,N LLCT (called XLCT for X = halide or pseudo-halide), IL(N,N), and σ(Re–L)→π*(N,N) SBLCT excited states. The latter emerges when L is a ligand bound to Re through a high-lying σ-orbital, as is the case for L = alkyl, benzyl or a metal-bonded ligand like $SnPh_3$, $Mn/Re(CO)_5$, etc [3, 18]. Although these states are the most relevant ones in the context of this article, it is necessary to stress that more types of excited states can be encountered in $[Re(L)(CO)_3(N,N)]^n$ complexes: Strongly electron-accepting axial ligands (e.g., *N*-methyl-4,4′-bipyridinium or 3,5-di-formyl-pyridine) may introduce Re→L MLCT excited states denoted MLCT(L), while L-localized IL(L) states occur in complexes with L = styrylpyridine or phenylazopyridine derivatives. To understand excited-state properties and dynamics, it is necessary to stress that the types of electronic states described above are only limiting cases. In reality, occupied frontier orbitals *d*π, *p*π(L), π(N,N), etc. can mix, resulting in mixed-character excited states. Another kind of character mixing occurs among the electronic states themselves. A pure

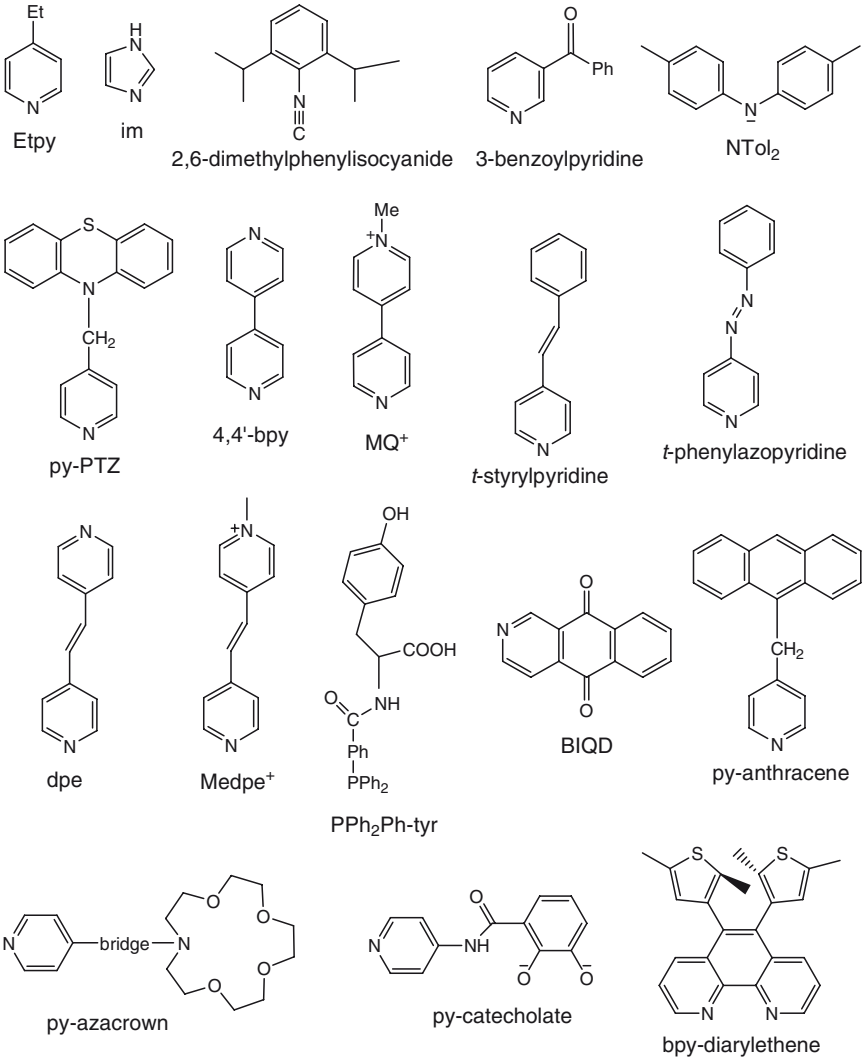

Chart 2 Structures of axial ligands L in $[Re(L)(CO)_3(N,N)]^n$. The same names and abbreviations are used in the text and the chart. "Bridge" in the lower-left structure stands for –NH–C(O)–ph–, –CH=CH–ph–, or –C≡C–ph–. Some of the pyridine-based ligands also form complexes of the type $[Re(Cl)(CO)_3(L)_2]^n$

MLCT state is essentially never encountered. In reality, we always deal with mixed MLCT–LLCT spin-singlets and MLCT–LLCT–IL(N,N) triplets, see Sect. 4.4. The extent of the state mixing depends on the particular $[Re(L)(CO)_3(N,N)]^n$ chromophore, as well as on its medium, and can change during excited-state relaxation. So, in the case of $[Re(L)(CO)_3(N,N)]^n$ chromophores, we deal with a high density of electronic excited states of different orbital parentage whose energies and characters change with time following optical excitation.

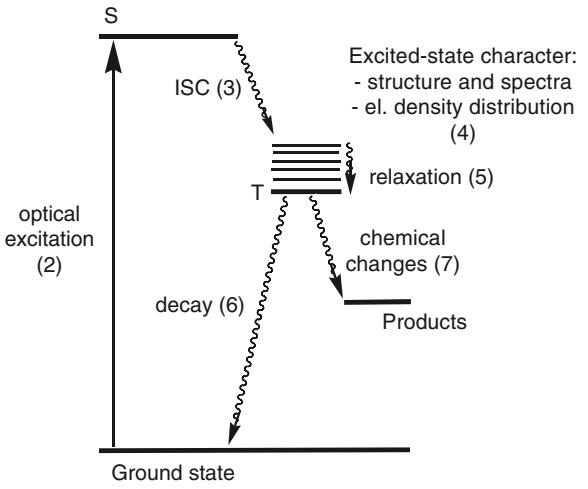

Fig. 2 Schematic Jablonski diagram. *S*, *T* stand for the optically populated singlet and the lowest triplet excited state, respectively. The *numbers in parenthesis* refer to the relevant sections of this article

In the rest of this work, individual photophysical processes ensuing photon absorption will be discussed, following the generalized Jablonski diagram shown in Fig. 2.

2 Optical Excitation

The lowest absorption bands of $[Re(L)(CO)_3(N,N)]^n$ occur in the near-UV region. They correspond to MLCT, mixed MLCT/LLCT, or MLCT/XLCT (generally called MLLCT) and IL(N,N) transitions [1, 4, 19–22]. In most cases, the CT bands lie at slightly longer wavelengths (330–400 nm ε~ 2,000–5,000 M^{-1} cm^{-1}) than the more intense IL(N,N) band, which peaks at ca. 320 nm for N,N = bpy. The CT bands are more isolated in the case of N,N = 1,4-diazabutadiene, whose IL bands lie in the UV region and the lowest CT is shifted to 450–500 nm. Most dynamic studies use laser-pulse irradiation at 400 nm that is directed to the lowest CT absorption band but it often overlaps with the red tail of a higher IL absorption. Most of the experimental information on optically excited Franck–Condon states comes from (pre)resonance Raman spectra, which allow us to analyze in detail structural changes upon excitation and, thus, the localization of the resonant electronic transition [1, 4, 15, 23–29]. However, the close proximity of several allowed electronic transitions of different origin complicates the analysis. In fact, all kinds of CT transitions as well as IL(N,N) transitions give rise to resonance enhancement of Raman bands due to N,N-localized vibrations of the N,N ligand, although with different intensity patterns. To assess the MLCT contribution, it is more

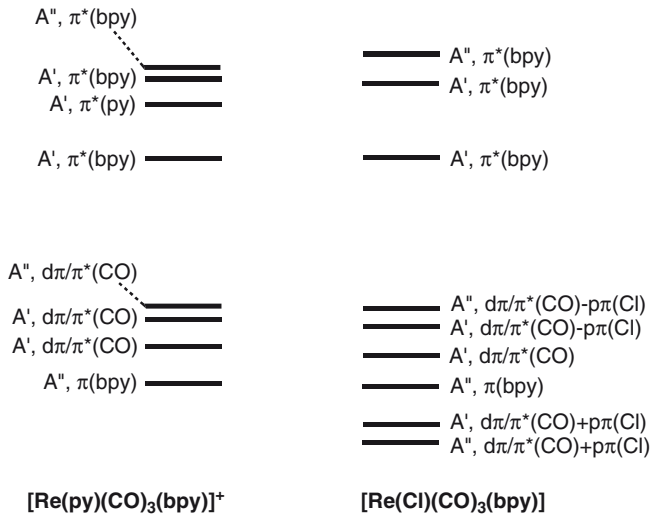

Fig. 3 Qualitative energy diagram of frontier molecular orbitals of $[Re(py)(CO)_3(bpy)]^+$ (*left*) and $[Re(Cl)(CO)_3(bpy)]$ (*right*), based on DFT calculations. Calculated orbital energies and MO compositions are given in the Supplementary Information to [10]. An idealized C_s symmetry is assumed

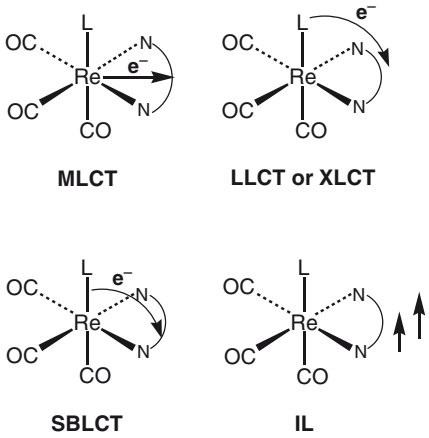

Fig. 4 The most common excited-state characters encountered in $[Re(L)(CO)_3(N,N)]^n$ complexes. Only limiting cases are shown; character mixing in electronic excitations and low-lying excited states is commonplace

informative to investigate the enhancement of the Raman band due to the in-phase totally symmetric ν(CO) vibration A′(1) that usually occurs between 2,020 and 2,035 cm^{-1}. For very electron-rich ligand L (amide, phosphide, alkyl, etc.), it is found between ~1,980 and 2,010 cm^{-1}. A strong enhancement of the A′(1) band arises predominantly from a large increase of the axial CO stretching force

constant upon excitation and indicates a high contribution from a $Re(CO)_3 \rightarrow N,N$ MLCT transition to the resonance Raman effect. The enhancement of the A′(1) Raman band (usually measured relative to the strongest Raman band due to a vibration of the N,N ligand) decreases or even vanishes if the resonant transition is predominantly LLCT or IL in character [1, 15, 27, 28, 30–32]. Further information on the optically prepared singlet states comes from TD-DFT calculations, which provide transition energies and compositions described as linear combinations of contributing one-electron excitations [11]. A typical absorption spectrum and its TD-DFT simulation are shown in Fig. 5. It follows that the lowest allowed

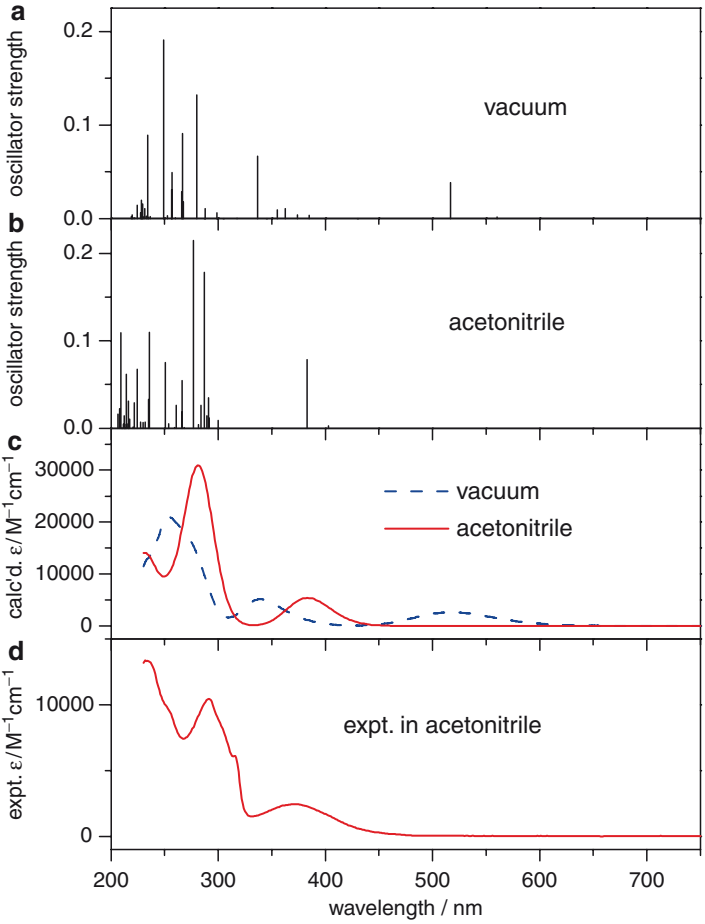

Fig. 5 Electronic transitions of $[Re(Cl)(CO)_3(bpy)]$ calculated in vacuum (**a**), acetonitrile (**b**), simulated absorption spectra in vacuum (**c**, *dashed*) and acetonitrile (**c**, *full*), and experimental absorption spectrum measured in acetonitrile (**d**). It follows that successful TD-DFT simulation of the absorption spectrum and singlet CT states requires using hybrid functionals and continuum dielectric models for the solvent [11, 33]. Calculation: TD-DFT G03/PBE0, CPCM for MeCN. Simulation: All calculated transitions included. Gaussian shapes (*fwhm* = 0.4 eV cm^{-1}) of the absorption bands are assumed. Band areas are proportional to calculated oscillator strengths. Simulated using the GaussSum software. Reprinted with permission from [33]

transition populates a state of an A′ symmetry, denoted a^1A', which is usually the second singlet excited state. Transitions to the lowest singlet excited state a^1A'' have negligible oscillator strengths. For L = pyridine derivatives, the two lowest singlet states have predominantly $Re(CO)_3 \rightarrow N,N$ MLCT character whereas the mixed MLCT/XLCT character (also called MLLCT) prevails for L = X = halide or NCS [1, 12, 15, 24]. The XLCT contribution increases as a function of X: Cl <Br <I. A predominant LLCT character of the lowest allowed singlet state is rare; in fact it was found only for $L = NTol_2$ or PPh_2 [13]. A very weak LLCT absorption band occurs in a chromophore-quencher complex (see Sect. 7) $[Re(py–PTZ)(CO)_3(4,4'\text{-}R_2–bpy)]^+$, which corresponds to optical excitation of an electron from a remote PTZ donor to bpy [34].

^{1}CT and ^{1}IL(NN) states mix very little (if at all), because of a large energy gap (However, this situation is profoundly different in the triplet manifold, see Sect. 4). There are not many Re complexes in which the lowest allowed electronic transition is ^{1}IL(NN). A typical case is presented by the family of complexes with N,N = pyridylimidazo[1,5-*a*]pyridine derivatives [35, 36], where the IL(N,N) state occurs below a ^{1}MLCT/XLCT state. $[Re(L)(CO)_3(R\text{-}dppz)]^n$ complexes are another example [28, 29].

Two typical examples of lowest allowed singlet states of Re complexes are shown in Fig. 7, the leftmost column: TD-DFT calculated maps of difference electron density of $[Re(py)(CO)_3(bpy)]^+$ and $[Re(Cl)(CO)_3(bpy)]$ clearly show that the electron density is transferred from $Re(CO)_3$ and $Re(Cl)(CO)_3$ moieties to the bpy ligand, respectively. No contribution from ππ* IL(bpy) excitation is discernible.

Structural changes occurring upon the lowest allowed ^{1}CT transition were calculated [10] by TD-DFT for $[Re(Cl)(CO)_3(bpy)]$ and $[Re(py)(CO)_3(bpy)]^+$. It follows that the bonds most affected are those within the bpy ligand, due to its partial reduction. The largest changes concern the inter ring C2–C2' bond and the N–C2,C2′ bonds, which shorten and lengthen, respectively. The C≡O bonds contract, as is expected for diminishing the π back bonding. Surprisingly large changes occur in the skeletal bonds: the Re–N(bpy) and Re–L bonds contract upon excitation while Re–C bonds elongate, and the skeletal angles C_{eq}–Re–C_{eq}, N–Re–N, Cl–Re–C_{ax}, and Cl–Re–N open. The calculations agree with resonance Raman spectra of $[Re(Cl)(CO)_3(bpy)]$, $[Re(Etpy)(CO)_3(bpy)]^+$ and similar complexes, which show [15, 25, 37] enhancement of Raman peaks due to *ν*(CC) and *ν*(NC), *ν*(CO), *ν*(ReN), *ν*(Re–halide), and *δ*$Re(CO)_3$ vibrations.

3 Dynamics of Singlet Excited States and Intersystem Crossing

Fluorescence from singlet excited states of $[Re(X)(CO)_3(bpy)]$ (X = Cl, Br, I) and $[Re(Etpy)(CO)_3(bpy)]^+$ appears concomitantly with 400 nm, 80 fs pulse excitation as a very broad band peaking at ~530 nm (in Chap. 1 of this book). The large instantaneous fluorescence Stokes shift and broadness indicate a femtosecond energy dissipation and ultrafast population of many vibrational modes. TD-DFT calculations [10]

suggest that low-frequency skeletal modes could be highly excited in the optically populated ^{l}CT state. The fluorescence undergoes conversion into the typical long-lived phosphorescence occurring at ~580 nm (L = Etpy) or ~610 nm (L = halide). Depending on the axial ligand, the fluorescence decays with a lifetime τ_1 of 80–140 fs (Table 1) while the phosphorescence rises bi-exponentially with the lifetimes τ_1 and τ_2, the latter in the range 300–1,200 fs, Table 2. Detailed kinetic analysis suggests that the optically populated singlet state $b^{l}A'$ undergoes two parallel intersystem crossing (ISC) processes populating simultaneously the lowest triplet state $a^{3}A''$ of a predominant charge-transfer character and a close-lying predominantly ^{3}IL state $b^{3}A''$. The τ_2 lifetime is then attributed to internal conversion between the two triplet states. This mechanism is shown in Fig. 6. An alternative assignment of τ_2 to relaxation of the lowest state $a^{3}A''$ is less probable, because the phosphorescence band does not show the expected characteristic rise on its low-energy side.

Table 1 Fluorescence decay lifetimes (in fs) of $[Re(L)(CO)_3(bpy)]^n$ and DFT-estimated spin-orbit coupling energies (in cm^{-1}). Data from [10]

L	Solvent	τ_1	τ_2	SO $B^{l}A'$–$b^{3}A''$	SO $B^{l}A'$–$a^{3}A''$
Etpy	CH_3CN	130 ± 20	870 ± 80	58	550
Cl	CH_3CN	85 ± 8	340 ± 50	92	503
Br	CH_3CN	128 ± 12	470 ± 50	–	–
I	CH_3CN	152 ± 8	1,180 ± 150	267	1,303
Cl	DMF	167 ± 7	1,420 ± 90	92	503
Br	DMF	157 ± 14	1,600 ± 200	–	–

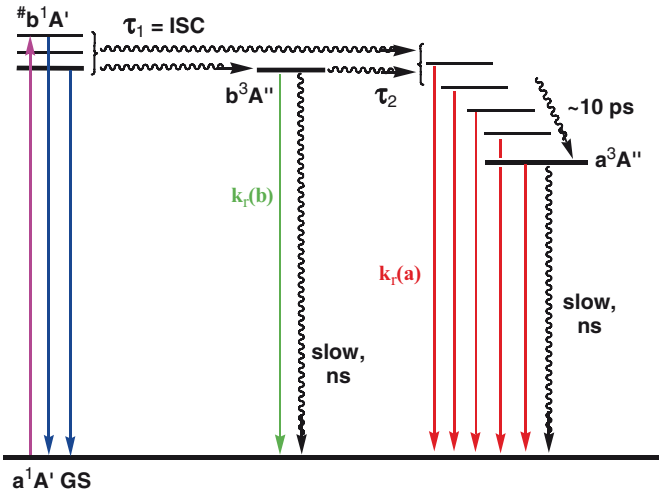

Fig. 6 Excited-state dynamics of $[Re(L)(CO)_3(bpy)]^n$ complexes; L = Etpy, Cl, Br, I *Color code*: Light absorption to $b^{l}A'$ in *violet*, fluorescence in *blue*, $b^{3}A''$ phosphorescence in *green*, and $a^{3}A''$ phosphorescence in *red* (*Hash* denotes vibrational excitation). The ~10 ps relaxation is discussed in Sect. 5. Reprinted with permission from [10]

For ISC to occur, it is necessary that the change in the spin momentum is compensated by a change in the angular momentum. In symmetry terms, this means that the direct product of the irreducible representations of the singlet and triplet states transform as rotations. This requirement is the basis of the well-known El Sayed's rules that are widely used in photophysics of organic compounds [38]. For $[Re(L)(CO)_3(bpy)]^n$ with an approximate C_s symmetry, ISC is allowed only between states of different symmetry, that is A′ and A″. The necessary orbital (i.e., angular momentum) rotation accompanying the spin change is accomplished by rotating the region of the unpaired spin density around the Re atom upon ISC. This is shown in Fig. 7, where the excited states involved are visualized by DFT-calculated maps of difference electron density. It can be seen that the regions of the unpaired spin density around the Re atom in the singlet and triplet states are mutually perpendicular. ISC in $[Re(L)(CO)_3(bpy)]^n$ is thus symmetry allowed and can be viewed as an inorganic manifestation of El Sayed's rules. Unlike in organic photophysics, ISC in $[Re(L)(CO)_3(bpy)]^n$ can occur between states of the same character, viz. singlet and triplet MLCT (or MLLCT).

It is very surprising that ISC in Re complexes is much slower than in $[Ru(bpy)_3]^{2+}$ (~20 fs) [39] or $[Ru(4,4'\text{-di-carboxy-bpy})_2(NCS)_2]$ (~43 fs) [40] despite much stronger spin-orbit (SO) coupling of Re than Ru. Moreover, data in Table 2 show that the ISC rates do not correlate with the SO energy even within the $[Re(L)(CO)_3(bpy)]$ series, which is expected to increase as the function of L in the order Cl <Br <I. In fact, an inverse correlation between ISC rate and the SO energy occurs. To explain this behavior, it has been suggested that the SO coupling energy

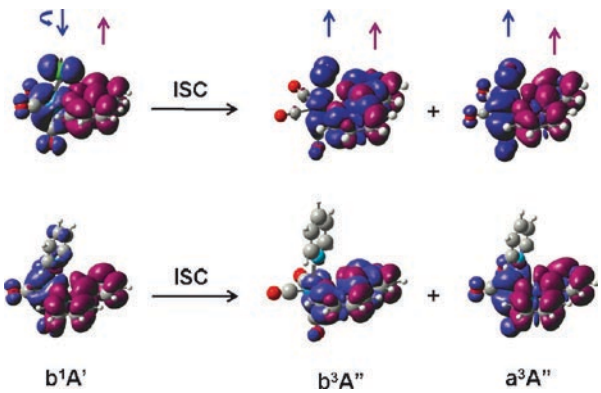

Fig. 7 Visualization of singlet and triplet excited states and intersystem crossing in $[Re(Cl)(CO)_3(bpy)]$ (*top*) and $[Re(py)(CO)_3(bpy)]^+$ (*bottom*) using difference electron density maps calculated by TD-DFT (B3LYP, singlets in CH_3CN/CPCM, triplets for L = Cl in CH_3CN/CPCM; L = py in vacuum). Cl or py ligands point up. The plots show the electron density in the given excited-state minus electron density in the ground state, at the optimized ground-state geometry. *Blue*, *violet*: regions where electron density decreases and increases upon excitation, respectively. These regions approximately correspond to those occupied by the two unpaired electrons in the excited states, shown by the *arrows* at the *top*. The orbital rotation accompanying the spin change is clearly seen. Adapted from [10]

in all these complexes (and also in $[Fe(bpy)_3]^{2+}$) [41] is "saturated," in other words, strong enough to allow for ultrafast ISC, regardless of its actual value. ISC rates are then determined by other factors, namely the shapes and relative energetics of the triplet and singlet potential energy surfaces. Understanding ISC in Re and Ru complexes is a big challenge for the theory. Before any quantum chemical calculations are attempted, it will be necessary to define the relevant coordinates. Some clues may be provided by DFT calculations of structural changes upon ISC in $[Re(Cl)(CO)_3(bpy)]$ and $[Re(py)(CO)_3(bpy)]^+$ [10]. It follows that the largest changes occur in skeletal bonds, namely the C_{eq}–Re–C_{eq} angle. Depending on the particular triplet, the bond angles N–Re–N, N–Re–Cl, L–Re–C_{ax}, N–Re–C_{ax}, and, to a lesser extent, the Re–C, Re–Cl, and Re–N(bpy) bond distances have different values in the singlet and triplet excited states. The intra bpy bond lengths are very similar in the CT states b^1A' and a^3A'', but they differ in the IL state b^3A''. The importance of low-frequency skeletal vibrations for ISC in Re complexes is underlined by the observation that the ISC lifetime τ_1 in $[Re(X)(CO)_3(bpy)]$ correlates linearly with the vibrational period of the Re–X stretching vibration [10].

Finally, it should be noted that singlet-state lifetimes in $[Re(L)(CO)_3(bpy)]^n$ are long enough to allow for ultrafast electron or energy transfer in supramolecular assemblies, at surfaces or molecule/nanoparticle interfaces, see Sect. 7.3. Indeed, a "hot electron injection" has been seen with TiO_2 nanoparticles [42] or in Re-labeled redox proteins [43].

4 Nature of Triplet Excited States

ISC from the optically prepared singlet state populates one or two low-lying A″ triplet states in a few hundreds of femtoseconds, see Sect. 3. Triplet states are initially populated "hot," that is nonequilibrated both in terms of the molecular structure and the medium. Relaxation processes, which occur on the timescale of picoseconds to nanoseconds (depending on the medium), will be discussed in Sect. 5. Herein, we will deal with thermally equilibrated (relaxed) lowest triplet states and their theoretical as well as experimental characterization.

4.1 Overview of the Character and Emission of Triplet Excited States

The character of triplet excited states of $[Re(L)(CO)_3(bpy)]^n$ is somewhat different from the corresponding singlets. This is caused mainly by the singlet–triplet splitting being much larger for IL than MLCT states. While ^{1}IL and ^{1}MLCT states are energetically well separated, the triplets lie in close proximity, opening the possibility for mixing between IL and MLCT characters in the lowest triplet states.

Rhenium carbonyl-diimine complexes were discovered in the mid 1970s [44, 45] as strongly emissive complexes. The long emission lifetime (tens–hundreds of ns) and structureless and broad shapes of emission bands and a prominent rigidochromism

(emission blue-shift on going from fluid solution to a glass) indicated that, in most cases, the emission occurs from a ^{3}MLCT state [1, 4, 20, 45]. This assignment was further supported by electrochemistry, which has shown that the Re atom and the diimine ligand undergo one-electron oxidation and reduction, respectively, and that the emission energy correlates with the redox energy, that is the difference between the oxidation and reduction potential [5]. However, it was soon found [15, 24] that the lowest excited state in halide complexes [Re(X)(CO)$_3$(N,N)] is of a mixed Re→N,N MLCT and X→N,N XLCT character, the variable halide contribution influencing emission lifetimes, solvatochromism, and resonance Raman spectra [1, 15].

[Re(L)(CO)$_3$(polypyridyl)]^n complexes have close-lying ^{3}CT and ^{3}IL excited states [1]. Although the ^{3}CT state is usually the lowest, there are cases where both states are energetically so close that both of them are populated simultaneously [10, 46]. A dual emission is then observed and time-resolved IR spectra (Sect. 4.3) show bands due to both states. This is, for example, the case of [Re(Etpy)(CO)$_3$(4,4′-(NH$_2$)$_2$-bpy)]$^+$ [47]. Other complexes, such as [Re(Cl)(CO)$_3$(pyridylimidazo[1,5--a]pyridines)] [35, 36], [Re(L)(CO)$_3$(dppz)]$^+$ (L = PPh$_3$, py, Cl) [47, 48] have ^{3}IL lowest excited state. The relative energetic order of ^{3}IL and ^{3}CT can depend on the medium. There are [Re(L)(CO)$_3$(polypyridyl)]^n complexes where ^{3}CT and ^{3}IL are the lowest states in fluid solution and rigid glasses, respectively [20, 45, 49, 50], while other complexes show simultaneous ^{3}CT and ^{3}IL emission in fluid solution at room temperature (e.g., [Re(Cl)(CO)$_3$(3-benzoylpyridine)$_2$] [51]) or in low-temperature rigid glasses (e.g., [Re(L)(CO)$_3$(R-phen)]$^+$ [50, 52]).

Depending on their structure and the solvent, complexes with lowest ^{3}SBLCT states are either strongly photoreactive in fluid solutions or they show long-lived emission [53]. This behavior has been extensively reviewed elsewhere [1, 3, 18].

Because of their triplet character and strong spin-orbit coupling of the Re atom, the lowest excited state of [Re(L)(CO)$_3$(N,N)]^n is split into three spin-orbit components. The magnitude of this splitting, so-called zero-field splitting, ZFS, is related to the Re participation in the emitting state [54]. Large ZFS signifies a predominant ^{3}MLCT character of the emitting state and its value decreases with increasing contribution of a ^{3}IL character. ZFS values were determined [46, 55] for [Re(Cl)(CO)$_3$(bpy)], [Re(Cl)(CO)$_3$(dmb)], and [Re(Cl)(CO)$_3$(phen)] as 90.4, 75.7, and 42.1 cm^{-1}, respectively. The value measured for [Re(Cl)(CO)$_3$(bpy)] is one of the largest among emissive metal complexes [54]. Population of all three sublevels is supposed to be thermally equilibrated at room temperature. In the case of the bpy complex, the population of the three sublevels is 38, 37, and 25%, assuming that ZFS is the same in fluid solution as in glass. (In fact, it can be larger due to smaller IL-CT mixing, allowing for even more unequal population of the sublevels.)

Structural and medium effects on emission spectra and lifetimes of [Re(L)(CO)$_3$(N,N)]^n complexes are extensively discussed in [1]. Here, it was proposed to use "energy-gap law maps," that is, dependences of the logarithms of excited-state lifetimes on the emission energy in series of structurally related complexes, to obtain information on the character of the emissive states. Quantitative analysis of the shapes of emission bands of [Re(L)(CO)$_3$(N,N)]^n affords information on structural differences between the ground- and emitting triplet states (Sect. 6) and can thus be used to further characterize the lowest excited states. Hereafter, we will

discuss the character of lowest triplet excited states of $[Re(L)(CO)_3(N,N)]^n$ complexes in more detail, focusing on information provided by time-resolved IR spectroscopy (TRIR) and DFT or TD-DFT calculations.

4.2 Excited-State DFT and TD-DFT Calculations

Applications of DFT and TD-DFT methods to model excited-states of Re carbonyl-diimines and other organometallic complexes have recently been reviewed in depth [11]. Herein, we will only summarize the essential points and conclusions relevant to Re carbonyl-diimines:

(a) Reliable calculations of singlet and triplet excitation energies require the use of hybrid functionals such as PBE0 or B3LYP. The solvent has to be included. Continuum solvent models COSMO or CPCM are sufficient for most applications. Using pure DFT functionals or neglecting the solvent unrealistically underestimates the energies of CT transitions for both excited singlets (Fig. 5) and triplets. Energies of IL transitions are less sensitive to computational details. Calculations of electronic transitions to singlet states are validated by comparison with experimental UV–Vis absorption spectra.

(b) Excited-state structures can be optimized either by TD-DFT (applicable to all excited states, regardless of their spin or symmetry) or by UKS (unrestricted Kohn–Sham, applicable to the lowest triplet state of each symmetry only). Calculations of lowest triplet states can be validated by comparison of calculated and experimental emission and excited-state energies and excited-state IR spectra in the region of CO stretching vibrations, ν(CO). Achieving a good correspondence between calculated and experimental data allows us to draw other conclusions from the calculation, for example on the excited-state character and electron-density distribution. Although low-lying triplets were reliably modeled for several $[Re(L)(CO)_3(N,N)]^n$, the search for an optimal procedure continues. The use of hybrid functionals is essential. UKS calculations in solvents (CPCM or COSMO) give generally better agreement with experimental excited-state IR spectra than TD-DFT for halide or pseudohalide complexes [11]. However, UKS/solvent calculations systematically underestimate excited-state ν(CO) energies of cationic complexes such as $[Re(py)(CO)_3(bpy)]^+$ or $[Re(im)(CO)_3(phen)]^+$. Acceptable correspondence with experimental values is found when the UKS calculation is performed in vacuum. The problem seems to originate in exaggerated IL-MLCT mixing, see Sect. 4.4.

(c) Singlet and triplet excited states at given geometry are described by TD-DFT as linear combinations of one-electron excitations between ground-state orbitals [11]. Characters of the orbitals involved and the weights of contributing excitations provide information on the excited-state character. This is conveniently visualized by maps of difference electron densities, which show the electron density distribution in the excited state minus that in the ground state [11] (See Fig. 7 for examples). Alternatively, pictures showing

spin densities can be used for triplets. Generally, DFT calculations predict mixing between ^{3}MLCT and ^{3}XLCT excitations in the lowest excited states of halide and NCS complexes, which was indeed proven experimentally [12]. The IL(N,N) excitations are admixed to the lowest ^{3}CT triplet excited state of an A″ symmetry. The IL(N,N) contribution is larger for L = pyridine or imidazole derivatives than for L = halide or NCS, see Fig. 7. The calculated magnitude of the mixing is sensitive to computational details [11, 56, 57]. Although it might be exaggerated in some calculations, the CT/IL mixing in the lowest A″ excited state seems to be a general feature of $[Re(L)(CO)_3(N,N)]^n$ complexes, supported both by calculations and experiments. This will be discussed in more detail in Sect. 4.4.

4.3 *Excited-State Infrared Spectra*

Ground-state IR spectra of $[Re(L)(CO)_3(N,N)]^n$ show three IR bands due to C≡O stretching vibrations, ν(CO) in the range of ~1,900–2,040 cm^{-1}, which are schematically shown in Fig. 8. The highest band corresponds to a totally symmetric

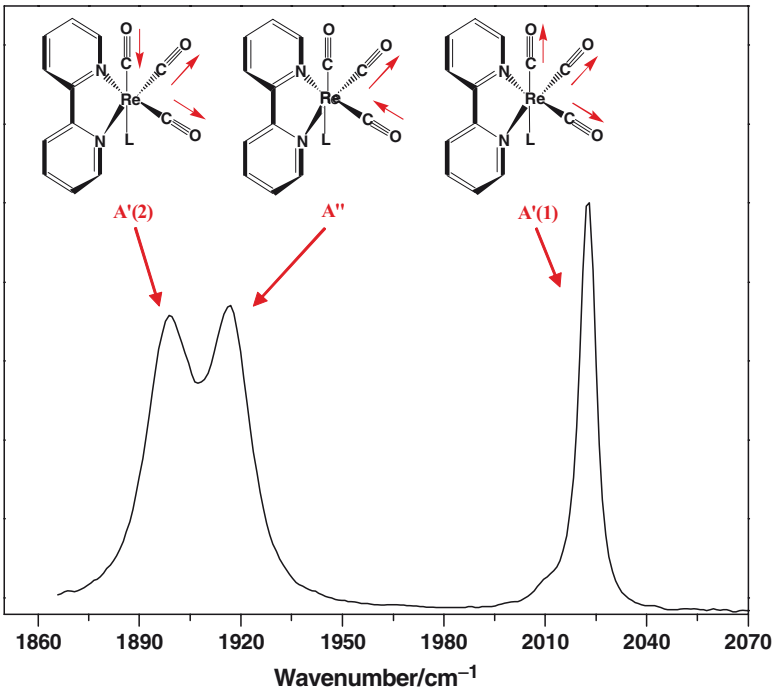

Fig. 8 FTIR spectrum of $[Re(Cl)(CO)_3(bpy)]$ in MeCN and the corresponding ν(CO) vibrations

in-phase ν(CO) vibration, denoted A′(1). The two lower bands belong to the out-of-phase totally symmetric A′(2) vibration and the asymmetric vibration of the equatorial CO ligands, A″. These two vibrations occur at similar energies and the separation of the corresponding bands depends on the axial ligand L. Two well-developed bands are observed in complexes with halide-, *O*- or *P*-coordinated ligands. On the other hand, the A′(2) and A″ bands are merged into one broad band if L is *N*-coordinated, e.g., pyridine, imidazole or NCS^-. They can become slightly separated (by 10–15 cm^{-1}) upon changing the solvent or embedding the Re unit into a supramolecular environment. The assignment of the two lower IR bands was based on ^{13}C-enrichment [58], polarized spectra [59], and DFT calculations [60, 61]. For L = halide or NCS^-, the following energetic order of ground-state ν(CO) vibrations was established: A′(2) <A″ <A′(1). For L = pyridine and its derivatives, DFT calculations in vacuum predict [60] the reverse order of the two lower bands: A″ <A′(2) <A′(1) with the A″–A′(2) separation of 9 cm^{-1}. Experimentally, however, the A″ and A′(2) energies are almost equal and the corresponding bands are undistinguishable. This A″–A′(2) quasidegeneracy is usually explained by a pseudo C_{3v} symmetry of the $Re(CO)_3$ unit, when coordinated by three N-donor atoms. However, since this quasidegeneracy is observed (depending on the solvent!) also when the axial and the diimine ligands are rather dissimilar (L = NCS, N,N = bpy or iPr-DAB; L = im, N,N = phen, etc.), it should better be ascribed to an accidental identity of the axial and equatorial stretching force constants.

Owing to the high sensitivity of ν(CO) vibrational energies to the electron density distribution, the changes of the ν(CO) spectral pattern and shifts of IR bands upon excitation provide detailed information on the character of the populated excited state. Qualitatively, decreasing electron density on the $Re(CO)_3$ moiety shifts ν(CO) bands up in energy (i.e., increases ν(CO) frequencies) due to diminishing Re→CO π back donation. Strengthening σ Re←CO donation may also contribute. Increase of electron density on Re has the opposite effect. In short, partial oxidation and reduction of the Re atom in $[Re(L)(CO)_3(N,N)]^n$ shifts the ν(CO) bands higher and lower in energy, respectively. The ν(CO) energies are sensitive enough to detect even small electronic changes in the vicinity of the $Re(CO)_3$ unit such as π→π* excitation localized on the N,N ligand.

Turner and George reported the first excited-state IR spectrum of a metal carbonyl complex in 1989, using $[Re(Cl)(CO)_3(4,4'\text{-bpy})_2]$ as an example [62]. The upward shift of all three ν(CO) bands upon excitation was interpreted [58, 62] as an evidence for Re→bpy MLCT character of the excited state, where the Re atom is effectively oxidized to Re^{II} and the ligand reduced to bpy^{-}: $*[Re^{II}(Cl)(CO)_3(4,4'\text{-bpy}^{-})(4,4'\text{-bpy})]$. Any deeper discussion of excited-state IR spectra requires correct assignment of the ν(CO) bands. This is not straightforward because of the ambivalence of the assignment of A″/A′(2) vibrations in facial C_s tricarbonyls. The definitive assignment was accomplished only recently [59] by labeling 2-dimensional TRIR spectroscopy (2D-TRIR) for $[Re(Cl)(CO)_3(dmb)]$ (dmb = 4,4′-di-methyl-2,2′-bpyridine) and by DFT calculations [60, 61, 63] for the cationic complex $[Re(Etpy)(CO)_3(bpy)]^+$. In both cases, the energy order of the ν(CO) vibrations in the lowest ^{3}MLCT state was established as A″< A′(2) < A′(1). This means that the out-of-phase A′(2)

vibration undergoes the largest up-shift upon excitation. In terms of the EFFF approximation [64–67], it can be concluded that the axial C≡O stretching force constant increases upon MLCT excitation much more than the equatorial one while the average interaction force constant decreases.

To assign the character of the lowest excited state of $[Re(L)(CO)_3(N,N)]^n$ from TRIR spectra, it is necessary to examine the change in the ν(CO) IR spectral pattern as well as the sign and magnitude of the IR band shift upon excitation. The latter is most accurately determined for the highest A′(1) band. Excited-state IR spectra obtained on a variety of $[Re(L)(CO)_3(bpy)]^n$ complexes allow us to formulate general relations between the excited-state character and its IR spectrum:

(a) Excited states of a predominant $Re(CO)_3 \rightarrow N,N$ ^{3}MLCT character show an upward shift of all three ν(CO) bands, which is the largest for A′(2). The highest A′(1) band shifts by ca. +40 cm^{-1} for N,N =bpy, measured in common dipolar solvents [12, 47, 48, 58–63, 68–78] Larger A′(1) shifts are observed when the excited electron density is located far away from the Re center such as in 5-nitro-phen [74] or dppz [48] complexes.

(b) An excited state of a predominant $Re(CO)_3 \rightarrow L$ ^{3}MLCT character has been studied for $[Re(MQ^+)(CO)_3(dmb)]^{2+}$ (*N*-methyl-4,4′-bipyridinium) [79]. A rather large A′(1) shift of +62 cm^{-1} and merged A″ +A′(2) band up-shifted by ca. 63 cm^{-1} were found. So far, this is the only example of an IR-characterized ^{3}MLCT(L) state.

(c) L→N,N LLCT excited states were observed [13] for L = amides $NTol_2$, NHTol and phosphide PPh_2. The A′(1) is shifted downwards by 5–10 cm^{-1}. Excited-state A″ and A′(2) bands are also slightly shifted downwards, but their strong overlap with the corresponding ground-state bands prevents determining their exact positions. The small decrease in CO stretching energies is caused by reduction of the bpy ligand on excitation, which increases the electron density on the $Re(CO)_3$ moiety through diminishing $d\pi(Re) \rightarrow \pi^*(bpy)$ π back bonding. This effect is only partly compensated by electronic depopulation of the amido or phosphido ligand. Interestingly, the excited-state IR spectrum of $*^3[Re(NTol_2^{\cdot+})(CO)_3(bpy^{\cdot-})]$ looks like an average of the spectra of the reduced and oxidized complexes, $[Re^I(NTol_2)(CO)_3(bpy^{\cdot-})]^-$ and $[Re(NTol_2^{\cdot+})(CO)_3(bpy)]^+$. A redox-separated state $[Re(py\text{-}PTZ^{\cdot+})(CO)_3(Me_2dppz^{\cdot-})]^+$ is like a kind of LLCT state in which the "hole" on PTZ is remote from the Re^I atom and the excited electron is delocalized over the dppz ligand, also away from the Re atom. Excited-state A′(1) and A″ +A′(2) bands are downshifted from their ground-state positions by −6 and −19 cm^{-1}, respectively [61]. Similar types of ^{3}LLCT occur in $[Re(py\text{-}azacrown)(CO)_3(bpy)]^+$ complexes, where the electron is transferred from the azacrown nitrogen atom to bpy (see Sect. 7.3). Accordingly, the excited-state IR spectrum shows A′(1) and A″ +A′(2) bands downshifted by −25 and −29 cm^{-1}, respectively [77].

(d) ππ* ^{3}IL states are manifested by a small (−5 to −10 cm^{-1}) down-shift of all three ν(CO) bands, whether the ^{3}IL state is localized on the N,N or the L ligand [31, 32, 47, 48, 61]. The quasidegeneracy of the A″ +A′(2) band in the ground

state is preserved upon ^{3}IL excitation. Changes in IR spectra are caused by population of the ligand π* orbital in the excited state, which interacts with *d*π(Re) orbitals. The electron density on the $Re(CO)_3$ moiety is thus increased. Slightly more negative shifts (−11 and −27 cm^{-1} for the A′(1) and A″ +A′(2) bands, respectively) occur upon ^{3}IL excitation of $[Re(Etpy)(CO)_3(4,4'\text{-}(NH_2)_2\text{-}bpy)]^+$ [47], which involves a shift of electron density from the amino group to the region of the bpy rings and nitrogen donor atoms.

(e) σπ* ^{3}SBLCT excited states are very hard to detect because of their high chemical reactivity. An IR spectrum of a ^{3}SBLCT-excited Re complex was reported [80] only for [Re(benzyl)$(CO)_3$(iPr-DAB)] in heptane. The A′(1) band undergoes a very small up-shift by ~8 cm^{-1} whereas the A′(2) and A″ bands shift to lower energies by less than 10 cm^{-1}. The small IR shifts observed upon SBLCT excitation indicate that the decrease of electron density on Re due to diminished σ donation from benzyl is compensated by population of the DAB π* orbital that strongly interacts with *d*π(Re) orbitals. Similarly, a small admixture of a SBLCT character to a predominantly ^{3}MLCT state is manifested by diminishing A′(1) shift. This is the case of [Re(Et)$(CO)_3$(bpy)] whose lowest excited state shows the A′(1) band up-shifted by 28 cm^{-1} whereas the typical emissive ^{3}MLCT state of [Re(Me)$(CO)_3$(bpy)] exhibits an A′(1) shift of +43 cm^{-1} [73].

Besides TRIR, it is also possible to employ excited-state resonance Raman spectroscopy (TR^3 or TR^2) to characterize excited-states of $[Re(L)(CO)_3(N,N)]^n$ complexes [25, 27, 37, 48, 79, 81, 82]. The spectra show bands due to vibrations of the N,N ligand and provide information on its structural changes upon excitation. Picosecond TR^3 spectra of Re complexes give very weak signals [37]. Measurements on the ns timescale are more informative. In the case of ^{3}CT and ^{3}IL states of [Re(py)$(CO)_3$(dppz)]$^+$ and the ^{3}LLCT state of [Re(py-azacrown)$(CO)_3$(bpy)]$^+$ [16, 27], complementary vibrational information was provided by TR^3 and TRIR measured in the fingerprint region.

4.4 Character Mixing in the Lowest Excited States

Electronic transitions and excited states of metal complexes are traditionally described in terms of text-book categories such as MLCT, LLCT (XLCT), IL, MC (=LF or dd), LMCT, etc. It was mentioned several times above that MLCT, LLCT, and IL characters in the case of $[Re(L)(CO)_3(N,N)]^n$ represent only limiting cases. In reality, electronic transitions and excited states have mixed character owing to two factors: (1) delocalization of the optical orbitals (i.e., frontier orbitals involved in electronic transitions), and (2) combining several one-electron excitations in an electronic transition.

The large ν(CO) shifts occurring upon excitation of complexes such as [Re(Cl)$(CO)_3$(bpy)] or $[Re(Etpy)(CO)_3(bpy)]^+$ clearly show that the traditional description

of their lowest excited states as ^{3}MLCT is incomplete and that the electron density is transferred from the whole $Re(CO)_3$ fragment rather than from the Re atom. This effect can be traced down to delocalization of HOMO and HOMO-1. For example, it was calculated for $[Re(py)(CO)_3(bpy)]^+$ that the optical orbital HOMO-1 contains 65 and 26% Re and CO character, respectively [10].

Mixing between $Re(CO)_3 \rightarrow$N,N MLCT and X→N,N XLCT (X = halide) characters was first recognized by Stufkens when analyzing spectroscopic effects of changing the halide ligand X in complexes $[Re(X)(CO)_3(N,N)]$ [1, 15, 24]. Resulting excited states are called MLCT/XLCT or more generally MLCT/LLCT or MLLCT. As was discussed in Sect. 2, this type of character mixing results from $d\pi$(Re) and $p\pi$(X) orbital mixing in HOMO and HOMO-1, which both are Re–X π-antibonding orbitals. The $p\pi$(X) character increases on going from chloride to bromide and iodide and this trend is accompanied by changes in excited-state UV–Vis absorption spectra [15]. It is not straightforward to prove this mixing experimentally since it is hard to probe changes of electron density on monoatomic halide ligands. To circumvent this problem, we have synthesized a pseudohalide complex $[Re(NCS)(CO)_3(bpy)]$ and measured the shifts of IR bands due to ν(CO) and $\nu(NC)_{NCS}$ vibrations upon population of the lowest triplet state, Fig. 9 [12]. The ν(CO) bands shift upwards (+41 cm^{-1}) due to the decreasing electron density on the $Re(CO)_3$ unit while the $\nu(NC)_{NCS}$ band shifts downwards by ca. −47 cm^{-1} owing to partial depopulation of the N=C π-bonding orbital of the NCS^- ligand. This is exactly the result expected for a mixed $Re(CO)_3 \rightarrow$bpy MLCT and

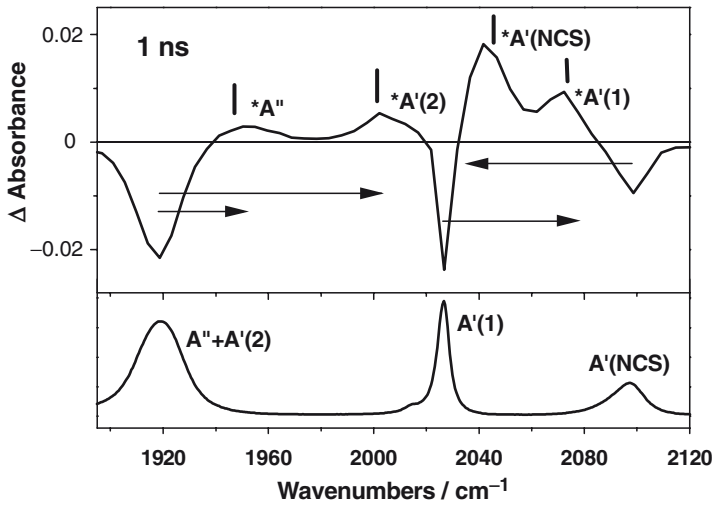

Fig. 9 Difference time-resolved IR spectra of $[Re(NCS)(CO)_3(bpy)]$ in MeCN measured at 1 ns after 400 nm, 150 fs laser pulse excitation [12], *top panel*. Positive bands correspond to the excited state, negative to the depleted ground-state population. Experimental points are separated by 4–5 cm^{-1}. *Horizontal arrows* show the band shifts upon excitation. *Vertical bars* show the DFT-calculated vibrational wavenumbers for the a^3A'' MLCT state. *Asterisk* denotes the excited state. *Bottom panel*: Ground-state FTIR spectrum

NCS→N,N LLCT excited-state, which was further supported by DFT calculations, Fig. 10 [11, 12]. Such excited states are more correctly viewed as delocalized Re(L)$(CO)_3$→N,N ^{3}MLLCT states. They are not limited to halide or NCS^- complexes. A ^{3}MLLCT lowest state was identified by DFT also in [Re(2,6-dimethylphenylisocyanide) $(CO)_3$(R-phen)]$^+$ complexes, where the ligand-to-ligand CT contribution originates in electron excitation from an occupied phenylisocyanide π orbital to π*(N,N) [16, 17]. An im→phen contribution to the lowest triplet state was also indicated by DFT for [Re(im)$(CO)_3$(phen)]$^+$ (im =imidazole). MLCT/LLCT mixing is a general feature of [Re(L)$(CO)_3$(N,N)]^n complexes that occurs in low-lying singlet as well as triplet states of either symmetry (A′, A″), whenever the axial ligand L is electron-rich, possessing a high-lying occupied π orbital that overlaps with a Re *d*π orbital(s).

Mixing between CT and ππ* IL(N,N) characters is not important for the singlet excited states of [Re(L)$(CO)_3$(N,N)]^n, for the ^{1}IL states usually lie well above the optically populated ^{1}CT state. However, the IL-CT mixing becomes much more pronounced in low-lying triplet states of A″ symmetry, because the ^{3}IL and ^{3}CT states lie very close in energy. Most [Re(L)$(CO)_3$(polypyridyl)]^n complexes have two low-lying A″ triplets of a predominantly IL and CT (i.e., MLCT or MLLCT) characters which occur within the range ca. 0.5 eV wide [10–12, 74, 76]. In most complexes, the ^{3}IL state lies above ^{3}CT. TD-DFT calculations show that these states result from linear combinations of π→π* and HOMO-1→π* one-electron excitations, which introduce the IL and CT characters, respectively:

$$^3\mathrm{IL} = a(\pi \rightarrow \pi^*) - b(\mathrm{HOMO}-1 \rightarrow \pi^*),$$

$$^3\mathrm{CT} = b(\pi \rightarrow \pi^*) + a(\mathrm{HOMO}-1 \rightarrow \pi^*).$$

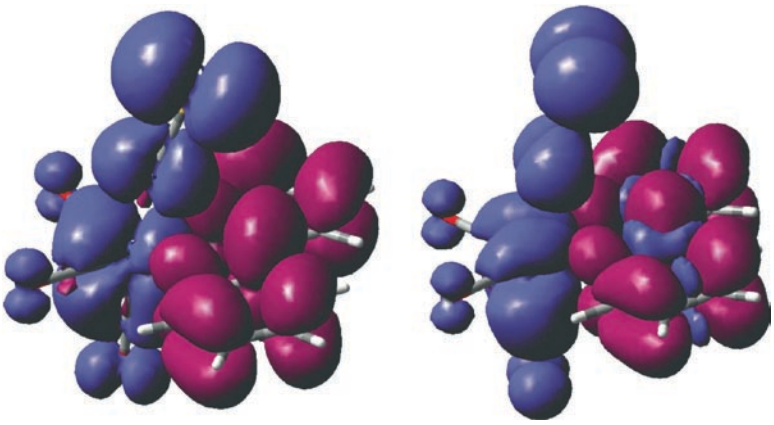

Fig. 10 Maps of the electron density difference for the MLLCT triplet excited states a^{3}A′ (*left*) and a^{3}A″ (*right*). Calculated by TD-DFT (PBE0/CPCM) in a CH_3CN solution. *Blue*, *violet*: regions where electron density decreases and increases upon excitation, respectively. Reprinted with permission from [11]

For example, in the case of [Re(Cl)$(CO)_3$(bpy)], TD-DFT (B3LYP, in MeCN) predicts b^2 =0.16 [10]. This result means that the higher-lying (3.13 eV) state b^3A'' is ca. 84% IL and 16% MLLCT in character, while the lowest (2.77 eV) a^3A'' state is 84% MLLCT with a 16% IL contribution (note that $a^2 + b^2 = 1$). The CT–IL mixing is clearly visualized in the maps of difference electron density as regions of decreased electron density within the N,N ligand in the predominantly ^{3}CT state or as regions of decreased electron density on the Re(L)$(CO)_3$ moiety in the case of predominantly ^{3}IL states. However, it is hard to assess accurately the magnitude of the IL-CT mixing using DFT calculations. The calculated mixing coefficients *a* and *b* are very sensitive to the functional and the way the solvent is included in the calculation. In the above example of [Re(Cl)$(CO)_3$(bpy)], the mixing is calculated as almost 50:50 if the PBE0 functional is used instead of B3LYP. On the other hand, the calculated energies hardly change. Essentially, increasing the weight of the Hartree–Fock exchange in the functional pushes the ^{3}CT state up in energy, towards the ^{3}IL state, increasing their mixing. Inclusion of solvent to the calculation has the same effect. Therefore, it is necessary to validate DFT calculations of triplet states by comparing calculated and experimental excited-state IR spectra, which are very sensitive to the extent of IL-CT mixing: Both calculated and experimental ν(CO) shifts on excitation decrease as the mixing increases. Indeed, experimentally validated DFT calculations are currently the best source of information on the extent of IL-CT mixing.

The ZFS values determined from temperature-dependent emission decay [46, 55] (Sect. 4.1) show that the IL-CT mixing in the lowest emissive ^{3}CT state of [Re(Cl)$(CO)_3$(N,N)] increases on changing the N,N ligand from bpy to phen and upon methylation of either ligand. The former effect is due to lower ^{3}IL energy in the more delocalized phen and the latter is caused by increasing the ^{3}CT energy on methylation. Both ligand variations diminish the energy gap between the two states, increasing their mixing. This conclusion is supported by TRIR spectra which show larger A′(1) ν(CO) shift for bpy than phen complexes.

Experimentally, it is necessary to distinguish the effects of IL-CT mixing from simultaneous population of both the ^{3}IL and ^{3}CT states that could be in fast thermal equilibrium. (Note that an energy difference of 0.5 eV would amount to ca. 5% population of the upper state at room temperature.) Simultaneous population of these two states can be observed in TRIR spectra, where the predominantly ^{3}IL state is manifested by a weak band occurring below the ground-state A″ +A′(2) band while the lower-lying predominantly ^{3}CT state shows the characteristic pattern of three up-shifted bands. This is, for example the case of [Re(Etpy)$(CO)_3$(4,4′-$(NH_2)_2$-bpy)]$^+$ [47] and [Re(py)$(CO)_3$(dppz)]$^+$ [48]. Time-dependent simultaneous population of ^{3}IL and ^{3}MLCT states was detected by TRIR for [Re(Et)$(CO)_3$(bpy)]$^+$ in ionic liquids until a few hundreds of ps after excitation [76] and by photoluminescence upconversion for [Re(L)$(CO)_3$(bpy)]^n (L = Etpy, halide) in MeCN on a femtosecond timescale [10].

Finally, it should be noted that IL-CT mixing in the lowest triplet for any given [Re(L)$(CO)_3$(N,N)]^n is strongly medium dependent. ^{3}CT state energies are much more sensitive to medium variations than ^{3}IL. Essentially, any change in the medium (liquid-to-solid transition, decrease in the dielectric response function,

etc.) that pushes the ^{3}CT state up in energy toward the ^{3}IL state will also increase the IL-CT mixing. This effect is responsible for the IR rigidochromism, whereby smaller excited-state IR shifts are observed in glasses than in fluid solvents [70]; it can contribute to emission rigidochromism [20, 45] and the red shift observed in the course of curing of a polymeric media [83, 84]. The extent of IL-CT mixing can also change during excited-state relaxation [76], opening the possibility to use $[Re(L)(CO)_3(N,N)]^n$ complexes as probes of solvation dynamics. This aspect will be discussed in the next section.

5 Relaxation of Triplet Excited States

Irradiation of $[Re(L)(CO)_3(N,N)]^n$ complexes with 400 nm light into the red edge of their lowest absorption band deposits in the excited molecule energy of about 7,000 cm^{-1} above the relaxed (thermally equilibrated) lowest triplet state. A large part of this energy (~600 cm^{-1}) is redistributed on a femtosecond timescale amongst low-energy vibrational modes, as is manifested by the "instantaneous" Stokes shift of the fluorescence band [10] to ~530 nm and its broadness, see Sect. 3. This vibrational excitation is carried over by ISC to the triplet state. In addition to vibrational excitation, the electronically excited ^{3}*$[Re(L)(CO)_3(N,N)]^n$ molecule initially finds itself in a highly unequilibrated solvent arrangement, whereby the dipolar solvent molecules are oriented to optimize solvation of the electronic ground state that has different charge distribution and dipole moment, see Fig. 11. Reorientation of solvent dipoles takes from hundreds of femtoseconds to units of picoseconds [85] and

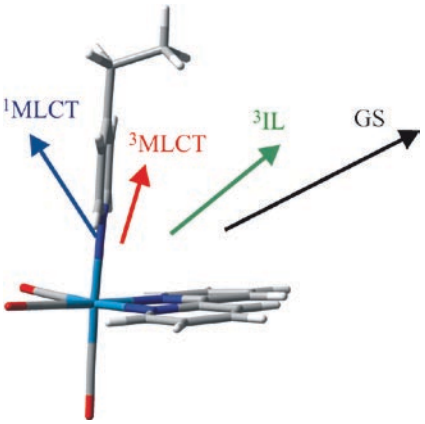

Fig. 11 Relative size and orientation of dipole moment vectors of the ground state (*black*) and the excited states ^{1}MLCT (b^1A'), ^{3}IL (b^3A''), and ^{3}MLCT (a^3A'') of $[Re(Etpy)(CO)_3(bpy)]^+$, projected onto the optimized ground-state molecular structure. Dipole moment vectors originate in the center of charge calculated using Mulliken population analysis. They lie in the molecular symmetry plane. (Calculated by TD-DFT G03/PBE0/vacuum at the optimized ground state geometry.) Reproduced with permission from [76]

occurs after the ISC, as part of the triplet-state relaxation. Even slower relaxation motions take place if the excited chromophore is imbedded in more complex media such as proteins [75] or ionic liquids [76].

Relaxation of the lowest triplet excited state ^{3}*[Re(L)(CO)$_3$(N,N)]^n manifests itself experimentally in different ways:

(a) Increasing intensity of the sharp excited-state band at ~380 nm due to the bpy$^{\cdot-}$ unit, which occurs during the first ~20 ps after excitation. This effect was first observed for [Re(Etpy)(CO)$_3$(dmb)]$^+$ and [Re(Cl)(CO)$_3$(bpy)] in MeCN [37].

(b) Increasing intensity of excited-state Raman bands (excited at 400 nm) due to vibrations of the bpy$^{\cdot-}$ ligand, which occurs during the first ~20 ps after excitation. This effect was observed in time-resolved resonance Raman spectra of [Re(Etpy)(CO)$_3$(dmb)]$^+$ and [Re(Cl)(CO)$_3$(bpy)] in MeCN. It is probably related through resonance enhancement to the rise of the 380 nm excited-state band [37].

(c) Dynamic red shift of the ^{3}MLCT phosphorescence band of [Re(Etpy)(CO)$_3$(bpy)]$^+$, which was observed in slowly relaxing ionic liquid [BMIM]PF$_6$ [76].

(d) Dynamic evolution of TRIR spectra in the ν(CO) region, which is strongly dependent on the medium and its dielectric and dynamic properties [13, 37, 71, 72, 74–76, 86–88]. Owing to the high sensitivity to medium variations, the combination of [Re(L)(CO)$_3$(N,N)]^n complexes and TRIR emerges as a new and very promising way to interrogate solvation dynamics in various media, ranging from dipolar solvents to biomolecules. The detailed mechanisms relating relaxation dynamics and excited-state ν(CO) IR spectra are far from understood, and are currently being investigated in the author's laboratory.

Dynamic up-shift of the A′(1) ν(CO) band of the lowest excited state is the most pronounced IR effect of excited-state relaxation. Time-dependences of the A′(1) ν(CO) energies measured for various complexes in different media have revealed [37, 75, 76, 86] that relaxation involves four different lifetimes (Fig. 12):

(a) An instantaneous IR shift occurs within the experimental time resolution of ~1 ps. It encompasses effects of the electron-density redistribution upon optical excitation, ISC, ultrafast intramolecular vibrational energy redistribution (IVR) into low-frequency modes, electronic polarization of the solvent molecules, and inertial movements of solvent molecules. For fast-relaxing solvents (MeCN), it includes diffusional dipole reorientation as well.

(b) The "fast" kinetic component of the IR shift, which occurs with a time constant of 1–4 ps. It is ascribed to later stages of IVR, which might include [86] vibrations of strongly solvating molecules of the medium. This kinetic component has been observed (~4.5 ps) even for a Re complex adsorbed at a dry ZrO_2 surface [87, 88]. In slowly relaxing dipolar solvents, this component can include later stages of solvent dipole reorientation.

(c) The "intermediate" kinetic component, 10–20 ps, has been observed in all investigated media except dry ZrO_2. It is accompanied by the rise of the ~380

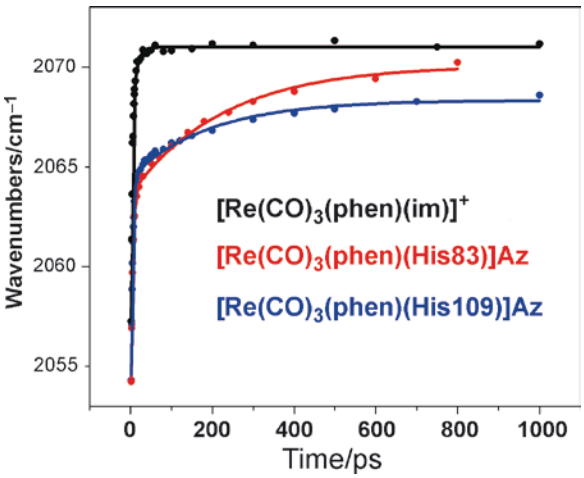

Fig. 12 Time-dependent wavenumber of the excited-state A′(1) ν(CO) IR band of [Re(im)$(CO)_3$(phen)]$^+$ in D_2O (*black*) and azurins with Re$(CO)_3$(phen) chromophore attached to His83 (*red*) and His109 (*blue*). Measured in D_2O (*p*D = 7) after 400 nm, 150 fs laser pulse excitation. Exact IR band positions were determined by Lorentzian fitting. Reproduced with permission from [75]

nm band in the excited-state electronic spectrum, see above. The detailed physical nature of the relaxation processes responsible are still under investigation. It is too slow for solvent dipole reorientation, while the accompanying evolution of the excited-state UV–Vis spectra indicates structural changes within the chromophore. Vibrational energy relaxation (VER) by energy flow from the excited chromophore to the solvent seems to be the main underlying physical process. Preliminary data suggest [86] that rearrangement of a "local solvent" (i.e., ordered solvent molecules that are in close contact with the chromophore) could be an important part of this relaxation process. The assignment of the fast and intermediate relaxation components to IVR and VER is supported by observation of a narrowing of the excited-state A′(1) IR band on the same time-scale. Both IVR and VER entail structural changes of the excited chromophore, to which the high-frequency ν(CO) vibrations respond by spectral shift to higher energies. This effect can be also described by invoking anharmonic coupling [89] between the low-frequency skeletal vibrations and ν(CO). Its strength is high when low-frequency modes are excited and diminishes during vibrational relaxation, allowing the A′(1) ν(CO) energy to increase towards the value corresponding to a harmonic vibration.

(d) The "slow" kinetic component of hundreds of ps or even units of ns was observed only in slow-relaxing media such as ionic liquids [76] or proteins [75]. In the former case, it was convincingly demonstrated [76] that the slow IR spectral shift is caused by rearrangement of the electric field (so called reaction field) that the medium exerts on ^{3}*[Re(L)$(CO)_3$(N,N)]^n. As can be

seen in Fig. 11, excitation of $[Re(L)(CO)_3(N,N)]^n$ to a ^{3}CT state ^{3}*$[Re(L)(CO)_3(N,N)]^n$ decreases and reorients the molecular dipole moment within the first few hundreds of fs. Polar or charged molecules of the solvent respond to excitation by changing their orientation, optimizing thus solvation of the excited state. In fast-relaxing dipolar solvents, the solvent response is fast and contributes to the fast and, in some cases, intermediate relaxation components. It becomes directly observable by TRIR in slowly relaxing media, such as proteins and ionic liquids. Relaxation in these media involves additional interactions such as H-bonding, peptide chain movements, or correlated ion translation, respectively.

The dynamic upshift of ν(CO) during relaxation of the medium (i.e., the slow component) can be explained as follows: Because the ^{3}CT-excited Re complex is less polar than the ground state (Fig. 11), the reaction field is initially directed against the charge separation driven by electronic excitation. As the solvent relaxes, the reaction field weakens and reorients, allowing the charge separation in the excited Re molecule to evolve to completion. Transfer of electron density from the $Re(L)(CO)_3$ unit in the course of solvent relaxation is manifested by a dynamic upward shift of the A′(1) ν(CO) IR band. On a deeper physical level, the link between solvent relaxation and excited-state evolution of the Re chromophore can be described by time-dependent IL-CT mixing in the lowest triplet state: Immediately after ISC, the ^{3}CT state lies high in energy, close to ^{3}IL. The IL-CT mixing is strong and limits the charge transfer from $Re(L)(CO)_3$ to N,N. The ^{3}CT state shifts lower in energy during solvent relaxation. Increasing energy separation from ^{3}IL results in less mixing and, hence, more extensive charge transfer that increases the ν(CO) energies. This explanation is based on changing the excited-state wavefunctions in response to time-dependent changes of the solvent reaction field. In other words, it assumes large polarizability of electronically excited Re complexes, due to high excited-state density. Electronic changes indeed seem to be the principal factor responsible for the dynamic IR shifts seen during solvent relaxation. In addition, anharmonic coupling also responds to the reaction field and could contribute to the observed dynamic IR shifts [87].

The sensitivity of the slow kinetic component of the IR dynamic shift to the nature of the medium is truly remarkable. For example, Fig. 12 shows the difference between the behavior of $[Re(im)(CO)_3(phen)]^+$ in a fluid D_2O solution and appended to two different sites of the same protein. The slow component is missing in D_2O and emerges only in the proteins, its rate being strongly dependent on the position at the protein surface where the Re chromophore is attached. Relaxation dynamics of the Re complex thus report on the flexibility of the protein binding site and the motions of its peptide chains and associated solvent (D_2O) molecules. Measuring TRIR spectra of Re complexes in various media has a great potential to reveal new aspects of relaxation dynamics. The fast and intermediate kinetic components provide information on intramolecular structural relaxation of the excited chromophore and, possibly, on local solvation. The slow component is most informative, reporting on motions in organized, complex chemical media and their

response to the charge redistribution in the solute. It should be stressed that the response of the medium to CT excitation involves the same molecular and collective motions which accompany fast photoinduced electron transfer (ET) reactions. Interrogating relaxation processes using Re probes and TRIR spectroscopy could therefore lead to new understanding of relations between solvation (medium) dynamics and electron transfer. The same is true about vibrational relaxation, which couples to ultrafast ET reactions too [79, 90].

A case of solvent-driven electronic relaxation has been observed [76] for $[Re(Etpy)(CO)_3(bpy)]^+$ in ionic liquids: TRIR spectra have shown at early times a weak signal due to the ^{3}IL state, in addition to much stronger bands of the ^{3}MLCT state. Although no accurate kinetic data are available, the ^{3}IL state converts to ^{3}MLCT with a rate that is commensurate with the solvent relaxation time. Fluorescence up-conversion provided an evidence [10] for population of an upper ^{3}IL state in MeCN, which converts to ^{3}CT with a much faster lifetime of 870 fs (Table 1). The solvent dynamic effect on the ^{3}IL→^{3}CT internal conversion can be rationalized by different polarities of the ^{3}IL and ^{3}CT states, Fig. 11. The solvent relaxation stabilizes the ^{3}CT state relative to ^{3}IL, driving the conversion.

6 Decay of the Lowest Triplet Excited State

In the absence of photochemical reactions, the lowest excited states of $[Re(L)(CO)_3(N,N)]^n$ complexes decay to the ground state both radiatively and nonradiatively. The lifetimes in fluid solutions range from tens of nanoseconds to microseconds, depending on L, N,N and the medium. Complexes where N,N = 1,4-diazabutadiene are mostly nonemissive in fluid solutions, having excited-state lifetimes of hundreds of picoseconds. Excited-state decay of Re complexes is a much studied phenomenon. It has been dealt with in several review articles [1, 91] and Chap. 2 of this book. Herein, we will only stress some crucial aspects:

(a) Emission in fluid solution is known for ^{3}MLCT, ^{3}MLLCT (i.e., ^{3}MLCT/XLCT), and ^{3}IL states of $[Re(L)(CO)_3(N,N)]^n$. ^{3}SBLCT are emissive only in the absence of Re–L homolysis, usually in rigid glasses. Emission from ^{3}LLCT states $*[Re^I(L^{\cdot+})(CO)_3(N,N^{\cdot-})]^n$ (see Sect. 5) is rather unusual, akin to radiative charge recombination [92].
(b) ^{3}CT emission in fluid solution is usually broad and structureless. Admixture of a ^{3}IL character manifests itself by appearance of a vibronic structure on the emission band.
(c) Because of spin-orbit coupling, the lowest triplet state is split into three components, even in the absence of an external magnetic field, see Sect. 4.1. The highest spin sublevel is the fastest decaying one [46, 55].
(d) Emission from CT states shows strong rigidochromism, shifting to higher energies as the medium solidifies [20, 45, 84]. This effect is caused by the lack

of medium relaxation in rigid environments. Solvatochromism is rather weak; the ^{3}CT emission shifting slightly to higher energies with decreasing solvent polarity.

(e) Franck–Condon analysis of the emission band shape yields important parameters related to structural differences between the emitting state and electronic ground state. The emission band is expressed as a sum of bands due to vibronic transitions from the zero vibrational level of the emitting state to one or two sets of vibrational levels of the ground state. (Two sets can be used meaningfully only if the emission band has a well-resolved structure. Broad structureless CT emission bands should be fitted with one set only. For the corresponding equations, see [16, 93–95]) Each set of vibrations corresponds to a normal coordinate along which the emissive excited state is distorted relative to the ground state. Fitting of the emission bands yields the following parameters: the difference of zero-level energies of the emissive state and the ground state, E_o, energies (frequencies) of the vibrational acceptor modes $h\nu_1$ and $h\nu_2$ (interpreted as average energies of high- and low-frequency contributing modes, respectively), the respective Huang–Rhys factors S_1 and S_2 and full-width at half-maximum of the zero–zero component of the emission spectra $\nu_{1/2}$. The Huang–Rhys factor or electron-vibrational coupling constant is defined as $S = \Delta Q_e^{\,2}\,(\mu\omega/2h) = \Delta Q_e^{\,2}/2\,\Delta Q_0^{\,2}\,]$, where μ is the reduced mass, $\omega = 2\pi\nu$ is the vibrational frequency, and ΔQ_e is the distortion between the ground and excited state along the corresponding normal coordinate. S is a measure of the excited state distortion relative to the amplitude of the corresponding vibration, ΔQ_o at the zero vibrational level; $v = 0$. ($2\Delta Q_o$ is the change of the amplitude upon vibrational excitation by a single quantum; $\Delta v = 1$.) The width parameter $\nu_{1/2}$ includes broadening due to unresolved vibronic transitions involving low-frequency and solvent modes. This type of analysis has been applied to emission spectra of many Re complexes, see, for example, [16, 91, 92, 96–98]. When fitted using only one mean accepting vibration, emission from ^{3}MLCT and ^{3}MLCT/XLCT states is generally characterized by large S values (often 1–2) and relatively low vibrational energies hν, especially in comparison with Ru^{II} or Os^{II} polypyridines. This result indicates large excited-state distortion of Re complexes and involvement of low-frequency skeletal modes that were also revealed [10] by DFT calculations. The important contribution from low-frequency modes becomes more apparent when two-mode fitting is used [16], yielding mean energies of high- and low-frequency vibrations of 1,400 and 500 cm^{-1}, respectively, for the ^{3}MLLCT emission from [Re(2,6-dimethylphenylisocyanide)$(CO)_3$(R-phen)]$^+$ complexes. The importance of low-frequency vibrations diminishes or even vanishes as the ^{3}IL character in the emitting state builds up [16]. Extensive MLCT-IL mixing is probably the reason for large $h\nu$ and small S values determined [97] for a series of [Re(L)$(CO)_3$(2,3-Di(2-pyridyl)quinoxaline]$^+$ complexes, in contrast to typical ^{3}MLCT values of analogous [Re(L)$(CO)_3$(2,3-Di(2-pyridyl)pyrazine]$^+$. On the basis of trends in S, it was argued

that the distortion of the N,N ligand upon excitation and extent of charge transfer increases in series of structurally related complexes with increasing emission energies [96]. However, this argument should be taken with care, because increasing ^{3}CT energy could lead to enhanced mixing with a ^{3}IL state. A small S factor was found for $Re(CO)_3 \rightarrow L$ ^{3}MLCT(L) state $*[Re^{II}(BIQD^{\cdot-})(CO)_3(4,4'\text{-}R_2\text{-}bpy)]^n$ (BIQD = reducible quinone-type ligand) [92]. The widths of vibronic bands $\nu_{1/2}$ determined for Re complexes are much larger than those obtained for Ru and Os polypyridines, indicating large solvent reorganization energy between the ground state and emissive CT states of Re complexes. The broadness of the emission vibronic components is the reason for the general lack of distinct structure of emission from many Re complexes. It also limits the accuracy and possibilities of Franck–Condon analysis. (It should be noted that band-shape fitting was often performed with fixed $h\nu$ value(s), affecting thus the S values obtained. Also, the analysis is based on the assumption of identical vibrational frequencies in the ground and excited state, which is not fully valid.)

(f) Radiative rate constant k_r of ^{3}MLCT and ^{3}MLLCT emission of Re complexes occurs in the range of 10^4–10^5 s^{-1}. It drops to 10^1–10^2 s^{-1} for ^{3}LLCT states [92]. The radiative rate constant is proportional to the square of the transition moment and the mean third power of the emission frequency. The radiative decay is spin-forbidden, which is overcome by spin-orbit induced coupling with a ^{1}CT state [54]. On the basis of spin-orbit considerations, one would expect that in series of halide complexes $[Re(X)(CO)_3(bpy)]$, k_r will increase in the order X = Cl < Br < I. In reality, only a small dependence on the halide was found, in the order Br >Cl >I [15]. Faster radiative decay of ^{3}CT than ^{3}IL states can be explained by spin-orbit coupling that is stronger for ^{3}CT states, due to larger involvement of metal orbitals. A simple two-state model was used to explain radiative decay of low-lying ^{3}MLCT(L) and $\sigma(Re–O)\pi^*(L)$ ^{3}SBLCT states [92]. k_r was estimated using the electronic coupling between the excited and ground states and the vector difference of their dipole moments [92]. This simple model also predicts ^{3}CT states to be stronger emitters because of larger electronic coupling between the ground and the excited state and larger difference of their dipole moments.

(g) Re complexes are in their majority weak emitters in fluid solutions because of nonradiative decay being about two orders of magnitude faster than radiative decay. This limits emission quantum yields to <0.01. Nonradiative decay is much slower and emission stronger in rigid media. ^{3}MLLCT states of [Re(2,6-dimethylphenylisocyanide)$(CO)_3$(R-phen)]$^+$ complexes are a notable exception with emission quantum yields as high as ~0.8 in fluid solutions at room temperature [16, 17]. Despite long lifetimes, ^{3}IL emission is usually rather weak due to small k_r values.

(h) The nonradiative decay rate constants are temperature dependent: $k_{nr}=k^0_{nr} + k'_{nr}(T)$. The Arrhenius T-dependent term corresponds to activated nonradiative decay. Its physical origin, however, is far from clear. It can hardly be attributed to thermal population of short-lived ^{3}dd states as in the case of Ru^{II} polypyridyls,

since there is neither theoretical nor experimental evidence for such states occurring in a relevant energy range. Given the large structural distortions of Re excited states, it is possible that $k'_{nr}(T)$ corresponds to decay to the ground state in a strong-coupling limit [99] and the thermal activation is needed to bring the system to the spatial region where the potential energy surfaces of excited and ground states approach each other. k^0_{nr} corresponds to nonradiative decay in the weak-coupling limit, which is well described by the energy gap law, EGL [91, 99, 100]. Accordingly, in a series of structurally related Re complexes the logarithm of k_{nr} decreases linearly with increasing emission energy [1, 15, 91, 96, 97, 101]. The slopes and intercepts of the $\ln(k_{nr})$–E_{em} correlations depend on the mean energy of the accepting vibration $h\nu$ and the electron-vibrational coupling constant S. In addition, the intercept depends on the vibronic coupling between the ground and excited state and the vibronic bandwidth $\nu_{1/2}$. These three parameters, in turn, depend on the character of the excited state. For example, different $\ln(k_{nr})$–E_{em} linear correlations were found [97] for the series of complexes $[Re(L)CO)_3(bpy)]^+$, $[Re(L)(CO)_3(2,3\text{-di}(2\text{-pyridyl})pyrazine]^+$, and $[Re(L)(CO)_3(2,3\text{-di}(2\text{-pyridyl})quinoxaline]^+$ in which the ligand L was varied. The $\ln(k_{nr})$–E_{em} correlations were elaborated further [1] to include ^{3}SBLCT and ^{3}MLCT/XLCT states. The resulting "EGL maps" show regions characteristic for individual types of excited states and classes of compounds, as well as switchovers in excited-state character upon structural variations [1]. Detailed analysis of $\ln(k_{nr})$–E_{em} correlations for Re complexes have pointed to the important role of interactions between the excited complex and the solvent in facilitating the nonradiative decay [96, 97]. Interactions between solvents and the CO ligands seem to be especially important, making the nonradiative decay of Re complexes faster in comparison with Ru^{II} and Os^{II} polypyridyls that emit at similar energies.

(i) The parameters $h\nu$, S, and $\nu_{1/2}$ can be obtained independently from analysis of emission bands [see the item (c)] and used to calculate the slopes of $\ln(k_{nr})$–E_{em} correlations. Good correspondence between calculated and experimental values has been obtained [96].

(j) The EGL treatment of nonradiative decay of CT states is conceptually very similar to the theory of nonadiabatic electron transfer in a highly inverted region ($-\Delta G >> Sh\nu$), provided that the energies of accepting vibrations are much higher than k_BT; $h\nu >> k_BT$. If the thermally activated term $k'_{nr}(T)$ indeed corresponds to a direct conversion to the ground state by strong coupling at higher energies, then the overall nonradiative excited-state decay would be essentially equivalent to inverted electron transfer. This approach has been applied to the nonradiative decay of ^{3}MLCT(L) and $\sigma(Re–O)\pi^*(L)$ ^{3}SBLCT states, which was treated as an $L^{\cdot-} \rightarrow Re^{II}$ electron transfer (L = reducible quinone-type ligand) [92]. All the parameters needed to calculate k_{nr} using electron-transfer equations were obtained by Franck–Condon analysis of the emission spectra [92]. Calculated values are close to those determined directly by time-resolved emission and absorption measurements.

(k) Nitropolypyridine Re complexes $[Re(L)(CO)_3(phen\text{-}NO_2)]^n$ (L = Cl, im, 2,6-dimethylphenylisocyanide) are not emissive in fluid solutions and their excited states decay to the ground state exceptionally fast. This is caused by the presence of a ^{3}IL(phen-NO_2) excited state which is predominantly localized on the nitro group and lies between the ^{3}MLCT state and the ground state. This intervening nonemissive state was characterized by combining picosecond TRIR spectra and DFT calculations of $[Re(Cl)(CO)_3(5\text{-}NO_2\text{-phen})]$ [74]. TRIR spectroscopy has shown that the ^{3}MLCT $\rightarrow$ ^{3}IL(phen-NO_2) conversion occurs with a lifetime of 10 ps, followed by a ~30 ps decay to the ground state. The same mechanism probably explains the lack of emission and exceptional photophysics and photochemistry of nitropolypyridine complexes of Cr^0, Mo^0, W^0, or Ru^{II}.

7 Photochemistry

Re carbonyl-diimine complexes show very rich photochemistry [1, 2, 3, 4, 18, 170] which is reviewed in Chap. 1 of this book. Herein, we will only briefly comment on photochemical Re-ligand bond splitting, sensitization of ligand-based photochemistry by CT excitation and on several novel aspects of intramolecular excited-state electron transfer.

7.1 Rhenium-Ligand Bond Splitting

Most of Re carbonyl-diimine complexes are stable toward ligand photodissociation when irradiated into their low-lying CT absorption bands in the near-UV spectral region. However, CO dissociation or photoinduced *fac*→*mer* isomerization occurs under UV irradiation (≤313 nm) [102, 103]. Complexes where ^{3}SBLCT is the lowest-lying excited state are prone to ultrafast homolysis of the bond between Re and the axial ligand, producing radicals. This is the case of $[Re(alkyl)(CO)_3(N,N)]$ and $[Re(M)(CO)_3(N,N)]$ complexes, where M represents metal-bonded ligands, for example $Re(CO)_5$, $Mn(CO)_5$, $SnPh_3$, etc. The mechanism, rate, and yield of photochemical Re–alkyl or Re–metal bond homolysis are strongly dependent on subtle structural variations in the diimine, the alkyl or M-bonded ligands and the solvent [1–3, 18, 73, 104–111]. For example, while $[Re(Me)(CO)_3(bpy)]$ is emissive and photostable, $[Re(Et)(CO)_3(bpy)]$ undergoes subpicosecond Re–Et bond homolysis with a quantum yield of unity because changing the alkyl ligand from Me to Et is enough to change the energy order of the ^{3}SBLCT and ^{3}MLCT states [73]. Re–L bond homolysis from ^{3}SBLC has been also investigated theoretically, using high-level quantum chemical calculations [112–114].

7.2 *Intramolecular Energy Transfer: Sensitization of Axial Ligand Isomerization*

Photochemical reactions (usually isomerizations) of the axial ligand L in $[Re(L)(CO)_3(N,N)]^n$ can be induced by near-UV (400 nm) CT excitation of the $Re(CO)_3(N,N)$ chromophoric unit, provided that L possesses a low-lying reactive triplet excited state, usually $^3\pi\pi^*$ or $^3n\pi^*$. For example, complexes where L is a derivative of styrylpyridine [14, 30, 31, 115–125] or phenylazopyridine [32, 116, 126] undergo *trans*→*cis* photoisomerization of a –CH=CH– or –N=N– bond, respectively.

These reactions follow the same mechanism [31], whereby the low-energy ^{1}CT and ^{1}IL excitations are followed by a femtosecond ISC to the ^{3}CT state that undergoes an internal conversion to a L-localized triplet state ^{3}IL(L), from which a parallel isomerization and a return to the ground state occur, Fig. 13. This mechanism has several remarkable aspects:

(a) Photochemistry of the organic ligand L is induced by excitation of the $Re(CO)_3(N,N)$ chromophore using irradiation wavelengths that are not absorbed by free L. Hence, we can talk about "intramolecular sensitization." The ^{1}CT state acts as an excitation energy gateway to the molecule.
(b) Because of large spin-orbit coupling of the Re atom, intersystem crossing to the triplet excited state manifold occurs on a femtosecond timescale [10, 31].

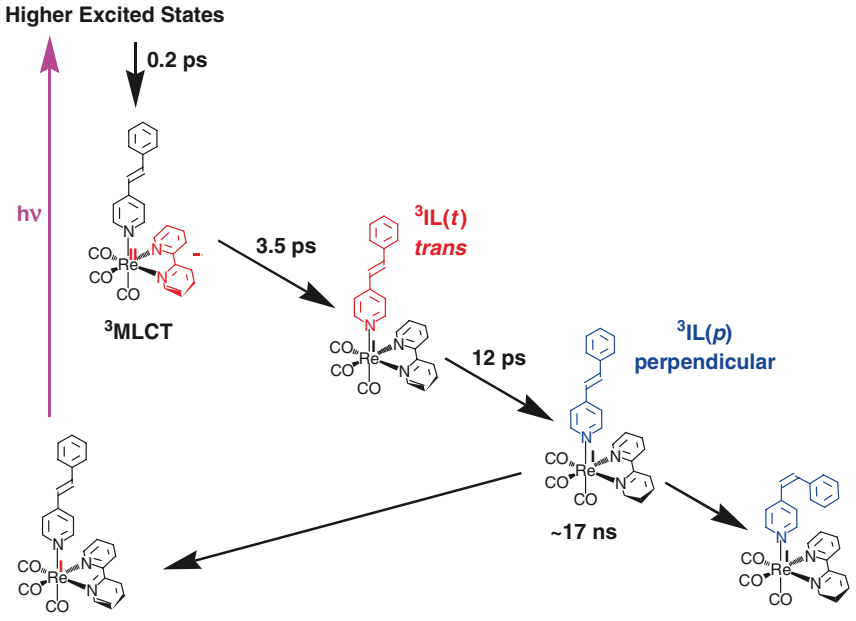

Fig. 13 Intramolecular sensitization of ligand isomerization in $[Re(t\text{-styrylpyridine})(CO)_3(bpy)]^+$ by energy transfer from the ^{3}MLCT state of the $Re(CO)_3(bpy)$ chromophore to the $^3IL(\pi\pi^*)$ state of *t*-styrylpyridine [31]. (For theoretical treatment see [14])

The photochemistry of Re-bound L occurs from a ligand-localized triplet excited state ($^3\pi\pi^*$ or $^3n\pi^*$). This contrasts the photochemistry of free species L, which react from the corresponding singlet states. Binding L to Re in $[Re(L)(CO)_3(N,N)]^+$ or $[Re(Cl)(CO)_3(L)_2]$ thus presents an excellent opportunity to generate the lowest triplet state of L in high yields and study its spectroscopic properties and reactivity. This is very difficult to accomplish for free L.

(c) The $^3CT \rightarrow {}^3IL(L)$ conversion can be regarded as a Dexter-type intramolecular energy transfer from the $^{3*}Re(CO)_3(N,N)$ unit to L. It can be formally described as a double-electron exchange, see Fig. 14 [31]. This is an ultrafast reaction whose time constant has been determined for [Re(*t*-styrylpyridine)$(CO)_3$(bpy)]$^+$ and [Re(*t*-phenylazopyridine)$(CO)_3$(bpy)]$^+$ as 3–4 ps [31, 32].

TRIR investigation of photochemical *trans*→*cis* isomerization of [Re(*t*-styrylpyridine)$(CO)_3$(bpy)]$^+$ has revealed that the $^3\pi\pi^*$ state of planar *t*-styrylpyridine first undergoes a half-rotation (by ~90°) around the –CH=CH– bond with a 12 ps time constant to form a perpendicular intermediate [31]. The reaction is then completed by further ~90° rotation, which is much slower, 17–28 ns [119, 127]. For [Re(*t*-phenylazopyridine)$(CO)_3$(bpy)]$^+$, the first half-rotation around the –N=N– bond takes less than 40 ps, similarly to the styrylpyridine complex. The second step, which completes the isomerization, is much faster, 100–120 ps [32].

Interestingly, the photoisomerizing styrylpyridine and 1,2-di(4-pyridyl)-ethylene (dpe) rhenium complexes behave as luminescence switches [123–125]. This phenomenon originates in the different nature of the lowest excited state of the *trans* and *cis* isomers, ^{3}IL(L) and ^{3}MLCT, respectively. Near-UV irradiation converts the nonemissive *trans* isomer to the *cis* form, which shows strong phosphorescence from its ^{3}MLCT state. Emission can be switched off by UV (254 nm) light that induces a reverse *cis*→*trans* isomerization.

Reversible photocyclization of diarylethene annealed to a bpy ligand in [Re(Cl)$(CO)_3$(bpy-diarylethene)] follows the same general mechanism as isomerizations (Fig. 13) [128]. Near-UV excitation into the Re→bpy ^{1}CT transition of the open form sensitizes cyclization of the diarylethene unit, which is accompanied by growth of an absorption band in the visible spectral region, between 500 and 600 nm. Energy transfer to the diarylethene unit and following cyclization occur with time

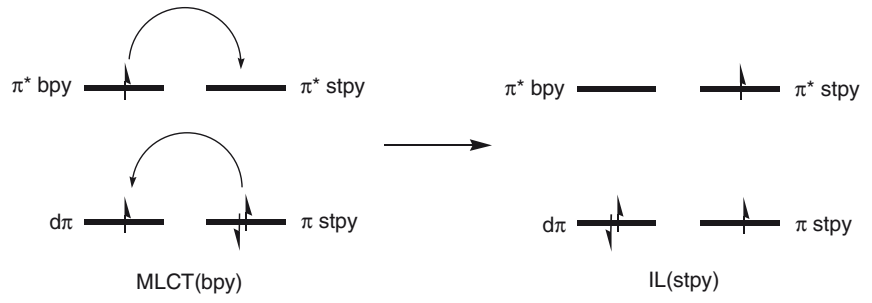

Fig. 14 Schematic orbital view of the ^{3}MLCT→^{3}IL energy transfer in [Re(*t*-styrylpyridine)$(CO)_3$(bpy)]$^+$ as a double electron transfer. Reproduced with permission from [31]

constants of 1.8 and 7 ns, respectively [128]. Reverse ring opening can be driven by visible light. This system thus behaves as a reversible photochromic switch.

Intramolecular energy transfer EnT from ^{3}MLCT states of $[Re(L)(CO)_3(N,N)]^+$ has been observed in assemblies containing a suitable energy acceptor that possesses a low-lying triplet excited state. For example, EnT has been studied in a series of $[Re(py\text{-}anthracene)(CO)_3(N,N)]^+$ complexes where N,N was varied. The (nanosecond) rate increases with the increasing energy difference between the ^{3}MLCT(N,N) donor and $^3\pi\pi^*$(anthracene) acceptor states, but only up to a limit where the inverted region is reached [129]. This study has indicated that the reorganization energy λ connected with energy transfer (~0.15 eV) is much smaller than that of electron transfer reactions of Re complexes. Hence, the maximal rate (at $-\Delta G = \lambda$) of EnT occurs at much smaller driving force values than for electron transfer. Competition between $bpy^{\cdot-} \rightarrow MQ^+$ ET and $^*Re(CO)_3(bpy) \rightarrow$anthracene EnT has been studied in $[Re(MQ^+)(CO)_3(bpy\text{-}CH_2\text{–}O\text{–}CH_2\text{–}anthracene)]^{2+}$ [130]. Energy transfer from Re- to Ru-based ^{3}MLCT states was observed in di- and oligonuclear complexes containing a $(N,N)(CO)_3Re^I(\mu\text{–}CN)Ru^{II}(N,N)_2$-motif [131, 132]. A 10 ps EnT time constant has been determined [132] for $[(phen)(CO)_3Re(\mu\text{–}CN)Ru(bpy)_2(CN)]^+$. Energy transfer from the Re-based MLCT states in $[Re(py\text{-}CpM^{II}(arene))(CO)_3(N,N)]^{2+}$ (M = Ru, Fe; N,N = bpy derivatives) occurs to reactive ^{3}dd states of the CpM(arene) unit, leading to its dissociation [133].

7.3 Electron Transfer

Electronic excitation makes $[Re(L)(CO)_3(bpy)]^n$ and $[Re(L)(CO)_3(phen)]^n$ strong excited-state oxidants and slightly weaker, but still good, reductants. Bimolecular photochemical redox reactions of Re complexes had already been described in the 1970s [21, 134]. The great potential of Re chromophores for intramolecular electron transfer has been utilized by Meyer to develop the, so called, chromophore-quencher complexes, where a redox-active group is attached to the ligand L, usually through a pyridine unit. Two types of intramolecular ET mechanisms are possible, depending on whether the remote group is a reductant or oxidant, Fig. 15a,b. Another kind of excited-state ET reaction occurs in complexes where the reducing group is attached to the N,N ligand, namely bpy [135–138], Fig. 15c.

Molecular systems where a $Re(CO)_3(N,N)$ chromophore acts as a photoreductant (Fig. 15a) are represented by $[Re(MQ^+)(CO)_3(dmb)]^{2+}$, where MQ^+ is a *N*-methyl-4,4′-bipyridinium cation, which can be viewed as a "half-methylviologen." It is a strong oxidant that undergoes significant internal reorganization (planarization, formation of a quinoidal structure) upon oxidation. The ^{3}MLCT(dmb) state $^*[Re^{II}(MQ^+)(CO)_3(dmb^{\cdot-})]^{2+}$ undergoes a $dmb^{\cdot-} \rightarrow MQ^+$ interligand electron transfer (ILET), producing the ^{3}MLCT(MQ^+) state $^*[Re^{II}(MQ^{\cdot})(CO)_3(dmb)]^{2+}$ [79, 115, 139–142]. This reaction occurs on two timescales: <1 ps (~60%) and 8–17 ps (~40%), the latter value depending on the solvent [79, 142]. The subpicosecond kinetic component corresponds either to ILET from the ^{1}MLCT(dmb) state or to optical transition to ^{1}MLCT(MQ^+) followed by ISC. Analysis of the kinetics in

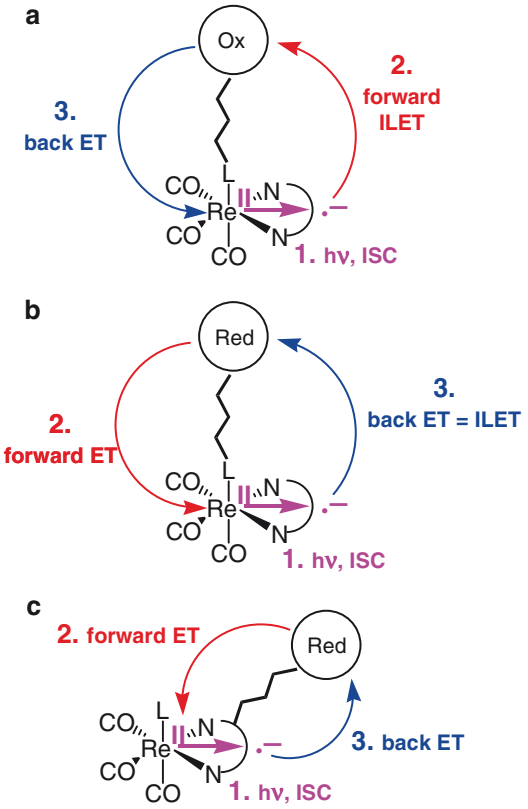

Fig. 15 Photoinduced electron transfer in Re-based dyads (chromophore-quencher complexes)

terms of Marcus theory has shown that ILET is strongly accelerated by the initial vibrational excitation of the precursor state ^{3}MLCT(dmb). ILET takes place in the same time domain as the intermediate kinetic component of the excited-state relaxation, see Sect. 5. Indeed, TRIR spectra recorded in the course of ILET show spectral shifts due to relaxation, which occur concomitantly with the conversion of *[Re^{II}(MQ$^+$)(CO)$_3$(dmb$^{\cdot-}$)]$^{2+}$ to the ILET product *[Re^{II}(MQ$^{\cdot}$)(CO)$_3$(dmb)]$^{2+}$. The latter species is weakly emissive. It decays back to the ground state by a MQ$^{\bullet}$→Re^{II} ET, which is strongly inverted and seems to occur through higher vibrational levels of the product, i.e., the electronic ground state [Re^{I}(MQ$^{\cdot+}$)(CO)$_3$(dmb)]$^{2+}$ [143]. An interesting case is presented by a bi-functional Medpe$^+$ ligand (*trans*-py–CH=CH–methylpyridinium) that can act either as an electron acceptor (like MQ$^+$) or an energy acceptor (like styrylpyridine, see Sect. 7.2). Depending on which function prevails, [Re(Medpe$^+$)(CO)$_3$(bpy)]$^{2+}$ may, in principle, undergo either ILET or *trans*→*cis* isomerization, respectively. Only ~10 ps energy transfer followed by ~21 ps half-rotation (isomerization) has been observed in CH_2Cl_2 or MeCN solutions, showing that the ππ* ^{3}IL(Medpe$^+$) state lies below ^{3}MLCT(Medpe$^+$) [30, 115]. The situation is different in [Re(Cl)(CO)$_3$(Medpe$^+$)$_2$]$^{2+}$, where optical excitation populates

the ^{3}MLCT(Medpe$^+$) state that decays nonradiatively to the ground state with lifetimes of 40 and 430 ps [30, 115].

Irradiation of [Re(Cl)(CO)$_3$(4,4′-(COOH)$_2$-bpy)] adsorbed at nanocrystalline TiO$_2$ results in ultrafast, <100 fs, electron injection from the excited Re complex into TiO$_2$ [42, 144, 145]. At longer times, the IR spectrum of [Re(Cl)(CO)$_3$(4,4′-(COOH)$_2$-bpy)]/TiO$_2$ films in dry aprotic solvents (DMF) consists of signals due to injected electrons, oxidized Re complex, and a relaxed ^{3}MLLCT state [42]. This result shows that the electron injection occurs predominantly from the optically populated ^{1}MLLCT state, in competition with the expected [10] ~100 fs ISC. The energy of the relaxed ^{3}MLLCT state is comparable with the TiO$_2$ band-edge. Hence, there is no sufficient driving force for electron injection from the relaxed triplet state. Picosecond electron injection from ^{3}MLLCT has been observed when the TiO$_2$ band edge is lowered by variations of the solvent, water content, and pH [144].

There are a great many systems where the Re chromophore acts as a photooxidant (Fig. 15b), the axial ligand bearing a reducing group (Red), usually PTZ. The excited-state ET proper, that is PTZ→Re^{II}, is rather fast: A two-phase kinetics have been observed [146] for [Re(py-CH$_2$–PTZ)(CO)$_3$(bpy)]$^+$, consisting of a prompt (<30 ps) and 200 ps steps, both of which form an LLCT state [Re(py-CH$_2$–PTZ$^{\cdot+}$)(CO)$_3$(bpy$^{\cdot-}$)]$^+$. The bpy$^{\cdot-}$→PTZ$^+$ back reaction (ILET) is much slower (~25 ns), occurring in the Marcus inverted region. Detailed studies of the back reaction kinetics led to a deep understanding of structural and medium effects on inverted ET [34, 91, 98, 146–148]. Interestingly, the LLCT state in chromophore-quencher complexes can be prepared also optically, albeit with a very low efficiency. Absorption spectra of the complexes [Re(py-CH$_2$–PTZ)(CO)$_3$(N,N)]$^+$ (N,N = 4,4′-disubstituted bpy derivatives, 2,2′-bipyrazine, and Me$_4$-phen) show a very weak ($\varepsilon \sim 2\ M^{-1}\ cm^{-1}$) shoulder at 600–400 nm that corresponds to a direct PTZ→N,N charge transfer transition [34]. Analysis of its shape based on the Marcus–Hush theory has afforded values of the electronic coupling between the ground and LLCT states, which were then used to estimate the rates of the bpy$^{\cdot-}$→PTZ$^+$ back electron transfer (ILET). A reasonable agreement with directly measured rates was achieved [34]. (It should be noted that the back ET occurs from a ^{3}LLCT state while the coupling energies were obtained from transitions to a ^{1}LLCT state.)

"Chromophore-quencher" complexes (Fig. 15) belong to the broad family of ET dyads, in which an oxidizing and reducing site are covalently linked. Re-based triads with a reducing group (e.g., –NR$_2$) attached to the N,N ligand and an oxidizing group at the axial position have also been prepared [149, 150]. Excitation of the Re center leads to a double ET, whereby a long-lived (units of μs) charge-separated excited state can be produced:

$$[(\mathrm{Ox}-\mathrm{L})\mathrm{Re}^{\mathrm{I}}(\mathrm{CO})_3(\mathrm{N,N}-\mathrm{Red})] \xrightarrow{h\nu} {}^{3*}[(\mathrm{Ox}-\mathrm{L})\mathrm{Re}^{\mathrm{II}}(\mathrm{CO})_3(\mathrm{N,N}^{\cdot-}-\mathrm{Red})] \rightarrow [(\mathrm{Ox}^{\cdot-}-\mathrm{L})\mathrm{Re}^{\mathrm{I}}(\mathrm{CO})_3(\mathrm{N,N}-\mathrm{Red}^{\cdot+})].$$

Another type of chromophore-quencher complex, developed by Schanze [151–154], contains an axial ligand L, which undergoes irreversible intraligand bond

splitting upon oxidation. [Re(py-α-aminoalcohol)$(CO)_3$(bpy)]$^+$ is a typical example. Photochemical splitting of the –CH(OH)Ph group from [Re(py-CH_2–NH–CH(Ph)–CH(OH)Ph)$(CO)_3$(bpy)]$^+$ proves the occurrence of an ET from the aminoalcohol group to the Re^{II} atom in the ^{3}MLCT state. Its kinetic studies provided information on the mechanism and rates of oxidative C–C bond splitting, which is kinetically competitive with the back electron transfer from $bpy^{\cdot-}$ to the oxidized aminoalcohol$^{\cdot+}$. The same photochemistry has been observed [1, 152–155] for a range of redox-active axial ligands.

An interesting type of chromophore-quencher complexes (or, in other words, ET dyads) is presented by [Re(py-azacrown)$(CO)_3$(bpy)]$^+$ complexes, where the azacrown unit is linked to the pyridine ligand by various linkers based on amide, –CH=CH– or –C≡C– bond [27, 77, 156, 157]. ET in the ^{3}MLCT(bpy) excited state [Re^{II}(py-azacrown)$(CO)_3$($bpy^{\cdot-}$)]$^+$ occurs from the nitrogen lone pair of the azacrown to Re^{II}, producing a LLCT state [Re^{I}(py-azacrown$^{\cdot+}$)$(CO)_3$($bpy^{\cdot-}$)]$^+$. A time constant of 500 ps has been determined [156] for a complex with a –NH–C(O)–phlink between py and the azacrown nitrogen atom in MeCN. The $bpy^{\cdot-}$→azacrown$^{\cdot+}$ back ET can be viewed as an ILET reaction. It is a strongly inverted process, which occurs with a time constant of 19 ns [156]. The forward ET from the excited state can be switched off by protonation of the azacrown nitrogen atom or by complexation with metal cations, making these complexes optical cation sensors [157]. This aspect is discussed in Chap. 1 of this book. Photophysics of these complexes are, in fact, more complicated due to the presence of optically populated intraligand CT states (ILCT), whereby the electron is excited from the azacrown to the pyridine moiety. Nevertheless, the ^{3}ILCT state appears to lie above both the ^{3}MLCT and ^{3}LLCT states. Similar behavior has been observed for [Re(py-catecholate)$(CO)_3$(bpy)]$^+$ complexes, which act as molybdenum sensors [158].

The redox-active aminoacid tryptophan (trp) linked to a $Re(CO)_3$(N,N) unit in [Re(py-trp)$(CO)_3$(N,N)]$^+$ (N,N = bpy, phen) is oxidized upon MLCT excitation, Fig. 16. The trp→Re^{II} ET occurs with a time constant of 33 ns for N,N = bpy, in MeCN solution [159, 160]. The charge-separated intermediate [Re(py-trp$^{\cdot+}$)$(CO)_3$(N,$N^{\cdot-}$)]$^+$ has been characterized by TRIR, showing down-shifted ν(CO) IR

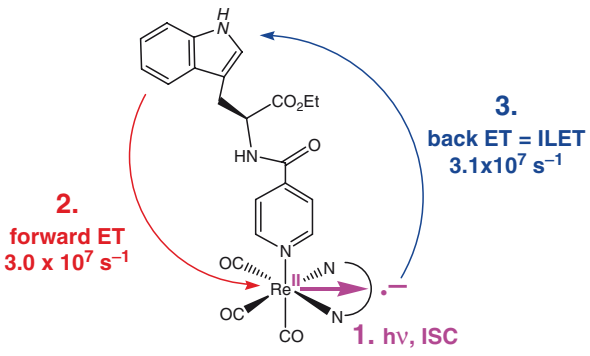

Fig. 16 Photoinduced electron transfer in [Re(py-trp)$(CO)_3$(N,N)]$^+$ [159, 160]. The rate constant values are for N,N = bpy in MeCN. The same mechanism operates in complexes where trp is attached to the 3-position of the pyridine ligand or to imidazole

bands. However, it cannot be accumulated in high yields since the $bpy^{\cdot-} \rightarrow trp^{\cdot+}$ back ET (ILET) is surprisingly fast, occurring with a comparable time constant of 32 ns. The trp→Re^{II} ET is responsible for the dramatic acceleration of a long-range ET in a Re-derivatized protein azurin [43]. Here, the $Re(CO)_3(Me_2\text{-phen})$ chromophore is attached to the peptide backbone through an imidazole side group of histidine at the 124 position of the *Pseudomonas aeruginosa* azurin, Fig. 17. The indole group of a nearby (122) tryptophan lies nearly parallel to the phen ligand at a distance of ~3.8 Å, which permits electronic interaction. Optical excitation of the Re(His-124)$(CO)_3(Me_2\text{-phen})$ chromophore to the MLCT state Re^{II}(His-124)$(CO)_3(Me_2\text{-phen}^{\cdot-})$ is followed by a trp(122)→Re^{II} ET. The kinetics are multiphasic, with time constants ranging from femtoseconds to nanoseconds. The reaction mechanism is shown in Fig. 17. The subpicosecond step probably involves ET from ^{1}MLCT while the ps ET occurs concomitantly with vibrational cooling of ^{3}MLCT, see Sect. 5. The relaxed ^{3}MLCT state is in a fast equilibrium with the charge-separated state Re^{I}(His-124)$(CO)_3(Me_2\text{-phen}^{\cdot-})\cdots(trp^{\cdot+}$ 122), followed by a nanosecond ET from a distant Cu^I center to ($trp^{\cdot+}$ 122). Photooxidation of Cu^I by the excited Re chromophore over 19.4 Å is accomplished in a few tens of nanoseconds. The same reaction occurs even in the absence of the nearby trp122 unit, but at least 100-times slower. The large acceleration seen in the presence of trp122 originates in splitting the long range $Cu^I \rightarrow {}^*Re^{II}$ ET into two "electron hopping" steps: $trp^{\cdot+} \rightarrow {}^*Re^{II}$ and Cu^I

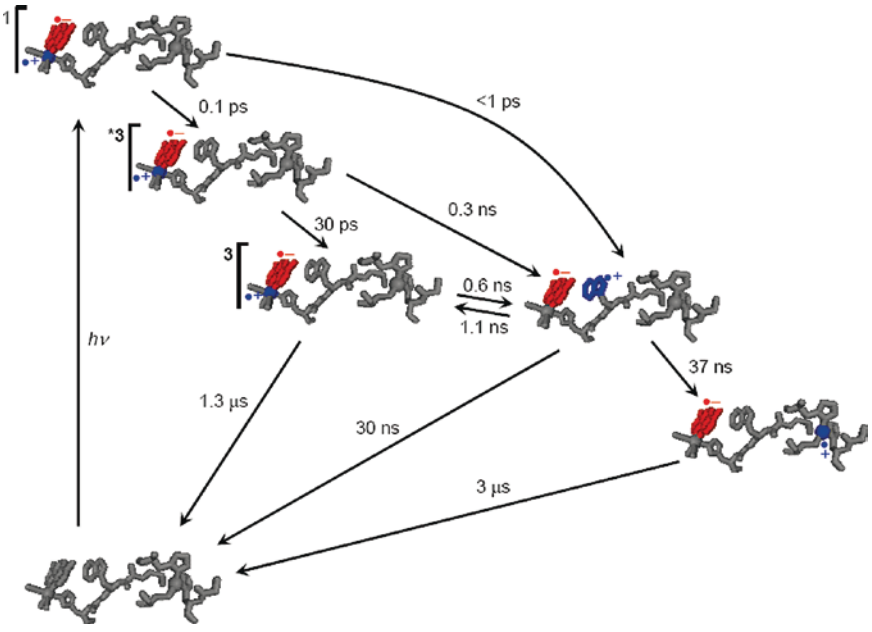

Fig. 17 Photoinduced electron transfer in Re-derivatized *Pseudomonas aeruginosa* azurin (Az) by hopping through a proximal tryptophan: $Re^{I}(CO)_3(Me_2\text{-phen})$(H124)|(W122)|AzCu^I. Only the part of the protein structure that bears the Re chromophore (*at the left end of the chain*) is shown. The trp indole group is nearly parallel with the phen ligand, sticking up from the chain. The Cu^I center is on the *right*. Reprinted with permission from [43]

$\rightarrow$ trp$^{\cdot+}$. However, there is a price to pay for the ET acceleration in lowering the reaction yield by the phen$^{\cdot-}\rightarrow$ trp$^{\cdot+}$ back ET in the hopping intermediate.

Tyrosine (tyr) is harder to reduce by excited Re chromophores than tryptophan. [Re(py-tyr)(CO)$_3$(bpy)]$^+$ does not undergo photoinduced ET in MeCN, unless the tyr –OH group is deprotonated by addition of Bu_4NOH [159, 160]. No tyr$\rightarrow$*Re^{II} ET occurs in an azurin where tyr is placed at the 122 position instead of trp. Linking tyr to bpy in a strong excited-state oxidant [Re(CN)(CO)$_3$(bpy)] does not help either: no tyr photooxidation has been seen in [Re(CN)(CO)$_3$(bpy-tyr)] without deprotonation [138]. However, fluotyrosine in [Re(CN)(CO)$_3$(bpy-F*n*tyr)] can be oxidized at all pHs [137], following the general mechanism shown in Fig. 15c. This photoreaction has been employed to generate tyrosine radicals in ribonucleotide reductase [161]. Tyrosine itself is photooxidized at all pHs when appended to a PPh_3 ligand in [Re(PPh_2Ph-tyr)(CO)$_3$(bpy)]$^+$. This is made possible by the high excited-state oxidation potential of the [Re(PPh_3)(CO)$_3$(bpy)]$^+$ chromophore [138].

Note added in proofs: Several important papers appeared during the production of this chapter, which ought to be mentioned: (i) quantum yields of Re^{I} complexes with styrylpyridine-type ligands have been determined as a function of excitation wavelength, obtaining more mechanistic information, and developing these compounds as rigidity sensors [162], (ii) a comprehensive study of Re^{I} carbonyl complexes with dppz derivatives have revealed that their photobehavior is determined by an interplay between three different excited states, *viz*. dppz-localized $\pi\pi^*$ and CT to the phenanthroline and phenazine parts of the dppz ligand; contributing to our understanding of the "light switch effect" [163], (iii) Re$^{I}\rightarrow$Ru^{II} photoinduced energy transfer in assemblies where the two photoactive units are linked by a flexible chain was found to follow complex kinetics with lifetimes of 20 ps, 1 ns and 13 ns, attributed to different conformations and excited states [164], (iv) assemblies where three Re^{I} carbonyl-diimine chromophores are attached to a central Fe(acac)$_3$ unit (acac = acetylacetonate derivatives) were synthesized. It was found that the Re^{I} ^{3}MLCT state is rapidly (450 ps, 755 ps, 2.5 ns, depending on the diimine) quenched by Förster energy transfer to LF states of high-spin Fe^{III} [165].

Acknowledgments The scientific contributions of all coworkers and collaborators involved in our research on rhenium photophysics and photochemistry is much appreciated: Ana Maria Blanco Rodríguez, Michael Busby, Anders Gabrielsson, Davina Liard, Ian Farrel (QMUL), Pavel Matousek and Mike Towrie (Rutherford Appleton Lab), Franti Hartl (Univ. Reading, UK and Univ. Amsterdam), the late Derk J. Stufkens (Univ. Amsterdam), Chantal Daniel (CNRS Strasbourg), Stanislav Záliš, Martin Hof and Jan Sýkora (J. Heyrovský Institute of Physical Chemistry, Prague), Majed Chergui and Andrea Cannizzo (EPFL, Switzerland), Harry B. Gray, Jay R. Winkler, Crystal Shih and Anna Katrine Museth (California Institute of Technology). Funding was provided by EPSRC, QMUL, STFC (CMSD43), European collaboration program COST D35, ESF-DYNA, and the Ministry of Education of the Czech Republic (1P05OC068).

References

1. Stufkens DJ, Vlček A Jr (1998) *Coord Chem Rev* 177:127
2. Stufkens DJ, Aarnts MP, Nijhoff J, Rossenaar BD, Vlček A Jr (1998) *Coord Chem Rev* 171:93
3. Stufkens DJ, Aarnts MP, Rossenaar BD, Vlček A Jr (1997) *Pure Appl Chem* 69:831
4. Stufkens DJ (1992) *Comments Inorg Chem* 13:359

5. Vlček A Jr (2001) In: Balzani V, Astruc D (eds) Electron transfer in chemistry, vol 2. Wiley, Weinheim, p 804
6. Stor GJ, Hartl F, van Outersterp JWM, Stufkens DJ (1995) *Organometallics* 14:1115
7. Klein A, Vogler C, Kaim W (1996) *Organometallics* 15:236
8. Paolucci F, Marcaccio M, Paradisi C, Roffia S, Bignozzi CA, Amatore C (1998) *J Phys Chem B* 102:4759
9. Juris A, Campagna S, Bidd I, Lehn J-M, Ziessel R (1988) *Inorg Chem* 27:4007
10. Cannizzo A, Blanco-Rodríguez AM, Nahhas A, Šebera J, Záliš S, Vlček A Jr, Chergui M (2008) *J Am Chem Soc* 130:8967
11. Vlček A Jr, Záliš S (2007) *Coord Chem Rev* 251:258
12. Blanco-Rodríguez AM, Gabrielsson A, Motevalli M, Matousek P, Towrie M, Šebera J, Záliš S, Vlček A Jr (2005) *J Phys Chem A* 109:5016
13. Gabrielsson A, Busby M, Matousek P, Towrie M, Hevia E, Cuesta L, Perez J, Záliš S, Vlček A Jr (2006) *Inorg Chem* 45:9789
14. Bossert J, Daniel C (2006) *Chem Eur J* 12:4835
15. Rossenaar BD, Stufkens DJ, Vlček A Jr (1996) *Inorg Chem* 35:2902
16. Villegas JM, Stoyanov SR, Huang W, Rillema DP (2005) *Inorg Chem* 44:2297
17. Villegas JM, Stoyanov SR, Huang W, Rillema DP (2005) Dalton:1042
18. Stufkens DJ, Vlček A Jr (1996) *Spectrum* 9:2
19. Stufkens DJ (1990) *Coord Chem Rev* 104:39
20. Lees AJ (1987) *Chem Rev* 87:711
21. Kalyanasundaram K (1986) *J Chem Soc Faraday Trans 2* 82:2401
22. Hino JK, Della Ciana L, Dressick WJ, Sullivan BP (1992) *Inorg Chem* 31:1072
23. van Slageren J, Klein A, Záliš S, Stufkens DJ (2001) *Coord Chem Rev* 219-221:937
24. Stor GJ, Stufkens DJ, Oskam A (1992) *Inorg Chem* 31:1318
25. Smothers WK, Wrighton MS (1983) *J Am Chem Soc* 105:1067
26. Lewis JD, Perutz RN, Moore JN (2004) *J Phys Chem A* 108:9037
27. Lewis JD, Clark IP, Moore JN (2007) *J Phys Chem A* 111:50
28. Flood A, Girling RB, Gordon KC, Hester RE, Moore JN, Polson MIJ (2002) *J Raman Spectrosc* 33:434
29. Walsh PJ, Gordon KC, Lundin NJ, Blackman AG (2005) *J Phys Chem A* 109:5933
30. Busby M, Hartl F, Matousek P, Towrie M, Vlček A Jr (2008) *Chem Eur J* 14:6912
31. Busby M, Matousek P, Towrie M, Vlček A Jr (2005) *J Phys Chem A* 109:3000
32. Busby M, Matousek P, Towrie M, Vlček A Jr (2007) *Inorg Chim Acta* 360:885
33. Vlček A Jr, Záliš S (2005) *J Phys Chem A* 109:2991
34. Katz NE, Mecklenburg SL, Graff DK, Chen P, Meyer TJ (1994) *J Phys Chem* 98:8959
35. Salassa L, Garino C, Albertino A, Volpi G, Nervi C, Gobetto R, Kenneth I Hardcastle KI (2008) *Organometallics* 27:1427–1435
36. Garino C, Ruiu T, Salassa L, Albertino A, Volpi G, Nervi C, Gobetto R, Hardcastle KI (2008) Eur Inorg Chem:3587
37. Liard DJ, Busby M, Matousek P, Towrie M, Vlček A Jr (2004) *J Phys Chem A* 108:2363
38. Turro NJ (1978) Modern molecular photochemistry. Benjamin, Menlo Park
39. Cannizzo A, van Mourik F, Gawelda W, Zgrablic G, Bressler C, Chergui M (2006) *Angew Chem Int Ed* 45:3174
40. Bhasikuttan AC, Okada T (2004) *J Phys Chem B* 108:12629
41. Gawelda W, Cannizzo A, Pham V-T, van Mourik F, Bressler C, Chergui M (2007) *J Am Chem Soc* 129:8199
42. Wang Y, Asbury JB, Lian T (2000) *J Phys Chem A* 104:4291
43. Shih C, Museth AK, Abrahamsson M, Blanco-Rodriguez AM, Di Bilio AJ, Sudhamsu J, Crane BR, Ronayne KL, Towrie M, Vlček A Jr, Richards JH, Winkler JR, Gray HB (2008) *Science* 320:1760
44. Wrighton MS, Morse DL (1974) *J Am Chem Soc* 96:998
45. Geoffroy GL, Wrighton MS (1979) Organometallic photochemistry. Academic, New York
46. Striplin DR, Crosby GA (2001) *Coord Chem Rev* 211:163

47. Schoonover JR, Strouse GF, Dyer RB, Bates WD, Chen P, Meyer TJ (1996) *Inorg Chem* 35:273
48. Dyer J, Blau WJ, Coates CG, Creely CM, Gavey JD, George MW, Grills DC, Hudson S, Kelly JM, Matousek P, McGarvey JJ, McMaster J, Parker AW, Towrie M, Weinstein JA (2003) *Photochem Photobiol Sci* 2:542
49. Giordano PJ, Wrighton MS (1979) *J Am Chem Soc* 101:2888
50. Wallace L, Rillema DP (1993) *Inorg Chem* 32:3836
51. Giordano PJ, Fredericks SM, Wrighton MS, Morse DL (1978) *J Am Chem Soc* 100:2257
52. Fredericks SM, Luong JC, Wrighton MS (1979) *J Am Chem Soc* 101:7415
53. Luong JC, Faltynek RA, Wrighton MS (1980) *J Am Chem Soc* 102:7892
54. Yersin H, Finkenzeller WJ (2008) In: Yersin H (ed) Highly efficient OLEDs with phosphorescent materials. Wiley, Weinheim, p 1
55. Striplin DR, Crosby GA (1994) *Chem Phys Lett* 221:426
56. Záliš S, Ben Amor N, Daniel C (2004) *Inorg Chem* 43:7978
57. Turki M, Daniel C, Záliš S, Vlček A Jr, van Slageren J, Stufkens DJ (2001) *J Am Chem Soc* 123:11431
58. Gamelin DR, George MW, Glyn P, Grevels F-W, Johnson FPA, Klotzbücher W, Morrison SL, Russell G, Schaffner K, Turner JJ (1994) *Inorg Chem* 33:3246
59. Bredenbeck J, Helbing J, Hamm P (2004) *J Am Chem Soc* 126:990
60. Dattelbaum DM, Omberg KM, Schoonover JR, Martin RL, Meyer TJ (2002) *Inorg Chem* 41:6071
61. Dattelbaum DM, Omberg KM, Hay PJ, Gebhart NL, Martin RL, Schoonover JR, Meyer TJ (2004) *J Phys Chem A* 108:3527
62. Glyn P, George MW, Hodges PM, Turner JJ (1989) J Chem Soc Chem Commun:1655
63. Dattelbaum DM, Martin RL, Schoonover JR, Meyer TJ (2004) *J Phys Chem A* 108:3518
64. Cotton FA, Kraihanzel CS (1962) *J Am Chem Soc* 84:4432
65. Kraihanzel CS, Cotton FA (1963) *Inorg Chem* 2:533
66. Cotton FA (1964) *Inorg Chem* 3:702
67. Braterman PS (1975) Metal carbonyl spectra. Academic, London
68. George MW, Johnson FPA, Westwell JR, Hodges PM, Turner JJ (1993) J Chem Soc Dalton Trans:2977
69. George MW, Turner JJ (1998) *Coord Chem Rev* 177:201
70. Clark IP, George MW, Johnson FPA, Turner JJ (1996) Chem Commun:1587
71. Busby M, Gabrielsson A, Matousek P, Towrie M, Di Bilio AJ, Gray HB, Vlček A Jr (2004) *Inorg Chem* 43:4994
72. Busby M, Matousek P, Towrie M, Clark IP, Motevalli M, Hartl F, Vlček A Jr (2004) *Inorg Chem* 43:4523
73. Gabrielsson A, Blanco-Rodríguez AM, Matousek P, Towrie M, Vlček A Jr (2006) *Organometallics* 25:2148
74. Gabrielsson A, Matousek P, Towrie M, Hartl F, Záliš S, Vlček A Jr (2005) *J Phys Chem A* 109:6147
75. Blanco-Rodríguez AM, Busby M, Grădinaru C, Crane BR, Di Bilio AJ, Matousek P, Towrie M, Leigh BS, Richards JH, Vlček A Jr, Gray HB (2006) *J Am Chem Soc* 128:4365
76. Blanco-Rodríguez AM, Ronayne KL, Záliš S, Sýkora J, Hof M, Vlček A Jr (2008) *J Phys Chem A* 112:3506
77. Lewis JD, Towrie M, Moore JN (2008) *J Phys Chem A* 112:3852
78. Vlček A Jr, Farrell IR, Liard DJ, Matousek P, Towrie M, Parker AW, Grills DC, George MW (2002) J Chem Soc Dalton Trans:701
79. Liard DJ, Busby M, Farrell IR, Matousek P, Towrie M, Vlček A Jr (2004) *J Phys Chem A* 108:556
80. Rossenaar BD, George MW, Johnson FPA, Stufkens DJ, Turner JJ, Vlček A Jr (1995) *J Am Chem Soc* 117:11582
81. Caspar JV, Westmoreland TD, Allen GH, Bradley PG, Meyer TJ, Woodruff WH (1984) *J Am Chem Soc* 106:3492

82. Schoonover JR, Bates WD, Meyer TJ (1995) *Inorg Chem* 34:6421
83. Kotch TG, Lees AJ, Fuerniss SJ, Papathomas KI, Snyder RW (1993) *Inorg Chem* 32:2570
84. Lees AJ (1998) *Coord Chem Rev* 177:3
85. Horng ML, Gardecki JA, Papazyan A, Maroncelli M (1995) *J Phys Chem* 99:17311
86. Blanco-Rodríguez AM, Towrie M, Collin J-P, Záliš S, Vlček A Jr (2009) Dalton Trans in press
87. Asbury JB, Wang Y, Lian T (2002) *Bull Chem Soc Jpn* 75:973
88. Lenchenkov VA, She C, Lian T (2004) *J Phys Chem B* 108:16194
89. Asher SA, Murtaugh J (1983) *J Am Chem Soc* 105:7244
90. Kang YK, Duncan TV, Therien MJ (2007) *J Phys Chem B* 111:6829
91. Chen P, Meyer TJ (1998) *Chem Rev* 98:1439
92. Claude JP, Omberg KM, Williams DS, Meyer TJ (2002) *J Phys Chem A* 106:7795
93. Allen GH, White RP, Rillema DP, Meyer TJ (1984) *J Am Chem Soc* 106:2613
94. Caspar JV, Meyer TJ (1983) *Inorg Chem* 22:2444
95. Caspar JV, Meyer TJ (1983) *J Am Chem Soc* 105:5583
96. Worl LA, Duesing R, Chen P, Della Ciana L, Meyer TJ (1991) J Chem Soc Dalton Trans:849
97. Baiano JA, Kessler RJ, Lumpkin RS, Munley MJ, Murphy WR Jr (1995) *J Phys Chem* 99:17680
98. Chen P, Duesing R, Graff DK, Meyer TJ (1991) *J Phys Chem* 95:5850
99. Englman R, Jortner J (1970) *Mol Phys* 18:145
100. Kober EM, Caspar JV, Lumpkin RS, Meyer TJ (1986) *J Phys Chem* 90:3722
101. Caspar JV, Meyer TJ (1983) *J Phys Chem* 87:952
102. Sato S, Sekine A, Ohashi Y, Ishitani O, Blanco-Rodríguez AM, Vlček A Jr, Unno T, Koike K (2007) *Inorg Chem* 46:3531
103. Sato S, Morimoto T, Ishitani O (2007) *Inorg Chem* 46:9051
104. Rossenaar BD, Kleverlaan CJ, van de Ven MCE, Stufkens DJ, Vlček A Jr (1996) *Chem Eur J* 2:228
105. Rossenaar BD, Lindsay E, Stufkens DJ, Vlček A Jr (1996) *Inorg Chim Acta* 250:5
106. Kleverlaan CJ, Martino DM, van Willigen H, Stufkens DJ, Oskam A (1996) *J Phys Chem* 100:18607
107. Aarnts MP, Wilms MP, Stufkens DJ, Baerends EJ, Vlček A Jr (1997) *Organometallics* 16:2055
108. Kleverlaan CJ, Stufkens DJ, Clark IP, George MW, Turner JJ, Martino DM, van Willigen H, Vlček A Jr (1998) *J Am Chem Soc* 120:10871
109. Kleverlaan CJ, Martino DM, van Slageren J, van Willigen H, Stufkens DJ, Oskam A (1998) *Appl Magn Reson* 15:203
110. Kleverlaan CJ, Stufkens DJ (1999) *Inorg Chim Acta* 284:61
111. Farrell IR, Matousek P, Kleverlaan CJ, Vlček A Jr (2000) *Chem Eur J* 6:1386
112. Daniel C (2002) *Coord Chem Rev* 230:65
113. Bruand-Cote I, Daniel C (2002) *Chem Eur J* 8:1361
114. Guillaumont D, Daniel C (1999) *J Am Chem Soc* 121:11733
115. Vlček A Jr, Busby M (2006) *Coord Chem Rev* 250:1755–1762
116. Yam VW-W, Lau VC-Y, Wu L-X (1998) J Chem Soc Dalton Trans:1461
117. Wrighton MS, Morse DL, Pdungsap L (1975) *J Am Chem Soc* 97:2073
118. Sun S-S, Robson E, Dunwoody N, Silva AS, Brinn IM, Lees AJ (2000) Chem Commun:201
119. Dattelbaum DM, Itokazu MK, Iha NYM, Meyer TJ (2003) *J Phys Chem A* 107:4092
120. Lewis JD, Perutz RN, Moore JN (2000) Chem Commun:1865
121. Sun S-S, Lees AJ (2002) *Organometallics* 21:39
122. Itokazu MK, Polo AS, de Faria DLA, Bignozzi CA, Iha NYM (2001) *Inorg Chim Acta* 313:149
123. Wenger OS, Henling LM, Day MW, Winkler JR, Gray HB (2004) *Inorg Chem* 43:2043
124. Yam VW-W, Yang Y, Zhang J, Chu BW-K, Zhu N (2001) *Organometallics* 20:4911

125. Sarto Polo AS, Itokazu MK, Frin KM, de Toledo Patrocinio AO, Iha NYM (2006) *Coord Chem Rev* 250:1669–1680
126. Sun S-S, Lees AJ (2000) *J Am Chem Soc* 122:8956
127. Blanco-Rodríguez AM, Towrie M, Vlček A Jr (2009) Dalton Trans. in press
128. Ko C-C, Kwok W-M, Yam VW-W, Phillips DL (2006) *Chem Eur J* 12:5840
129. MacQueen DB, Eyler JR, Schanze KS (1992) *J Am Chem Soc* 114:1897
130. Mecklenburg SL, Opperman KA, Chen P, Meyer TJ (1996) *J Phys Chem* 100:15145
131. Kalyanasundaram K, Grätzel M, Nazeeruddin MK (1992) *Inorg Chem* 31:5243
132. Bignozzi CA, Argazzi R, Garcia CG, Scandola F (1992) *J Am Chem Soc* 114:8727
133. Wang Y, Schanze KS (1994) *Inorg Chem* 33:1354
134. Luong JC, Nadjo L, Wrighton MS (1978) *J Am Chem Soc* 100:5790
135. Partigianoni CM, Chodorowski-Kimmes S, Treadway JA, Striplin D, Trammell SA, Meyer TJ (1999) *Inorg Chem* 38:1193
136. Batey HD, Whitwood AC, Duhme-Klair A-K (2007) *Inorg Chem* 46:6516
137. Reece SY, Seyedsayamdost MR, Stubbe J, Nocera DG (2006) *J Am Chem Soc* 128:13654
138. Reece SY, Nocera DG (2005) *J Am Chem Soc* 127:9448
139. Chen P, Curry M, Meyer TJ (1989) *Inorg Chem* 28:2271
140. Westmoreland TD, Le Bozec H, Murray RW, Meyer TJ (1983) *J Am Chem Soc* 105:5952
141. Chen P, Danielson E, Meyer TJ (1988) *J Phys Chem* 92:3708
142. Liard DJ, Vlček A Jr (2000) *Inorg Chem* 39:485
143. Liard DJ, Kleverlaan CJ, Vlček A Jr (2003) *Inorg Chem* 42:7995
144. She C, Guo J, Lian T (2007) *J Phys Chem B* 111:6903
145. Asbury JB, Hao E, Wang Y, Ghosh HN, Lian T (2001) *J Phys Chem B* 105:4545
146. Chen P, Westmoreland TD, Danielson E, Schanze KS, Anthon D, Neveux PE Jr, Meyer TJ (1987) *Inorg Chem* 26:1116
147. Chen P, Mecklenburg SL, Meyer TJ (1993) *J Phys Chem* 97:13126
148. Chen P, Mecklenburg SL, Duesing R, Meyer TJ (1993) *J Phys Chem* 97:6811
149. Ziessel R, Juris A, Venturi M (1997) Chem Commun:1593
150. Ziessel R, Juris A, Venturi M (1998) *Inorg Chem* 37:5061
151. Wang Y, Hauser BT, Rooney MM, Burton RD, Schanze KS (1993) *J Am Chem Soc* 115:5675
152. Wang Y, Schanze KS (1996) *J Phys Chem* 100:5408
153. Lucia LA, Wang Y, Nafisi K, Netzel TL, Schanze KS (1995) *J Phys Chem* 99:11801
154. Wang Y, Lucia LA, Schanze KS (1995) *J Phys Chem* 99:1961
155. Trammell S, Goodson PA, Sullivan BP (1996) *Inorg Chem* 35:1421
156. Lewis JD, Bussotti L, Foggi P, Perutz RN, Moore JN (2002) *J Phys Phem A* 106:12202
157. Lewis JD, Moore JN (2004) Dalton Trans:1376
158. Peacock AFA, Batey HD, Raendler C, Whitwood AC, Perutz RN, Duhme-Klair A-K (2005) *Angew Chem Int Ed* 44:1712 –1714
159. Blanco-Rodríguez AM, Gabrielsson A, Towrie M, Vlček A Jr manuscript in preparation
160. Towrie M, Parker AW, Vlček A Jr, Gabrielsson A, Blanco Rodriguez AM (2005) *Appl Spectrosc* 59:467
161. Reece SY, Seyedsayamdost MR, Stubbe J, Nocera DG (2007) *J Am Chem Soc* 129:13828
162. Patrocinio AOT, Iha NYM (2008) *Inorg. Chem*. 47: 10851
163. Kuimova MK, Alsindi WZ, Blake AJ, Davies ES, Lampus DJ, Matousek P, McMaster J, Parker AW, Towrie M, Sun X-Z, Wilson C, George MW (2008) *Inorg. Chem*. 47: 9857
164. Easun TL, Alsindi WZ, Towrie M, Ronayne KL, Sun X-Z, Ward MD, George MW (2008) *Inorg. Chem*. 47: 5071
165. Knight TE, Guo D, Claude JP, McCusker JK (2008) *Inorg. Chem*. 47: 7249

Top Organomet Chem (2010) 29: 115–158
DOI: 10.1007/3418_2009_3

Published online: 20 May 2009

Exploitation of Luminescent Organometallic Rhenium(I) and Iridium(III) Complexes in Biological Studies

Kenneth Kam-Wing Lo

Abstract The rich photophysical and photochemical properties of organometallic rhenium(I) and iridium(III) complexes have been well studied. The interesting luminescence behaviour has been exploited in various areas such as emissive supramolecular assemblies, photovoltaic cells, chemosensing, and light-emitting device fabrication. Recently, the applications of these luminescent complexes in biological studies have received much attention. Herein, we review luminescent organometallic rhenium(I) and iridium(III) complexes that have been employed as biological probes, with an emphasis on biological targets including DNA, proteins, and cellular components. In particular, the molecular structures, spectroscopic and photophysical properties of the complexes, emissive behaviour, and potential applications of the labelled bioconjugates are described.

Keywords Cells • DNA • Iridium • Luminescence • Proteins • Rhenium

Contents

1 Introduction 118
2 Rhenium(I) Systems 119
2.1 DNA Probes 119
2.2 Protein Probes 125
2.3 Cellular Probes 136
3 Iridium(III) Systems 140
3.1 DNA Probes 140
3.2 Protein Probes 143
3.3 Cellular Probes 153
4 Conclusion 155
References 156

Kenneth Kam-Wing Lo (✉)
Department of Biology and Chemistry, City University of Hong Kong,
Tat Chee Avenue, Kowloon, Hong Kong, P. R. China
e-mail: bhkenlo@cityu.edu.hk

Abbreviations

Az	Azurin
bpy	2,2′-Bipyridine
bpy–CH_2–NH–C_2–NH–biotin	4-(*N*-(2-(Biotinamido)ethyl)aminomethyl)-4′-methyl-2,2′-bipyridine
bpy–CONH–$C_{10}H_{21}$	4-(*n*-Decylaminocarbonyl)-4′-methyl-2,2′-bipyridine
bpy–CONH–$C_{18}H_{37}$	4-(*n*-Octadecylaminocarbonyl)-4′-methyl-2,2′-bipyridine
bpy–CONH–C_2H_5	4-(Ethylaminocarbonyl)-4′-methyl-2,2′-bipyridine
bpy–CONH–C_6–NH–biotin	4-((6-(Biotinamido)hexyl)aminocarbonyl)-4′-methyl-2,2′-bipyridine
bpy–NCS	4-Isothiocyanato-2,2′-bipyridine
bpy–NH_2	4-Amino-2,2′-bipyridine
bpy–NHCO–CH_2I	4-Iodoacetamido-2,2′-bipyridine
BSA	Bovine serum albumin
cryo-TEM	Cryogenic transmission electron microscopy
CT	Charge-transfer
CTAB	Cetyltrimethylammonium bromide
DFT	Density functional theory
Dpp[5]	1,5-Bis(4-pyridyl)pentane
dppn	Benzo[*i*]dipyrido[3,2-*a*:2′,3′-*c*]phenazine
dppz	Dipyrido[3,2-*a*:2′,3′-*c*]phenazine
dppz-biotin	11-((2-(Biotinamido)ethyl)aminocarbonyl) dipyrido[3,2-*a*:2′,3′-*c*]phenazine
dpq	Dipyrido[3,2-*f*:2′,3′-*h*]quinoxaline
dpqa	2-(*n*-Butylaminocarbonyl)dipyrido[3,2-*f*:2′,3′-*h*]quinoxaline
dpq-biotin	2-((2-(Biotinamido)ethyl)aminocarbonyl) dipyrido[3,2-*f*:2′,3′-*h*]quinoxaline
DSPC	1,2-Distearoyl-*sn*-glycero-3-phosphocholine
ELISA	Enzyme-linked immunosorbent assay
EPR	Electron paramagnetic resonance
ERα	Estrogen receptor α
EtG	9-Ethylguanine
FPR	Formyl peptide receptor
HABA	4′-Hydroxyazobenzene-2-carboxylic acid
Hbsb	2-((1,1′-Biphenyl)-4-yl)benzothiazole
Hbsn	2-(1-Naphthyl)benzothiazole
Hbt	2-Phenylbenzothiazole
Hbtth	2-(2-Thienyl)benzothiazole
Hbzq	7,8-Benzoquinoline
Hdfpy	2-(2,4-Difluorophenyl)pyridine

Hmppy	2-(4-Methylphenyl)pyridine
Hmppz	3-Methyl-1-phenylpyrazole
Hpba	4-(2-Pyridyl)benzaldehyde
Hppy	2-Phenylpyridine
Hppy–$CH_2NH–C_4H_9$	2-(4-(*N*-(*n*-Butyl)aminomethyl)phenyl)pyridine
Hpq	2-Phenylquinoline
HSA	Human serum albumin
IgG	Immunoglobulin G
IL	Intra-ligand
LLCT	Ligand-to-ligand charge-transfer
Me_2–Ph_2–phen	2,9-Dimethyl-4,7-diphenyl-1,10-phenanthroline
Me_2–phen	2,9-Dimethyl-1,10-phenanthroline
Me_4–phen	3,4,7,8-Tetramethyl-1,10-phenanthroline
MLCT	Metal-to-ligand charge transfer
MTT	3-(4,5-Dimethyl-2-thiazolyl)-2,5-diphenyltetrazolium
N^C	Anionic cyclometallating ligands
N^N	Diimine ligands
NHE	Normal hydrogen electrode
NHS	*N*-Hydroxysuccinimide
OLED	Organic light-emitting diode
PBS	Phosphate-buffered saline
Ph_2–phen	4,7-Diphenyl-1,10-phenanthroline
phen	1,10-Phenanthroline
phen–NCS	5-Isothiocyanato-1,10-phenanthroline
phen–NH_2	5-Amino-1,10-phenanthroline
phen–NHCO–CH_2I	5-Iodoacetamido-1,10-phenanthroline
py	Pyridine
py–3–CH_2Cl	3-Chloromethylpyridine
py–3–CH_2OH	3-Hydroxylmethylpyridine
py–3–CONH–C_2H_4–indole	*N*-(3-Pyridoyl)tryptamine
py–3–mal	*N*-(3-Pyridyl)maleimide
py–3–NCS	3-Isothiocyanatopyridine
py–4–CH_2–NH–biotin	4-(Biotinamidomethyl)pyridine
py–4–CH_2–NHCO–C5–NH–biotin	4-(*N*-(6-(Biotinamido)hexanoyl)aminomethyl)pyridine
py–4–COOH	Isonicotinic acid
py–4–NH_2	4-Aminopyridine
py–4–NMe_2	4-(Dimethylamino)pyridine
py–biotin–NCS	3-Isothiocyanato-5-((2-(biotinamido)ethyl)aminocarbonyl)pyridine
py–biotin–TU–Et	3-Ethylthioureidyl-5-((2-(biotinamido)ethyl)aminocarbonyl)pyridine
py–CH_2CH_2–py	1,2-Bis(4-pyridyl)ethane

py–C6–est	4-(*N*-(6-(4-(17α-Ethynylestradiolyl) benzoylamino)hexanoyl)aminomethyl)pyridine
Quqo	2-(2-Quinolinyl)quinoxaline
RET	Resonance energy transfer
SBLCT	Sigma-bond-to-ligand charge-transfer
SCE	Standard calomel electrode
SDS	Sodium dodecylsulfate
TMRE	Tetramethylrhodamine ethyl ester
Tpm	Tris(1-pyrazolyl)methane
TX	Triton X-100

1 Introduction

Radioactive isotopes have been commonly used as biological labels for DNA sequencing, hybridisation, and immunological applications owing to their high detection sensitivity. However, because of the relatively long experimental time, short shelf-lives of expensive reagents, and the potential hazards of radioactive materials, alternative reagents derived from fluorescent organic compounds [1] and luminescent lanthanide chelates [2] have been sought. Additionally, many luminescent organometallic complexes, by virtue of their intense and long-lived luminescence with tunable emission energy, have emerged as useful probes for biological systems. Importantly, the emission of these systems is very sensitive to their local surroundings, such as the hydrophobicity of the environment, which can be exploited for biosensing purposes [3–5].

Herein, we review luminescent organometallic rhenium(I) and iridium(III) complexes that have been employed as biological probes, with an emphasis on biological targets including DNA, proteins, and cellular components. In general, the biological binding described herein involves the following four major strategies.

(1) Molecular structures: organometallic complexes have been designed to possess special structural properties that allow them to bind to biomolecules such as DNA. Binding of small molecules to DNA relies on electrostatic attractions, groove-binding, and intercalation [6–9]. As can be seen in the following sections, many rhenium(I) and iridium(III) complexes have been coordinated with an extended planar polypyridine ligand or appended with a planar aromatic molecule, which allow the complexes to intercalate into the base pairs of double-stranded DNA molecules.
(2) Functionalisation of the complexes with reactive groups: a number of metal complexes have been modified with (1) an NHS ester, isothiocyanate, and aldehyde, which can react readily with amines of lysine and the *N*-terminal of proteins; and (2) iodoacetamide and maleimide that can react with sulfhydryls of the cysteine residue [3–5, 10]. These facile reactions lead to covalent attachment of luminescent complexes to the target proteins and amine-/sulfhydryl-modified oligonucleotides.

(3) Use of labile ligands: some complexes contain substitutionally labile ligands (such as a solvent molecule) that can be displaced readily by the imidazole moiety of the histidine residue. Various proteins have been labelled with luminescent complexes by this method [11].
(4) Attachment of biologically relevant molecules: the most common non-covalent probes for biomolecules are designed in such a way that a biologically relevant substrate or unit is attached to the complex as a pendant [3, 4]. Specific binding of this moiety to the biological target usually results in changes of the emission properties of the probes due to their sensitivity to the local surroundings.

In the following sections, luminescent organometallic rhenium(I) and iridium(III) polypyridine complexes relying on the labelling or binding strategies mentioned above will be described. We focus on the molecular structures, spectroscopic and photophysical properties of the complexes, and the emissive behaviour and potential applications of the labelled bioconjugates.

2 Rhenium(I) Systems

The spectroscopy, photophysics, and photochemistry of rhenium(I) polypyridine complexes such as $[Re(N^N)(CO)_3(py)]^+$ have attracted great interest for more than 30 years [12–16]. The emission energy of these complexes depends strongly on the π^* orbital of the diimine ligands, indicating that the excited state is ^{3}MLCT ($d\pi(Re) \rightarrow \pi^*(N^N)$) in nature. However, ^{3}IL ($\pi \rightarrow \pi^*$) (N^N) emission has also been identified in some systems, and the relative dominance of MLCT and IL emission is controlled by the energetic separation of the two emissive states, which can be manipulated by changing both the polypyridine ligands and temperature. An important characteristic of luminescent rhenium(I) polypyridine complexes is that their ^{3}MLCT emission shows a bathochromic shift, reduced luminescence quantum yield, and shortened excited-state lifetime upon increasing the polarity of the solvent system. Another distinctive property of these luminescent rhenium(I) polypyridine complexes is their exhibition of a blue-shifted emission maxima in rigid media, which is known as rigidochromism. Since the first report on the luminescence of rhenium(I) polypyridine systems, the environment-sensitive luminescence behaviour, photoinduced electron-transfer, and photocatalytic properties of these complexes have been extensively studied. Additionally, their applications as sensors for various analytes have attracted much interest.

2.1 DNA Probes

Despite the rich emission properties of rhenium(I) polypyridine complexes being well documented, reports on the interactions of related complexes with DNA are limited compared to the ruthenium(II) analogues. The DNA-binding properties of

luminescent rhenium(I) diimine complexes were first reported by Schanze in 1993 [17]. Rhenium(I) polypyridine complexes appended with an anthracene moiety through a flexible linker of various lengths such as $[Re(bpy)(CO)_3(py–spacer–anthracene)]^+$ (**1**) have been synthesised [17, 18]. In polar aqueous solution, the anthracene unit approaches the hydrophobic rhenium(I)-bpy core, and the ^{3}MLCT ($d\pi(Re) \rightarrow \pi^*(bpy)$) luminescence is significantly quenched by the anthracene unit via Dexter exchange triplet-triplet energy-transfer. Upon addition of double-stranded DNA, the anthracene moiety strongly intercalates into the double-helix, leading to an increase of the separation between the rhenium(I)-bpy and anthracene unit. Thus, the intramolecular energy-transfer quenching becomes inefficient and the ^{3}MLCT emission is restored (Fig. 1).

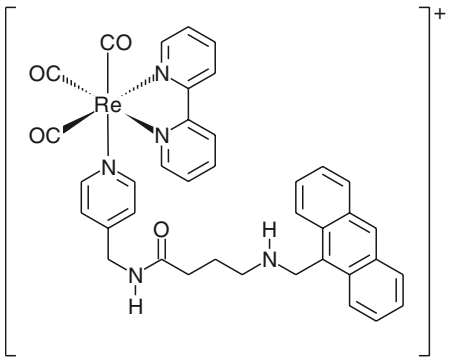

1

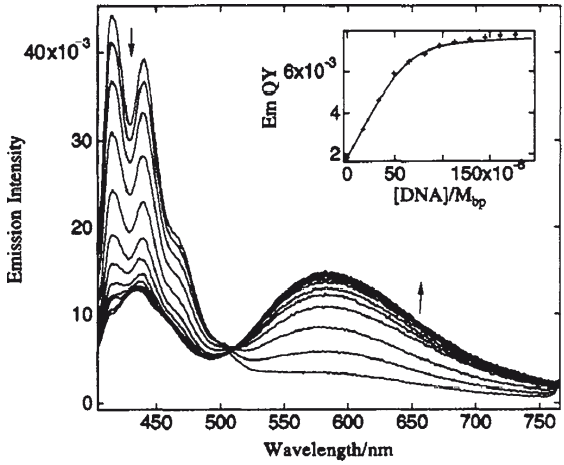

Fig. 1 Corrected emission spectra of a rhenium anthracene complex as a function of [DNA]/[Re]. *Arrows* indicate direction of change with increasing [DNA]/[Re]. [DNA]/[Re] ratios: 0, 0.5, 1.0, 1.5, 2.0, 2.5, 3.0, 3.5, 4.0, 4.5, 5.0, and 5.5. *Inset* shows a plot of Φ_{em} MLCT vs. [DNA] for the same emission titration experiment. Conditions: Tris buffer; pH = 7.0; [Re] = 33 μM [17]

The crystal structure and photophysics of a rhenium(I) bipyridine 9-ethylguanine complex $[Re(bpy)(CO)_3(EtG)]^+$ (**2**) have been reported by Thorp and co-workers [19]. In CH_2Cl_2 solution, the complex emits at ca. 600 nm with a lifetime of 0.17 μs and an emission quantum yield of 0.054. Electrochemical measurements reveal that EtG is similar electronically to electron-rich pyridines, such as py–4–NMe_2 and py–4–NH_2, and is a much better π-donor ligand than pyridine, trimethylphosphine, and acetonitrile.

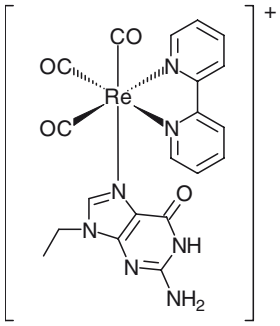

2

The luminescence properties of the complexes, $[Re(N^N)(CO)_3(L)]^+$ (N^N = dppz, dppn; L = pyridine, 4-methylpyridine) (**3**) with an extended planar diimine

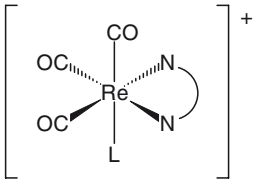

3

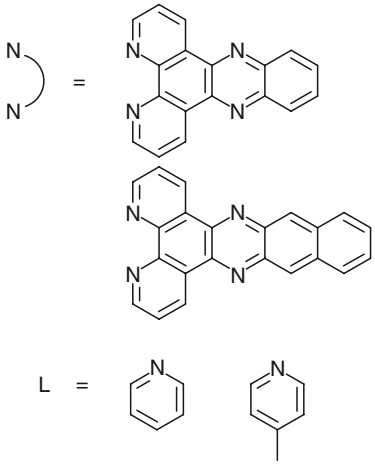

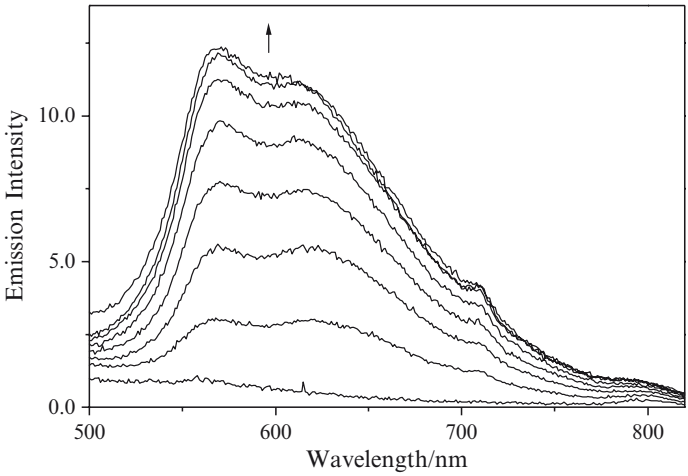

Fig. 2 Emission spectral traces of $[Re(dppz)(CO)_3(py)]^+$ (62 μM) in aqueous MeOH/buffer (20 mM Tris–HCl, pH 7.0) at 298 K in the presence of 0, 11, 22, 33, 45, 56, 67, and 134 μM poly(dA)•poly(dT) [22]

ligand have been studied by Schanze [20] and Yam [21, 22]. Luminescence and transient absorption spectroscopy showed that the dppz complexes exhibit an ^{3}IL ($\pi \rightarrow \pi^*$) (dppz) emissive state. However, the emissive state of the dppn complexes possesses substantial ^{3}MLCT ($d\pi(Re) \rightarrow \pi^*$(dppn)) character. These complexes bind tightly to double-stranded calf thymus DNA and synthetic oligonucleotides by intercalation, as revealed by absorption spectral changes and enhanced emission intensities (Fig. 2). Upon irradiation, these complexes cleave the DNA plasmid pBR322 efficiently. Interestingly, the excited complex $[Re(dppz)(CO)_3(py)]^{+*}$ oxidises the DNA molecule directly due to its strong oxidising properties. However, in the case of the dppn complex $[Re(dppn)(CO)_3(py)]^+$, DNA strand scissions result from superoxide and hydroxyl radicals produced from the reaction of the excited complex and oxygen in the air.

Thomas and co-workers developed dinuclear rhenium(I) dppz complexes such as $[\{Re(dppz)(CO)_3\}_2(py–CH_2CH_2–py)]^{2+}$ (**4**) [23]. Unlike their monomeric counterparts, these dinuclear complexes are non-emissive in organic solvents and aqueous solutions. Absorption titrations reveal two-stage binding for the two dppz moieties. However, the tether is insufficiently long for both rhenium(I) centres to intercalate into the same duplex. Thus, initially at least, the complex functions as a mono-intercalating system and the second rhenium centre may be free to interact with other DNA duplexes (interstrand binding). Recently, a related heterobimetallic complex $[\{Ru(tpm)(dppz)(\mu\text{-dpp}[5])(CO)_3Re(dppz)\}]^{3+}$ (**5**) has been isolated that possesses both DNA-light switch and photocleavage properties [24].

Zubieta and co-workers reported the reactions of amine-modified thymidine and uridine with 2-pyridinecarboxaldehyde and 2-quinolinecarboxaldehyde, respectively, to form chelating nucleosides [25]. These chelates have been coordinated

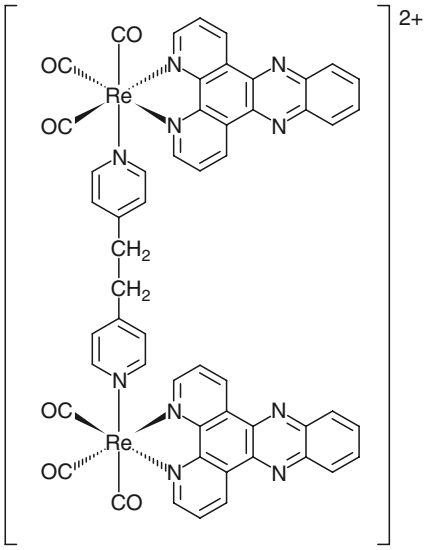

4

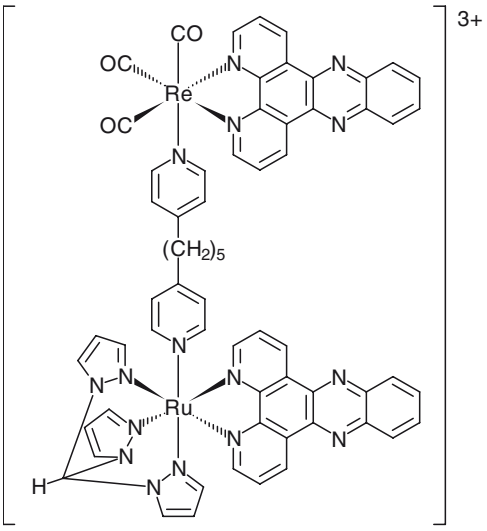

5

to a $[Re(CO)_3]^+$ unit to form new metallonucleosides such as (**6**). The quinoline complexes absorb strongly in the UV–Vis region. The absorption bands at 225–290 nm and 300–380 nm are assigned to ^{1}IL ($\pi \rightarrow \pi^*$) and ^{1}MLCT ($d\pi(Re) \rightarrow \pi^*$(ligand)) transitions, respectively. Upon photoexcitation under ambient conditions, these rhenium(I)-nucleosides display green to yellow emission. The emission occurs at ca. 552–565 nm (τ_o = 14–19 μs) in various solvents and the emissive state has been proposed to be ^{3}MLCT in nature.

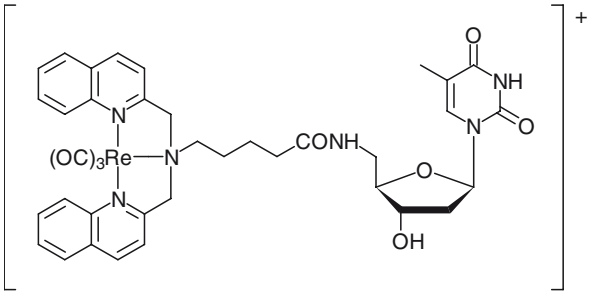

6

Lo and co-workers synthesised a series of rhenium(I) polypyridine isothiocyanate $[Re(N^N)(CO)_3(py–3–NCS)]^+$ (**7**) [26] and maleimide $[Re(N^N)(CO)_3(py–3–mal)]^+$ (**8**) [27] complexes that can act as biological labels. Similar to most rhenium(I) diimines, irradiation of all the complexes results in intense and long-lived ^{3}MLCT ($d\pi(Re) \rightarrow \pi^*(N^N)$) emission. The isothiocyanate complex $[Re(phen)(CO)_3(py–3–NCS)]^+$ has been used to label a universal M13 reverse sequencing primer that has been modified with an aminohexyl group at the 5′-end,

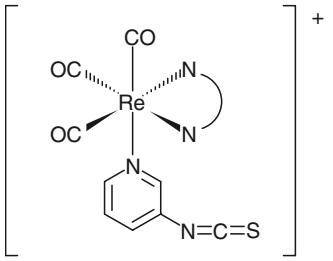

7

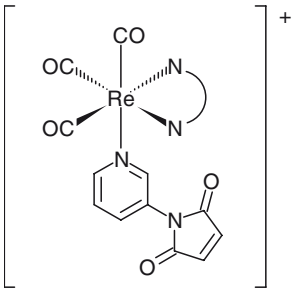

8

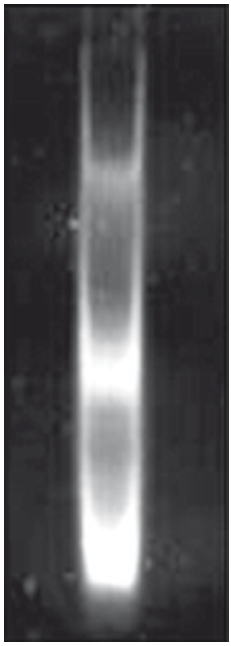

Fig. 3 Polyacrylamide gel electrophoresis result of a hybridisation mixture of an M13 reverse sequencing primer labelled with $[Re(phen)(CO)_3(py–3–NCS)]^+$ and three unmodified oligonucleotides of various lengths [26]

5′–H_2N–$(CH_2)_6$–AACAGCTATGACCATG–3′. The labelled primer has been isolated, purified, and shown to exhibit yellow luminescence (λ_{em} = 548 nm, τ_o = 0.52 μs) in degassed Tris–Cl buffer (50 mM) at pH 7.4 at 298 K upon irradiation. It has been used to detect unmodified oligonucleotides by the formation of luminescent double-stranded DNA molecules, as revealed by PAGE analysis (Fig. 3). On the basis of the specific reaction of the maleimide moiety with the sulfhydryl group, the rhenium(I) maleimide complexes have been used to label a thiolated oligonucleotide. All the labelled oligonucleotides exhibit intense and long-lived ^{3}MLCT emission in aqueous buffer upon irradiation.

2.2 Protein Probes

On the basis of the strong photo-oxidising behaviour of $[Re(phen)(CO)_3(imidazole)]^+$ (**9**) (Re(I)*/Re(0) = ca. +1.3 V vs. NHE in CH_3CN), Gray and co-workers reacted $[Re(phen)(CO)_3(H_2O)]^+$ with azurin, resulting in the formation of $[Re(phen)(CO)_3(His83)]^+$-$AzCu^+$, and studied the electron-transfer in this mutant [28]. Excitation of the rhenium(I) complex leads to direct oxidation of the copper(I) centre of the protein to copper(II). Using the flash-quench technique with

$[Co(NH_3)_5Cl]^{2+}$ as a quencher, photogeneration of Re^{2+} followed by production of tryptophan and tyrosine radicals in these rhenium(I)-conjugated azurin proteins, have been observed [29]. The EPR spectra of frozen solutions of irradiated $[Re(phen)(CO)_3(H83)]^+$–$AzZn^{2+}$/$[Co(NH_3)_5Cl]^{2+}$ and $[Re(phen)(CO)_3(H107)]^+$–$AzZn^{2+}$/$[Co(NH_3)_5Cl]^{2+}$ (Y72F mutant, leaving only one tyrosine, Y108, in the protein) reveal the appearance of tryptophan and tyrosine radicals, respectively. The tryptophan signal is attributable to a W48 radical while the tyrosine signal could originate from a Y108 radical. In a related study, additional rhenium(I)-modified azurin mutants have been studied [30]. Transient absorption spectroscopic measurements reveal that the tunnelling occurs directly from copper(I) to the rhenium-coordinated histidine radical. DFT calculations show that the unpaired electron in the "rhenium(II)" species, generated from the electron-transfer from $[Re(phen)(CO)_3(imidazole)]^{+*}$ to the cobalt(III) acceptor, resides on both the imidazole and the metal centre. Remarkably, when the copper(I) oxidation rates are plotted against Cu-surface histidine distances, an excellent agreement with those predicted based on the standard distance-decay constant β of 1.1 $Å^{-1}$ is observed, concluding the involvement of the metal-coordinated histidine in the electron-transfer. In another study, the ^{3}MLCT relaxation dynamics displayed by two structurally characterised mutants $[Re(phen)(CO)_3(HisX)]$–Az (X = 83, 109) in D_2O have been examined by picosecond time-resolved infrared spectroscopy [31]. A much slower medium relaxation has been ascribed to the reorientation of the solvent molecule and the structural reorganisation of the rhenium complex and the nearby polar amino acid residues.

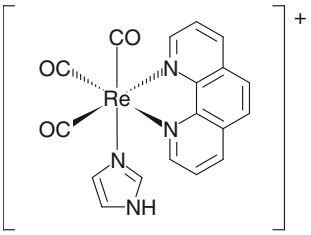

9

Winkler, Gray and co-workers studied the photoinduced electron-transfer of rhenium(I) perfluorobiphenyl diimine complexes (**10**) to the haem of nitric oxide synthase [32]. All the complexes bind tightly to the oxidase domain of the protein. Interestingly, the complexes containing an imidazole pendant ligate the haem iron. Transient absorption spectroscopic measurements indicate reduction of the haem centres by the excited complexes. The active-site iron(III) is reduced to iron(II) within 300 ps, almost ten orders of magnitude faster than the initial reduction of nitric oxide synthase by its reductase module. It is proposed that a neighbouring tryptophan residue reductively quenches the excited rhenium(I) complex to generate a tryptophan radical and a rhenium(0) species. Electron-transfer from the rhenium(0) species to the iron(III) of the haem occurs with a rate constant of about 6×10^8 s^{-1}.

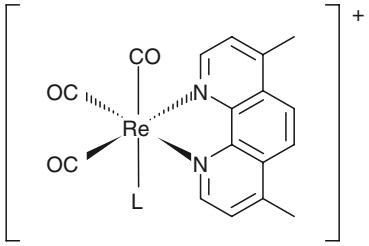

10

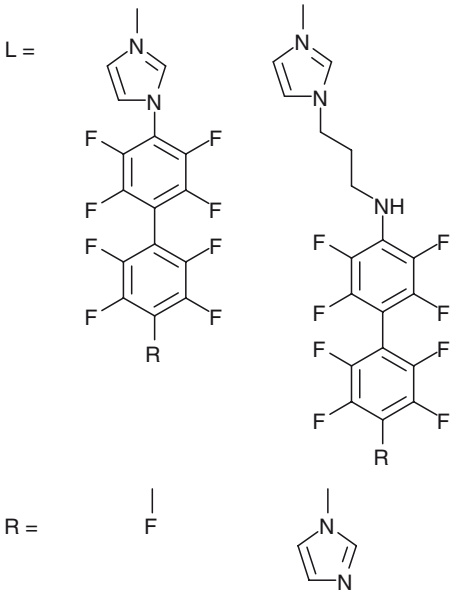

It is likely that this very fast reduction involves electron hopping through the perfluorobiphenyl bridge or possibly through a tyrosine residue near the haem.

Lakowicz and co-workers modified transition metal polypyridine complexes with amine-specific functional groups such as NHS ester and isothiocyanate, and attached these complexes to various proteins [33]. For example, the rhenium(I) complexes $[Re(Me_2–Ph_2–phen)(CO)_3(py–4–COOH)]^+$ (**11**) [34] and $[Re(phen–NHCO–CH_2I)(CO)_3Cl]$ (**12**) [35] have been isolated, characterised, and their photophysical properties studied. The former complex is activated by NHS and coupled to various biomolecules including HSA and IgG. The conjugates show intense and long-lived emission at ca. 550 nm (τ_o = ca. 2.8–4.1 μs). The rhenium(I) iodoacetamide complex is reactive towards the sulfhydryl group of biomolecules. Upon irradiation, the HSA conjugate of this complex displays strong emission (τ_o = ca. 1 μs). The possibility of use of these rhenium(I) conjugates as anisotropic probes has been investigated.

Zubieta, Valliant and co-workers have synthesised an amino-acid-containing tridentate $(quinoline–CH_2)_2–NR$ ligand that can react with $[Re(CO)_3Br_3]^{2-}$ to form

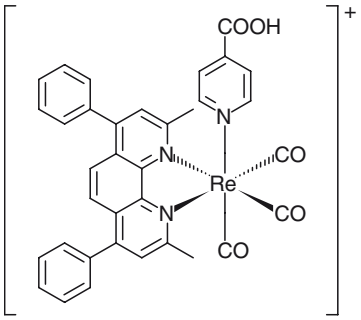

11

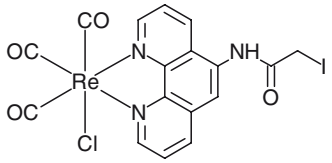

12

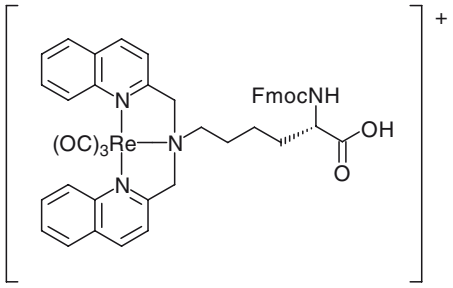

13

a luminescent complex (**13**) [36]. This complex shows dual emission at 425 and 580 nm with a lifetime of ca. 4.31–9.76 μs. A short peptide fMLF has been labelled with this luminescent rhenium(I) complex and the conjugate has been used to probe the biological target human FPR studied by flow cytometry and fluorescence microscopy. Related (quinoline–CH_2)$_2$–NR ligands containing a maleimide moiety and their rhenium(I) complexes have been isolated and shown to possess rich luminescence properties [37]; for example, complex **14** emits at 550 nm (τ_o = 16 μs) in ethylene glycol at room temperature. These labels have been reacted with sulfhydryl-containing biomolecules resulting in the formation of luminescent conjugates.

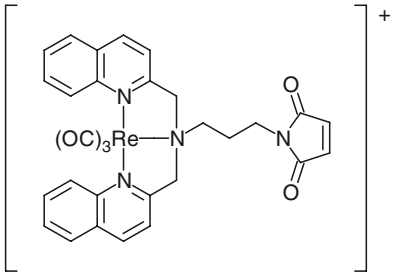

14

Lo and co-workers have conjugated the rhenium(I) polypyridine isothiocyanate $[Re(N^N)(CO)_3(py–3–NCS)]^+$ (**7**) [26] and maleimide $[Re(N^N)(CO)_3(py–3–mal)]^+$ (**8**) [27] complexes to various proteins, on the basis of the amine- and sulfhydryl-specific reactivity, respectively, of these complexes. For example, $[Re(phen)(CO)_3(py–3–NCS)]^+$ has been coupled to HSA, resulting in the formation of a luminescent conjugate. This conjugate exhibits intense and long-lived yellow ^{3}MLCT ($d\pi(Re) \rightarrow \pi^*(phen)$) emission ($\lambda_{em}$ = 534 nm, bi-exponential decay: τ_1 = 0.79 μs, τ_2 = 0.13 μs) in aqueous buffer upon excitation. The rhenium(I) maleimide complex $[Re(phen)(CO)_3(py–3–mal)]^+$ has been covalently linked to a cysteine-containing peptide, glutathione (γ-Glu-Cys-Gly), and the proteins BSA and HSA. Upon irradiation, all the bioconjugates display intense and long-lived yellow ^{3}MLCT ($d\pi(Re) \rightarrow \pi^*(phen)$) luminescence in buffer solutions. While the glutathione bioconjugate exhibits a single-exponential decay, both labelled albumin conjugates show bi-exponential decays with emission-lifetime components of ca. 1.1 and 0.2 μs. The observation of such long emission lifetimes indicates that these rhenium(I) maleimide labels and their isothiocyanate counterparts are promising candidates for time-resolved bioassays.

The avidin–biotin system is a useful tool in immunology, histochemistry, and in situ hybridisation; for example, antibodies multiply labelled with biotin can increase the sensitivity of heterogeneous bioassays by signal amplification [38, 39]. Also, biotinylated biomolecules can be purified with affinity chromatography and detected by ELISA and blotting techniques. Although organic fluorophore-biotin conjugates have been designed [40], they suffer from significant emission quenching upon binding to avidin. In 2002, Lo and co-workers synthesised a family of luminescent rhenium(I) polypyridine biotin complexes $[Re(N^N)(CO)_3(py–spacer–biotin)]^+$ (**15**) [41, 42] as the first luminescent biotin derivatives. Upon excitation, the complexes display orange to green triplet MLCT ($d\pi(Re) \rightarrow \pi^*(N^N)$) emission in fluid solutions at 298 K. The binding of the complexes to avidin has been studied by the standard HABA assay. The most important result is that the complexes display enhanced emission intensities and extended lifetimes upon binding to avidin. The emission titration curves for $[Re(Me_2–Ph_2–phen)(CO)_3(py–4–CH_2–NHCO–C5–NH–biotin)]^+$ are shown in (Fig. 4). At [Re]:[avidin] = 4:1, the emission intensities of this class of complexes are enhanced by ca. 1.2–3.0-fold and the emission lifetimes are extended by ca. 1.3–2.4-fold. Since no similar

changes are observed when excess biotin is present from the outset, the increase in emission intensities and lifetimes is a consequence of the specific binding of the complexes to the biotin-binding sites of avidin. The avidin-induced photophysical changes are ascribed to the increased hydrophobicity and rigidity of the surroundings

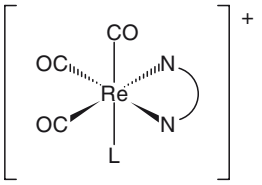

15

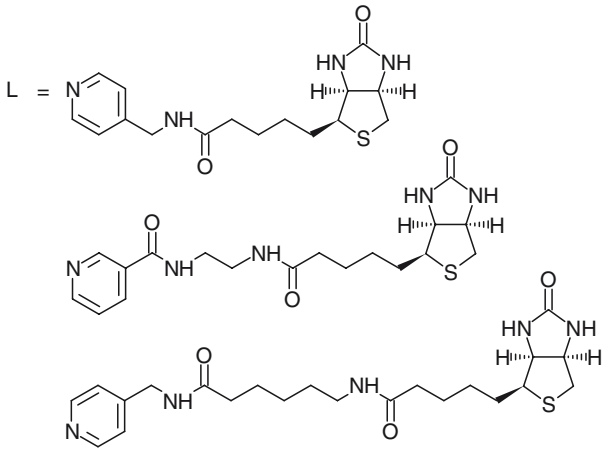

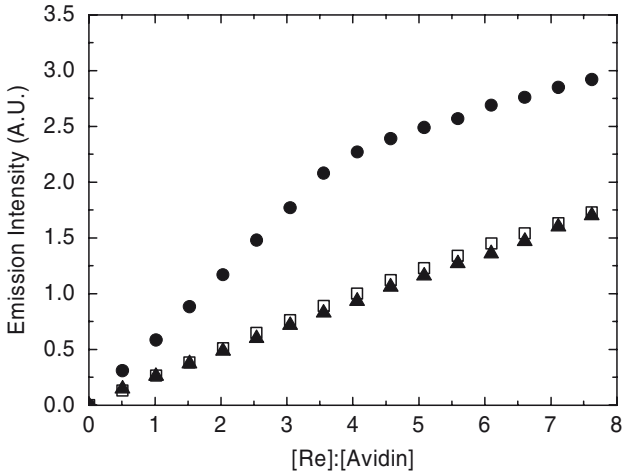

Fig. 4 Luminescence titration curves for the titrations of (1) 3.8 μM avidin (*filled circle*), (2) 3.8 μM avidin and 380.0 μM unmodified biotin (*filled triangle*), and (3) a blank phosphate buffer solution (*open square*) with $[Re(Me_2–Ph_2–phen)(CO)_3(py–4–CH_2–NHCO–C5–NH–biotin)]^+$ [42]

of the complexes upon the binding event. The K_d values range from ca. 5.5×10^{-11} to 3.4×10^{-9} M, which are about four to six orders of magnitude larger than that of the native biotin–avidin system (K_d = ca. 10^{-15} M). The weaker binding is ascribed to the bulkiness of the rhenium–polypyridine moieties.

With an aim to develop sensitive assays for avidin and biotin, one strategy is to use a quencher to selectively suppress the emission of the free rhenium(I) biotin complex by distance-dependent RET quenching. With a water-soluble negatively charged polypeptide (poly(E/K) 6:4) modified with the energy-acceptor dye QSY-7 NHS ester as the quencher, the emission enhancement factor of one of the complexes increases from ca. 1.5 to 4.0 upon binding to avidin (Fig. 5) [42]. Another approach to increasing the emission enhancement factors is to identify a system that inherently shows very weak emission in aqueous buffer, but intense emission in more hydrophobic media. Thus, new rhenium(I) biotin complexes [Re(dpqa)$(CO)_3$(py–spacer–biotin)]$^+$ (**16**) have been designed [43]. The amide substituent of the diimine ligand renders the complexes very weakly emissive in aqueous buffer. As expected, the complexes show increased emission intensities and lifetimes upon binding to avidin. Importantly, the emission intensity enhancement factors vary from ca. 3.1 to 8.1, which are more pronounced compared to those of the dpq analogues (ca. 1.2–1.8) (Fig. 6).

New rhenium(I) biotin complexes containing the extended planar diimine ligands dppz and dppn (**17**) have been prepared to explore bifunctional biological probes [44]. These complexes bind to double-stranded calf thymus DNA by intercalation, as revealed by absorption and emission titrations. HABA assays show that all the complexes bind to avidin with a stoichiometry of 4:1 ([Re]:[avidin]). Similar to other rhenium(I) diimine biotin complexes described above, the emission intensities

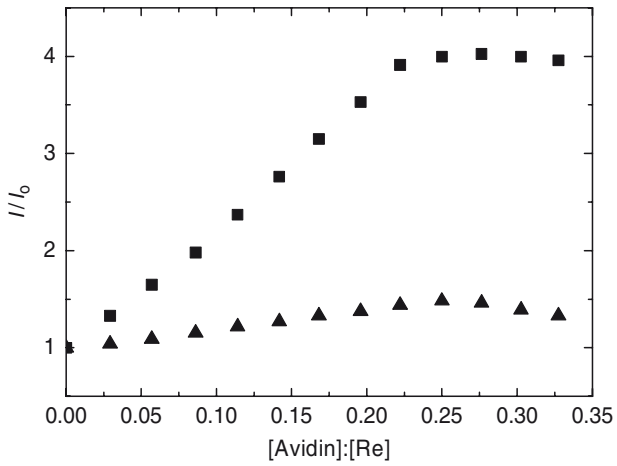

Fig. 5 Luminescence titration curves for the titrations of [Re(Me_2–Ph_2–phen)$(CO)_3$(py–4–CH_2–NHCO–C5–NH–biotin)]$^+$ (5.5 μM) in the absence (*filled triangle*) and presence (*filled square*) of poly(E/K)–QSY (1.1 μM) in water at 298 K, where I_o and I are the emission intensities in the absence and presence of avidin, respectively [42]

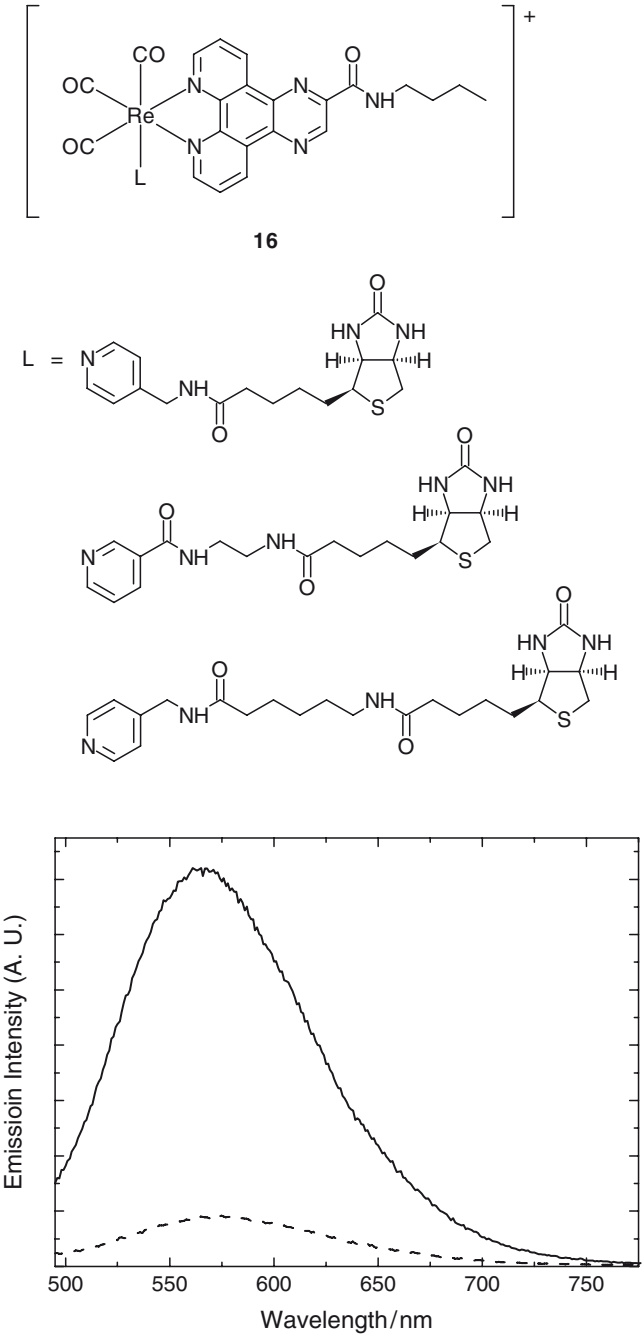

Fig. 6 Emission spectra of $[Re(dpqa)(CO)_3(py–4–CH_2–NH–biotin)]^+$ (17.3 μM) in the presence of 0 μM (*broken line*) and 3.8 μM (*solid line*) avidin in 50 mM potassium phosphate buffer pH 7.4/DMSO (97:3, v/v) at 298 K [43]

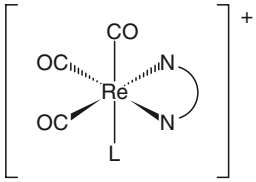

17

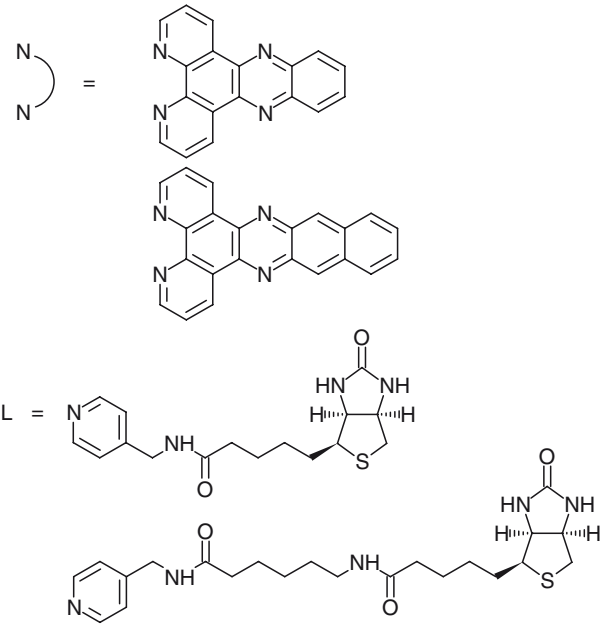

and lifetimes of these complexes increase in the presence of avidin. In particular, the complex $[Re(dppz)(CO)_3(py–4–CH_2–NH–biotin)]^+$ exhibits a remarkably large emission enhancement factor of ca. 40 (Fig. 7), which is a consequence of the extremely weak emission of the unbound form in aqueous solution.

The important physiological activities of indole and its derivatives have been the subject of many studies [45, 46]. Various approaches have been adopted to examine the substrate-binding properties of the biological receptors of indole compounds; for example, radioactive indole derivatives [47], indole–biotin conjugates [48], and fluorescent indole compounds [49] have been utilised. Lo and co-workers designed a series of luminescent rhenium(I) diimine indole complexes $[Re(N^N)(CO)_3(py–spacer–indole)]^+$ (**18**) as probes for indole–binding proteins [50, 51]. Upon visible-light irradiation, the complexes exhibit ^{3}MLCT ($d\pi(Re) \rightarrow \pi^*(N^N)$) emission in fluid solutions at 298 K and in low-temperature glass. These rhenium(I) indole complexes show much lower luminescence quantum yields and shorter emission lifetimes than those of their indole-free counterparts due to self-quenching. Since the excited complexes are very oxidising, ($E^o[Re^{+*/0}]$ = ca. +1.25 to

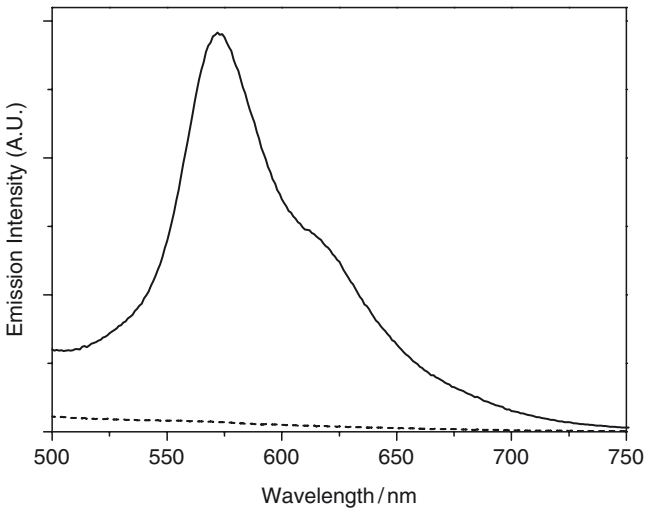

Fig. 7 Emission spectra of $[Re(dppz)(CO)_3(py–4–CH_2–NH–biotin)]^+$ in the absence (*broken line*) and presence (*solid line*) of avidin in degassed potassium phosphate buffer [44]

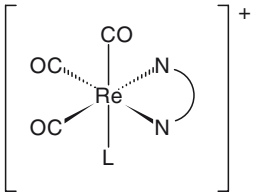

18

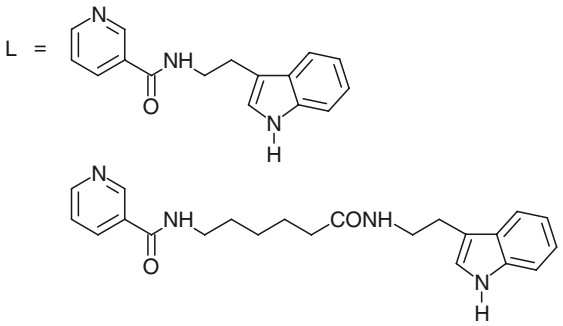

+1.49 V vs. SCE), reductive quenching of the excited complexes by the appended indole (E^o[indole$^{+/0}$] < +1.06 V vs. SCE) is favoured by > 0.2–0.4 eV. From this, together with results from transient absorption spectroscopic measurements, it is concluded that the emission quenching of the indole-containing complexes is a result of electron-transfer. The interactions of these rhenium(I) indole complexes with

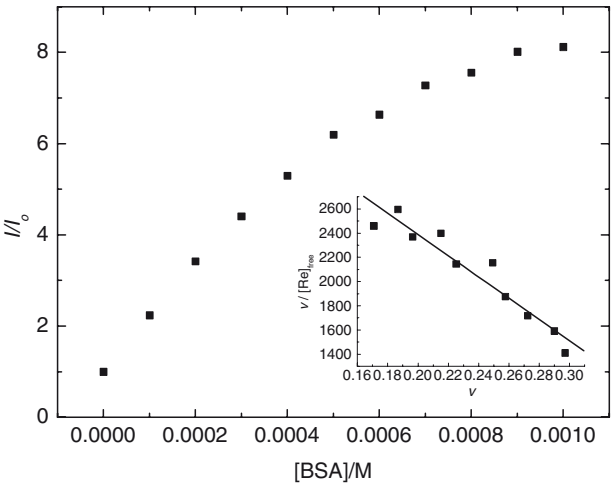

Fig. 8 Results of emission titration of $[Re(Me_2–phen)(CO)_3(py–3–CONH–C_2H_4–indole)]^+$ with BSA. I_o and I are the emission intensity of the complex in the absence and presence of BSA, respectively. The *inset* shows the Scatchard plot [51]

indole-binding proteins such as BSA have been studied by emission titrations. The emission intensities of the indole-containing complexes are enhanced by up to 17-fold in the presence of BSA. Results of the emission titration of $[Re(Me_2–phen)(CO)_3(py–3–CONH–C_2H_4–indole)]^+$ with BSA are shown in (Fig. 8) as an example. The binding constants of the complexes to BSA have been determined to be in the order of 10^4 M^{-1} from Scatchard analysis. Additionally, the rhenium(I) indole complexes inhibit the indole-binding enzyme tryptophanase. A standard assay, which is based on the conversion of L-serine to pyruvate by the enzyme, has been studied. Under the standard experimental conditions, at [L-serine] = 800 mM, free indole inhibits 53% of the enzyme activity, while the indole-containing complexes and their indole-free counterparts cause ca. 77–43 and 8–3% inhibition, respectively. In a related study, the synthesis and characterisation of luminescent rhenium(I) dpq and dpqa indole complexes $[Re(N^N)(CO)_3(py–spacer–indole)]^+$ (N^N = dpq, dpqa) (**19**) are reported [52]. The amide moiety of the dpqa ligand effectively suppresses the emission intensity of the free complexes in aqueous solutions, which gives rise to large BSA-induced emission enhancement factors of ca. 8.0–13.4.

Estradiol is the most potent natural estrogen responsible for the development and maintenance of the secondary sexual characteristics and functions of the reproductive system in females [53]. The physiological effects of estradiol are triggered by its binding to estrogen receptors [54]. Owing to the important roles of both estradiol and its receptor on female physiology, the design of new biological probes for estradiol-binding proteins has attracted much attention. A series of luminescent rhenium(I)

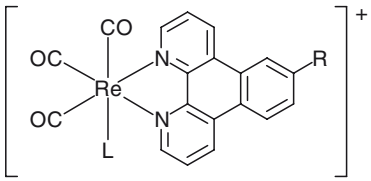

19

R = H

$CONHCH_2CH_2CH_2CH_3$

L =

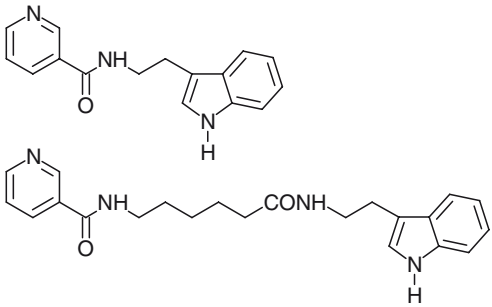

polypyridine estradiol complexes $[Re(N^N)(CO)_3(py–spacer–estradiol)]^+$ (**20**) has been reported by Lo and co-workers [55]. Upon irradiation, the complexes exhibit intense and long-lived ^{3}MLCT ($d\pi(Re) \rightarrow \pi^*(N^N)$) emission. The lipophilicity of these complexes has been determined by reversed-phase HPLC. Upon binding to ERα, the emission intensities of the py–C6–est complexes are enhanced (ca. 5.1–6.1-fold) and the emission maxima are blue-shifted, suggestive of increased hydrophobicity and rigidity of the local environments of the complexes. The binding constants of these complexes to ERα are estimated to be in the order of 10^7 M^{-1}, which are two orders of magnitude smaller than that of unmodified estradiol ($K_a = 5 \times 10^9$ M^{-1}) [56]. The lower binding affinity is a result of the bulkiness of rhenium(I) polypyridine moieties. However, this binding affinity is comparable or larger than that of related estradiol systems such as 17α–[(L)$Re(CO)_3$]–estradiol (L = 4′,4′-bis(ethanethio)-4′-carboxy-butyn-1′-yl, 6′,6′–bis(ethanethio)-6′-carboxy-hexyn-1′-yl; $K_a = 1.3 \times 10^7$ and 1.1×10^7 M^{-1}, respectively) [57] and 17α-[$(CCCH_2N(CH_3)C_2H_4N(CH_3)_2)Pt(X)$]-estradiol (X = diiodide, malonato; $K_a = 1.0 \times 10^7$ and 2.5×10^6 M^{-1}, respectively) [58].

2.3 Cellular Probes

Rhenium(I) pyrazolyl–diamine complexes appended with an anthracen-9-yl group (**21**) have been isolated and characterised [59]. The binding of these complexes to double-stranded calf-thymus DNA has been investigated with absorption, fluorescence, circular dichroism, and linear dichroism spectroscopy. The results indicate that the complexes bind to the DNA molecules by intercalation of the

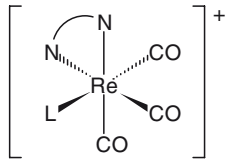

20

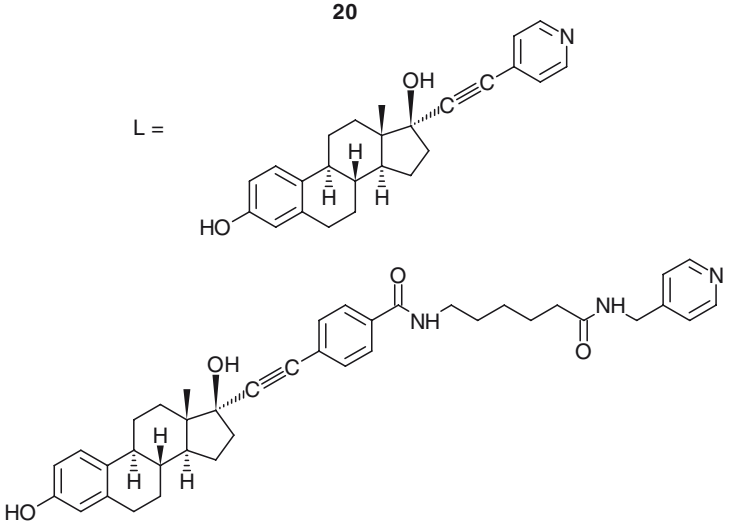

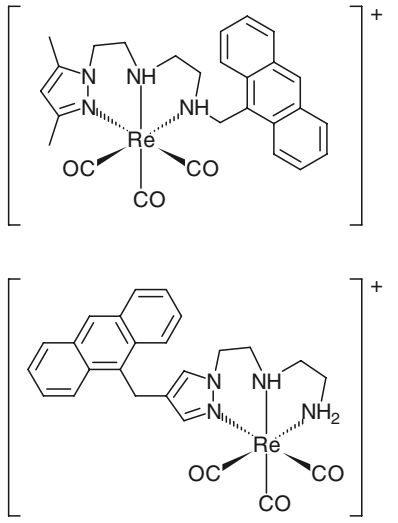

21

anthracene moiety, and a binding constant between 3.5×10^3 and 2.0×10^4 M^{-1} has been determined. The cellular-uptake properties of the complexes have been studied by fluorescence microscopy using B16-F1 murine melanoma cells as an example.

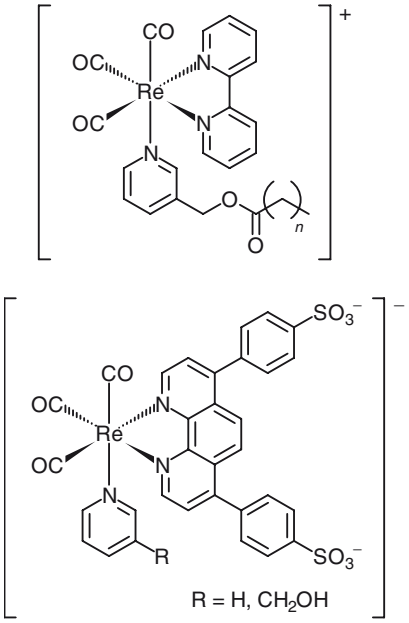

22

The results reveal that the complexes can enter the cells efficiently with a significant accumulation in the nucleus, especially in the nucleoli. This is in sharp contrast to the case of the free ligands, which remain in the cytosol upon cellular uptake.

Coogan and co-workers reported a series of lipophilic and hydrophilic luminescent rhenium(I) diimines $[Re(bpy)(CO)_3(py–3–CH_2OOC\{CH_2\}nCH_3)]^+$ (n = 6, 12, 16) and $[Re(phen\{C_6H_4–4–SO_3\}_2)(CO)_3(py–3–R)]^-$ (R = H, CH_2OH) (**22**) [60]. The complexes display ^{3}MLCT emission at 552–566 nm in CH_3CN or water upon photoexcitation. Lipophilicity studies using liposomes as a model reveal that the complexes bearing lipophilic chains reside mainly in the lipid membranes, whereas the bathophenanthroline sulfate complexes reside in the polar aqueous phase and are membrane-impermeable. Incubation of the lipophilic complexes with *Spironucleus vortens*, a parasitic flagellate, leads to accumulation of the complexes in the internal membranes partitioning cell compartments and with constituents within organelles. The more polar sulfonated complexes, however, appear to localise in digestive vacuoles as a result of phagocytosis. This illustrates that the choice of ligand for metal complexes has a decisive role on the cellular internalisation and trafficking of metal complexes.

The same group designed a new rhenium complex containing a chloromethylpyridine ligand as a sulfhydryl-specific group $[Re(bpy)(CO)_3(py–3–CH_2Cl)]^+$ (**23**) [61]. The complex has been reacted with glutathione to form a bioconjugate. Both the complex and the conjugate are emissive, with emission maxima occurring at ca. 550 nm (τ_o = ca. 120 ns). Incubation of the complex with MCF-7 cells leads to efficient cellular uptake, as revealed by confocal microscopy. The microscopy images suggest localisation of the complexes in mitochondria, which is in accordance

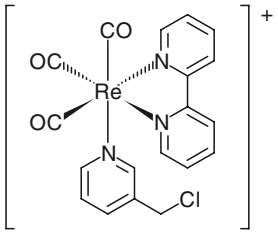

23

with the cationic, lipophilic, and thiol-reactive nature of the complex. The mitochondria-specificity has been confirmed with co-localisation experiments using TMRE, which is known to accumulate in mitochondria.

The first class of luminescent biotinylation reagents, derived from rhenium(I) polypyridine complexes $[Re(N^N)(CO)_3(py–biotin–NCS)]^+$ (**24**), have been reported by Lo and co-workers [62]. To investigate the amine-specific reactivity

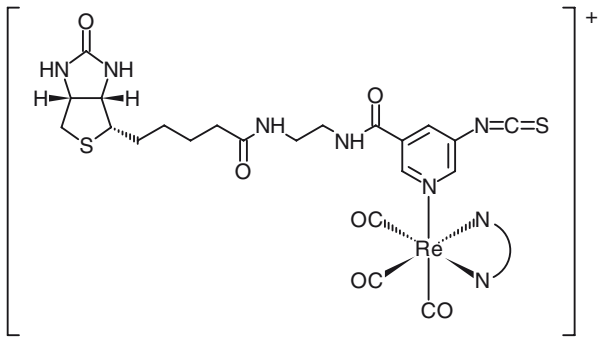

24

of the isothiocyanate complexes, they have been reacted with a model substrate ethylamine, resulting in the formation of the thiourea complexes $[Re(N^N)(CO)_3(py–biotin–TU–Et)]^+$ (**25**). All the rhenium(I) complexes have been characterised and their photophysical properties have been studied. The avidin-binding properties of the thiourea complexes have been examined by the HABA assay and emission titrations (I/I_o = ca. 1.4–1.5). Additionally, BSA has been biotinylated with the isothiocyanate complexes. All the resultant rhenium–BSA bioconjugates display intense and long-lived orange-yellow to greenish-yellow emission upon irradiation in aqueous buffer under ambient conditions. The cytotoxicity of the thiourea complexes towards the HeLa cells has been examined by MTT assays. The IC_{50} values are between ca. 17.5 and 28.5 μM, which are comparable to that of cisplatin (26.7 μM) under the same conditions. The cellular uptake of one of the thiourea complexes has been investigated by fluorescence microscopy, and the results show that the complex is localised in the perinuclear region after interiorisation.

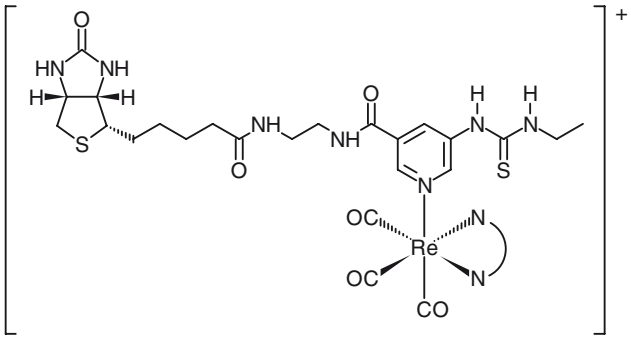

25

3 Iridium(III) Systems

Various types of ligands including bidentate (N^N), (N^O), and (O^O) and tridentate (N^N^N) ligands, halides, pseudohalides, phosphines, and cyclometallating ligands such as (N^C), (N^C^N), and (C^N^C) have been coordinated to the iridium(III) centre to give complexes of high structural diversity, many of which exhibit interesting luminescence properties [63, 64]. There have been an increasing number of studies devoted to the design of luminescent iridium(III) polypyridine complexes as phosphorescent emitters in OLED, photosensitisers for solar cells, and photocatalysts for water splitting. Unlike other d^6 systems, the nature of the emissive states of iridium(III) polypyridine complexes varies widely. The most common emissive states are ^{3}IL and ^{3}MLCT in character. Additionally, assignments of ^{3}LLCT and ^{3}SBLCT excited states have also been put forward in some systems.

3.1 DNA Probes

The use of luminescent cyclometallated iridium(III) polypyridine complexes as biological labels was first reported by Lo and co-workers in 2001 [65]. Two luminescent cyclometallated iridium(III) complexes $[Ir(ppy)_2(phen–R)]^+$ (R = NCS, NHCO–CH_2I) (**26**) that can specifically react with primary amine and sulfhydryl groups, respectively, have been prepared and characterised. Upon irradiation, the complexes show intense and long-lived orange-yellow ^{3}MLCT ($d\pi(Ir) \rightarrow \pi^*$(phen-R)) luminescence in fluid solutions at room temperature and in low-temperature glass. These isothiocyanate and iodoacetamide complexes have been used to label a universal M13 reverse sequencing primer modified with an amine and a sulfhydryl group, respectively, at the 5′-end. The labelled DNA molecules exhibit intense and long-lived orange-yellow luminescence upon excitation. In degassed buffer solutions, the oligonucleotides emit at ca. 572–580 nm, with lifetimes in the sub-

microsecond range. These labelled oligonucleotides have been hybridised with their unmodified complementary oligonucleotides to form luminescent double-stranded DNA molecules. The photophysical properties of these duplexes are similar to those of the labelled probes; the emission is derived from a ^{3}MLCT (dπ(Ir) $\rightarrow$ π^*(N^N)) excited state.

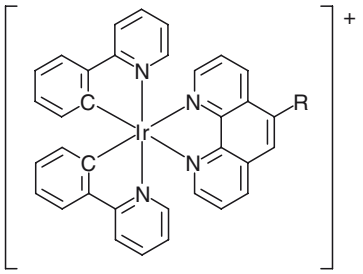

26

R = NCS, $NHCOCH_2I$

Luminescent cyclometallated iridium(III) complexes containing an extended planar diimine ligand, $[Ir(ppy)_2(N^N)]^+$ (**27**) (N^N = dpq, dpqa, dppz, dppn), have been synthesised and their photophysical properties studied [66]. The complexes display long-lived green to orange ^{3}MLCT (dπ(Ir) $\rightarrow$ π^*(N^N)) luminescence under ambient conditions but do not emit in aqueous solution. The binding of these complexes to

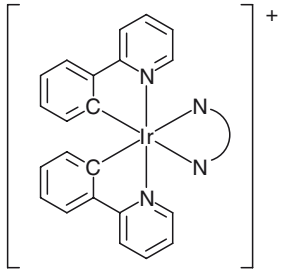

27

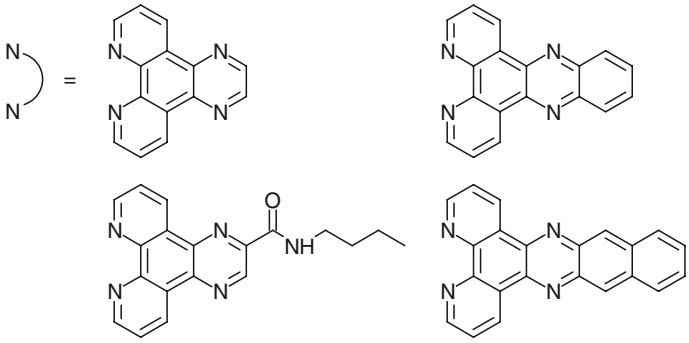

double-stranded calf thymus DNA and synthetic double-stranded oligonucleotides poly(dA)•poly(dT) and poly(dG)•poly(dC) has been investigated by spectroscopic and emission titrations. These complexes strongly intercalate into the double-stranded DNA, as revealed by the emission enhancement (Fig. 9). For example, the luminescence of the dpq complex is enhanced by up to 38-fold in the presence of calf-thymus DNA and synthetic double-stranded oligonucleotides, whereas the emission intensity of the dpqa complex is increased by ca. 40 and 46-fold in the presence of double-stranded calf-thymus DNA and poly(dA)•poly(dT), respectively.

Barton and co-workers reported a series of luminescent cyclometallated iridium(III) dppz complexes $[Ir(ppy)_2(dppz–R)]^+$ (R = H, $–O(CH_2)_5COOMe$, –COOEt, $–C{\equiv}C(CH_2)_3COOEt$) (**28**) [67]. The intercalative binding of the complexes to λ-DNA in aqueous buffer has been probed by electronic absorption titrations. In contrast to results described in the previous report, the very weak emission of $[Ir(ppy)_2(dppz)]^+$ is quenched upon addition of calf thymus DNA and $[poly(dA–dT)]_2$. EPR measurements of the complex bound to DNA reveal the formation of a guanine radical upon irradiation, resulting from oxidative photoinduced electron-transfer. Reductive photoinduced electron-transfer from the excited complex to the thymine base in DNA has also been observed. Recently, a related iridium(III) dppz complex has been tethered to oligonucleotides, and the photoredox properties of these adducts have been utilised in the studies of DNA-mediated hole transport and electron transport [68].

Sheldrick and co-workers reported the synthesis and DNA-binding behaviour of a number of organometallic iridium(III) dppz complexes such as $[(\eta^5\text{-}C_5Me_5)Ir(H\text{-}methionine)(dppz)]^{3+}$ (**29**) [69]. These interesting complexes bind to double-stranded calf thymus DNA by intercalation, as revealed by various spectroscopic techniques.

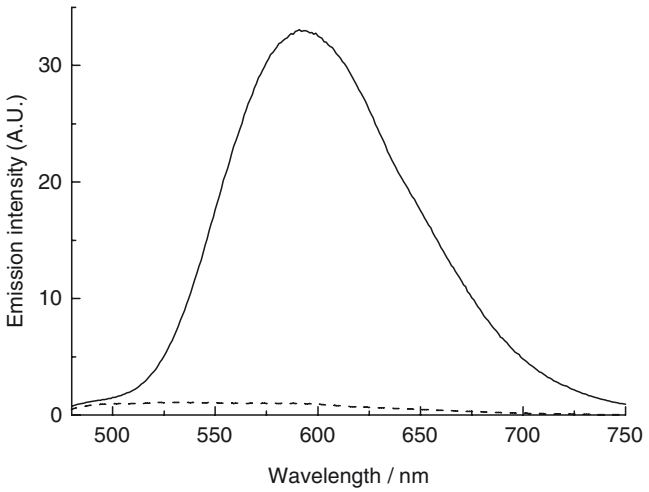

Fig. 9 Emission spectra of complex $[Ir(ppy)_2(dpq)]^+$ (137 μM) in a mixture of Tris–Cl buffer (50 mM, pH 7.4) and methanol (7:3, v/v) in the absence (*broken line*) and presence (*solid line*) of double–stranded calf thymus DNA (744 μM) [66]

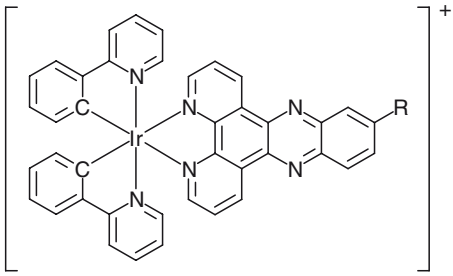

R = H, –O(CH$_2$)$_5$COOMe, –COOEt, –C≡C(CH$_2$)$_3$COOEt

28

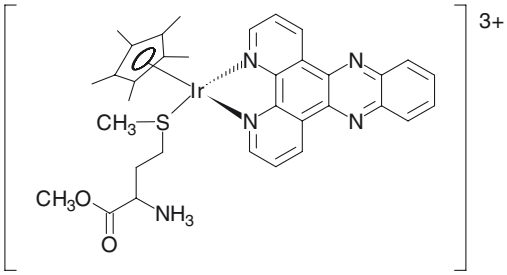

29

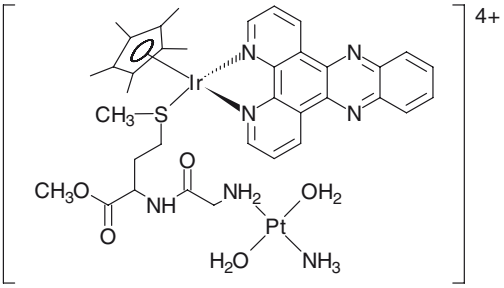

30

Recently, bifunctional complexes such as [(η^5-C$_5$Me$_5$)Ir(dppz)(μ-peptide-κS:κN){Pt(H$_2$O)$_2$(NH$_3$)}]$^{4+}$ (**30**) have been designed, which show both intercalative (Ir-dppz) and covalent (Pt) DNA-binding properties [70]. The cytotoxicity and cellular uptake of some of these interesting complexes have also been studied [71].

3.2 Protein Probes

The complexes [Ir(pba)$_2$(N^N)]$^+$ (**31**) coordinated with different diimine ligands (N^N) and the aldehyde-containing cyclometallating ligand pba can react with the primary amine of biomolecules to form a stable secondary amine after reduction [72].

In fluid solutions at room temperature, all the complexes show a similar vibronically structured emission band (ca. 530, 565 (sh) nm) with a very long emissive lifetime (ca. 5 μs). It is conceivable that the emissive state is ^{3}IL ($\pi \rightarrow \pi^*$) (pba) in nature. The complexes have been used to crosslink L-alanine and avidin, respectively. Interestingly, the Me_4–phen conjugates emit with a green colour (λ_{em} = 480, 510, 550 (sh) nm) while the Ph_2–phen analogues show orange-yellow emission (λ_{em} = 570 nm). Thus, the conversion of the aldehyde moiety to a secondary amine changes the emissive-state character from ^{3}IL ($\pi \rightarrow \pi^*$) (pba) to ^{3}MLCT ($d\pi$(Ir) $\rightarrow \pi^*$(N^N)).

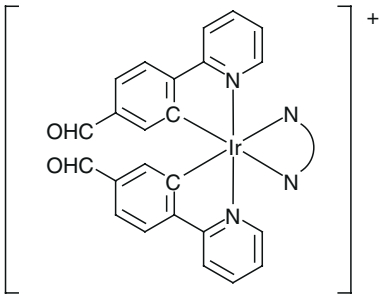

31

Amines, aldehyde, isothiocyanate, and iodoacetamide groups have been incorporated into the diimine ligands (N^N) of the cyclometallated iridium(III) complexes $[Ir(N^C)_2(N^N–R)]^+$ (N^C = ppy, mppy, mppz, bzq, pq; R = NH_2, CHO, NCS, NHCO–CH_2I) (**32**) [65, 73, 74]. Upon irradiation, all the complexes display intense and long-lived orange-red to greenish-yellow luminescence under ambient conditions and in alcohol glass at 77 K. The emission of $[Ir(N^C)_2(N^N–R)]^+$ is assigned to a triplet MLCT ($d\pi$(Ir) $\rightarrow \pi^*$(N^N–R)) excited state. The assignment is supported by the findings that the amine-containing complexes emit at the highest energy, followed by their aldehyde and iodoacetamide counterparts, while the isothiocyanate complexes emit at the lowest energy. In some cases, ^{3}IL emissive states associated with the phen–NH_2 and pq ligands are identified. Amine- and sulfhydryl-containing biological molecules have been labelled with a selection of the luminescent iridium(III) aldehyde, isothiocyanate, and iodoacetamide complexes. Upon photoexcitation, all the bioconjugates display intense and long-lived emission in aqueous buffer at 298 K. The emission of most of the conjugates is assigned to a ^{3}MLCT ($d\pi$(Ir) $\rightarrow \pi^*$(diimine)) excited state. A new bioassay for the cardiac drug digoxin has been developed using one of the luminescent iridium(III)-avidin conjugates (Fig. 10) [73].

The moderately emissive bis(cyclometallated)iridium(III) complexes $[Ir(ppy)_2(solvent)_2]^+$ (solvent = H_2O, CH_3CN) (**33**) contain weakly bound solvent molecules that can be readily displaced by histidine, resulting in the formation of a strongly blue-emitting $[Ir(ppy)_2(histidine)_2]^+$ complex [75]. This property allows the solvato

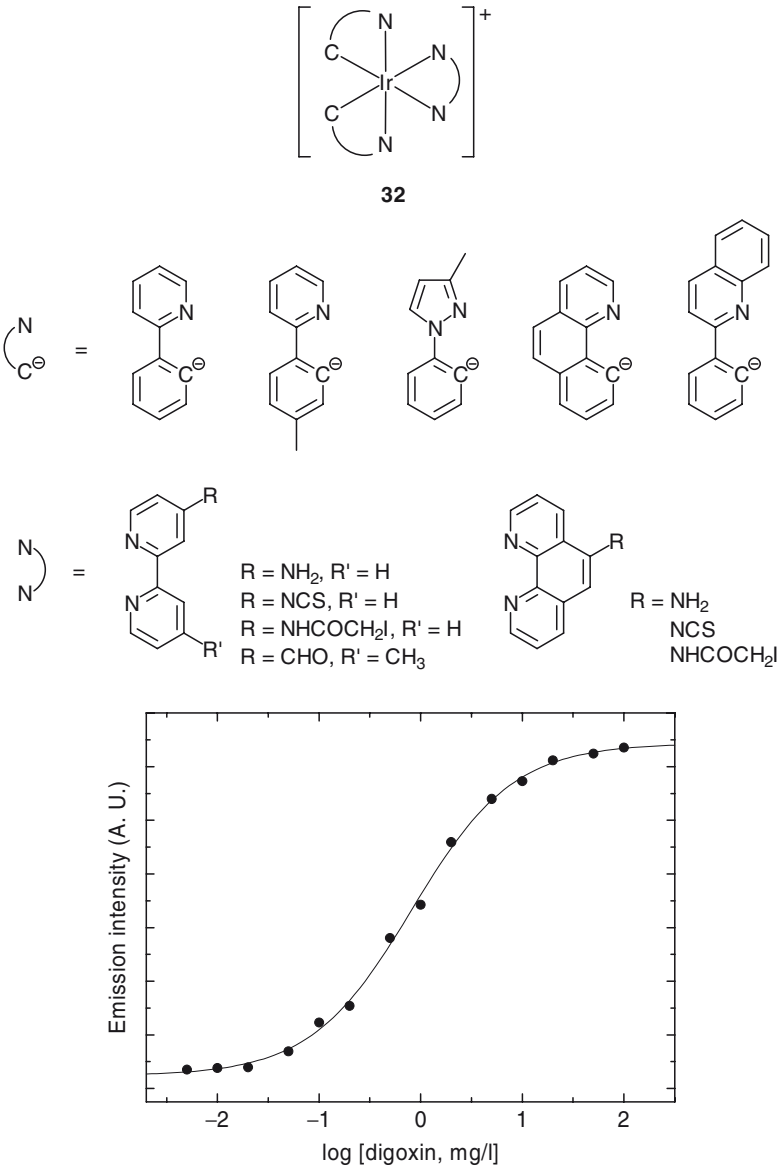

Fig. 10 Results of a heterogeneous competitive assay for digoxin using digoxin–modified microspheres, biotinylated anti–digoxin and the avidin labelled with $[Ir(pq)_2(phen–NCS)]^+$ [73]

complex to function as a switch-on probe for histidine and histidine-rich proteins, and staining agent for gel electrophoresis and Western blots.

Luminescent cyclometallated iridium(III) polypyridine biotin complexes $[Ir(N^C)_2(bpy–CH_2–NH–C2–NH–biotin)]^+$ (N^C = ppy, mppy, ppz, mppz, bzq, pq)

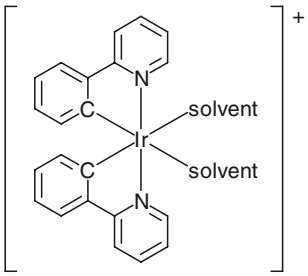

solvent = H_2O, CH_3CN

33

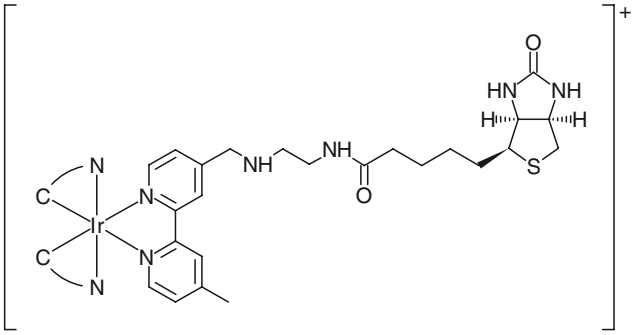

34

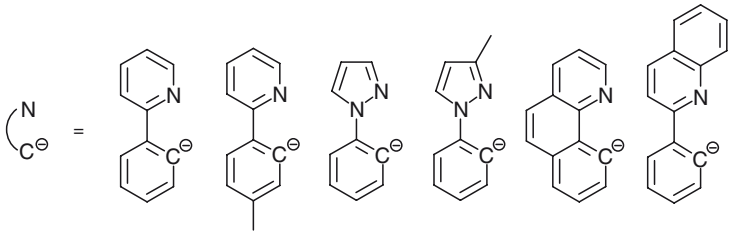

(**34**) have been designed [76]. The intense and long-lived orange to greenish-yellow emission of the complexes has been assigned to an excited state of ^{3}MLCT (dπ(Ir) → π*(N^N)) character. The pq complex [Ir(pq)$_2$(bpy–CH$_2$–NH–C2–NH–biotin)]$^+$, however, shows structured emission spectra and very long emission lifetimes (τ_o = ca. 2–3 μs) in fluid solutions at 298 K, suggestive of substantial ^{3}IL (π → π*) (pq) character in the excited state. Binding of these iridium(III) biotin complexes to avidin is confirmed by HABA assay. Luminescence titrations using the complexes

as titrants show that all the complexes display enhanced emission intensities upon binding to avidin. At the equivalence points, the emission intensities and lifetimes of the complexes are increased by ca. 1.5–3.3-fold. It is noteworthy that the pq complex, being more hydrophobic than the other complexes, exhibits a higher degree of emission enhancement (ca. 3.3) after binding to avidin. On the basis of these results, another series of luminescent cyclometallated iridium(III) arylbenzothiazole biotin complexes $[Ir(N^C)_2(bpy–CONH–C6–NH–biotin)]^+$ (N^C = bt, bsb, btth, bsn) (**35**) of higher hydrophobicity has been synthesised [77]. In solutions at 298 K, these complexes give intense and long-lived (in the microsecond timescale) emission with a much wider range of emission wavelengths (λ_{em} = 528–712 nm) (Fig. 11). In view of very long emission lifetimes and rich structural features of the emission bands, the emission is assigned to a ^{3}IL ($\pi \rightarrow \pi^*$) (N^C) excited state, perhaps with mixing of some ^{3}MLCT ($d\pi(Ir) \rightarrow \pi^*(N^C)$) character. As expected, all these complexes display enhanced emission intensities and extended emission lifetimes upon binding to avidin. Interestingly, the highly hydrophobic biphenyl bsb and naphthyl bsn complexes show very significant emission enhancement factors (8.1 and 5.8, respectively), illustrating the importance of the hydrophobicity of a luminescent protein probe and its detection sensitivity.

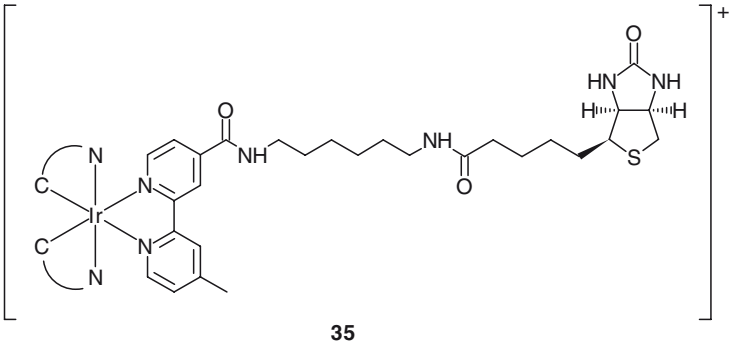

35

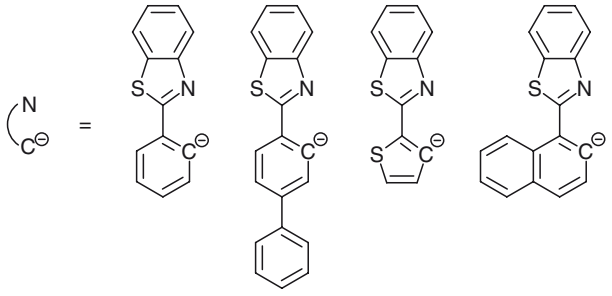

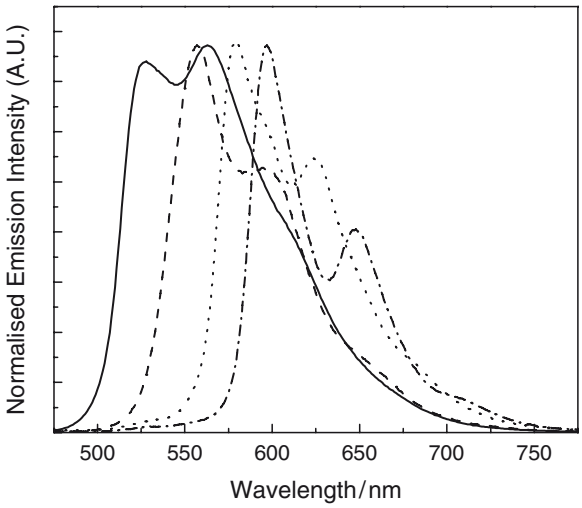

Fig. 11 Emission spectra of $[Ir(N^C)_2(bpy–CO–NH–C6–NH–biotin)]^+$ (N^C = bt (*solid line*), bsb (*broken line*), btth (*dotted line*), and bsn (*broken dotted line*) in degassed CH_2Cl_2 at 298 K [77]

Two cyclometallated iridium(III) biotin complexes with extended planar diimine ligands $[Ir(ppy)_2(N^N–biotin)]^+$ (N^N–biotin = dpq–biotin, dppz–biotin) (**36**) have been isolated [66]. The complexes show typical ^{3}MLCT ($d\pi(Ir) \rightarrow \pi^*(N^N–biotin)$)

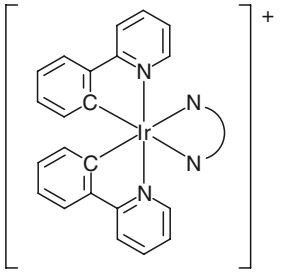

36

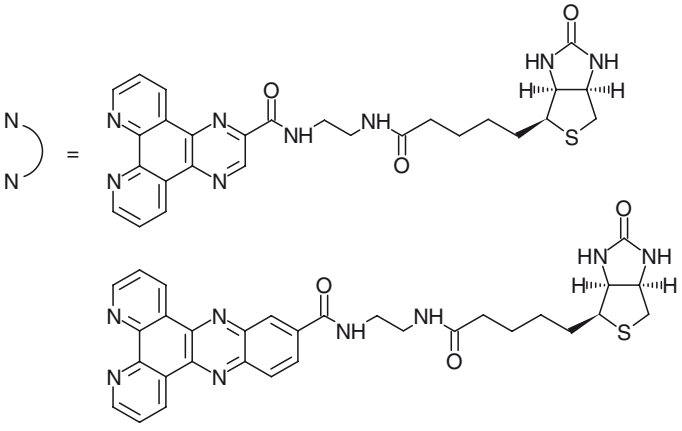

emission at ca. 600 nm in aprotic solvents. However, in aqueous buffer, the complexes are non-emissive, probably due to hydrogen bonding interactions of the amide substituents with water molecules. Both complexes bind to avidin as revealed by HABA assays. Interestingly, in the presence of avidin, the complexes exhibit a new structured emission band at ca. 490, 520 (sh) nm (τ_o = ca. 2 μs), which is much higher in energy than the ^{3}MLCT emission of the complexes (Fig. 12). The emissive state of the avidin-bound complexes is tentatively assigned to ^{3}IL ($\pi \rightarrow \pi^*$) (N^N–biotin).

Hong and co-workers reported a neutral tripod system that consists of emissive iridium(III) bis((4,6-difluorophenyl)pyridinato)picolinate as an energy acceptor (λ_{em} = 472 nm), *N*,*N*′-dicarbazolyl-3,5-benzene as an energy donor, and a biotin pendant (**37**) [78]. Upon binding of the biotin unit to avidin, the donor and acceptor are forced closer to each other by the protein matrix, leading to more efficient energy transfer from the donor to the emitting iridium complex and thus a higher emission intensity (I/I_o = 14).

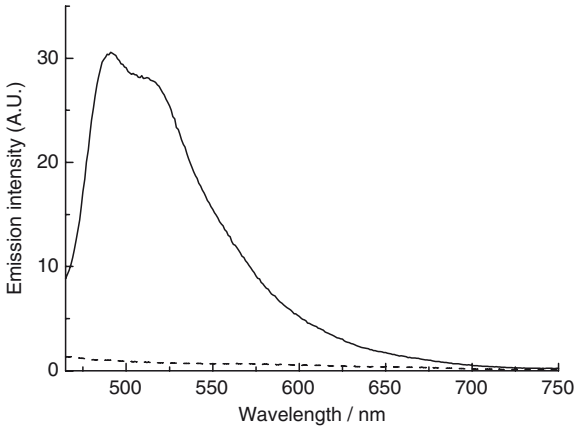

Fig. 12 Emission spectra of complex $[Ir(ppy)_2(dpq–biotin)]^+$ (22 μM) in a mixture of potassium phosphate buffer (50 mM, pH 7.4) and methanol (9:1, v/v) in the absence (*broken line*) and presence (*solid line*) of avidin (5.5 μM) [66]

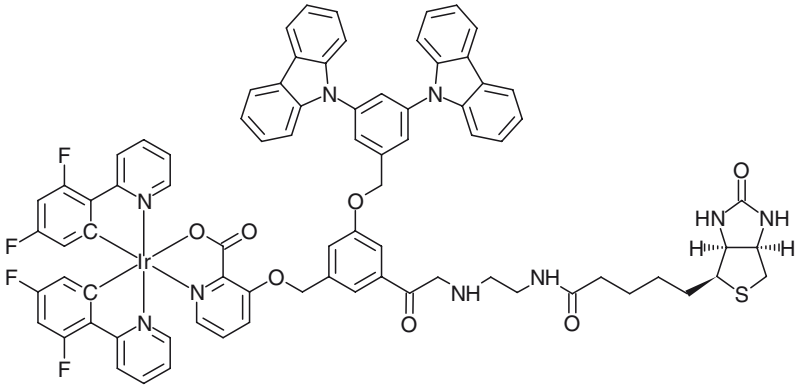

37

Four luminescent cyclometallated iridium(III) diimine complexes [Ir(ppy–spacer-biotin)$_2$(N^N)]$^+$ (N^N = Me$_4$–phen, Ph$_2$–phen) (**38**), each containing two biotin units, have been synthesised and characterised by Lo and co-workers [79]. Photoexcitation of these iridium(III) diimine bis(biotin) complexes in fluid solutions at 298 K and in alcohol glass at 77 K results in intense and long-lived ^{3}MLCT (dπ(Ir) $\rightarrow$ π^*(N^N))/^{3}IL ($\pi \rightarrow \pi^*$) (Me$_4$–phen) emission. HABA assays and emission titrations indicate that the two biotin moieties of each complex are functional. RET-based emission-quenching experiments, microscopy studies using avidin-conjugated microspheres, and HPLC analysis all reveal that the complexes with a

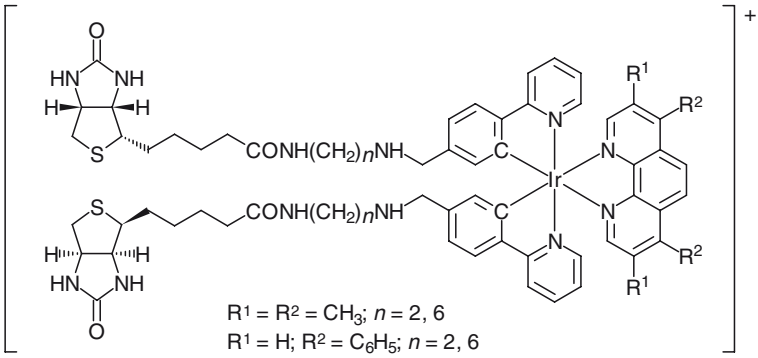

38

longer spacer-arm (distance between the carboxy carbons of biotins, r = ca. 34 Å) are more efficient crosslinkers for avidin, whereas the analogues with a shorter-spacer arm (r = ca. 23 Å) bind to avidin intramolecularly with respect to the protein.

A new series of luminescent cyclometallated iridium(III) bipyridine estradiol conjugates [Ir(N^C)$_2$(bpy–spacer–estradiol)]$^+$ (N^C = ppy, ppz, bzq, pq, bsb) (**39**) has been designed [80]. As expected, all the complexes display intense and long-lived ^{3}MLCT (dπ(Ir) $\rightarrow$ π^*(N^N and N^C))/^{3}IL ($\pi \rightarrow \pi^*$) (N^N and N^C) emission in fluid solutions at 298 K and in low-temperature glass. The lipophilicity of all the complexes, determined by reversed-phase HPLC, is strongly dependent on the nature of the cyclometallating ligands. Upon binding to ERα, all these iridium(III) estradiol conjugates exhibit emission enhancement (I/I_o = 1.3–4.8) and lifetime extension (τ/τ_o = 2.4–7.0) as a result of increased hydrophobicity and rigidity of the local environments of the complexes. In the absence of the protein, the emission of the iridium(III) estradiol complexes is significantly quenched by ferricyanide [Fe(CN)$_6$]$^{3-}$, ($K_{SV} = 9.1 \times 10^4 - 7.4 \times 10^5$ M^{-1}). Interestingly, in the presence of ERα, the quenching becomes much less effective ($K_{SV} = 4.3 \times 10^2 - 2.4 \times 10^3$ M^{-1}), which is ascribed to protection of the complexes by the protein. Thus, the emission titrations are repeated using [Fe(CN)$_6$]$^{3-}$ (100 μM) as a quencher in the solution. Remarkably, the emission intensities of all the complexes are increased by ca.

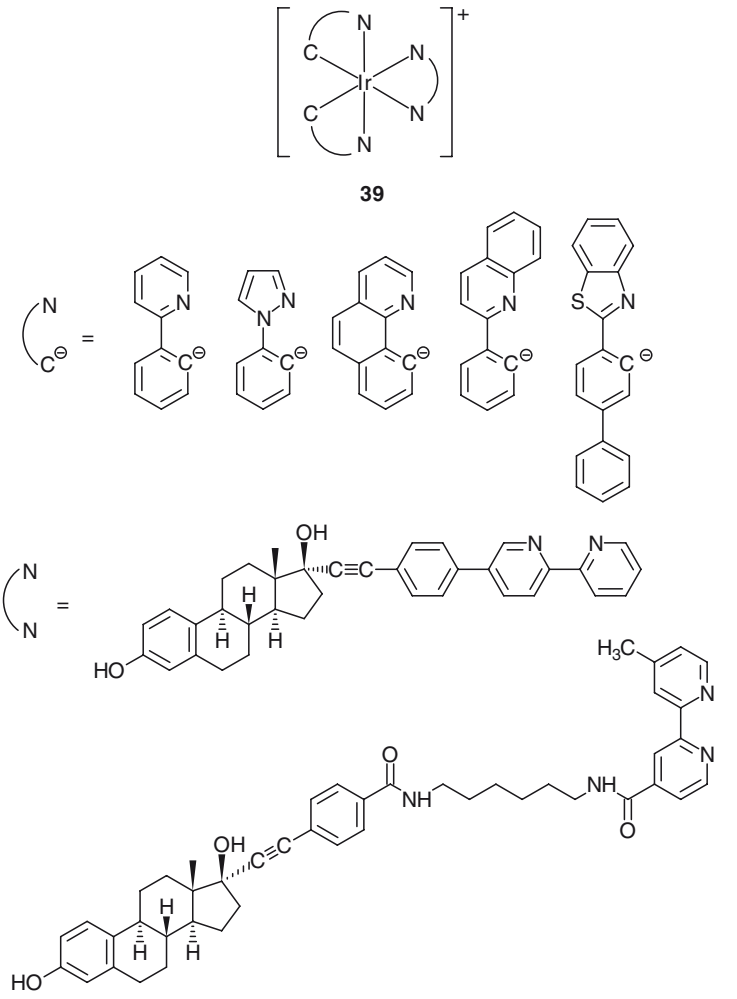

39

7.7–49 times upon binding to the biological receptor (Fig. 13). These interesting results indicate that the complexes act as effective luminescent probes for ERα and are useful in the development of new homogeneous bioassays.

Lo and co-workers designed a series of novel dual-emissive cyclometallated iridium(III) polypyridine complexes [81]. The complex $[Ir(ppy–CH_2NH–C_4H_9)_2(bpy–CONH–C_2H_5)]^+$ (**40**) exhibits dual emission in fluid solutions at room temperature, with a high-energy (HE) structured band at ca. 500 nm (τ_o = 1.1–2.5 μs) and a low-energy (LE) broad band/shoulder at ca. 593 – 619 nm (τ_o = 0.1–0.3 μs). In degassed non-polar solvents such as CH_2Cl_2, the emission intensity of the LE band is higher than or comparable to that of the HE band, whereas in more polar solvents such as CH_3CN and CH_3OH, it becomes much weaker; in aqueous buffer the spectrum is dominated by the HE band (Fig. 14). The HE and LE features are

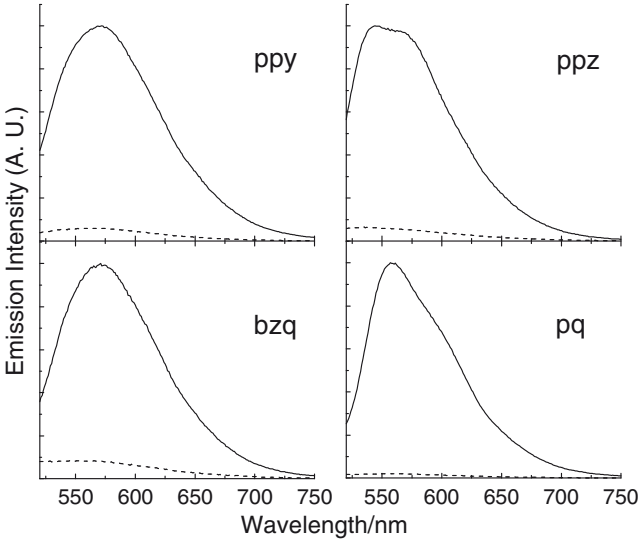

Fig. 13 Emission spectra of complexes $[Ir(N^C)_2(bpy–spacer–estradiol)]^+$ (N^C = ppy, ppz, bzq, pq) in the absence (*broken line*) and presence (*solid line*) of ERα (375 nM) in potassium phosphate buffer (50 mM, pH 7.4)/methanol (9:1, v/v) at 298 K containing 100 μM $[Fe(CN)_6]^{3-}$ [80]

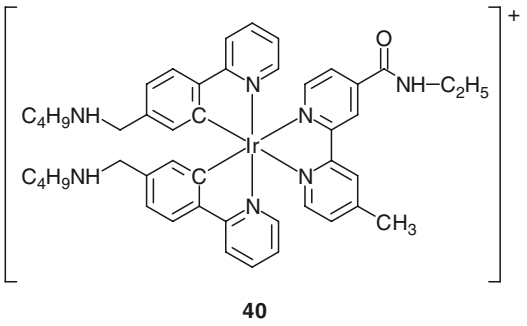

40

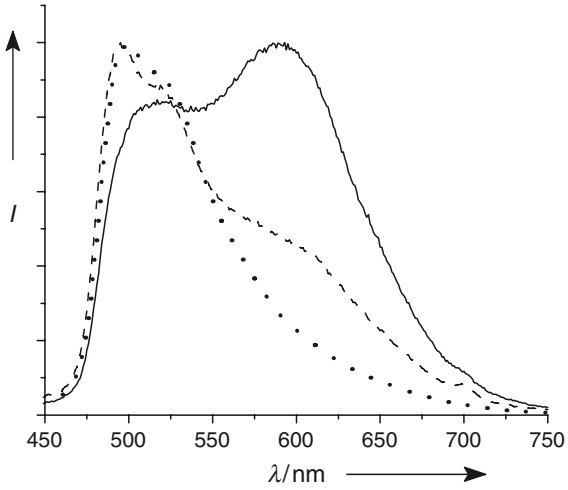

Fig. 14 Normalised emission spectra of $[Ir(ppy–CH_2NH–C_4H_9)_2(bpy–CONH–C_2H_5)]^+$ in degassed CH_2Cl_2 (*solid line*), CH_3CN (*broken line*), and phosphate buffer (*dotted line*) at 298 K [81]

assigned to a ^{3}IL ($\pi \rightarrow \pi^*$) (N^N and N^C) and a ^{3}CT excited state, respectively. Related complexes appended with a biotin, an estradiol, and an octadecyl chain have been designed. Their interesting dual-emissive behaviour has been utilised in the development of luminescent sensors for avidin, estradiol, lipid-binding proteins, and liposome bilayers.

3.3 Cellular Probes

Li and co-workers reported the two cyclometallated iridium(III) complexes $[Ir(dfpy)_2(bpy)]^+$ and $[Ir(dfpy)_2(quqo)]^+$ (**41**) which emit strongly in the green (λ_{em} = 530 nm) and red (λ_{em} = 643 nm), respectively, in DMSO/phosphate buffer solution (pH 7, 1:49, v/v) [82]. Incubation of HeLa cells with 20 μM of either complex in DMSO/PBS (pH 7, 1:49, v/v) leads to intense intracellular luminescence (λ_{em} = 512 and 617 nm, respectively). The exclusive staining in cytoplasm, low cytotoxicity, and reduced photobleaching of the two iridium(III) complexes render them promising candidates for luminescent imaging agents.

Lo and co-workers reported a series of new luminescent cyclometallated iridium(III) polypyridine complexes $[Ir(N^C)_2(N^N)]^+$ (N^C = ppy, ppz, pq; N^N =

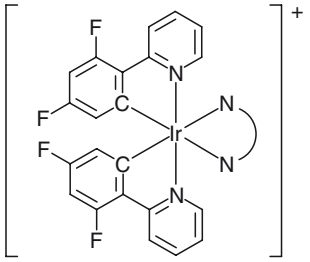

41

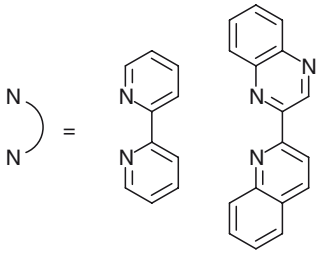

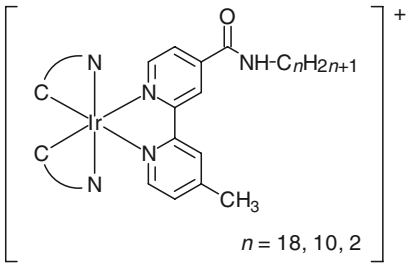

42

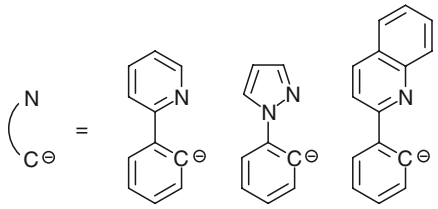

bpy–CONH–$C_{18}H_{37}$, bpy–CONH–$C_{10}H_{21}$, bpy–CONH–C_2H_5) (**42**) bearing an alkyl pendant [83]. Upon irradiation, all the complexes exhibit intense and long-lived ^{3}MLCT (dπ(Ir) $\rightarrow$ π*(N^N)) emission in homogeneous fluid solutions at 298 K and in alcohol glass at 77 K. All the complexes have been incorporated into phospholipid vesicles composed of DSPC and the resulting liposomes have been examined by cryo-TEM and luminescence spectroscopy. The emission properties of the complexes in aqueous solutions containing the surfactants SDS, TX, and CTAB have been studied. Additionally, the cytotoxicity of these iridium(III) complexes towards the HeLa cell line has been evaluated by MTT assays (Fig. 15). The cellular uptake of all the complexes by HeLa cells has been examined by flow cytometry and laser-scanning confocal microscopy. Incubation of HeLa cells with one of the complexes at 37°C under a 5% CO_2 atmosphere for 5 h led to efficient cellular interiorisation. Most of the complex molecules are distributed inside the cytoplasm with a lower extent of nuclear uptake. Importantly, a higher degree of localisation of the complexes in the perinuclear region is likely to result from the interactions of the complex molecules with hydrophobic organelles such as endoplasmic reticulum, mitochondria, and Golgi apparatus. When the cells are incubated at 4°C, no internalisation is observed, implying that the cellular uptake of the complex and its subsequent localisation are due to energy-requiring processes such as endocytosis [84]. These interesting results emphasise the potential of luminescent iridium(III) polypyridine complexes as intracellular imaging reagents and in vivo luminescent probes.

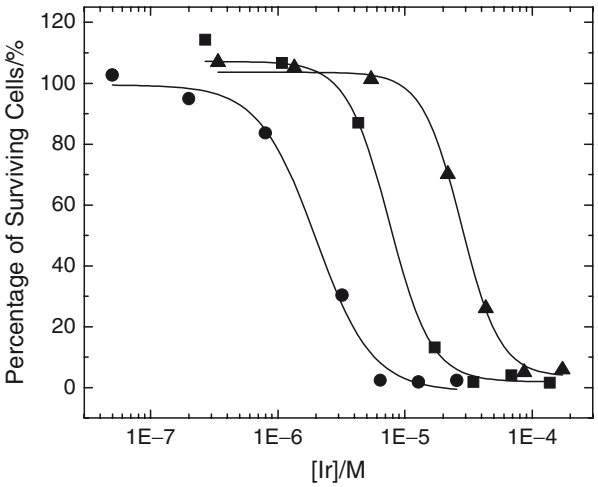

Fig. 15 Dose dependence of surviving HeLa cells after exposure to $[Ir(ppz)_2(N^N)]^+$ (N^N = bpy–CONH–$C_{18}H_{37}$ (*filled square*), bpy–CONH–$C_{10}H_{21}$ (*filled circle*), bpy–CONH–C_2H_5 (*filled triangle*)) for 48 h [83]

4 Conclusion

Herein we reviewed the use of luminescent organometallic rhenium(I) and iridium(III) complexes as biological probes, which has attracted enormous interest in the past decade. Traditionally, the role of luminescent transition metal complexes in biological studies has been dominated by ruthenium(II) polypyridine complexes owing to their well-documented emission properties. However, as illustrated by the examples described herein, the unique, versatile, and highly variable emissive behaviour of rhenium(I) and iridium(III) polypyridine probes has qualified them as promising candidates in this exciting research area at the interface of chemistry and biology. Indeed, the high structural variation and rich photophysical and photoredox properties of these complexes allow them to act as a new generation of probes in studies of the structures and dynamics of biomolecules such as DNA, peptides, and proteins at the molecular level. With the knowledge of the interactions of these complexes with fundamental biological molecules, a recent exciting focus is the role of these complexes in understanding more complex biological systems. In this context, reports on the cytotoxicity, cellular uptake, and live-cell imaging associated with this class of complexes have emerged recently. It is anticipated that with the interesting structural and photophysical characteristics of organometallic rhenium(I) and iridium(III) complexes, more effective probes for a fundamental understanding of biological structures and processes, and various analytical, diagnostic, and therapeutic purposes can be developed.

Acknowledgements I would like to thank the Hong Kong Research Grants Council and City University of Hong Kong for financial support. I am very grateful to previous and current members of my research group for their hard work and assistance in the preparation of this article, and to my collaborators, whose names appear in the reference list.

References

1. Haugland RP (2005) The handbook – a guide to fluorescent probes and labeling technologies, 10th edn. Molecular Probes, Eugene, OR
2. Sammes PG, Yahioglu G (1996) Nat Prod Rep 13:1
3. Lo KKW, Tsang KHK, Sze KS, Chung CK, Lee TKM, Zhang KY, Hui WK, Li CK, Lau JSY, Ng DCM, Zhu N (2007) Coord Chem Rev 251:2292
4. Blasius R, Moucheron C, Kirsch-De Mesmaeker A (2004) Eur J Inorg Chem:3971
5. Terpetschnig E, Szmacinski H, Lakowicz JR (1997) Methods Enzymol 278:295
6. McMillin DR, McNett KM (1998) Chem Rev 98:1201
7. Erkkila KE, Odom DT, Barton JK (1999) Chem Rev 99:2777
8. Metcalfe C, Thomas JA (2003) Chem Soc Rev 32:215
9. Pierard F, Kirsch-De Mesmaeker A (2006) Inorg Chem Commun 9:111
10. Hermanson GT (1996) Bioconjugate techniques. Academic, San Diego
11. Winkler JR, Gray HB (1992) Chem Rev 92:369
12. Wrighton MS, Morse DL (1974) J Am Chem Soc 96:998
13. Lees AJ (1987) Chem Rev 87:711
14. Balzani V, Scandola F (1990) Supramolecular photochemistry. Ellis Horwood, New York
15. Kalyanasundaram K (1991) Photochemistry of polypyridine and porphyrin complexes. Academic, San Diego
16. Roundhill DM (1994) Photochemistry and photophysics of metal complexes. Plenum, New York
17. Thornton NB, Schanze KS (1993) Inorg Chem 32:4994
18. Thornton NB, Schanze KS (1996) New J Chem 20:791
19. Oriskovich TA, White PS, Thorp HH (1995) Inorg Chem 34:1629
20. Stoeffler HD, Thornton NB, Temkin SL, Schanze KS (1995) J Am Chem Soc 117:7119
21. Yam VWW, Lo KKW, Cheung KK, Kong RYC (1995) J Chem Soc Chem Commun:1191
22. Yam VWW, Lo KKW, Cheung KK, Kong RYC (1997) J Chem Soc Dalton Trans:2067
23. Metcalfe C, Webb M, Thomas JA (2002) Chem Commun:2026
24. Foxon SP, Phillips T, Gill MR, Towrie M, Parker AW, Webb M, Thomas JA (2007) Angew Chem Int Ed 46:3686
25. Wei L, Babich J, Eckelman WC, Zubieta J (2005) Inorg Chem 44:2198
26. Lo KKW, Ng DCM, Hui WK, Cheung KK (2001) J Chem Soc Dalton Trans:2634
27. Lo KKW, Hui WK, Ng DCM, Cheung KK (2002) Inorg Chem 41:40
28. Connick WB, Di Bilio AJ, Hill MG, Winkler JR, Gray HB (1995) Inorg Chim Acta 240:169
29. Di Bilio AJ, Crane BR, Wehbi WA, Kiser CN, Abu-Omar MM, Carlos RM, Richards JH, Winkler JR, Gray HB (2001) J Am Chem Soc 123:3181
30. Miller JE, Di Bilio AJ, Wehbi WA, Green MT, Museth AK, Richards JH, Winkler JR, Gray HB (2004) Biochim Biophys Acta 1655:59
31. Blanco-Rodriguez AM, Busby M, Grădinarudinaru C, Crane BR, Di Bilio AJ, Matousek P, Towrie M, Leigh BS, Richards JH, Vlček Jr A, Gray HB (2006) 128:4365
32. Belliston-Bittner W, Dunn AR, Nguyen YHL, Stuehr DJ, Winkler JR, Gray HB (2005) J Am Chem Soc 127:15907
33. Szmacinski H, Terpetschnig E, Lakowicz JR (1996) Biophys Chem 62:109
34. Guo XQ, Castellano FN, Li L, Szmacinski H, Lakowicz JR, Sipior J (1997) Anal Biochem 254:179
35. Dattelbaum JD, Abugo OO, Lakowicz JR (2000) Bioconjugate Chem 11:533

36. Stephenson KA, Banerjee SR, Besanger T, Sogbein OO, Levadala MK, McFarlane N, Lemon JA, Boreham DR, Maresca KP, Brennan JD, Babich JW, Zubieta J, Valliant JF (2004) J Am Chem Soc 126:8598
37. Banerjee SR, Schaffer P, Babich JW, Valliant JF, Zubieta J (2005) Dalton Trans:3886
38. Wilchek M, Bayer EA (1990) Methods in enzymology. Academic, San Diego, CA
39. Savage MD, Mattson G, Desai S, Nielander GW, Morgensen S, Conklin EJ (1992) Avidin-biotin chemistry: a handbook. Pierce Chemical, Rockford, IL
40. Gruber HJ, Hahn CD, Kada G, Riener CK, Harms GS, Ahrer W, Dax TG, Knaus HG (2000) Bioconjugate Chem 11:696
41. Lo KKW, Hui WK, Ng DCM (2002) J Am Chem Soc 124:9344
42. Lo KKW, Hui WK (2004) Inorg Chem 43:5275
43. Lo KKW, Tsang KHK, Sze KS (2006) Inorg Chem 45:1714
44. Lo KKW, Tsang KHK (2004) Organometallics 23:3062
45. Ishida T, Hamada M, Inoue M, Wakahara A (1990) Chem Pharm Bull 38:851
46. Bartel B (1997) Annu Rev Plant Physiol 48:51
47. Bilang J, Macdonald H, King PJ, Sturm A (1992) Plant Physiol 102:29
48. Dolušsić E, Kowalczyk M, Magnus V, Sandberg G, Normanly J (2001) Bioconjugate Chem 12:152
49. Mazzini A, Cavatorat P, Iori M, Favilla R, Sartor G (1992) Biophys Chem 42:101
50. Lo KKW, Tsang KHK, Hui WK, Zhu N (2003) Chem Commun:2704
51. Lo KKW, Tsang KHK, Hui WK, Zhu N (2005) Inorg Chem 44:6100
52. Lo KKW, Sze KS, Tsang KHK, Zhu N (2007) Organometallics 26:3440
53. Parker PM, Parker JN (2004) Estradiol – A medical dictionary, bibliography, and annotated research guide to internet references. ICON Health, San Diego, CA
54. Nilsson S, Gustafsson JÅ (2002) Crit Rev Biochem Mol Biol 37:1
55. Lo KKW, Tsang KHK, Zhu N (2006) Organometallics 25:3220
56. Katzenellenbogen JA, Johnson Jr HJ, Myers HN (1973) Biochemistry 12:4085
57. Luyt LG, Bigott HM, Welch MJ, Katzenellenbogen JA (2003) Bioorg Med Chem 11:4977
58. Cassino C, Gabano E, Ravera M, Cravotto G, Palmisano G, Vessières A, Jaouen G, Mundwiler S, Alberto R, Osella D (2004) Inorg Chim Acta 357:2157
59. Vitor RF, Correia I, Videira M, Marques F, Paulo A, Pessoa JC, Viola G, Martins GG, Santos I (2008) ChemBioChem 9:131
60. Amoroso AJ, Coogan MP, Dunne JE, Fernandez-Moreira V, Hess JB, Hayes AJ, Lloyd D, Millet C, Pope SJA, Williams C (2007) Chem Commun:3066
61. Amoroso AJ, Arthur RJ, Coogan MP, Court JB, Fernández-Moreira V, Hayes AJ, Lloyd D, Millet C, Pope SJA (2008) New J Chem 32:1097
62. Lo KKW, Louie MW, Sze KS, Lau JSY (2008) Inorg Chem: 47:602
63. Dixon IM, Collin JP, Sauvage JP, Flamigni L, Encinas S, Barigelletti F (2000) Chem Soc Rev 29:385
64. Williams JAG, Wilkinson AJ, Whittle VL (2008) Dalton Trans:2081
65. Lo KKW, Ng DCM, Chung CK (2001) Organometallics 20:4999
66. Lo KKW, Chung CK, Zhu N (2006) Chem Eur J 12:1500
67. Shao F, Elias B, Lu W, Barton JK (2007) Inorg Chem 24:10187
68. Shao F, Barton JK (2007) J Am Chem Soc 129:14733
69. Herebian D, Sheldrick WS (2002) J Chem Soc Dalton Trans:966
70. Gençaslan S, Sheldrick WS (2005) Eur J Inorg Chem:3840
71. Schäfer S, Ott I, Gust R, Sheldrick WS (2007) Eur J Inorg Chem:3034
72. Lo KKW, Chung CK, Zhu N (2003) Chem Eur J 9:475
73. Lo KKW, Chung CK, Lee TKM, Lui LH, Tsang KHK, Zhu N (2003) Inorg Chem 42:6886
74. Lo KKW, Chan JSW, Chung CK, Tsang VWH, Zhu N (2004) Inorg Chim Acta 357:3109
75. Ma DL, Wong WL, Chung WH, Chan FY, So PK, Lai TS, Zhou ZY, Leung YC, Wong KY (2008) Angew Chem Int Ed 47:3735
76. Lo KKW, Chan JSW, Lui LH, Chung CK (2004) Organometallics 23:3108
77. Lo KKW, Li CK, Lau JSY (2005) Organometallics 24:4594
78. Kwon TH, Kwon J, Hong JI (2008) J Am Chem Soc 130:3726

79. Lo KKW, Lau JSY (2007) Inorg Chem 46:700
80. Lo KKW, Zhang KY, Chung CK, Kwok KY (2007) Chem Eur J 13:7110
81. Lo KKW, Zhang KY, Leung SK, Tang MC (2008) Angew Chem Int Ed 47:2213
82. Yu M, Zhao Q, Shi L, Li F, Zhou Z, Yang H, Yi T, Huang C (2008) Chem Commun:2115
83. Lo KKW, Lee PK, Lau JSY (2008) Organometallics 27:2998
84. Reaven E, Tsai L, Azhar SJ (1996) Biol Chem 271:16208

Top Organomet Chem (2010) 29: 159–191
DOI: 10.1007/3418_2009_1

Published online: 13 June 2009

Platinum^{II} Acetylide Photophysics

Maria L. Muro, Aaron A. Rachford, Xianghuai Wang, and Felix N. Castellano

Abstract The photophysics of Pt^{II} acetylide chromophores represents an important emergent area of research and development. The present review exclusively deals with photophysical processes in square planar Pt^{II} complexes of the general formulae: $Pt(N^N)(C{\equiv}CR)_2$, $[Pt(N^N^N)(C{\equiv}CR)]^+$, $Pt(N^N^C)(C{\equiv}CR)$, *trans*-$Pt(PR_3)_2(C{\equiv}CR)_2$, and *cis*-$Pt(P^P)(C{\equiv}CR)_2$, where N^N is a bidentate 2,2'-bipyridine, N^N^N and N^N^C are tridentate polypyridines, PR_3 is a monodentate phosphine and P^P is a bidentate phosphine ligand. These molecules exhibit a range of photophysical attributes depending upon the nature of the lowest electronic triplet excited state(s) which are either charge-transfer, ligand-localized, or an admixture of the two. Under special circumstances, intermolecular interactions further complicate the electronic structures of the ground and excited states and the resulting spectroscopy. Recent computational approaches emphasizing the successful application of DFT and TD-DFT methods towards understanding the absorption and emission processes of these chromophores are also presented.

Keywords Chromophores • Electron transfer • Energy transfer • Excited-state chemistry • Metal–organic chromophores • Photoluminescence • Photophysics • Platinum

Contents

1 Introduction and Scope 160
2 Pt^{II} Acetylides with Bidentate Polypyridyl Ligands 161
2.1 Background 161
2.2 $[Pt(N^N)(C{\equiv}CR)_2]$ Complexes 161
3 Pt^{II} Acetylide Complexes Containing Tridentate Polypyridyl Ligands 167
3.1 Background 167
3.2 $[Pt(N^N^N)(C{\equiv}CR)]^+$ Complexes 168
3.3 Pt^{II} Acetylide Complexes with Other Tridentate Polypyridyl Ligands 175
4 Pt^{II} Acetylides with Phosphine-Containing Ligands 177
4.1 Introduction 177
4.2 Photophysics of Pt–Acetylide Phosphine Chromophores 177

M.L. Muro, A.A. Rachford, X. Wang, and F.N. Castellano (✉)
Department of Chemistry and Center for Photochemical Sciences,
Bowling Green State University, Bowling Green, OH 43403, USA
e-mail: castell@bgsu.edu

5 Electronic Structures of Platinum Acetylides 181
6 Concluding Remarks..... 187
References 188

1 Introduction and Scope

Element 78 of the periodic table is the late transition metal platinum whose four-coordinate square-planar d^8 Pt^{II} complexes provide the inspiration for this work. Given the enormity of the field, the present contribution focuses exclusively on the photophysics, with some brief photochemistry highlights, of Pt^{II} chromophores bearing at least one alkyl or aryl acetylide (C≡CR) ligand. Depending upon the nature of the remaining ligands, these species can exhibit a variety of unique ground and excited-state configurations with concomitant photophysical attributes. This is particularly intriguing when the arylacetylide structure encompasses a chromophore with low-lying singlet and triplet manifolds. The presence of the internal heavy atom with a large spin–orbit coupling constant substantially accelerates singlet→triplet intersystem crossing (ISC) in these molecules, rapidly producing the lowest triplet state on ultrafast time scales and yielding strong triplet-based photoluminescence (triplet→singlet) on the order of microseconds in most instances. The latter opens the pathway for bimolecular diffusion-controlled excited-state chemistry crucial for light-to-chemical energy conversion and generates extremely bright phosphorescence suitable for organic light-emitting diode (OLED) technology. The coordinative unsaturation of the square planar metal center provides a conduit wherein the filled nonbonding d_z^2 orbital promotes intimate interactions with other Pt^{II} molecules in addition to entities such as Lewis basic solvents. The former processes are almost universally studied in the solid state and many researchers utilize bulky ligand structures along with low (μM) concentrations to circumvent intermolecular metal–metal (σ) interactions in solution. However, some researchers, Vivian Yam in particular, have dedicated significant effort towards understanding the photophysics of aggregates resulting from Pt^{II} intermolecular interactions in solution. As the reader proceeds, he/she will realize that the photophysical processes in this class of chromophores is quite rich, amalgamating the properties of traditional coordination complexes and organometallics with the same chemical structure.

The following sections are purposely separated into specific structural classes of square planar Pt^{II} complexes of the general formulae: $Pt(N^N)(C{\equiv}CR)_2$, $[Pt(N^N^N)(C{\equiv}CR)]^+$, $Pt(N^N^C)(C{\equiv}CR)$, *trans*-$Pt(PR_3)_2(C{\equiv}CR)_2$, and *cis*-$Pt(P^P)(C{\equiv}CR)_2$, where N^N is a bidentate 2,2′-bipyridine, N^N^N and N^N^C are tridentate polypyridines, PR_3 is a monodentate phosphine, and P^P is a bidentate phosphine ligand. The final section of this work is dedicated to recent electronic structure calculations on these molecules with an emphasis on the successful application of DFT (density functional theory) and TD-DFT (time-dependent density functional theory) methods towards understanding the absorption and emission processes of these chromophores.

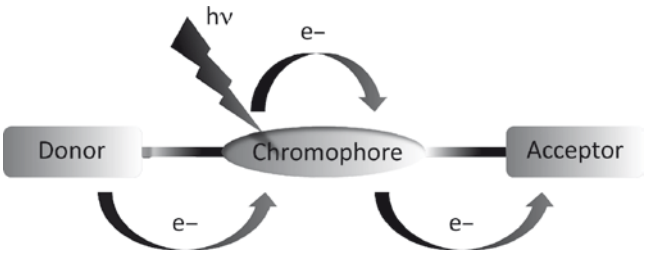

Fig. 1 Schematic of the methodology used for intramolecular photoinduced charge separation in metal–organic charge-transfer chromophores

2 Pt^{II} Acetylides with Bidentate Polypyridyl Ligands

2.1 Background

There has been a recent surge in research related to the photophysics and photochemistry of Pt^{II} chromophores bearing acetylide linkages. Consequently, there have been a number of outstanding reviews to this end on a variety of related subjects [1–4]. For example, a nicely detailed account of the photophysics of Pt^{II} complexes was recently presented by J. A. Gareth Williams that included sections on bidentate N^N ligands and acetylides along with related structural classes [4]. Other recent interest concerning these chromophores has focused on the ability to produce intramolecular charge-separated species by providing appropriate derivatives either on the acetylide moiety or on the π-acceptor charge-transfer (CT) ligand, Fig. 1. This type of arrangement allows the metal center to act as a bridge between said donors and acceptors while producing a visible-absorbing sensitizer to initiate photoinduced charge separation. In an effort to prevent significant overlap with the discussion of featured subjects in these reviews, the reader is strongly encouraged to consult these articles as they highlight many relevant papers that have been put forth over the past decade. For the purposes of highlighting the most recent discoveries and innovations in this field, we will briefly discuss relevant publications, some of which are mentioned in these previous reviews, while emphasizing the most contemporary work in the field.

2.2 [Pt(N^N)(C≡CR)$_2$] Complexes

The first published report on a photoluminescent CT Pt^{II} acetylide chromophore appeared in 1994 [5]. This field remained rather dormant until 1997 when the synthesis of Pt(dbbpy)(CCPh)$_2$ appeared from James and coworkers [6], which is currently considered one of the benchmark chromophores in this class of molecules. It was not until 2000 that Eisenberg and coworkers investigated the detailed photophysics of two series of Pt^{II} acetylide CT structures displaying variation in the N^N CT ligand using different bpy and phen derivatives [7]. This study demonstrated the profound substituent

influence on the charge-transfer ligands while little variation in energy of the excited state was observed when the substituent of the arylacetylide was modified. The Eisenberg group also incorporated the acetylide motif in the design of a molecular triad such that charge separation is observed through the intramolecular formation of a phenothiazine (PTZ) radical cation and nitrobenzene radical anion via transient absorption (TA) spectroscopy upon visible excitation at 405 nm [8]. In 2001, the Schanze group published a detailed investigation on the electronic effects of the excited state when changing substituents on the acetylide moiety as well as varying the electronic nature of the bipyridyl ligand [9]. Within this series of complexes, it was demonstrated that for most cases, the photophysics of these chromophores were dominated by the low-energy ^{3}CT excited state. Quantitative analysis of the nonradiative rate constant (k_{nr}) showed that k_{nr} decreased logarithmically as the ^{3}CT energy increased. Briefly, tuning the emission maximum from 670 to 553 nm resulted in a two order of magnitude decrease of k_{nr} from 4.98×10^7 s^{-1} to 5.6×10^5 s^{-1}. This clearly established a quantitative energy gap law relationship for the ^{3}CT emission processes in this class of chromophores, similar to other complexes displaying ^{3}MLCT (metal-to-ligand charge transfer) excited states.

In 2003, Eisenberg utilized picosecond transient absorption spectroscopy to investigate the intramolecular excited-state quenching of molecular dyads which incorporate bipyridyl derivatives as the charge-transfer ligand while the arylacetylide was substituted with the electron donor phenothiazine (**2.1**) [10]. These studies showed that charge-separation occurred in the Marcus normal region while charge-recombination occurred in the inverted region. This investigation also demonstrated that intramolecular excited-state quenching could be modulated by taking advantage of the solvent sensitive nature of the ^{3}CT excited state. In agreement with the negative solvatochromic nature of these complexes, the ^{3}CT excited state could be lowered sufficiently relative to the CS excited state so that inversion of the two states occurs. In 2005 similar work along these lines demonstrated a facile synthetic pathway to produce related chromophores which also exhibited an efficient intramolecular charge-separated state [11].

In 2003, the first report from our group in this area, demonstrated the utility of incorporating Pt^{II} acetylide linkages to produce long-lived phosphorescence from the

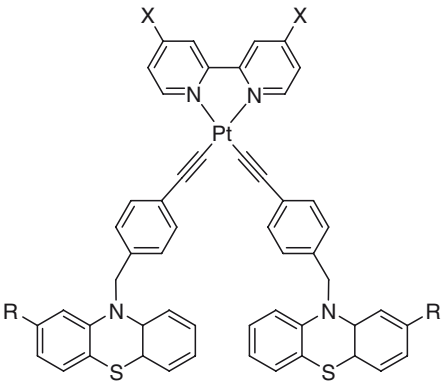

2.1

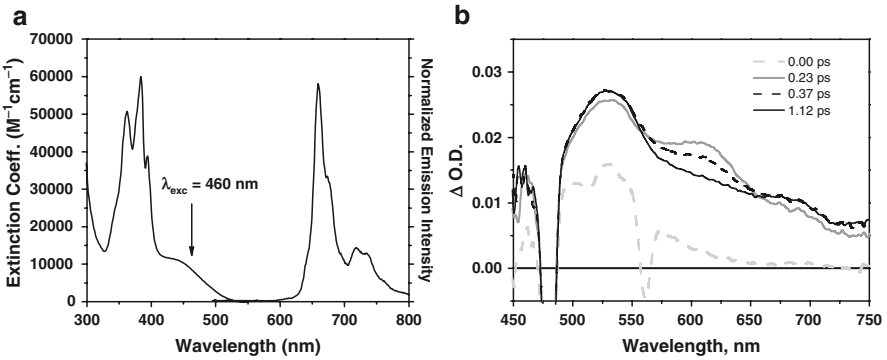

Fig. 2 Absorption and emission (**a**) and ultrafast transient absorption (**b**) of **2.3** in deaerated CH_2Cl_2 and 2-MeTHF, respectively

appended arylacetylide [12]. Specifically, the long-lived (48 μs) room temperature red phosphorescence of pyrenylacetylide (intraligand triplet state, ^{3}IL) was intramolecularly sensitized to visible excitation using the low energy Pt → π* ^{1}CT absorption band in **2.3**, see Fig. 2a. Here we note that the long wavelength structured phosphorescence indicates that the lowest-energy excited state is indeed centered on pyrenylacetylide. The solvent-sensitive nature of the ^{3}CT excited state was taken advantage of in another contribution from our group in 2004 in **2.2** [13]. Through judicious choice of solvent, the lowest-energy excited state could be tuned to exhibit predominant ^{3}CT (low polarity) or ^{3}IL (high polarity) character, the ^{3}IL state being localized on the naphthylacetylide chromophore. Further excited-state switching was demonstrated between RT and 77 K glasses of varying polarity. In particular, the lowest-energy excited states changed from ^{3}CT to mostly ^{3}IL character as these solutions were cooled from 298 to 77 K. However, a pure ^{3}IL or ^{3}CT could not be definitively assigned at any temperature as the excited-state characteristics typically showed a combination of both states in all experiments, including nanosecond laser flash photolysis. In 2005, we continued our investigation of **2.3** utilizing ultrafast transient absorption spectrometry (Fig. 2b), showing that the lowest-energy ^{3}IL pyrenylacetylide excited state is formed in 240 ± 40 fs [14]. Specifically, the excited-state absorption at 610 nm (attributed to contributions from both ^{3}CT excited state and the ^{3}IL state) decays with a time constant of 240 fs. Thus, we interpreted that the ^{3}IL was formed within 240 fs. These results suggested that the energetically proximate ^{3}CT state accelerated the formation of the triplet state of the pendant pyrenylacetylide. We continued to tune the excited-state properties using similar molecular motifs, eventually producing high quantum efficiency green photoluminescence by changing the relative σ-donor strength of the pendant alkylacetylides [15]. Here it is also important to note that we have recently studied, in collaboration with Julia Weinstein, the ultrafast time-resolved IR spectroscopy of [Pt(dnpebpy)(C≡Cnaph)$_2$], a derivative of **2.2**, and observe shifts in both ν(C≡O) and ν(C≡C) consistent with a charge-transfer assignment in dichloromethane [16].

In 2006, we sought to further investigate the influence of the acetylide framework by incorporating a chelating diacetylide into the square planar Pt^{II} platform, namely

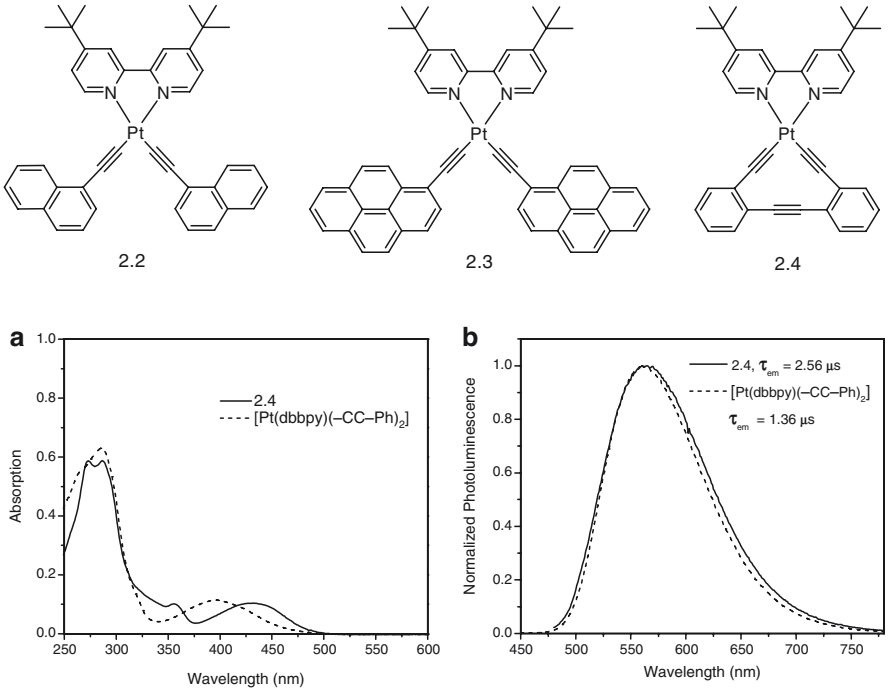

Fig. 3 Room temperature absorption (**a**) and emission (**b**) spectra of **2.4** and [Pt(dbbpy)(C≡CPh)$_2$] in deaerated CH_2Cl_2

Pt(dbbpy)(tda), **2.4** [17]. The initial work discussed the steady-state absorption and emission (RT and 77 K) along with emission lifetimes as well as electrochemistry, revealing that cyclometallation of the two acetylides into one chelating ligand imposed substantial rigidity into the system. The planarity and added rigidity leads to a lower-energy absorbing chromophore with enhanced photophysics relative to the non-macrocyclic analog Pt(dbbpy)(C≡CPh)$_2$. The absorption and emission of **2.4** in CH_2Cl_2 are depicted in Fig. 3. Upon substitution of the two monodentate -C≡CPh ligands by tda, the absorption shifts to lower energy from 397 to 427 nm. Although the emission maxima are similar, we note the emission lifetime of **2.4** is significantly longer (τ = 2.56 μs) than Pt(dbbpy)(C≡CPh)$_2$ (τ = 1.36 μs). There is also a corresponding increase in the emission quantum yields measured for both structures, 0.51 and 0.75 for Pt(dbbpy)(C≡CPh)$_2$ and **2.4**, respectively. Also of interest, 77 K emission measurements revealed the presence of tda-based ligand-localized phosphorescence in the low-temperature glass. This chromophore was then the subject of a more detailed examination in 2007, using a variety of electrochemical and spectroscopic techniques (including the single crystal X-ray structure) as well as theoretical calculations in an effort to more fully elucidate the nature of the ground and excited–state structures [18]. The full examination of this chromophore along with appropriate model chromophores further confirmed our earlier excited-state assignments, namely that the lowest RT excited state is purely ^{3}CT in nature with no contributions from the ^{3}IL states of the pendant tda cyclometallated ligand. More recent efforts from our group have produced

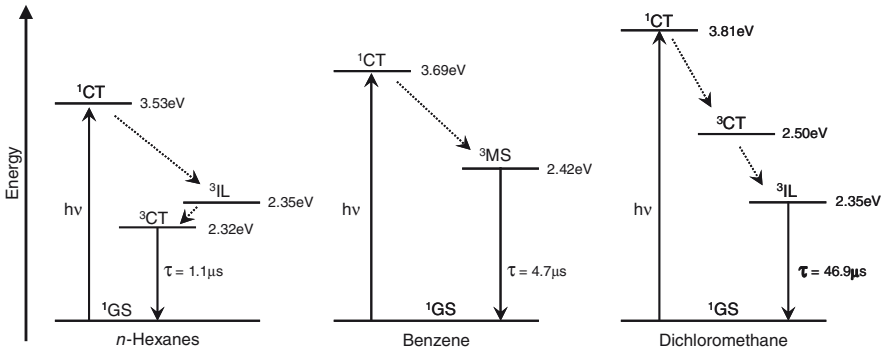

Fig. 4 Energy diagram depicting the solvent effect on the excited states and lifetime of **2.5**

Pt^{II} complexes possessing extensively conjugated aromatic organic chromophores tethered to the metal center via acetylide linkages, described in detail below.

Another recent effort from our group has produced molecular platform **2.5** containing the dbbpy charge-transfer ligand with two appended PE3 acetylides [19]. The PE3 ligand is highly conjugated, a phenyleneethynylene oligomer with three phenyl units, possessing low-energy π–π* transitions extending to ~400 nm. The ^{3}IL and ^{3}MLCT excited states are energetically proximate within this acetylide chromophore so that the solvent tuning ability demonstrated by us previously is now able to fully invert the lowest-energy excited state. As the polarity of the solvent is changed from nonpolar to polar, the steady-state emission and lifetimes changes from purely ^{3}CT to purely ^{3}IL in nature. Shown in Fig. 4 is a depiction of how the solvent affects the energetically proximate excited states in **2.5**. The solvent sensitive ^{3}CT excited state is shifted from 2.32 eV in hexanes to 2.50 eV in dichloromethane while the solvent insensitive ^{3}IL of PE3 remains constant at 2.35 eV in both solvent extremes. The shift of the ^{3}CT provides the necessary perturbation to obtain complete excited-state inversion upon going from hexanes to dichloromethane. The emission profiles quantitatively match the appropriate model chromophores as do the emission lifetimes, leaving little doubt about the spectroscopic assignments.

In addition to state inversion, we have also recently expanded the triplet excited-state sensitization of organic chromophores which typically do not display facile

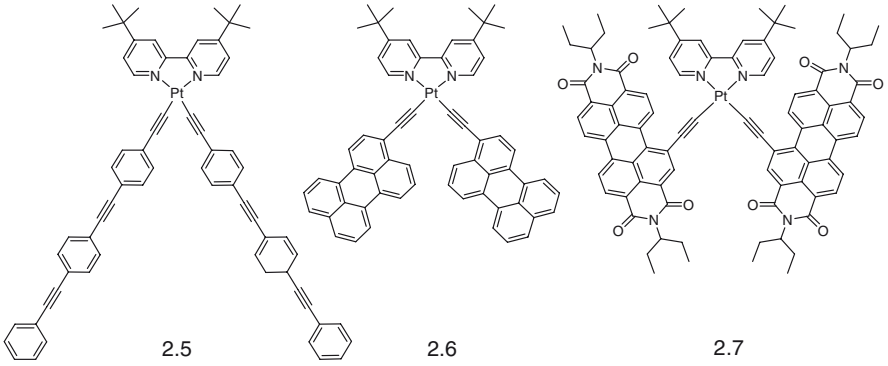

ISC to produce triplets. Again, this is accomplished through the Pt-acetylide motif. Two recent demonstrations describe the sensitization of the ^{3}IL state of either perylenylacetylide **2.6** [20] or perylenediimideacetylide (C≡C–PDI, **2.7**) [21]. In the case of perylenylacetylide, the nonemissive ^{3}IL state was observed by comparison of transient absorption spectroscopic features displayed by **2.6** and model chromophores that feature either ^{3}CT or ^{3}IL excited states. Interestingly, although **2.6** displayed excited-state absorption features consistent with a ^{3}IL excited state, the lifetime agreed with that of a ^{3}CT state. Similar results were also demonstrated in the terpyridyl analog, [Pt(^{t}Bu$_3$tpy)(C≡Cperylene)]$^+$. Intramolecular sensitization of the PDI ^{3}IL excited state was also accomplished by incorporating an acetylide linkage in the bay position of PDI to link the organic chromophore to the Pt center, providing increased spin-orbit coupling to facilitate ISC. This is important as it shows the utility of this molecular platform in generating complexes that exhibit strong absorption throughout the visible spectrum in both the ground and excited states. While the intense absorption is retained upon ligation to the Pt center, the typical high quantum efficiency PDI fluorescence is quantitatively quenched as the lowest-energy excited state is now assigned as ^{3}PDI, which is nonemissive throughout the visible and near-IR. Transient absorption spectroscopy shows intense excited-state absorptions in the visible with absorptions extending into the near-IR. Again, phosphine-based model chromophores lacking low-energy CT excited states confirmed our assignment of the ^{3}PDI excited state. The ability to sensitize singlet oxygen (^{1}O$_2$) phosphorescence in aerated solvents such as dichloromethane is attributed to the triplet nature of the excited state of these chromophores. Shown in Fig. 5 is the typical phosphorescence spectrum of ^{1}O$_2$. The ^{3}PDI excited state of **2.7** undergoes triplet-triplet energy transfer with ground-state ^{3}O$_2$ to produce the ^{1}O$_2$,

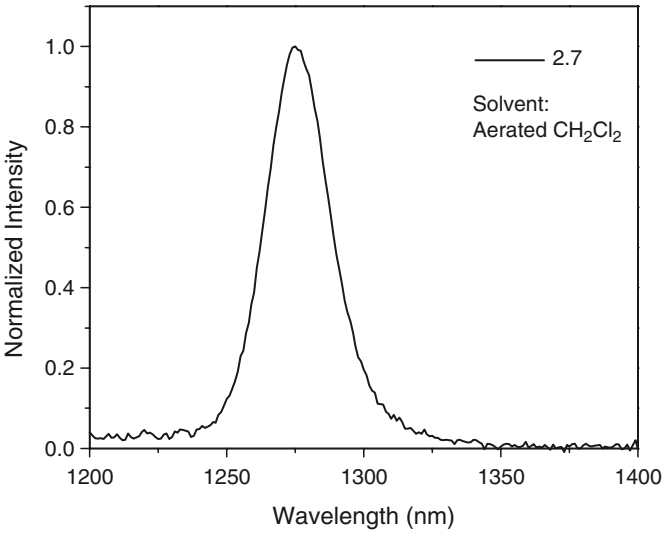

Fig. 5 Phosphorescence of ^{1}O$_2$ sensitized upon 442 nm excitation of an aerated dichloromethane solution containing **2.7**

which ultimately phosphoresces at 1,270 nm. This demonstrates that these relatively long-lived ^{3}IL excited states are poised for excited-state energy-transfer reactions and may be promising candidates for photodynamic therapy.

While the bulk of systems with a bidentate charge-transfer ligand focus on derivatives of either phenanthroline or bipyridine, Adams and Weinstein have shown the utility of a strongly electron-accepting mesBIAN ligand within this molecular genre [22]. Substitution of two monodentate acetylide ligands for the labile chloride ligands in the Pt(mesBIAN)Cl_2 (**2.8**) moiety results in CT-based absorption and emission in **2.9** that is significantly red-shifted relative to their bipyridine and phenanthroline analogs. The ground-state absorption can extend past 700 nm while the phosphorescence is tuned into the near-IR, ranging from 750 to 900 nm. These chromophores typically have shorter excited-state lifetimes (~10 ns), however, their ability to sensitize phosphorescence of $^1O_2$ provides strong evidence of the triplet nature of the excited state.

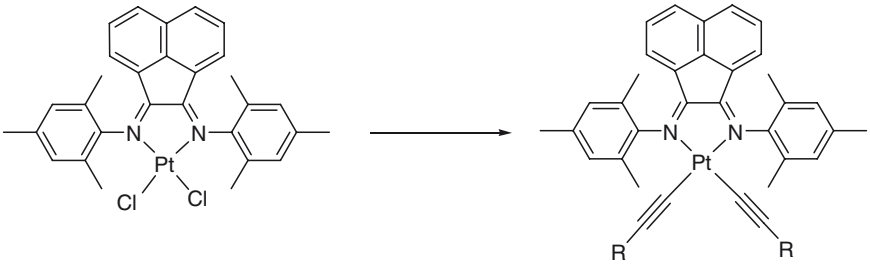

2.8 2.9

Finally, Ziessel and coworkers have recently designed novel molecular structures incorporating both a Pt^{II} and Ru^{II} center [23]. This work has shown the directionality of Pt→Ru energy transfer upon excitation of the Pt^{II} moiety, sensitizing the Ru-chromophore localized ^{3}CT emission. Upon ligation of the Ru moiety, the typical Pt^{II}-based luminescence near ~513 nm is quantitatively quenched while the long lifetime Ru^{II} emission appears around 610 nm.

3 Pt^{II} Acetylide Complexes Containing Tridentate Polypyridyl Ligands

3.1 Background

Platinum(II) complexes containing tridentate ligands have been known since 1934, but it was not until the early 1990s that the ground and excited-state properties of these complexes were investigated in detail. Many researchers have studied the photophysical properties of complexes with the general simplified formula [Pt(tpy)X]$^+$, where X ranges from halide ligands (normally Cl^-), to cyanides and hydroxides, and more

recent significant efforts have focused on investigations of acetylide derivatives due to the intriguing photophysical properties displayed by these complexes.

One of the reasons for choosing a terpyridyl platform in place of bipyridine is the extra rigidity that the tridentate ligand imparts to the structure, even though the bond angles and distances are not a perfect match to the square planar structure. The more rigid the structure, the less likely it is to undergo symmetry lowering distortions typically associated with nonradiative decay. This phenomenon is observed in several bipyridyl analogs where the twisting of the bpy ligand relative to the other ligands in the excited-state forces the molecule from square planar to a pseudo-tetrahedral structure, thereby increasing k_{nr} [4]. In general, $[Pt(tpy)X]^+$ complexes are nonluminescent at room temperature, due to the energetically proximate d-d states which are detrimental to the photophysics [24–28]. Substitution of the halide by a strong-field ancillary ligand generally neutralizes this effect, producing complexes that are strongly emissive in solution at RT [29–33]. In this contribution, the strong field ligands of focus are alkyl and aryl acetylides. Another interesting feature of the tpy platform is the dramatic changes in photophysical properties in the solid state resulting from alteration of the counterion and vapor sorption [34–40]. These latter features have been recently exploited by our group in VOC (volatile organic compound)-sensing microarrays for "artificial nose" applications [40]. To date Pt^{II} terpyridyl acetylides have demonstrated promise in widely diverse applications including singlet oxygen photosensitization [41], cation and pH sensors [42–45], DNA binding and molecular probes [46–48], optical limiting [49], photocatalytic hydrogen production [50–54], vapochromism [36], and photoinduced electron transfer [55].

3.2 [Pt(N^N^N)(C≡CR)]⁺ Complexes

In one of the first studies carried out by Yam and coworkers, the emission properties of $[Pt(tpy)(C{\equiv}CAr)]^+$ salts (**3.1**) were shown to depend on the nature of the substituents on the phenylacetylide ligand; observing that the energy of the ^3CT excited state in CH_3CN at room temperature red shifted as the electron-donating properties of the acetylide unit increased [32]. One of the downsides of these complexes is their low quantum yields in solution, ranging between 10^{-3} and 10^{-2}. Related work by Tung et al. [33] demonstrated that substitution in the tpy core together with tuning the electron density of the acetylide fragment enhances the excited-state lifetime and luminescence quantum yield of the terpyridyl Pt^{II} acetylide derivatives. They used 4′-tolyl-terpyridines in conjunction with different alkyl and aryl acetylide substituents (**3.2**), rendering complexes with high luminescence quantum yield and long excited-state lifetimes, up to 14 μs in duration. Consistent with the conclusions from Yam's group, it was confirmed that the emission energies (^3CT) of these complexes decrease as the electron-donating ability of the acetylide ligand increases.

Follow-up work by Yam and coworkers established that some of these molecules have the ability to aggregate at high concentrations, displaying photophysics emanating from Pt-Pt $\sigma(d_z^2)$-interactions, presumably arising from metal-metal-to-ligand

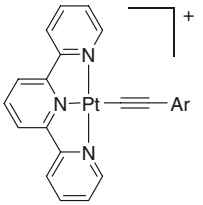

Ar = C_6H_5, C_6H_4Cl,$C_6H_4CH_3$, $C_6H_4OCH_3$, $C_6H_4NO_2$

3.1

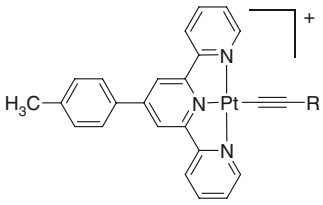

R = CH_2OH, *n*-propyl, C_6H_4Cl, C_6H_5, $C_6H_4CH_3$

3.2

charge-transfer (MMLCT) transitions ($\sigma^* \rightarrow \pi^*$) which are lower in energy relative to the spatially separated chromophores [39, 56]. One specific example is [Pt(tpy)(C≡C–C≡CH)]OTf [39]. This molecule crystallizes in two forms, one red and one green, concluding that the differences in color arise from the difference in the stacking of the molecules; the green form showed almost a perfect alignment of the Pt centers, while the red form showed a structure with short and long alternating distances, resembling a zigzag pattern. Later on, they demonstrated that polymers also induce aggregation of Pt^{II} terpyridyl acetylide complexes, observing remarkable changes in the UV/Vis and emission properties of the monomeric and aggregated structures [56]. More recently, Yam's group has investigated the gelation properties of Pt^{II} terpyridyl complexes incorporating appropriate alkoxy side-chains that facilitate the gelation process (**3.3**). This work also demonstrated that the specific counterion used substantially influences the aggregation process, changing the color and stability of the various metallogels studied [57].

Along similar lines, Ziessel et al. have investigated the gelation properties of related complexes, **3.4** [58]. Similar to Yam's work, introduction of long alkoxy chains into the acetylide core induces formation of gels and liquid crystals through Pt–Pt and π–π* interactions. In these particular systems, solvent was used to tune the emission properties of the complexes by inducing aggregation, Fig. 6. The

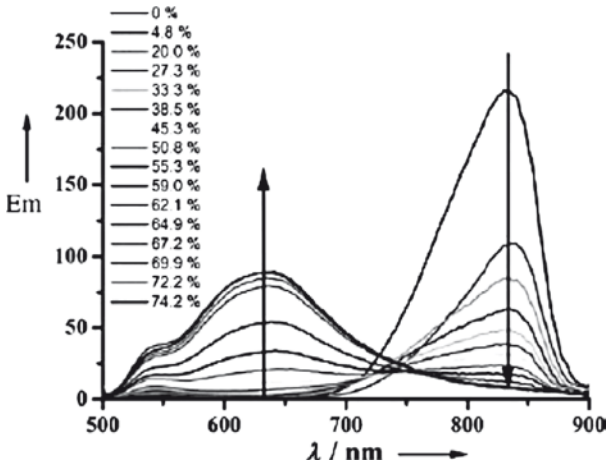

Fig. 6 Emission spectrum of **3.4** (R = $C_{12}H_{25}$) in dodecane upon addition of a solution of MeOH in CH_2Cl_2. Adapted from [58]

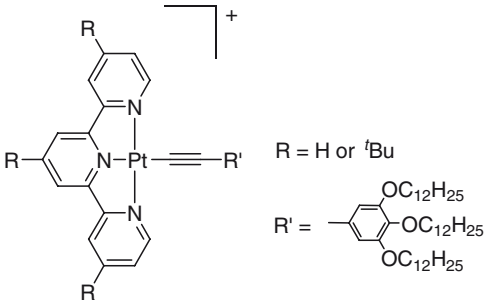

3.3

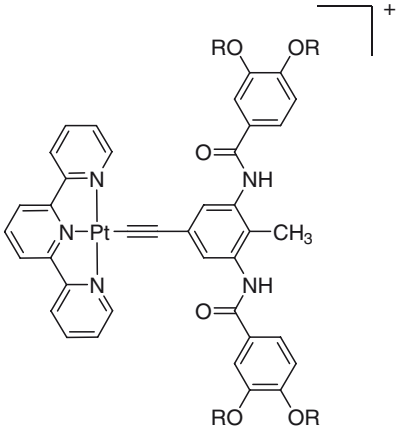

R = CH_3, $C_{12}H_{25}$, $C_{20}H_{41}$

3.4

emission band observed at 644 nm is assigned to a mixed ^{3}MLCT/^{3}LLCT (ligand-to-ligand charge transfer) excited state when the solvent used is a MeOH/CH_2Cl_2 mixture. Switching to pure dodecane induces a change in the lowest excited state to ^{3}MMLCT with an emission band at 830 nm.

Recent work by Tung et al. investigated the switching of the lowest excited state in acidic or basic media in complexes bearing amino groups or azacrown units [42, 59]. They propose that in neutral or basic media the photophysics are attributed to ligand-to-ligand charge-transfer processes from the acetylide (electron donor group) to the terpyridyl core (electron acceptor), but changing to acidic conditions induces a switch to a metal-to-ligand charge-transfer excited state ($d\pi(Pt) \rightarrow \pi^*(tpy)$). Yam and coworkers also performed similar experiments where they derivatized the phenylacetylide functionality with basic amino moieties, observing dramatic color changes and luminescence enhancement with increasing solution pH [44]. Other related systems also appear suitable for cation sensing in solution [43, 45, 60].

Related to their bipyridyl structures, Eisenberg and coworkers have also placed some effort in the design, synthesis, and photophysical characterization of complexes

that possess electron-donor and electron–acceptor groups linked to a platinum chromophore using the tpy platform, Fig. 1 [3, 61]. Transient absorption studies demonstrated that the complexes shown in **3.5** produce the D^+–C–A^- charge-separated species with approximately 1.6 eV stored in the transient. However, they found that the formation of the charge-separated state was not very efficient due to other competing steps.

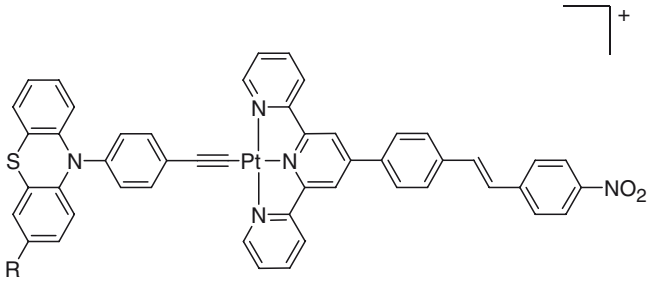

R = H or OCH_3

3.5

Similar to the work performed by Tung's group, Schanze and coworkers investigated the photophysical properties of 4′-tolylterpyridyl arylacetylide complexes, varying the substitution in the *para* position of the phenyl ring [49]. All of these complexes showed a ^{1}MLCT transition band in their absorption spectra around 420–430 nm, but also a solvatochromic band near 460–540 nm tentatively assigned to ^{1}MLCT or/and ^{1}ILCT. The systems studied here displayed room-temperature photoluminescence generally arising from a ^{3}CT excited state, except for the complex containing a nitrophenylacetylide ligand, wherein the emission appeared to emanate from the $^3\pi$–π^* manifold centered in the acetylide moiety.

Our group has also investigated the ground and excited-state properties of Pt^{II} terpyridyl acetylide complexes. In recent work, we prepared complexes with the general formula $[Pt(^tBu_3tpy)(C{\equiv}CR)]^+$ where R is either an alkyl or aryl group, **3.6** [62]. These complexes display bright photoluminescence along with long-lived excited-state lifetimes. It was demonstrated that the nature of the acetylide ligand plays a key role in modulating the absorption and emission properties of these complexes. The transient absorption spectra of these systems produced features at similar wavelengths regardless of the acetylide unit, however, when the acetylide ligand contained an aryl fragment, an increase in intensity was observed. The reductive spectroelectrochemical data for all the complexes studied showed that the $^tBu_3tpy$ radical anion is a strongly absorbing species that is not influenced by the nature of the ancillary acetylide ligand. Nevertheless, TA experiments performed in the presence of the reductive quencher DABCO demonstrated that the intense TA features observed in these species likely emanate from the photogenerated hole (or associated transitions) that is delocalized across the Pt center and the acetylide unit and not from the $^tBu_3tpy$ radical anion.

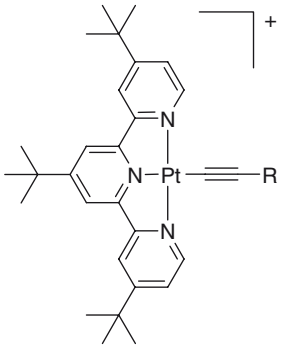

R = C_6H_5, ^{t}Bu, $Si(CH_3)_3$, *p*-tolyl

3.6

Related to our work on the bipyridyl acetylides, we have also demonstrated that proper selection of the acetylide ligand makes possible the design of Pt^{II} terpyridyl complexes that exhibit acetylide ^{3}IL excited states [20]. The perylene complexes **3.7** and **3.8** do not display photoluminescence, however, indirect evidence that the triplet excited state is indeed populated was indicated through the sensitization of singlet oxygen. Transient absorption measurements (Fig. 7) confirmed that regardless of the polyimine ligand used, the lowest excited state in these molecules is ^{3}IL localized in the perylenylacetylide moiety. It is clear in Fig. 7a and b that the identical features are observed in the absorption difference spectra of **3.7** and **3.8**, whereas the difference spectrum of the phenylacetylide complex is clearly distinct, illustrative of the marked differences between ^{3}IL and ^{3}CT excited absorptions.

Another report from our laboratory demonstrated how the photophysical properties of Pt^{II} chromophores can be altered by introduction of a terpyridylacetylide unit as the monodentate acetylide ligand, which provides a free tpy-based chelation site for metal ions such as Fe^{II} and Zn^{II} [63]. For the mononuclear complex, the excited-state properties are consistent with a ^{3}CT manifold, showing a broad structureless emission profile and a long-lived excited state. Once Fe^{II} is coordinated, the emission

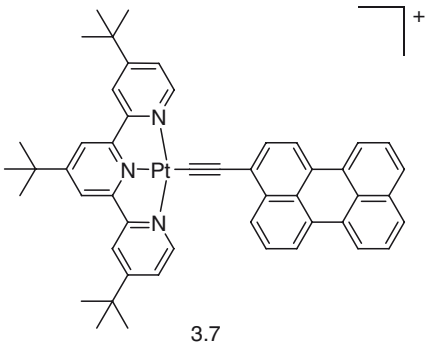

3.7

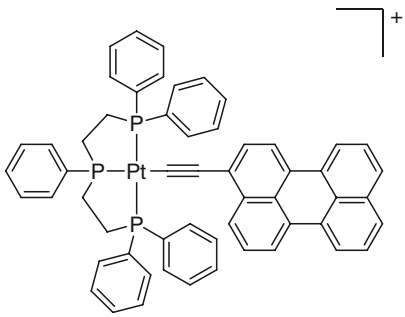

3.8

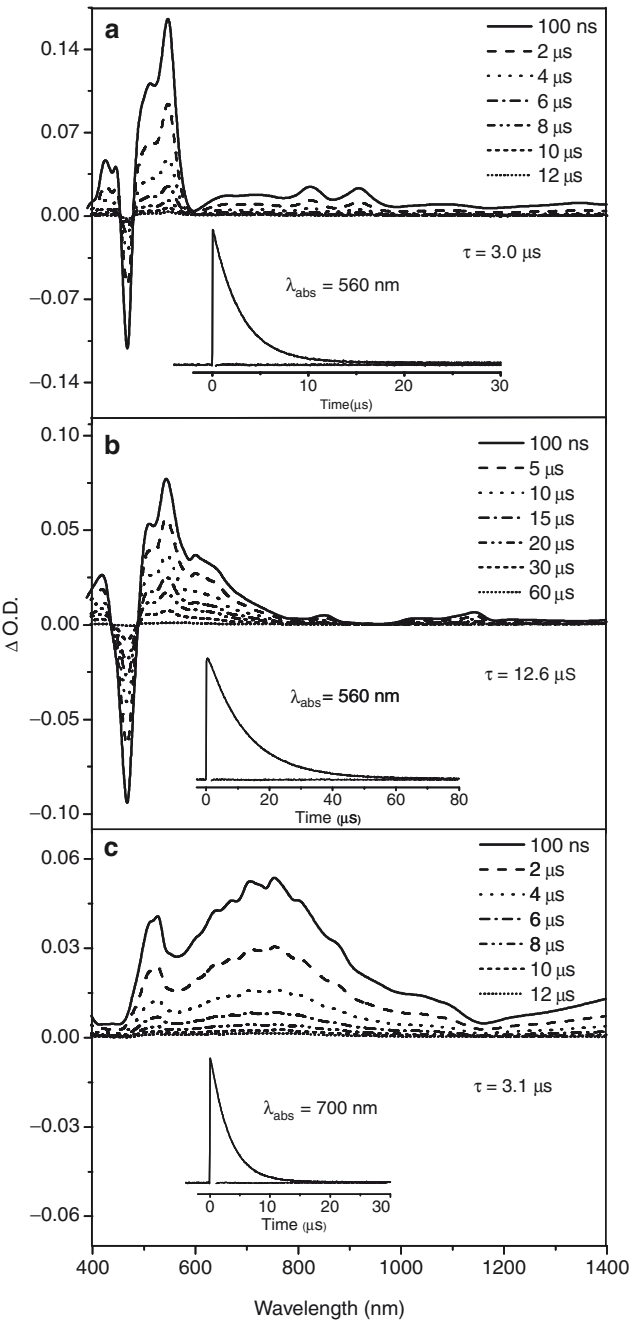

Fig. 7 Transient absorption difference spectra of **3.7** (**a**), **3.8** (**b**), and **[(^{t}Bu$_3$)tpyPtC≡CPh]$^+$** (**c**) measured in deaerated CH_2Cl_2 following a 475 nm, 5–7 ns fwhm, 2-mJ laser pulse. Single wavelength kinetic traces and residuals are inset in each panel. Adapted from [20]

is totally quenched (Fig. 8), in agreement with the presence of low-lying Fe-based ligand-field states providing efficient nonradiative deactivation. Upon chelation of Zn^{II}, our data was consistent with an excited state remaining CT in nature but at higher energy (stabilization of HOMO level) and with a shorter lifetime compared to the mononuclear complex, Figs. 8 and 9. We concluded that chelation of Zn^{II} is simply acid-base in nature since the control experiments with acid (H^+ ions) showed that it is possible to reproduce the same photophysics observed in the Pt–Zn–Pt complex. At low temperature, both complexes (and also the protonated molecule) displayed emission emanating from a ^{3}IL excited state, which is supported by the lifetimes obtained.

Another Pt^{II} molecule where the acetylide unit governs the photophysics of the metal complex has recently emerged. In this report the Pt^{II} contained an appended phenylacetylide that was substituted in the *para* position with a dipyrromethane–BF_2 (BODIPY) subunit, **3.9** [64].

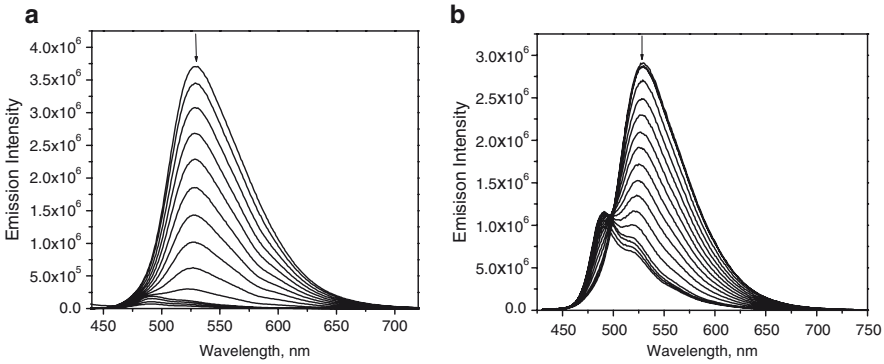

Fig. 8 Emission spectra of the formation of Pt–Fe–Pt (a) and Pt–Zn–Pt (b) in degassed CH_2Cl_2. Adapted from [63]

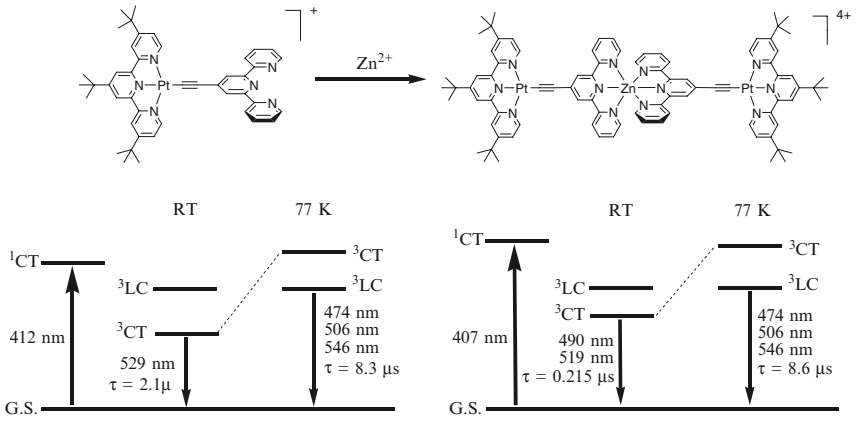

Fig. 9 Schematic representation of the energy levels in the monuclear Pt complex and the trinuclear Pt–Zn–Pt complex

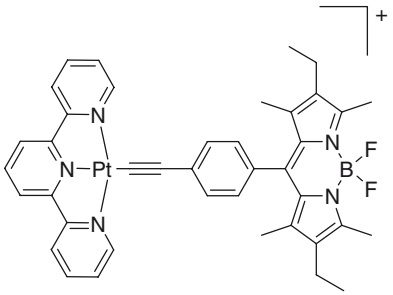

3.9

For this particular complex, the only emission observed at room temperature was residual fluorescence emanating from the BODIPY fragment and at low temperature, the presence of the platinum center induces intersystem crossing and phosphorescence from the BODIPY was indeed observed at 1.6 eV.

Work on Pt^{II} terpyridyl complexes has not been limited to just mononuclear systems. Yam and coworkers have also investigated complexes wherein two platinum centers are attached through alkynyl bridges; more specifically they studied chromophores of the type $[(^tBu_3tpy)Pt(C{\equiv}C)_nPt(^tBu_3tpy)]^{2+}$ (**3.10**) [65]. These structures exhibit photoluminescence in both the solid state and in room temperature solutions, the latter assigned as ^{3}CT in nature mixed with ^{3}IL and ^{3}LLCT character.

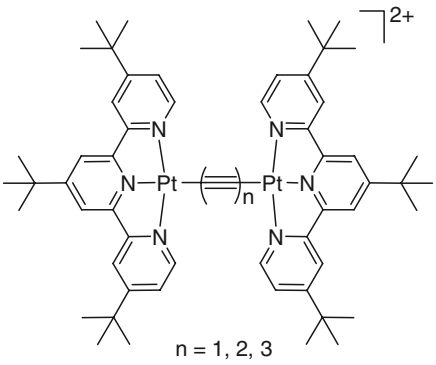

n = 1, 2, 3

3.10

3.3 Pt^{II} Acetylide Complexes with Other Tridentate Polypyridyl Ligands

Terpyridyl has not been the only tridentate ligand used as a platform for producing photoluminescent square-planar Pt^{II} complexes. Che and coworkers published one of the first reports on cyclometallated Pt^{II} complexes, using the N^N^C core together

with alkyl and aryl acetylides as the fourth ligand, **3.11** [66]. They demonstrated that the emission energies of the complexes are tuned from green to yellow to red by changing the substituents on the cyclometallating and the acetylide ligands, making these compounds promising for light-emitting materials, particularly as phosphorescent dopants for OLED applications. These molecules exhibit brightly photoluminescent excited states that depending on the characteristics of the ligands involved, are ^{3}CT, $^3\pi$–π^* (acetylide ligand localized), and/or ^{3}IL (cyclometallated ligand localized) in nature. One of the advantages of the N^N^C platform is that the d–d excited states are typically raised in energy relative to the N^N^N analogs. This can be explained based on the fact that the carbon ligating atom (C^-) is a very strong σ donor while the nitrogen rings are still good π acceptors, providing the same overall effect that coordination of acetylide ligands impart to Pt^{II} complexes.

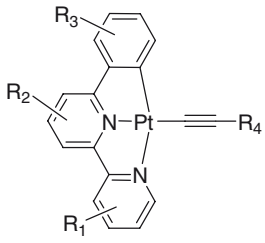

3.11

Berenguer et al. also investigated the photophysical properties of cyclometallated complexes, but focused their attention on the C^N^C platform, studying the anionic acetylide derivatives as well as other related structures, **3.12** [67]. Contrary to the results obtained by Che in the N^N^C structures, these complexes do not display photoluminescence in solution at RT. The absorption spectra in all cases are dominated by IL π–π^* and CT transitions. To the best of our knowledge these are the only reports on the photophysics of cyclometallated Pt^{II} acetylide complexes to date.

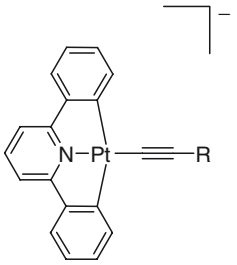

R = ^{t}Bu, Ph, Tol, or (*p*-OMe)C_6H_4

3.12

4 Pt^{II} Acetylides with Phosphine-Containing Ligands

4.1 Introduction

Interest in phosphine-containing Pt^{II} acetylides originally began in the 1970s from work on polymeric materials. In 1977, Sonogashira and Hagihara first demonstrated the facile synthesis of Pt–acetylides by the direct reaction of a metal halide with acetylenes in the presence of a secondary amine and catalytic amounts of CuI [68]. Upon establishing these mild synthetic reaction conditions, they went on to develop poly-yne monomers, oligomers, and polymers containing Pt^{II} and trialkylphosphines either in the *cis*- or *trans*- geometry with the latter being more prevalent [69–72]. This dramatically accelerated a new and burgeoning field of research as the electronic nature of these systems became the center of intense investigation. This reaction scheme also paved the way for developing other Pt^{II} systems containing acetylide ligands, many of which have been eluded to earlier in this work [12, 15, 17–20, 63, 73].

Since the middle of the 1990s, Pt–acetylides containing phosphine ligands have seen a dramatic increase in interest due to the versatility provided by the phosphine ligands and dramatic triplet-state photophysics that have been demonstrated in a variety of conjugated structures. For instance, phosphine ligands can be mono-, bi-, and tridentate while still leaving additional coordination sites for pendant acetylide ligands within the square–planar Pt^{II} molecular motif. As a result, many diverse structures have been envisioned and synthesized to probe the triplet-state photophysics of a wide variety of acetylinic moieties. While a tremendous amount of data has been reported for this class of chromophores, we will not be able to fully discuss every recent discovery. Here we intend to provide a reasonable overview of some of the significant contributions made over the past decade.

4.2 Photophysics of Pt–Acetylide Phosphine Chromophores

A large amount of research in this field has been directed toward Pt–acetylides containing monodentate phosphines for the simple fact that these ligands provide the ability to generate linear assemblies when *trans* disposed. In 2002, Schanze and coworkers [74] utilized this geometry to generate a series of Pt-acetylide oligomers containing up to 7 Pt^{II} centers, **4.1**. By extending this chain of acetylides, they

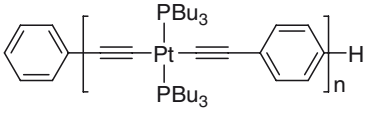

n = 1–5,7

4.1

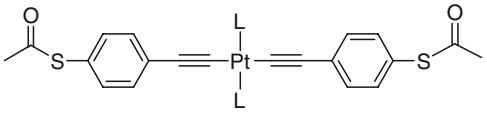

L = PCy_3, PBu_3, PPh_3, $P(OEt)_3$, $P(OPh)_3$

4.2

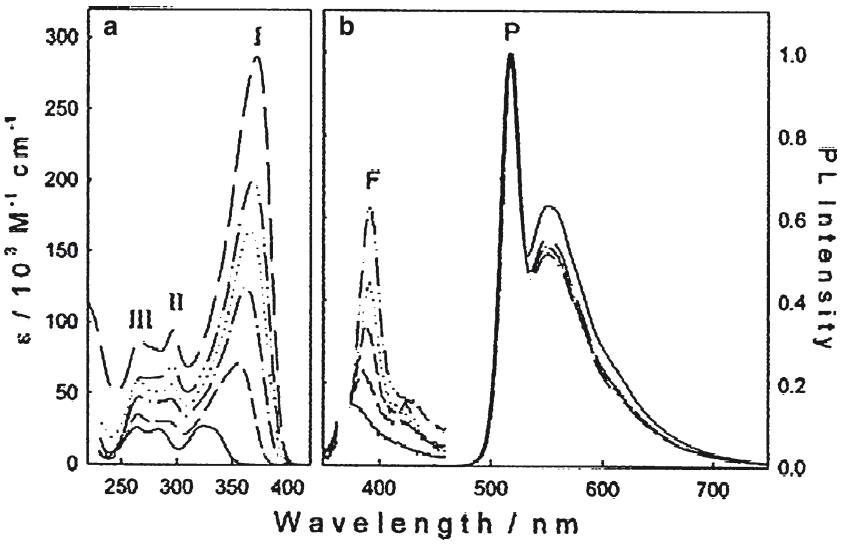

Fig. 10 (**a**) UV–Visible absorption spectra of the **4.1** (**Pt-n**) series of compounds in THF. In order of increasing intensity: **Pt-1**, **Pt-2**, **Pt-3**, **Pt-4**, **Pt-5**, **Pt-7**. (**b**) Photoluminescence spectra in deoxygenated THF. F is the fluorescence: in order of increasing intensity **Pt-2**, **Pt-3**, **Pt-4**, **Pt-5**, **Pt-7**. P is phosphorescence: in order of decreasing intensity in 01 band **Pt-2**, **Pt-3**, **Pt-4**, **Pt-5**, **Pt-7**. Note that the fluorescence intensity scale is magnified 100 as compared to phosphorescence. Reprinted with permission from [74]

showed that the singlet excited states in these molecules were delocalized, projecting through the pendant metal centers. Ground-state absorption and fluorescence measurements showed a shift to lower energy in the absorption and the singlet fluorescence spectra as the oligomer chain length was increased, Fig. 10. The data provided evidence that the singlet state was delocalized over approximately six repeat units. In contrast, the phosphorescence displayed little sensitivity to the chain length, suggesting that the triplet state was localized over one or at most two repeat units. These experimental results were corroborated by the theoretical study by Batista and coworkers in 2005 [75].

In 2003, Schull and coworkers investigated the effect of the phosphine ligand on conductance within a series of linear Pt–acetylides, **4.2** [76]. Although correlations in both molar absorptivity and alkyne vibrational frequency could be accounted for in the phosphine basicity, the conductance across the acetylide ligands did not accordingly change. In 2004, Marder and coworkers also investigated delocalization in Pt–acetylide systems by investigating the mixed valence compound **4.3**. By investigating the IVCT (intervalence charge transfer) in the mixed valence compound and comparing the absorption to the all-organic model chromophore previously investigated [77], they were able to make direct assessments of the delocalization facilitated by the Pt^{II} center. This work demonstrated that the electronic coupling across the Pt center was only slightly less than that observed in the "all-organic" benzene-bridged analogue. The AFRL group led by Cooper in 2004 reported

preliminary investigations of the photophysics of Pt-acetylides containing two $P(Oct)_3$ ligands providing the means of generating room-temperature liquid-phase chromophores which when cooled formed glasses [78]. They showed that they could increase the chromophore density 10-fold, thereby, increasing the nonlinear coefficient χ. In collaboration with Toscano, Cooper later reported the time-resolved infrared spectroscopy of *trans*-[$Pt(PBu_3)_2(PE2)_2$] (**4.4**) in an effort to understand structural changes that occur upon ISC to the triplet state of the acetylide ligand [79]. In accord with their DFT calculations, TRIR data was consistent with cumulenic vibrations in the triplet state.

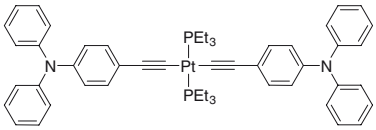

4.3

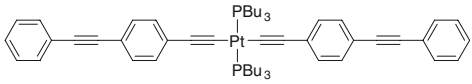

4.4

Phosphine-containing Pt–acetylides are often used as model chromophores as well, first demonstrated by our group in 2003 in *trans*-$Pt(PEt_3)_2(C{\equiv}CPyrene)_2$ which served as the ^{3}IL model for **2.3** [12]. When chelating phosphines are substituted for monodentate ligands, one can investigate the importance of geometry on the resulting photophysics of these compounds. In 2004, Schanze and coworkers utilized both *cis* and *trans* geometric isomers of stilbene-containing chromophores [80]. In addition, by the substitution of bipyridine for the diphosphine chelate, the effect of the presence of an additional charge-transfer transition was evaluated. In all of the cases explored, efficient ISC readily provided the $^3\pi\pi^*$ excited state of the acetylide. Additional work from the Schanze group in 2005, explored aggregation effects on the triplet state and intrachain triplet-energy transfer [81, 82]. Through judicious choice of the bulky acetylide bridging ligand, they demonstrated the ability to minimize excited-state aggregation. Interestingly, both the monomer and polymer exhibited superimposable phosphorescence spectra in the solid state. Parallel studies incorporating the nonbulky 1,4-diethynylphenylene produced aggregate emission. In 2005, Yam and coworkers also successfully designed a series of branched and π-conjugated Pt^{II} acetylides. In that particular work they assigned the room-temperature emission as predominately ^{3}IL with some ^{3}CT contributions [83].

The use of Pt-acetylides containing phosphine ligands was extended further by the Schanze group in 2006 [84, 85]. In one contribution, they incorporated platinum–acetylide polymers into photovoltaic devices which demonstrate good device efficiency. Transient absorption studies provide definitive evidence for photoinduced electron transfer from the Pt–acetylide to PCBM by the temporal evolution of the TA spectrum, observing the formation of the PCBM radical anion at 1,050 nm. The same system was eventually demonstrated to operate as a bulk heterojunction photovoltaic device [84].

Two contributions from the Cooper group in 2006 focused on the delocalization of the triplet excitons in Pt–acetylides [86, 87]. They investigated the effect of symmetry within the complexes by comparing chromophores with either one pendant acetylide or two symmetric acetylides *trans* disposed to each other. Similar to earlier

results, they found the singlet exciton to be delocalized across the Pt^{II} center whereas the triplet is localized over a lone acetylide moiety.

2007 brought another year of many investigations into the excited-state photophysics of the phosphine-containing Pt–acetylides. The AFRL group demonstrated simultaneous two-photon absorption in a series of Pt-acetylides. This was demonstrated through a variety of techniques including transient absorption induced by two-photon absorption [88]. The Schanze, Reynolds, and Castellano groups collaboratively studied a fulleropyrrolidine end-capped platinum acetylide donor-acceptor triad **4.5** [89]. Through utilization of ultrafast transient absorption studies, photoinduced intramolecular charge transfer was shown to occur rapidly and electron transfer was believed to occur predominately through the triplet state as ISC crossing was efficient. The resultant charge-separated state is formed within 1 ps and then decays by charge-recombination within 400 ps. With this knowledge in hand, photovoltaic devices produced from this triad demonstrated modest efficiency with a short circuit photocurrent of 0.5 mA cm^{-2} and open circuit voltage of 0.41 V with 100 mW cm^{-2}/AM1.5 illumination. The Schanze group furthermore investigated polaron states within oligomer segments [90] as well as the effects of conformation on triplet excited-state localization [91].

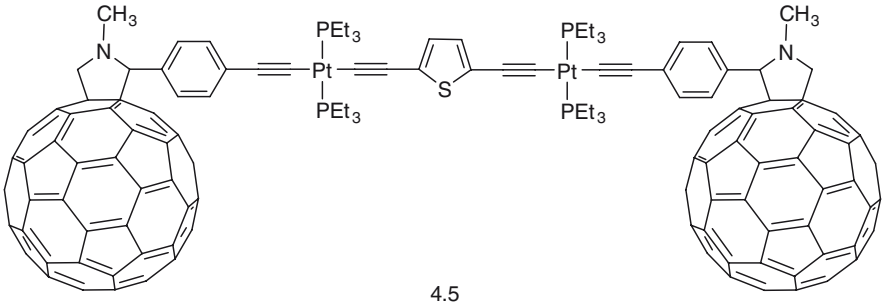

4.5

2008 also proved to be an active year for the synthesis of Pt–acetylides and investigation of their corresponding excited-state dynamics. The Schanze group continued to investigate the photophysics of Pt–acetylides with the corresponding phosphine ligand motif [92, 93]. Their transient absorption studies on the chain length dependence revealed efficiently produced $^3\pi\pi^*$ excited states that demonstrate strongly allowed triplet–triplet absorptions [92]. They also published a series of Pt–acetylides that exhibit reversible gelation between 40 and 50°C as a result of chromophore aggregation (**4.6**). The aggregation of these PAO's induced a blue shift in the absorption spectra arising from H-like aggregates [93].

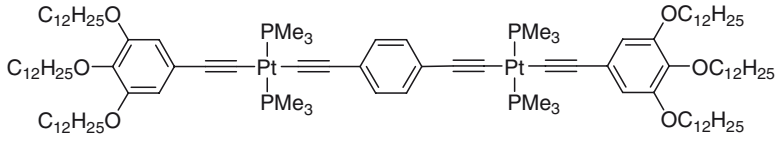

4.6

The nonlinear absorption of Pt^{II} acetylide chromophores has also continued to retain the interest of many researchers. Malmstrom and coworkers have recently investigated Pt-acetylide chromophores blended with solid-state polymer matrices [94]. An example of such a complex is **4.7**. They found that the photoluminescence properties of the blends agreed well with that of dilute THF solutions containing the Pt–acetylides. Optical power limiting experiments showed that the clamping levels for dyes nonbonded to the polymer host were about half that for dyes in the highly cross-linked solids at similar concentrations.

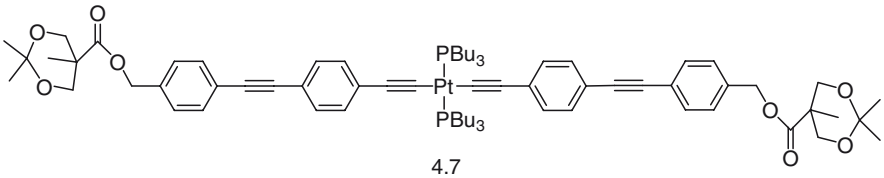

4.7

Pt^{II}–acetylide phosphine complexes also continued to serve as valuable model chromophores for the triplet-state dynamics of appended organic moieties, as ISC is typically efficient in these systems. Our group has previously used this molecular platform to assist in excited-state assignments [13, 18–21]. Here we note that in 2008, our group utilized tridentate **4.8**, bidentate **4.9**, and monodentate **4.10** phosphine architectures within Pt^{II} chromophores. These complexes served as model chromophores with perylene- and PDI–acetylide ^{3}IL excited states. Parallel studies of the photophysics of these molecular platforms have allowed us to assign lowest-energy excited states in Pt^{II} charge-transfer complexes which contain the ^{t}Bu$_3$tpy and dbbpy charge-transfer ligands. In both studies, transient absorption spectroscopy elucidated the excited-state absorption features of ^{3}perylene and ^{3}PDI. Comparison of the nanosecond TA data of the analogous charge-transfer structures demonstrated similar absorptions which confirmed the ^{3}IL excited-state assignment.

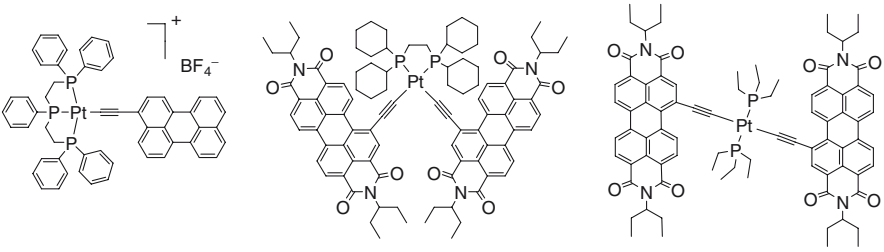

4.8 4.9 4.10

5 Electronic Structures of Platinum Acetylides

To understand the physical meaning of the electronic structures of platinum acetylide complexes, theoretical calculations have been employed to deduce information related to the molecular orbitals and the electronic transitions. The first theoretical

work on platinum acetylides was performed by Nakatsuji et al. [95] where they studied $Pt(PH_3)_2(CN)(C{\equiv}CCN)$ (**5.1**), the product of a photochemical isomerization reaction. The geometric parameters of the singlet ground state were obtained from the restricted Hartree–Fock (RHF) method and the energy of the singlet and triplet excited states were obtained from the single excitation and configuration interaction (SE–CI) method. Compared with the symmetry adapted cluster (SAC) method [96], the ground-state energy of this compound calculated by RHF is 0.31560 Hartree higher. The excited-state energy calculated by the SE–CI method has a lower correlation energy relative to the ground state.

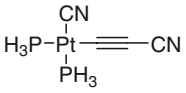

5.1

The extended Hückel method, which is a semiempirical quantum chemistry method, is often used as a preliminary step in the DFT study of molecular orbital analysis. The acetylide-bridged organometallic dinuclear complexes **5.2** were studied by Halet et al. using the extended Hückel method for qualitative analysis and DFT for additional electronic properties [97]. The extended Hückel analysis concluded that the main contribution of the Pt–C bond arises from σ type interactions while the π back-donation is very weak. The DFT/BP86 calculation gives a 2.371 eV HOMO–LUMO gap. The electronic communication parameter H_{ab} between the bis-ferrocene compound linked with platinum acetylide (**5.3**) was calculated to be 0.022 eV, compared with 0.025 eV obtained experimentally by Rapenne and coworkers using DFT and the extended Hückel method [98].

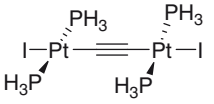

5.2

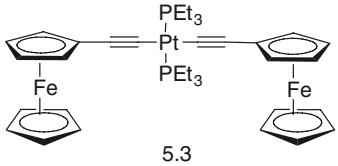

5.3

Forniés et al. [99] applied time-dependent density functional theory (TD-DFT) with the B3LYP method to study the photophysics of the bis(alkynyl)platinate compounds $[Pt(bzq)(C{\equiv}CR)_2]^-$ (bzq = benzoquinolinate; R = *t*-Bu, $SiMe_3$, Ph, Tol, $C_6H_4CF_3$, C_5H_4N, or C_6H_4–C≡CPh), **5.4**. The photophysical properties of the first six compounds were similar. The luminescence in the solid state and frozen matrices was strong while the corresponding emission in solution at room temperature was weak and red shifted. However, the emission spectrum of the compound with $R{=}C_6H_4$–C≡CPh has a structured profile both at low and room temperature. The TD-DFT calculation shows that for all the complexes, a metal perturbed ligand(acetylide)-to-ligand(benzoquinolinate) charge-transfer transition is observed, while in the complex containing the C_6H_4–C≡CPh unit the transition involves a metal perturbed π–π^* transition, imparting different character to the emission observed.

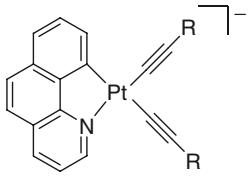

R = ^{t}Bu, $SiMe_3$, Ph, Tol, $C_6H_4CF_3$, C_5H_4N, C_6H_4–CCPh

5.4

Follow-up work by Forniés [100] investigated the luminescence properties of homoleptic Pt^{II} acetylide complexes $[Pt(C{\equiv}CR)_4](NBu_4)$ (where R is an electron-donating, electron–withdrawing, or an electron–delocalizing substituent) (**5.5**) applying TD–DFT/B3LYP calculations. The structured luminescence spectrum of $[Pt(C{\equiv}C(4\text{-}CN)C_6H_4)_4]^{2-}$ was assigned to a mixture of triplet intraligand $[\pi \rightarrow \pi^*(-C{\equiv}CR)]$ and metal-to-ligand $[d_\pi(Pt) \rightarrow \pi^*(-C{\equiv}CR)]$ transitions based on the TD-DFT/B3LYP calculations. The HOMO was found to be a π orbital on two C≡C(4-CN)C_6H_4 ligands with additional contributions from a Pt 5d orbital. The LUMO is a π^* orbital centered on the other two C≡C(4-CN)C_6H_4 ligands. Also, the theoretical excitation spectrum was obtained and aligned well with the experimental data.

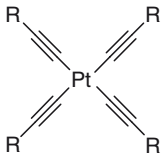

5.5

The spectroscopic properties of [Pt(2,2′,6′,2-terpyridine)(C≡CR)]$^+$ (R=H, CH_2OH, and C_6H_5) (**5.6**) were theoretically studied by Zhang et al. [101]. The second-order Møller–Plesset perturbation (MP2) was used to optimize the ground state and the single-excitation configuration interaction (CIS) method was employed to obtain the excited-state structure. The spectroscopic properties of the

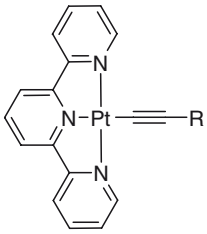

5.6

Pt^{II} complexes in dichloromethane were calculated with the TD-DFT/B3LYP method using the polarizable continuum model (PCM). Similar ground and excited-state geometries were found for different R groups even though their electronic structures were different. The LUMO, which is terpyridyl based, does not change in energy with different R groups; however, the HOMO energy levels, which are a mixture of Pt d-orbitals and a C≡C π orbital, increase dramatically in energy with electron-donating substituents. From the molecular orbital analysis, the lowest excited-state emission is assigned as triplet acetylide/Pt to terpyridine charge transfer, i.e., a mixture of ligand-to-ligand charge transfer (^{3}LLCT) and metal-to-ligand charge transfer (^{3}MLCT). The simulated absorption spectra showed that the lowest-energy absorption bands red shift, following the energetic order R = H > CH_2OH > C_6H_5.

Similar theoretical studies on the spectroscopic properties of two groups of terpyridylplatinum(II) acetylide complexes (**5.7**) were performed by Feng et al. [102]. In the first group of complexes (I), the substitution is on the tpy ligand, while in the other (II) the substitution takes place on the acetylide moiety. The ground-state geometries were obtained from the DFT/B3LYP method and the parameters matched the X-ray diffraction data. The molecular orbital analysis was used as a tool to understand the electronic structures of these molecules. They concluded that the energy of the LUMO levels in group I decreased with increasing the electron-withdrawing character of the substituents and the energy of the HOMO levels of the complexes in group II increased with electron-donating groups. The absorption spectra were obtained from TD-DFT/B3LYP calculations and the emission spectra were calculated based on first triplet excited state (T_1) optimized by the CIS method. The solvent effect was also considered by using the polarizable continuum model. The electronic structures were investigated by molecular orbital analysis. The lowest-energy absorption bands of all the complexes were assigned to a mixture of metal-to-ligand charge-transfer transitions (dπ(Pt)→π* tpy) and ligand-to-ligand charge-transfer transitions (π(C≡C)→π* tpy) except for the $-C_6H_4NH_2$ derivative, where the emission is assigned as ligand-to-ligand charge transfer.

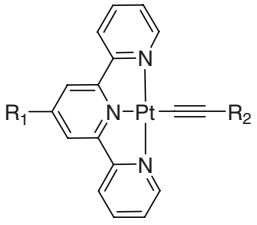

I: R_1 = H,CH_3, CN; R_2 = CH_2OH
II: R_1 = *p*-tolyl; R_2 = CH_2OH, n-propyl, C_6H_5,C_6H_4Cl, $C_6H_4NH_2$

5.7

Polymers and oligomers that are platinum-acetylide based have important optical and optoelectronic applications because the lowest triplet excited state involves a mixture of Pt^{II} (dπ) orbitals and organic π-conjugated orbitals that enhance the phosphorescence efficiency. Batista and Martin studied the low-lying

electronic excitations of [Pt(P(^{n}Bu)$_3$)$_2$(ethynylbenzene)$_2$] systems (**5.8**) using the TD-DFT/B3LYP method [75]. From their calculations, the lowest triplet excited state was found to be localized on one side of the ligand which breaks the ground-state symmetry. A 0.61 eV hopping barrier was obtained for the mixed valence excited states.

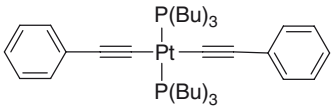

5.8

Lindgren et al. studied the excited state and phosphorescence of platinum(II) acetylides (**5.9**) with the DFT/B3LYP method [103]. The calculated UV/Vis absorption spectra revealed that the orientation of the phenyl rings relative to the P–Pt–P axis has a strong correlation with the intensity of the absorption band. The broken symmetry phenomenon was also confirmed in the lowest triplet excited state, which leads to a C≡C–Ph bond on one side and a C=C=C bond on the opposing side. Quadratic response calculations of spin-orbit coupling showed that the intensity of the phosphorescence of these complexes arises mainly from the $\sigma \rightarrow \pi^*$ type T_1–T_n transitions localized at the C≡C–Pt-P fragment, but not from the delocalized $\pi \rightarrow \pi^*$ type transitions. The quadratic response calculations also reproduced an increase of τ_R from PE_1 to PE_2 (**5.9**), which was also determined experimentally.

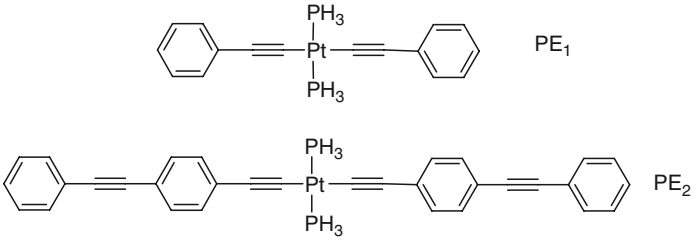

5.9

Schanze et al. studied triplet localization in platinum-acetylide oligomers using DFT/B3LYP and TD–DFT/B3LYP methods [91]. The triplet excited state was found to be localized on a single –[PtL$_2$–C≡C–(1,4–Ph)–C≡C–PtL$_2$]– unit (**5.10**). The DFT study also demonstrated that the ground-state energies are very close for two of the isomers with twisted and planar orientation of the 1,4-phenylenes relative to the PL_2C_2 plane. However, the triplet-state energy of the planar orientation is 3 kcal mol^{-1} lower than that of the twisted orientation, which agrees with the low-temperature experimental data.

One of the most recent works on the electronic structures of platinum acetylide complexes using theoretical calculations was performed by Ding et al [104]. In this

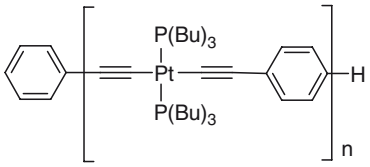

5.10 n = 2–5,7

report, they applied the DFT/B3LYP method to study the low-temperature absorption spectrum of platinum(II) terpyridyl acetylide complexes containing amino substituents (**5.11**). They observed that protonation of the amino groups induced changes in the excited-state properties of the complexes, going from LLCT, to IL and finally to MLCT.

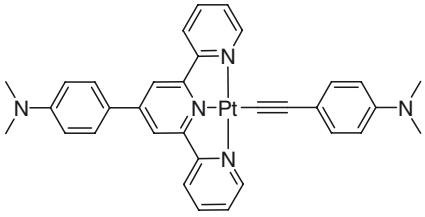

5.11

Our group has also employed DFT calculations to better understand the electronic structures of Pt^{II} bipyridyl acetylides. The low-lying excited states of Pt(bpy)$(C{\equiv}C{-}TMS)_2$ (**5.12**) and Pt(bpy)–$(C{\equiv}C{-}t{-}Bu)_2$ (**5.13**) were originally investigated [17]. The HOMOs were found to be a mixture of metal d and acetylide π orbitals and energy intervals between HOMO and LUMO were also predicted. The luminescence of the platinum(II) metallacycle **5.15** in CH_2Cl_2 was also investigated by DFT theory with the polarizable continuum model. The frontier orbitals were found to be a mixture of Pt d orbitals and aromatic acetylide ligand π orbitals. However, the HOMO and HOMO-1 are in reverse order for compounds **5.14** and **5.15** because of enhanced π conjugation in the latter. The calculated excitation energies and oscillator strengths matched well with the experimental data if a 0.52 eV offset was utilized, Fig. 11. The ΔSCF-derived shift method was also employed to treat both the

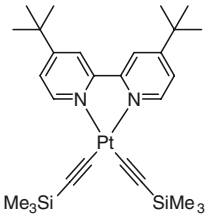

5.12

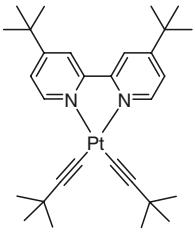

5.13

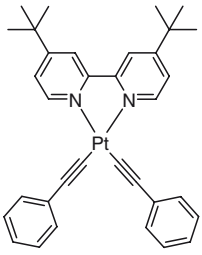

5.14

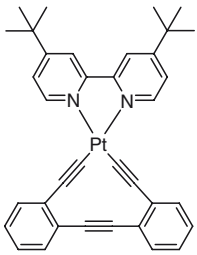

5.15

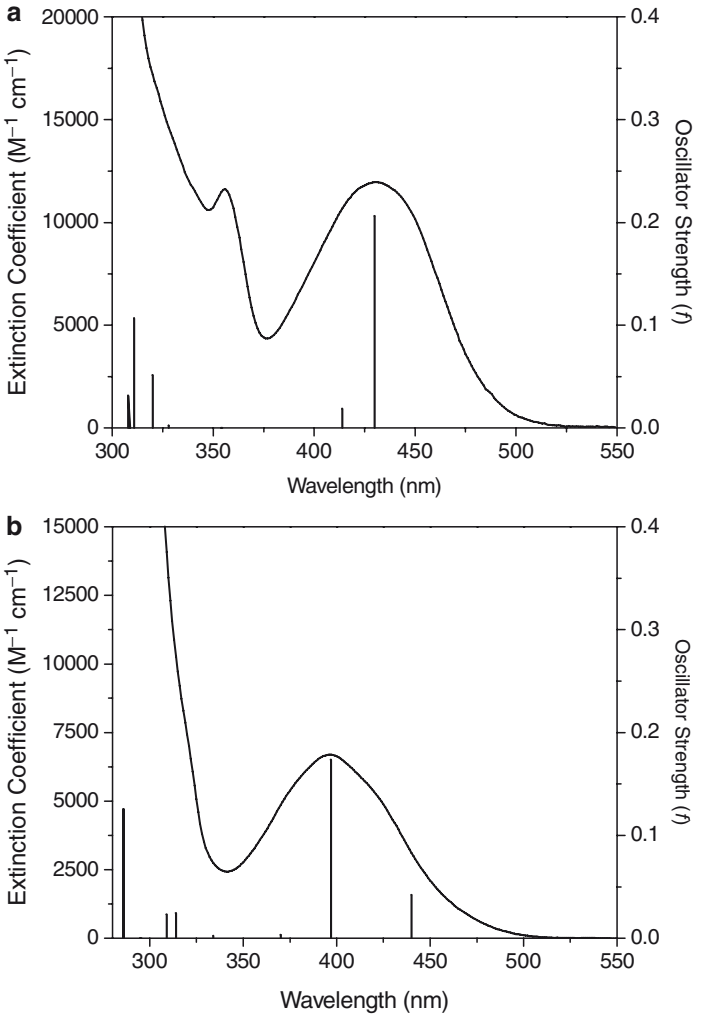

Fig. 11 Experimental absorption spectra and TDDFT calculated excitation energies and oscillator strengths of compound **5.14** (**a**) and **5.15** (**b**). Adapted from [18]

low-lying charge-transfer and ligand-localized excited states, which yielded excellent agreement between experimental and theoretical transition energies [18].

6 Concluding Remarks

Although the primary motivation for research in this area largely stems from the potential applications of these chromophores across a variety of disciplines, the fact remains that there are many interesting questions remaining and several lines of

investigation worth further exploration. This contribution was intended to outline current work in the field related predominately to the photophysical processes in platinum(II) acetylides. Even within this seemingly small group of related molecular structures, there exists an enormous complexity arising from the strong participation of the acetylide ligand(s) in the ground and excited states of these molecules. The extent of orbital mixing taking place is readily observed both experimentally and theoretically using density functional methods. Such intricacies are not usually observed in polyimine coordination compounds displaying rather straightforward MLCT-type photophysics. The photoluminescence of the Pt^{II} acetylides is noteworthy and can take the form of "pure" triplet charge-transfer like or "pure" triplet acetylide ligand-localized in character, depending upon the choice of supporting ligand(s), i.e., polyimine or phosphine, and acetylide ligand(s). It has also been shown that the photophysics can fall between those two extremes, best described as admixtures of ^{3}MLCT and ^{3}IL states, systematically tunable between both by varying solvent polarity. In one specific instance, the lowest triplet excited state in **2.5** can be completely inverted by simply changing the nature of the solvent, which completely transforms the emergent photophysics. Transient absorption and infrared methods have been extremely useful in identifying intermediates and products generated in both intra- and intermolecular energy and electron transfer reactions utilizing Pt^{II} acetylides. Although there are only a handful of reports to date, ultrafast kinetic methods clearly have a promising future in exploring the complexities resulting from the strong orbital mixing in these structures. The horizon appears bright for continued fundamental scientific exploration of platinum acetylides in addition to their widespread applications in photonics, medicine, nanomaterials, and photocatalysis.

Acknowledgments We gratefully acknowledge the following agencies for their generous support of our own research projects relevant to this review in Pt^{II} acetylide photophysics: the NSF (CAREER Award CHE-0134782, CHE-0719050, CBET-0731153), the AFOSR (FA9550-05-1-0276), the ACS-PRF (44138-AC3 and 36156-G6), and Bowling Green State University. We would also like to thank all of our collaborators worldwide for their intensity and strong intellectual contributions for work related to Pt^{II} acetylide photophysics. These individuals include Prof. Christopher J. Adams (Univ. Bristol), Prof. John R. Cable (BGSU), Dr. Thomas Cooper (AFRL), Dr. Evgeny Danilov (BGSU), Prof. Richard Eisenberg (Univ. Rochester), Prof. Joseph T. Hupp (Northwestern), Prof. David R. McMillin (Purdue), Prof. Alan A. Pinkerton (Univ. Toledo), Prof. Kirk S. Schanze (Univ. Florida), Prof. Julia A. Weinstein (Univ. Sheffield), and Dr. Raymond Ziessel (Strasbourg).

References

1. Hissler M, McGarrah JE, Connick WB, Geiger DK, Cummings SD, Eisenberg R (2000) Coord Chem Rev 208:115–137
2. Castellano FN, Pomestchenko IE, Shikhova E, Hua F, Muro ML, Rajapakse N (2006) Coord Chem Rev 250(13–14):1819–1828
3. Chakraborty S, Wadas TJ, Hester H, Schmehl R, Eisenberg R (2005) Inorg Chem 44(20):6865–6878

4. Williams JAG (2007) Top Curr Chem 281 (Photochemistry and Photophysics of Coordination Compounds II):205–268
5. Chan C-W, Cheng L-K, Che C-M (1994) Coord Chem Rev 132:87–97
6. James SL, Younus M, Raithby PR, Lewis J (1997) J Organometallic Chem 543:233–235
7. Hissler M, Connick WB, Geiger DK, McGarrah JE, Lipa D, Lachicotte RJ, Eisenberg R (2000) Inorg Chem 39(3):447–457
8. McGarrah JE, Kim Y-J, Hissler M, Eisenberg R (2001) Inorg Chem 40(18):4510–4511
9. Whittle CE, Weinstein JA, George MW, Schanze KS (2001) Inorg Chem 40(16):4053–4062
10. McGarrah JE, Eisenberg R (2003) Inorg Chem 42(14):4355–4365
11. Wadas TJ, Chakraborty S, Lachicotte RJ, Wang Q-M, Eisenberg R (2005) Inorg Chem 44:2628–2638
12. Pomestchenko IE, Luman CR, Hissler M, Ziessel R, Castellano FN (2003) Inorg Chem 42(5):1394–1396
13. Pomestchenko IE, Castellano FN (2004) J Phys Chem A 108(16):3485–3492
14. Danilov EO, Pomestchenko IE, Kinayyigit S, Gentili PL, Hissler M, Ziessel R, Castellano FN (2005) J Phys Chem A 109(11):2465–2471
15. Hua F, Kinayyigit S, Cable JR, Castellano FN (2005) Inorg Chem 44(3):471–473
16. Glik EA, Kinayyigit S, Ronayne KL, Towrie M, Sazanovich IV, Weinstein JA, Castellano FN (2008) Inorg Chem 47(15):6974–6983
17. Hua F, Kinayyigit S, Cable JR, Castellano FN (2006) Inorg Chem 45(11):4304–4306
18. Hua F, Kinayyigit S, Rachford AA, Shikhova EA, Goeb S, Cable JR, Adams CJ, Kirschbaum K, Pinkerton AA, Castellano FN (2007) Inorg Chem 46(21):8771–8783
19. Goeb S, Rachford AA, Castellano FN (2008) Chem Commun (7):814–816
20. Rachford AA, Goeb S, Ziessel R, Castellano FN (2008) Inorg Chem 47(10):4348–4355
21. Rachford AA, Goeb S, Castellano FN (2008) J Am Chem Soc 130(9):2766–2767
22. Adams CJ, Fey N, Harrison ZA, Sazanovich IV, Towrie M, Weinstein JA (2008) Inorg Chem 47(18):8242–8257
23. Ziessel R, Seneclauze JB, Ventura B, Barbieri A, Barigelletti F (2008) Dalton Trans (13):1686–1688
24. Field JS, Gertenbach J-A, Haines RJ, Ledwaba LP, Mashapa NT, McMillin DR, Munro OQ, Summerton GC (2003) Dalton Trans:1176–1180
25. Field JS, Haines RJ, McMillin DR, Summerton GC (2002) Dalton Trans:1369–376
26. Bailey JA, Hill MG, Marsh RE, Miskowski VM, Schaefer WP, Gray HB (1995) Inorg Chem 34(18):4591–4599
27. Yip H-K, Cheng L-K, Cheung K-K, Che C-M (1993) J Chem Soc Dalton Trans:2933–2938
28. Büchner R, Cunningham CT, Field JS, Haines RJ, McMillin DR, Summerton GC (1999) J Chem Soc Dalton Trans:711–717
29. Aldridge TK, Stacy EM, McMillin DR (1994) Inorg Chem 3(4):722–727
30. Crites DK, Cunningham CT, McMillin DR (1998) Inorg Chim Acta 273(1):346–353
31. McMillin DR, Moore JJ (2002) Coord Chem Rev 229(1):113–121
32. Yam VW-W, Tang RP-L, Wong KM-C, Cheung K-K (2001) Organometallics 20(22): 4476–4482
33. Yang Q-Z, Wu L-Z, Wu Z-X, Zhang L-P, Tung C-H (2002) Inorg Chem 41(22):5653–5655
34. Du P, Schneider J, Brennessel WW, Eisenberg R (2008) Inorg Chem 47:69–77
35. Grove LJ, Rennekamp JM, Jude H, Connick WB (2004) J Am Chem Soc 126:1594–1595
36. Lu W, Chan MCW, Zhu N, Che C-M, He Z, Wong K-Y (2003) Chem Eur J 9:6155–6166
37. Wadas TJ, Wang Q-M, Kim Y-j, Flaschenreim C, Blanton TN, Eisenberg R (2004) J Am Chem Soc (126):16841–16849
38. Grove LJ, Oliver AG, Krause JA, Connick WB (2008) Inorg Chem 47:1408–1410
39. Yam VWW, Wong KM-C, Zhu N (2002) J Am Chem Soc 124:6506–6507
40. Muro ML, Daws CA, Castellano FN (2008) Chem Commun:6134–6136
41. Zhang D, Wu L-Z, Yang Q-Z, Li X-H, Zhang L-P, Tung C-H (2003) Org Lett 5(18):3221–3224

42. Yang Q-Z, Tong Q-X, Wu L-Z, Wu Z-X, Zhang L-P, Tung C-H (2004) Eur J Inorg Chem (9):1948–1954
43. Yang Q-Z, Wu L-Z, Zhang H, Chen B, Wu Z-X, Zhang L-P, Tung C-H (2004) Inorg Chem 43(17):5195–5197
44. Wong KM-C, Tang W-S, Lu X-X, Zhu N, Yam VWW (2005) Inorg Chem 44:1492–1498
45. Tang W-S, Lu X-X, Wong KM-C, Yam VW-W (2005) J Mater Chem 15(27–28):2714–2720
46. Ma D-L, Shum TY-T, Zhang F, Che C-M, Yang M (2005) Chem Commun (37):4675–4677
47. Ratilla EMA, Brothers HM, Kostic NM (1987) J Am Chem Soc 109(15):4592–4599
48. Wong KM-C, Tang W-S, Chu BW-K, Zhu N, Yam VW-W (2004) Organometallics 23:3459–3465
49. Guo F, Sun W, Liu Y, Schanze K (2005) Inorg Chem 44(11):4055–4065
50. Du P, Schneider J, Jarosz P, Eisenberg R (2006) J Am Chem Soc 128(24):7726–7727
51. Narayana-Prabhu R, Schmehl RH (2006) Inorg Chem 45(11):4319–4321
52. Du P, Schneider J, Jarosz P, Zhang J, Brennessel WW, Eisenberg R (2007) J Phys Chem B 111(24):6887–6894
53. Du P, Knowles K, Eisenberg R (2008) J Am Chem Soc 130(38):12576–12577
54. Du P, Schneider J, Li F, Zhao W, Patel U, Castellano FN, Eisenberg R (2008) J Am Chem Soc 130:5056–5058
55. Cortes M, Carney JT, Oppenheimer JD, Downey KE, Cummings SD (2002) Inorg Chim Acta 333:148–151
56. Yu C, Wong KM-C, Chan KH-Y, Yam VWW (2005) Angew Chem Int Ed 44:791–794
57. Tam AY-Y, Wong KM-C, Wang G, Yam VW-W (2007) Chem Commun (20):2028–2030
58. Camerel F, Ziessel R, Donnio B, Bourgogne C, Guillon D, Schmutz M, Iacovita C, Bucher J-P (2007) Angew Chem Int Ed 46:2659–2662
59. Han X, Wu L-Z, Si G, Pan J, Yang Q-Z, Zhang L-P, Tung C-H (2007) Chem Eur J 13(4):1231–1239
60. Lo H-S, Yip S-K, Wong KM-C, Zhu N, Yam VW-W (2006) Organometallics 25(15):3537–3540
61. Chakraborty S, Wadas TJ, Hester H, Flaschenreim C, Schmehl R, Eisenberg R (2005) Inorg Chem 44:6284–6293
62. Shikhova E, Danilov EO, Kinayyigit S, Pomestchenko IE, Tregubov AD, Camerel F, Retailleau P, Ziessel R, Castellano FN (2007) Inorg Chem 46(8):3038–3048
63. Muro ML, Diring S, Wang X, Ziessel R, Castellano FN (2008) Inorg Chem 47(15):6796–6803
64. Nastasi F, Puntoriero F, Campagna S, Diring S, Ziessel R (2008) Phys Chem Chem Phys 10(27):3982–3986
65. Yam VW-W, Wong KM-C, Zhu N (2003) Angew Chem Int Ed 42(12):1400–1403
66. Lu W, Mi B-X, Chan MCW, Hui Z, Che C-M, Zhu N, Lee S-T (2004) J Am Chem Soc 126:4958–4971
67. Berenguer JR, Lalinde E, Torroba J (2007) Inorg Chem 46(23):9919–9930
68. Sonogashira K, Yatake T, Tohda Y, Takahashi S, Hagihara N (1977) J Chem Soc Chem Commun:291–292
69. Sonogashira K, Takahashi S, Hagihara N (1977) Macromolecules 10(4):879–880
70. Sonogashira K, Fujikura Y, Yatake T, Toyoshima N, Takahashi S, Hagihara N (1978) J Organomet Chem 145:101–108
71. Takahashi S, Kariya M, Yatake T, Sonogashira K, Hagihara N (1978) Macromolecules 11(6):1063–1066
72. Takahashi S, Murata E, Kariya M, Sonogashira K, Hagihara N (1979) Macromolecules 12(5):1016–1018
73. Shikhova E, Danilov EO, Kinayyigit S, Pomestchenko IE, Tregubov AD, Camerel F, Retaileau P, Ziessel R, Castellano FN (2007) Inorg Chem 46(8):3038–3048
74. Liu Y, Jiang S, Glusac K, Powell D, Herson DF, Schanze KS (2002) J Am Chem Soc 124(42):12412–12413
75. Batista ER, Martin RL (2005) J Phys Chem A 109(43):9856–9859

76. Schull TL, Kushmerick JG, Patterson CH, George C, Moore MH, Pollack SK, Shashidhar R (2003) J Am Chem Soc 125(11):3202–3203
77. Jones SC, Coropceanu V, Barlow S, Kinnibrugh T, Timofeeva T, Bredas J-L, Marder SR (2004) J Am Chem Soc 126(38):11782–11783
78. Cooper TM, Hall BC, Burke AR, Rogers JE, McLean DG, Slagle JE, Fleitz PA (2004) Chem Mater 16(17):3215–3217
79. Cooper TM, Blaudeau J-P, Hall BC, Rogers JE, McLean DG, Liu Y, Toscano JP (2004) Chem Phys Lett 400(1–3):239–244
80. Haskins-Glusac K, Ghiviriga I, Abboud KA, Schanze KS (2004) J Phys Chem B 108(16):4969–4978
81. Zhao X, Cardolaccia T, Farley RT, Abboud KA, Schanze KS (2005) Inorg Chem 44(8):2619–2627
82. Schanze KS, Silverman EE, Zhao X (2005) J Phys Chem B 109(39):18451–18459
83. Tao C-H, Zhu N, Yam VW-W (2005) Chem Eur J 11(5):1647–1657
84. Guo F, Kim Y-G, Reynolds JR, Schanze KS (2006) Chem Commun (17):1887–1889
85. Kim K-Y, Liu S, Koese ME, Schanze KS (2006) Inorg Chem 45(6):2509–2519
86. Cooper TM, Krein DM, Burke AR, McLean DG, Rogers JE, Slagle JE (2006) J Phys Chem A 110(50):13370–13378
87. Cooper TM, Krein DM, Burke AR, McLean DG, Rogers JE, Slagle JE, Fleitz PA (2006) J Phys Chem A 110(13):4369–4375
88. Rogers JE, Slagle JE, Krein DM, Burke AR, Hall BC, Fratini A, McLean DG, Fleitz PA, Cooper TM, Drobizhev M, Makarov NS, Rebane A, Kim K-Y, Farley R, Schanze KS (2007) Inorg Chem 46(16):6483–6494
89. Guo F, Ogawa K, Kim Y-G, Danilov EO, Castellano FN, Reynolds JR, Schanze KS (2007) Phys Chem Chem Phys 9(21):2724–2734
90. Cardolaccia T, Funston AM, Kose ME, Keller JM, Miller JR, Schanze KS (2007) J Phys Chem B 111(37):10871–10880
91. Glusac K, Koese ME, Jiang H, Schanze KS (2007) J Phys Chem B 111(5):929–940
92. Farley RT, Zheng Q, Gladysz JA, Schanze KS (2008) Inorg Chem 47(8):2955–2963
93. Cardolaccia T, Li Y, Schanze KS (2008) J Am Chem Soc 130(8):2535–2545
94. Westlund R, Glimsdal E, Lindgren M, Vestberg R, Hawker C, Lopes C, Malmstroem E (2008) J Mater Chem 18(2):166–175
95. Nakai H, Fukada S, Nakatsuji H (1997) J Phys Chem A 101:973–980
96. Nakatsuji H, Hirao K (1968) J Chem Phys 68:2053
97. Ouddai N, Costuas K, Bencharif M, Saillard J-Y, Halet J-F (2005) C R Chimie 8:1336–1350
98. Vives G, Carella A, Sistach S, Launay J-P, Rapenne G (2006) New J Chem 30(10):1429–1438
99. Fernandez S, Fornies J, Gil B, Gomez J, Lalinde E (2003) Dalton Trans:822–830
100. Benito J, Berenguer JR, Fornies J, Gil B, Gomez J, Lalinde E (2003) Dalton Trans (22):4331–4339
101. Zhou X, Zhang H-X, Pan Q-J, Xia B-H, Tang A-C (2005) J Phys Chem A 109(39):8809–8818
102. Liu X-J, Feng J-K, Meng J, Pan Q-J, Ren A-M, Zhou X, Zhang H-X (2005) Eur J Inorg Chem:1856–1866
103. Minaev B, Jansson E, Lindgren M (2006) J Chem Phys 125(9):094306/1–094306/11
104. Liu S, Ding Y, Wang X, Chen M, Fan Z (2008) J Theor Comput Chem 7(1):103–111
105. Cannizzo A, Blanco-Rodríguez AM, Nahhas A, Šebera J, Záliš S, Vlček A Jr, Chergui M (2008) J Am Chem Soc 130:8967

Top Organomet Chem (2010) 29: 193–235
DOI: 10.1007/3418_2009_6

Published online: 20 October 2009

Organometallic Pt(II) and Ir(III) Triplet Emitters for OLED Applications and the Role of Spin–Orbit Coupling: A Study Based on High-Resolution Optical Spectroscopy

Andreas F. Rausch, Herbert H. H. Homeier, and Hartmut Yersin

Abstract High-resolution optical spectroscopy of organometallic triplet emitters reveals detailed insights into the lowest triplet states and the corresponding electronic and vibronic transitions to the singlet ground state. As case studies, the blue-light emitting materials Pt(4,6-dFppy)(acac) and Ir(4,6-dFppy)$_2$(acac) are investigated and characterized in detail. The compounds' photophysical properties, being markedly different, are largely controlled by spin–orbit coupling (SOC). Therefore, we study the impact of SOC on the triplet state and elucidate the dominant SOC and state-mixing paths. These depend distinctly on the compounds' coordination geometry. Relatively simple rules and relations are pointed out. The combined experimental and theoretical results lead us towards structure-efficiency rules and guidelines for the design of new organic light emitting diode (OLED) emitter materials.

Keywords Emission quantum yields • High-resolution spectroscopy • Iridium complexes • OLED emitters • Organometallic compounds • Phosphorescence • Photophysics • Platinum complexes • Radiative rates • Spin–orbit coupling • Triplet emitters • Zero-field splitting • SOC • ZFS • SOC and geometry • SOC paths

Contents

1 Introduction and Scope 194
2 Ambient Temperature Properties of Pt(4,6-dFppy)(acac) and Ir(4,6-dFppy)$_2$(acac) 195
3 Detailed Studies of Pt(4,6-dFppy)(acac) 197
3.1 Electronic 0–0 Transitions 198
3.2 Thermalized Emission Decay 200
3.3 Vibrational Satellite Structures 202
3.4 Zero-Field Splittings at Different Sites and in Different Hosts 205

A.F. Rausch, H.H.H. Homeier, and H. Yersin (✉)
Institut für Physikalische und Theoretische Chemie, Universität Regensburg,
93053 Regensburg, Germany
e-mail: hartmut.yersin@chemie.uni-regensburg.de

4 Detailed Studies of Ir(4,6-dFppy)$_2$(acac) 205
4.1 Electronic 0–0 Transitions 206
4.2 Thermalized Emission Decay 207
4.3 Vibrational Satellite Structure 208
4.4 Matrix Dependence of T_1 State Properties 210
5 Pt(4,6-dFppy)(acac) and Ir(4,6-dFppy)$_2$(acac): Energy Level Diagrams, Zero-Field Splittings, and Decay Times 211
6 Spin–Orbit Coupling: Theoretical Considerations 212
6.1 General Aspects 212
6.2 Some Definitions 213
6.3 Orbitals and States 215
6.4 Spin–Orbit Coupling: General Aspects and Rules 216
6.5 Direct Spin–Orbit Coupling 220
6.6 Indirect Spin–Orbit Coupling 221
6.7 Trends in Realistic Systems 224
6.8 Spin–Orbit Coupling and Coordination Geometry 226
7 Spin–Orbit Coupling and Photophysical Trends: Conclusion 228
8 Appendix 231
References 231

1 Introduction and Scope

Within the last decade, phosphorescent organo-transition metal compounds have become a focus of intense research, particularly due to their applicability as efficient emitters in electroluminescent devices, such as organic light emitting diodes (OLEDs) [1–13]. These compounds can exhibit an emission of high quantum yield from the lowest excited triplet state to the singlet ground state. Although the triplet–singlet transitions are formally forbidden, they may become sufficiently allowed by spin–orbit coupling (SOC) induced by the heavy metal center. Keeping this in mind, we will often speak simply of triplet states meaning triplet states with SOC-induced singlet admixtures. Moreover, SOC leads to fast intersystem crossing processes from higher lying singlet states to the emitting triplet state T_1. Therefore, both singlet and triplet excitons, formed by electron-hole recombination, can contribute to the emission in an electroluminescence process. This allows an up to four times higher internal quantum efficiency than achievable with fluorescent emitters (triplet harvesting effect) [10–13].

The most frequently applied central metal ions in phosphorescent OLED emitters are Pt(II) and Ir(III). Especially Ir(III) compounds are, due to their outstanding photophysical properties, often the first choice as emitting materials [14–19]. The famous Ir(ppy)$_3$ (ppy$^-$ = phenylpyridinate), for example, exhibits a relatively short-lived green emission with a quantum yield of almost 100% in a thin film [20–22]. In addition, in the last few years, a growing number of Pt(II) compounds has been reported which are characterized by high photoluminescence quantum yields and emission decay times of several microseconds, making these compounds also attractive as emitters in OLEDs [23–28]. Pt(II) complexes can offer additional possibilities for the generation of light. Due to a strong tendency to form aggregates of

electronically strongly interacting monomers, many Pt(II) compounds exhibit a broad and red shifted emission band compared to the monomer emission [23, 24, 29–36]. In several cases, a combination of monomer and aggregate emission could be utilized for the generation of white electroluminescence in single dopant organic light emitting diodes (WOLEDs) [27, 31, 37–43].

However, despite the attractiveness and importance of Pt(II) and Ir(III) compounds, a detailed understanding of their excited state properties is still to be developed. Therefore, in this contribution, we study and compare the compounds Pt(4,6-dFppy)(acac) and Ir(4,6-dFppy)$_2$(acac) (4,6-dFppy = (4′,6′-difluorophenyl) pyridinate, acac = acetylacetonate) with modern techniques of high-resolution optical spectroscopy down to cryogenic temperatures. The investigations will focus on a series of photophysical properties, such as zero-field splitting (ZFS) of the emitting T_1 state into substates, individual decay times of the substates, vibrational satellite structures, excited state geometry changes, and matrix dependence of these properties. This information will lead us to assign the electronic transitions. Both compounds have the same chromophoric ligand (4,6-dFppy) and the same ancillary ligand (acac). This allows us, for example, to explore the influence of the central metal and the coordination geometry on properties of the emitting triplet state. The observed differences can largely be related to SOC routes to higher lying states that vary in effectiveness. For a better understanding, we will also give an introduction into theoretical models of SOC in organo-transition metal compounds. Moreover, the combined results of experiments at low temperature and of theoretical considerations will be set in relation to the materials' photophysical performance at room temperature. This combined approach also leads to guidelines for the design of new efficient emitter materials for OLEDs.

2 Ambient Temperature Properties of Pt(4,6-dFppy)(acac) and Ir(4,6-dFppy)$_2$(acac)

In this section we introduce to the photophysical properties of Pt(4,6-dFppy)(acac) and Ir(4,6-dFppy)$_2$(acac) at ambient temperature and to some OLED applications. Both compounds were first synthesized by Thompson and coworkers [44, 45].

Figure 1 shows absorption and emission spectra measured at ambient temperature in CH_2Cl_2. The absorption spectrum of Pt(4,6-dFppy)(acac) is slightly better resolved than that of Ir(4,6-dFppy)$_2$(acac). This is connected with the higher density of states of the Ir(III) compared to the Pt(II) complex due to the additional chromophoric ligand and the higher number of vibrational modes in Ir(4,6-dFppy)$_2$(acac). For both compounds, the strong transitions below ≈350 nm are assigned to be largely of ligand centered (LC) character, while the absorptions between ≈350 and ≈420 nm are classified as transitions from the singlet ground state to excited singlet states of strong metal-to-ligand charge transfer (MLCT, metal 5d-(4,6-dFppy)π*) parentage. The weak transitions in the long wavelength regions of the absorption spectra have been scaled up by a factor of 60 (Pt(4,6-dFppy)(acac)) and 15 (Ir(4,6-dFppy)$_2$(acac)),

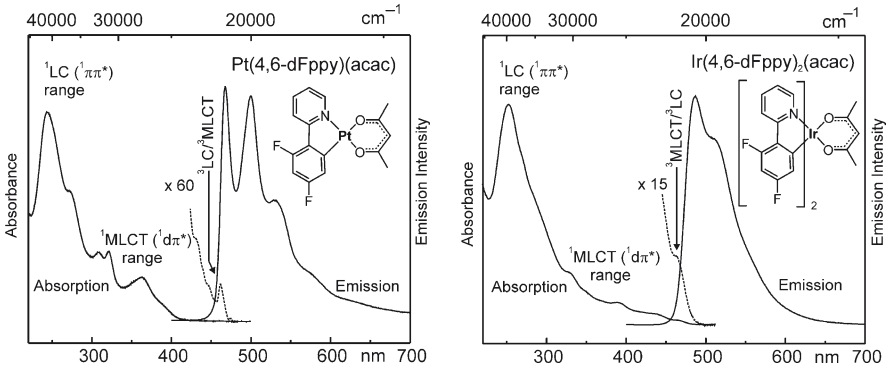

Fig. 1 Absorption and emission spectra of Pt(4,6-dFppy)(acac) and Ir(4,6-dFppy)$_2$(acac) in CH_2Cl_2 ($c \approx 10^{-5}$ mol L^{-1}, $\lambda_{exc} = 300$ nm) at $T = 300$ K. The *dashed lines*, showing the absorptions in the region of the lowest excited state, are scaled by the given factors (compare [50, 108])

respectively. Due to resonance with the respective high-energy emission flanks, the transitions near 21,700 cm^{-1} (461 nm, Pt(4,6-dFppy)(acac)) and 21,500 cm^{-1} (465 nm, Ir(4,6-dFppy)$_2$(acac)) can be related to the electronic transitions from the singlet ground state S_0 to the respective lowest triplet state T_1. Details will be discussed in Sects. 3.1 and 4.1.

The emission spectrum of Pt(4,6-dFppy)(acac) shows a series of resolved bands. The most intense one at 21,400 cm^{-1} (467 nm) corresponds to the electronic $T_1 \rightarrow S_0$ transition (involving ground state phonons, see below), while a second distinct band, peaking at 20,000 cm^{-1} (500 nm), is involving overlapping intra-ligand vibrations. The additional peaks at lower energy are assigned to vibrational progressions and/or combinations. Ir(4,6-dFppy)$_2$(acac) exhibits an emission maximum at 20,500 cm^{-1} (488 nm), which is related to the electronic transition from the T_1 state to the S_0 state. A second distinct peak at 19,400 cm^{-1} (515 nm) corresponds to overlapping vibrational satellites. The lower resolution of the emission spectrum of Ir(4,6-dFppy)$_2$(acac) as compared to the one of Pt(4,6-dFppy)(acac) is caused by significantly higher intensities of metal–ligand (M–L) vibrational satellites in the spectral region below ≈600 cm^{-1} relative to the electronic origin for the Ir(III) complex. These M–L satellites lead to a pronounced smearing out of the ambient temperature spectrum [46, 47]. The occurrence of high-intensity vibrational M–L satellites is a consequence of a high MLCT character of the emitting state. A comparable situation was also found for Ir(ppy)$_3$ [48]. In contrast, the better resolvable emission of Pt(4,6-dFppy)(acac) indicates a largely LC character of the emitting triplet. However, these coarse assignments should not be taken too strictly, since interactions of the compound with the matrix, for example electron–phonon interactions, may also result in substantial broadenings (see Sect. 4.3) [49].

Distinct differences between the two compounds are also found in the emission decay times and the emission quantum yields. The phosphorescence of Pt(4,6-dFppy)(acac) decays with 0.3 µs and the quantum yield amounts only to $\phi_{PL} = 2\%$ in

deaerated solution [27, 44], while for Ir(4,6-dFppy)$_2$(acac) values of 1.2 µs and $\phi_{PL} = 64\%$ are found [50]. The low quantum yield and the very short decay time of the Pt(II) compound can be ascribed to a relatively close-lying quenching dd* state, which gets thermally activated at ambient conditions.[1]

As also observed for other Pt(II) compounds [23, 24, 29–34], Pt(4,6-dFppy)(acac) has a strong tendency to form excimers or aggregates in concentrated solutions and solid films, respectively. The concentration-dependent excimer formation in solution has been investigated in detail [51], as well as the concentration- and temperature dependent dynamics of aggregate formation in solid films [52]. A balanced combination of the blue–green monomer and the red aggregate emission covers a large spectral range of the visible light. Thus, this phenomenon could be utilized for efficient white light emitting OLEDs [31, 37–40]. Recently, an efficient device with a power efficiency of 12.6 lm W^{-1} and an external quantum efficiency of 15.9% at 500 cd m^{-2}, based on Pt(4,6-dFppy)(acac) doped in the host material 26mCPy (2,6-bis(*N*-carbazolyl)pyridine), was reported [40].

Despite the remarkable quantum yield and the relatively short emission decay time of Ir(4,6-dFppy)$_2$(acac), much less research work has been published than for the related famous compound Ir(4,6-dFppy)$_2$(pic) (FIrpic, pic = picolinate), which exhibits a 15 nm blue shifted emission compared to Ir(4,6-dFppy)$_2$(acac) [50, 53]. Therefore, Ir(4,6-dFppy)$_2$(pic) is a more suited dopant for highly desired blue-emitting OLEDs [17, 54–56]. It is noted that by the implementation of strongly electron-withdrawing ancillary ligands, further shifts towards a deep blue emission could be achieved [45, 57, 58].

3 Detailed Studies of Pt(4,6-dFppy)(acac)

At ambient temperature, much information on the emitting triplet state and the related photophysical properties is lost due to thermal broadening or electron–phonon coupling and thermalization effects. Therefore, a detailed characterization is not feasible. At cryogenic temperatures, however, highly resolved and thus very informative emission and excitation spectra are obtainable. But this requires a suitable host. For example, for planar systems like Pd(II) [59–62] or Pt(II) compounds [32, 63–65] as well as many organic molecules [66–70], it has been shown that by use of linear alkanes as hosts – the so-called Shpol'skii matrices [66] – highly resolved electronic and vibronic spectra can be obtained. The resulting spectra are often more than a hundred times better resolved than found with glass forming or amorphous matrices.

When Pt(4,6-dFppy)(acac) is dissolved (doped) at low concentration ($c \approx 10^{-5}$ mol L^{-1}) in *n*-octane and cooled to cryogenic temperatures, for example to 4.2 K, a well resolved

[1]For Pt(4,6-dFppy)(acac) in a PMMA film, a distinctly higher quantum yield of 40% is found. This can be explained with a destabilization of quenching dd* states in the rigid PMMA host compared to fluid solutions.

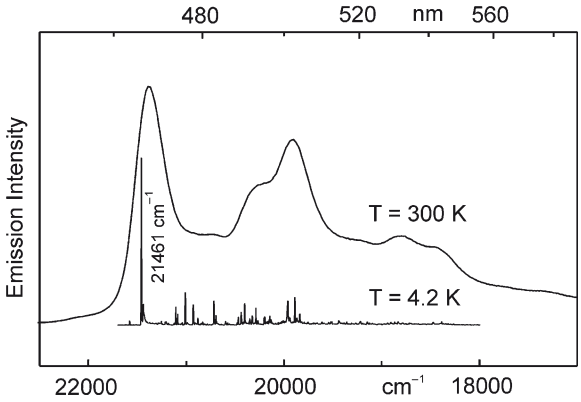

Fig. 2 Comparison of the emission spectra of Pt(4,6-dFppy)(acac) in *n*-octane ($c \approx 10^{-5}$ mol L^{-1}) at $T = 300$ K ($\lambda_{exc} = 370$ nm) and at $T = 4.2$ K. The 4.2 K spectrum represents the emission of the dominant low energy site, which was excited selectively into a vibrational satellite of the transition $0 \rightarrow$ II/III at 22,161 cm^{-1} (21,461 + 700 cm^{-1} vibration) (see Sect. 3.3) (compare also [71])

emission is found [71]. After UV excitation, it consists of a manifold of narrow lines with halfwidths of only a few cm^{-1} and a weak background (not shown). These lines correspond to a number of discrete sites of dopant molecules in the *n*-octane matrix. Using a tunable dye laser, a specific site can be excited selectively. For this purpose, the site of lowest energy was chosen, since its emission is well detectable and a perturbing excitation of higher lying sites can be avoided. In Fig. 2, the drastic effects of this strategy are illustrated by comparing the selectively excited emission spectrum of Pt(4,6-dFppy)(acac) in *n*-octane, measured at $T = 4.2$ K, to the emission at ambient temperature in the same solvent.

3.1 Electronic 0–0 Transitions

In this section, we will focus on the purely electronic 0–0 transitions between the substates of the emitting T_1 state of Pt(4,6-dFppy)(acac) in *n*-octane and the singlet ground state. Figure 3 shows a selectively detected excitation spectrum of the region of the electronic origins of the main site measured at $T = 1.2$ K (a) and several selectively excited emission spectra at different temperatures (b). At $T = 1.2$ K, the line at 21,453 cm^{-1} exhibits the highest intensity in emission. It can be assigned as purely electronic 0–0 transition I $\rightarrow$ 0 from the lowest T_1 substate I to the singlet ground state. At an energy of 21,461 cm^{-1} a second, weaker line can be observed. With temperature increase it drastically gains intensity and slightly broadens. It will be proven below that this line represents two purely electronic 0–0 transitions from the higher lying T_1 substates II and III to the ground state. These two lines cannot be resolved in the frame of the experimental resolution of ≈ 1 cm^{-1}. The assignment of the lines at 21,453 and 21,461 cm^{-1} as purely electronic transitions is substantiated

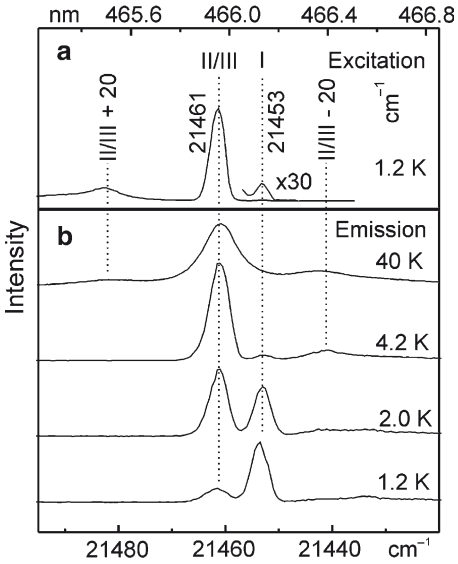

Fig. 3 Emission and excitation spectra of Pt(4,6-dFppy)(acac) in *n*-octane at selected temperatures. For the excitation spectrum (**a**), the emission was selectively detected at an energy of 21,012 cm^{-1}, which corresponds to a vibrational satellite of the transition I → 0 (21,453–441 cm^{-1} vibration). Note the scaling factor of 30 for the transition 0 → I. The emission spectra (**b**) were recorded after selective excitation into a vibrational satellite of the transition 0 → II/III at 22,161 cm^{-1} (21,461 + 700 cm^{-1} vibration) (compare [71])

by the fact that they appear resonantly in excitation and in emission and that the vibrational modes identified in the vibrational satellite structures, as will be discussed in Sect. 3.3, fit only to just these electronic transitions.

The excitation line I → 0 occurs only with very weak intensity (note the scaling factor of 30 in Fig. 3a), while the transitions 0 → II/III is relatively strong and by a factor of ≈190 more allowed. The additional lines observed in the emission and excitation spectra occurring 20 cm^{-1} at lower (higher) energy in emission (excitation) with respect to the 0–0 transitions 0 ↔ II/III are assigned to local phonon satellites which stem from vibrations of the dopant in its matrix cage. A corresponding satellite also appears in the 40 K emission spectrum as "hot band." Phonon satellites of similar energy are frequently observed in highly resolved spectra of transition metal compounds (for example, see [53, 63, 72] and Sect. 4.3).

Usually the triplet states of organo-transition metal compounds consist of three substates. However, the data presented allow us to identify only two 0–0 transitions. Therefore, Fig. 4 displays selectively excited emission spectra for the region of the electronic origins at high magnetic field strengths. Due to the Zeeman effect, distinct changes of the emission properties are expected with increasing B-field strength [49, 65, 71–77]. Indeed, the higher lying 0–0 transition at 21,461 cm^{-1} splits. Thus, all three substates become observable under application of magnetic fields. At zero field, the substates II and III lie within an energy range ≈1 cm^{-1}, while the splitting amounts to 9 cm^{-1} at $B = 12$ T.

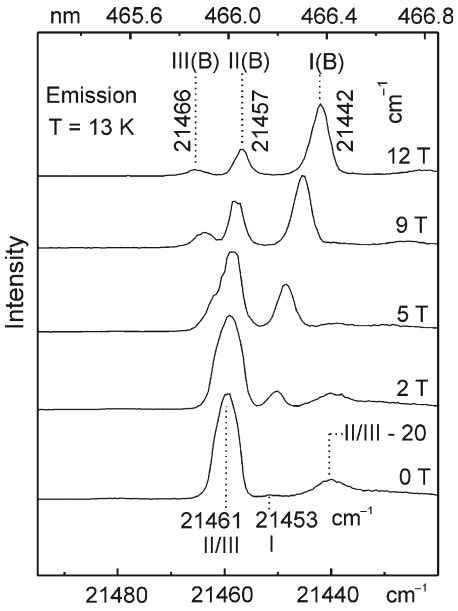

Fig. 4 Emission spectra of Pt(4,6-dFppy)(acac) in *n*-octane at different magnetic field strengths. The temperature of 13 K was chosen to provide a significant thermal population of all sublevels The sample was selectively excited into the 700 cm^{-1} vibrational satellite of the transition 0 → II(B) (compare [71])

Other significant spectral changes are also observed. The total splitting increases from 8.3 cm^{-1} at $B = 0$ T to 24 cm^{-1} at $B = 12$ T. Moreover, due to the field induced mixings of the wave functions, the radiative allowedness of the transitions from the T_1 substates to the ground state is strongly redistributed. The emission from the lowest B-field disturbed substate I(B) becomes dominant, while the transitions II(B) → 0 and III(B) → 0 lose intensity. This is also displayed in the emission decay time of substate I at 1.5 K, which becomes as short as 12 µs at 12 T, while it amounts to 85 µs at zero-field (see next section). Due to this B-field induced increase of radiative allowedness, it also becomes possible to tune magnetically other important properties like the mechanisms of vibrational deactivation [78–82].

3.2 Thermalized Emission Decay

In Sect. 3.1 it was shown that, at zero magnetic field, the transitions 0 ↔ I and 0 ↔ II/III of Pt(4,6-dFppy)(acac) in *n*-octane exhibit distinctly different properties with respect to their emission intensities, i.e., their oscillator strengths (radiative allowedness). This behavior is also expected to be reflected in the individual

emission decay times of the substates. At low temperature, for example at $T = 1.2$ K, one can often directly measure the decay time of the lowest substate. However, at higher temperature, usually only the thermalized emission decay time of the different substates is accessible from direct measurements, but not their individual decay times. Nevertheless, an indirect method can be applied to determine these values. Under the assumption of a fast thermalization, the occupation dynamics of excited states is governed by the expression [48, 49, 83–87]

$$\frac{\mathrm{d}N}{\mathrm{d}t} = -k_{\mathrm{therm}} N = -\sum_i k_i n_i, \tag{1}$$

where n_i denotes the Boltzmann occupation number and k_i is the total rate constant for depopulation of state i. N is the total occupation number of excited states and $k_{\mathrm{therm}} = 1/\tau_{\mathrm{therm}}$ stands for the rate constant for depopulation of the thermalized system of excited states. For three emitting states (i=I, II, III), the introduction of Boltzmann factors leads to the expression [48, 83–87]

$$k_{\mathrm{therm}} = \frac{1}{\tau_{\mathrm{therm}}} = \frac{k_{\mathrm{I}} + k_{\mathrm{II}} \cdot \exp\left(\frac{-\Delta E_{\mathrm{II-I}}}{k_{\mathrm{B}} T}\right) + k_{\mathrm{III}} \cdot \exp\left(\frac{-\Delta E_{\mathrm{III-I}}}{k_{\mathrm{B}} T}\right)}{1 + \exp\left(\frac{-\Delta E_{\mathrm{II-I}}}{k_{\mathrm{B}} T}\right) + \exp\left(\frac{-\Delta E_{\mathrm{III-I}}}{k_{\mathrm{B}} T}\right)}, \tag{2}$$

which describes the temperature dependence of the thermalized emission decay time. $\Delta E_{\mathrm{II-I}}$ and $\Delta E_{\mathrm{III-I}}$ are the energy differences between the substates I and II, and I and III, respectively. k_{B} is the Boltzmann constant. For a system of three excited states with the substates II and III being considered to be energetically almost degenerate, as observed for Pt(4,6-dFppy)(acac) in *n*-octane, (2) simplifies to [71]

$$k_{\mathrm{therm}} = \frac{1}{\tau_{\mathrm{therm}}} = \frac{k_{\mathrm{I}} + k_{\mathrm{II/III}} \cdot \exp\left(\frac{-\Delta E_{\mathrm{II/III-I}}}{k_{\mathrm{B}} T}\right)}{1 + 2 \cdot \exp\left(\frac{-\Delta E_{\mathrm{II/III-I}}}{k_{\mathrm{B}} T}\right)}, \tag{3}$$

with just one energy difference $\Delta E_{\mathrm{II/III-I}}$ and a combined rate constant $k_{\mathrm{II/III}} = k_{\mathrm{II}} + k_{\mathrm{III}}$.

In Fig. 5, the measured temperature dependent thermalized emission decay time is depicted together with a fit according to (3). The fit provides the individual decay times of $\tau_{\mathrm{I}} = (85.0 \pm 0.5)\,\mu\mathrm{s}$ and $\tau_{\mathrm{II/III}} = (2.6 \pm 0.2)\,\mu\mathrm{s}$, as well as an energy separation of $\Delta E_{\mathrm{II/III-I}} = (8.5 \pm 0.5)\,\mathrm{cm}^{-1}$. This latter value is in good agreement with the splitting of 8.3 cm^{-1} obtained from highly resolved spectra (see Sect. 3.1). The value for τ_{I} of 85.0 µs corresponds to the measured decay time at $T = 1.2$ K, indicating a negligible thermal population of the higher lying substates at that temperature. The weak allowedness observed for the transition 0 → I (Fig. 3a) and the long

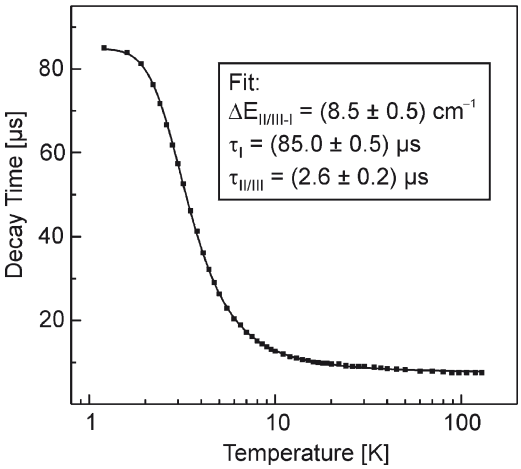

Fig. 5 Thermalized emission decay time of Pt(4,6-dFppy)(acac) in *n*-octane vs temperature. For temperatures of $T \leq 2$ K, the emission was detected at the energy of the 0–0 transition I → 0, while for $T > 2$ K, detection at the energy of the 0–0 transition II/III → 0 was chosen. The *solid line* represents a fit of (3) to the experimental data. The results obtained from the fit are shown in the *inset* (compare [71])

decay time indicate that substate I exhibits almost pure triplet character, while the relatively short decay time of the substates II/III of 2.6 µs and the much higher allowedness of the transitions 0 → II/III (Fig. 3a) show that these substates contain significant admixtures of higher lying singlet states.

Interestingly, the ratio of the rate constants $k_{II/III} = 1/\tau_{II/III} = 3.85 \times 10^5\,s^{-1}$ and $k_I = 1/\tau_I = 1.2 \times 10^4\,s^{-1}$ (as determined by the fitting procedure) amounts only to ≈32, and thus does not reach the value of 190, as one might conclude from the observed intensity ratio of the electronic 0–0 transitions as determined from the excitation spectrum (Fig. 3a). However, both values are only comparable if the involved states exhibit identical radiative and nonradiative deactivation paths/mechanisms. In the next section, it will be shown that the vibrational satellite structures in the emission of the substates II/III and I are induced by completely different vibronic mechanisms.

3.3 Vibrational Satellite Structures

The vibrational satellite structures in the highly resolved emission of Pt(4,6-dFppy)(acac) in *n*-octane display the different properties of the triplet substates in a very characteristic manner. Figure 6 shows the selectively excited emission spectra in *n*-octane at temperatures of 1.2, 4.2, and 20 K, together with a spectrum obtained at 77 K for comparison.

The low temperature spectra clearly display the electronic 0–0 transitions and a large number of vibrational satellites. Many of these correspond to fundamental vibrations.

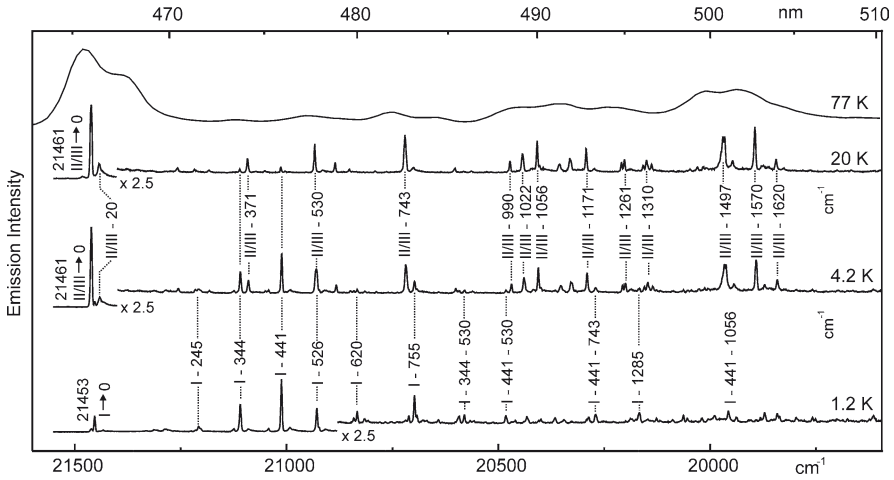

Fig. 6 Emission spectra of Pt(4,6-dFppy)(acac) in *n*-octane ($c \approx 10^{-5}$ mol L^{-1}) at different temperatures after selective excitation at 22,161 cm^{-1} (vibrational satellite of the 0 → II/III transition, (21,461 + 700) cm^{-1}). The energies of the vibrational satellites are given relative to the respective electronic 0–0 transitions (compare [108]). Note the scaling factors in the spectra. For comparison, the emission spectrum at 77 K in the same solvent is also depicted ($\lambda_{exc} = 370$ nm)

Low energy modes with energies up to ≈100 cm^{-1} relative to the electronic 0–0 transitions are largely determined by vibrations of the dopant in its matrix cage. They represent so-called local phonon modes (see, for example, the 20 cm^{-1} line in Figs. 3 and 6 and compare the spectra displayed in Sect. 4.3 for Ir(4,6-dFppy)$_2$(acac)). It should be noted that a mixing of low energy vibrations of the compound with such dopant-cage modes is still obvious up to ≈150 cm^{-1} [62]. Overlapping with this energy range up to 500/600 cm^{-1}, M–L vibrations can be found (for example I – 441 cm^{-1}, II/III – 530 cm^{-1}), while vibrations with fundamentals higher than ≈600 cm^{-1} can usually be assigned as internal ligand modes (for example II/III – 1,056 cm^{-1}, II/III – 1,570 cm^{-1}) [63].

The spectrum at $T = 1.2$ K is dominated by the emission from the lowest T_1 substate I. It can clearly be observed that the electronic 0–0 transition I → 0 at 21,453 cm^{-1} is less intense than several vibrational satellites in the M–L range, such as the I – 344 cm^{-1} and I – 441 cm^{-1} modes. Obviously, the radiative deactivation at the purely electronic transition is less efficient than the radiative deactivation involving vibrational modes. Moreover, for these fundamental vibrations no progressions occur. In analogy to the extensive investigations carried out with Pt(2-thpy)$_2$ [46, 49, 63, 88], it can be concluded that the observed vibrational satellite structure is mainly induced by processes of vibronic coupling of substate I to higher lying states. This type of coupling, called Herzberg–Teller (HT) coupling [63, 81, 89–93], is of particular importance if the electronic 0–0 transition is only weakly allowed. The satellites of HT active vibrational fundamentals represent so-called "false origins."

With temperature increase to 4.2 K, a completely different situation develops. Now, the emission stems dominantly from the substates II/III, which carry much higher allowedness with respect to the purely electronic transition to the ground state at 21,461 cm^{-1}. As consequence, the vibrational modes, which are active in the emission process, are different from those found in the emission of substate I at $T = 1.2$ K. In particular, for several fundamentals such as the 1,056 and 1,497 cm^{-1} modes, one can also observe weak second members of progressions (not displayed in Fig. 6). Therefore, it can be concluded that these modes represent totally symmetric Franck–Condon (FC) active modes [63, 90, 94–97]. The assignment concerning FC activity is in accordance with the observation that many of the FC modes (e.g., 530, 743, 1,056 cm^{-1}) are also built upon the false origins and occur as combinations in the 1.2 K spectrum. Using the equation (see for example [49, 63, 95–98])

$$S = v \cdot \frac{I_v}{I_{v-1}}, \tag{4}$$

where v is the vibrational quantum number and I_v is the intensity of the respective member of the FC progression, one can easily determine the Huang–Rhys parameter S for a specific FC active mode. This parameter is related to the FC factor for the corresponding transition and gives quantitative information about the shifts of nuclear equilibrium positions along the coordinates of the involved totally symmetric vibrations. For the modes II/III – 1,056 cm^{-1} and II/III – 1,497 cm^{-1} one finds values of $S \approx 0.2$. This indicates relatively small geometry changes between the singlet ground state and the T_1 substates II/III – at least in the rigid *n*-octane matrix at cryogenic temperatures. Interestingly, the magnitude of S can be related to the nature of the excited state. For compounds with LC T_1 states, like $Pd(2\text{-thpy})_2$ [63], $[Pt(bpy)_2]^{2+}$ [99], or $[Rh(bpy)_3]^{3+}$ [100], one finds larger values with $S \approx 0.3$, while for MLCT emitters like $[Os(bpy)_3]^{2+}$ [81], the Huang–Rhys factors are even smaller than 0.1. Thus, LC triplets are characterized by greater geometry changes of the ligands than observed for MLCT triplets. This behavior is a consequence of a larger smearing out of charge density changes induced by an excitation process for a MLCT than for a LC triplet [49, 63, 81]. Due to this correlation, it is indicated for Pt(4,6-dFppy)(acac) that the emitting state is largely of ^{3}LC character with only moderate MLCT perturbation (compare also Sect. 5).

Further temperature increase from 4.2 to 20 K does not lead to significant changes of the emission. Interestingly, the most intense HT induced satellites of substate I (e.g., 344, 441 cm^{-1}) can still be detected at 20 K. Vibronic coupling with respect to substate I seems to be very strong for these specific HT active modes. Although the vibrational satellite structure at 20 K is dominated by the emission stemming from the substates II/III, several weak satellites from substate I are also observed.

In summary, the substates I and II/III of Pt(4,6-dFppy)(acac) in *n*-octane exhibit different vibrational deactivation mechanisms. Since a huge amount of emission intensity stemming from substate I is carried by the vibrational satellites, the rate constant k_I is more dominantly governed by deactivation involving vibrational modes than it is the case for $k_{II/III}$ due to the relatively large portion of the emission intensity from the substates II/III in the electronic 0–0 transitions. As a consequence,

Table 1 Zero-field splitting values of the emitting triplet state of Pt(4,6-dFppy)(acac) at different sites of the compound in *n*-octane and in different matrices [107]

Matrix	*n*-octane			CH_2Cl_2	THF
	Site A[a]	Site B	Site C		
0–0 transition 0 ↔ I (cm^{-1})	21,453	21,574	21,612	21,858	
$\Delta E_{II/III-I}$ (cm^{-1})	8.3	7.9	8.6	9.1	8.6

[a]Main site, see Sects. 3.1–3.3

the decay time τ_I is shorter than expected from the ratio of $k_{II/III}/k_I \approx 190$ as determined from the excitation spectrum (compare Fig. 3 and Sects. 3.1 and 3.2).

3.4 Zero-Field Splittings at Different Sites and in Different Hosts

The properties of the lowest triplet state of Pt(4,6-dFppy)(acac) in *n*-octane are nearly independent of the site chosen. An investigation of two other discrete sites reveals ZFS values which do not deviate significantly from the values observed for the main site. Furthermore, even different host materials do not lead to remarkable changes. Corresponding data are summarized in Table 1. For CH_2Cl_2 the splitting could be measured directly by site-selective spectroscopy of one discrete site, while for THF only a broadband spectrum was obtained. In this case, the ZFS was obtained from the temperature dependence of the thermalized emission decay time by a fit of (3) as described in Sect 3.2.

Note that for Ir(III) compounds a different situation is often found. Usually, they exhibit a relatively strong dependence of the ZFS and the triplet substate properties on the individual site and the host, respectively. These important differences will be further discussed in Sect. 4.4.

4 Detailed Studies of Ir(4,6-dFppy)$_2$(acac)

In Sect. 3, it was shown that polycrystalline *n*-alkanes often represent excellent host materials for high-resolution spectroscopy of planar molecules like organometallic Pt(II) compounds. However, for quasi-octahedral Ir(III) compounds, only a few examples are known, for which highly resolved spectra have been obtained in *n*-alkane matrices [72, 101–103]. Recently, it has been shown that CH_2Cl_2 cooled to cryogenic temperatures represents a suitable host material for several Ir(III) compounds. By use of this matrix, high-resolution spectroscopic characterizations of the red emitting Ir(btp)$_2$(acac) [72, 101], the blue–green emitting Ir(4,6-dFppy)$_2$(pic) [53], and Ir(4,6-dFppy)$_2$(acac) [50] could be carried out.

4.1 Electronic 0–0 Transitions

Similarly to the situation found for Pt(4,6-dFppy)(acac) in *n*-octane, several discrete sites are observed in the nonselectively excited emission spectrum of Ir(4,6-dFppy)$_2$(acac) in CH_2Cl_2 at 4.2 K (not shown, but compare [50]). However, for the Ir(III) compound the inhomogeneously broadened background is much more intense. In Fig. 7, site-selectively excited emission spectra at different temperatures and a site-selectively detected excitation spectrum are displayed for the region of the electronic 0–0 transitions of the site of lowest energy, denoted as site A.

The emission spectrum measured at $T = 1.7$ K shows one intense line at 21,025 cm^{-1}, which represents the purely electronic 0–0 transition from the lowest T_1 substate I to the singlet ground state 0. With increasing temperature, an additional line appears at 21,041 cm^{-1}. This line results from the electronic 0–0 transition II → 0. With further temperature increase, line II gains intensity, but even at $T = 15$ K line I is still the most intense one. In the excitation spectrum, two lines at 21,041 and 21,134 cm^{-1} can be observed. The weak peak at lower energy is in resonance with the corresponding emission line as expected for an electronic 0–0 transition. Since no other line is observable in the relevant energy range, the line at 21,134 cm^{-1} can be assigned to the 0–0 transition from the singlet ground state to the highest T_1 substate III. The intensity ratio obtained from the excitation spectrum reveals that the transition 0 → III is by a factor of ≈21 more allowed than the transition 0 → II. Thus, the transition between triplet substate III and the singlet ground state 0 carries by far

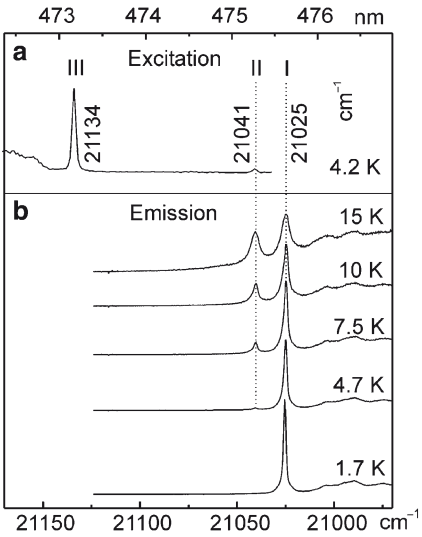

Fig. 7 Emission and excitation spectra of site A of Ir(4,6-dFppy)$_2$(acac) in CH_2Cl_2 at different temperatures. For the excitation spectrum (**a**), the emission was detected at an energy of 21,025 cm^{-1}, which corresponds to the electronic 0–0 transition I → 0. The emission spectra (**b**) were recorded after selective excitation of the 0–0 transition 0 → III at 21,134 cm^{-1} (compare [50])

the highest oscillator strength (radiative allowedness). In the next section it will be shown that it mainly governs the emission properties at ambient temperature.

4.2 Thermalized Emission Decay

Since only the lowest T_1 substate I emits at $T = 1.7$ K (Fig. 7b), its decay time can be measured directly, it amounts to $\tau_I = 44\,\mu s$. The decay times of the two higher lying substates have to be determined from the thermalized emission decay, as described in Sect. 3.2. The temperature dependence of the emission decay time of Ir(4,6-dfppy)$_2$(acac) is different when compared to the situation found for Pt(4,6-dFppy)(acac). Temperature increase up to about 4 K does not lead to a significant decrease of the decay time. This indicates that the emission in this temperature range stems almost exclusively from substate I. This is in accordance with the results obtained from highly resolved spectra (Fig. 7b). The individual decay times of the three substates result from a fit of (2) to the measured decay times, as depicted in Fig. 8. The obtained decay time for substate I of $\tau_I = 44\,\mu s$ corresponds to the one measured at $T = 1.7$ K.

The fitting procedure is performed with fixed ZFS values of $\Delta E_{II-I} = 16\ cm^{-1}$ and $\Delta E_{III-I} = 109\ cm^{-1}$ which are known from highly resolved spectra (Fig. 7). For the ratio of rate constants k_{III}/k_{II}, a value of 22 is found, which is in good agreement

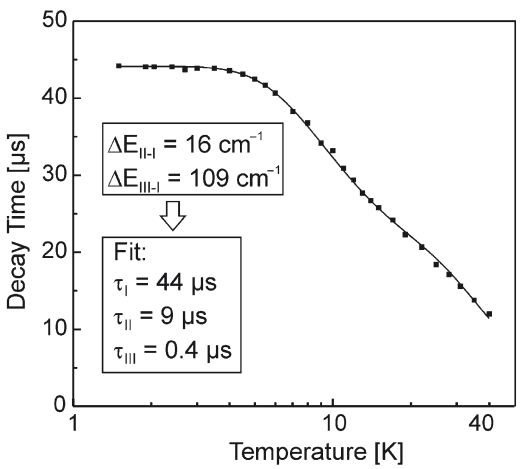

Fig. 8 Thermalized emission decay time of site A of Ir(4,6-dFppy)$_2$(acac) in CH_2Cl_2 vs temperature. The emission was detected at the energy of the 0–0 transition I → 0 at 21,025 cm^{-1}. The *solid line* represents a fit of (2) to the experimental data. The fit was performed with fixed values for ΔE_{II-I} and ΔE_{III-I}, which are known from highly resolved spectra (see *above*). The results obtained from the fit are shown in the *inset* (compare [50])

with the ratio determined from the excitation spectrum as shown in Fig. 7a. This behavior indicates comparable radiative and nonradiative deactivation mechanisms of the substates II and III.

4.3 Vibrational Satellite Structure

In Fig. 9, the selectively excited emission spectra of site A of Ir(4,6-dFppy)$_2$(acac) in CH_2Cl_2 at 1.7 and 10 K are displayed together with a spectrum obtained at 77 K for comparison.

Comparable to the situation found for Pt(4,6-dFppy)(acac) (Sect. 3.3), the spectrum at 1.7 K consists of narrow emission lines. However, a more intense inhomogeneous background is present, indicating less well defined orientations of the chromophores in the matrix than observed for Pt(4,6-dFppy)(acac) in *n*-octane. The electronic 0–0 transition I → 0 at 21,025 cm^{-1} represents by far the most intense peak, in contrast to the situation found for the 0–0 transition I → 0 of Pt(4,6-dFppy)(acac) in *n*-octane (Sect. 3.3). This indicates that the electronic transition I → 0 of Ir(4,6-dFppy)$_2$(acac) in CH_2Cl_2 is allowed by direct SOC and that processes of spin-vibronic HT coupling are of minor importance [49, 63, 88, 92]. Presumably, the vibrational satellite structure in the emission of substate I can be assigned to result from FC activity. Due to the weak intensities of the satellites that correspond to fundamental vibrations and due to the relatively intense background, second members of FC progressions could not be resolved. Most (intra-ligand) vibrational satellites,

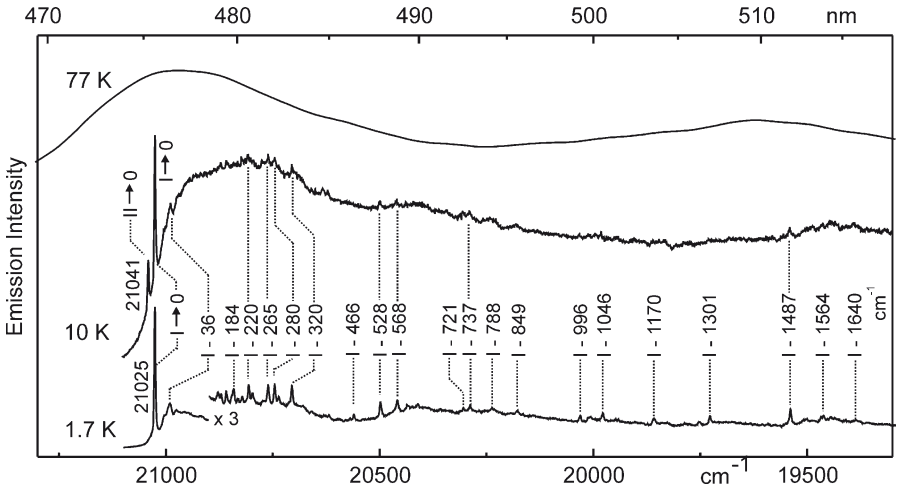

Fig. 9 Emission spectra of site A of Ir(4,6-dFppy)$_2$(acac) in CH_2Cl_2 at $T = 1.7$ and 10 K after selective excitation of the electronic 0–0 transition 0 → III at 21,134 cm^{-1}. For comparison, the emission spectrum at $T = 77$ K is also depicted

which were assigned to totally symmetric FC modes observed in the emission of the substates II/III of Pt(4,6-dFppy)(acac) (Sect. 3.3), can also be observed in the emission of substate I of Ir(4,6-dFppy)$_2$(acac). In Table 2, the corresponding vibrational energies are summarized for Ir(4,6-dFppy)$_2$(acac) in CH_2Cl_2 and Pt(4,6-dFppy)(acac) in *n*-octane and CH_2Cl_2, respectively. In cases where the vibrational energies show differences of more than 5 cm^{-1}, the given correlations are substantiated due to the observed intensity patterns in the respective emission spectra. Interestingly, the energies of all prominent modes observed in emission fit well to the vibrational energies of the free 4,6-dFppy ligand as determined from a Raman spectrum. This supports the assumption that, for both compounds, 4,6-dFppy can be regarded as chromophoric ligand, while the ancillary ligand acac is not directly involved in the emission process. A corresponding interpretation also results from a recent theoretical investigation of Ir(4,6-dFppy)$_2$(acac) [104].

In the emission of substate I of Ir(4,6-dFppy)$_2$(acac), distinctly more vibrational satellites are found in the range of M–L vibrations (up to 500/600 cm^{-1}) than in the emission of the substates II/III of Pt(4,6-dFppy)(acac). The relatively high-intensity of the corresponding satellites is characteristic of a large participation of the central metal ion – in particular of the d-orbitals – in the emitting triplet state of Ir(4,6-dFppy)$_2$(acac). Among other effects, these M–L vibrational satellites are responsible for a smearing out of the emission spectra at ambient temperature. This effect is more distinct for Ir(4,6-dFppy)$_2$(acac) than for Pt(4,6-dFppy)(acac) (compare Fig. 9 to Fig. 6).

The temperature dependence of the selectively excited emission spectra in Fig. 9 is very different from the situation observed for Pt(4,6-dFppy)(acac) (Fig. 6).

Table 2 Comparison of intra-ligand vibrational energies as determined from emission spectra of the main sites of Ir(4,6-dFppy)$_2$(acac) in CH_2Cl_2 (T=1.7 K, electronic 0–0 transition I → 0 at 21,025 cm^{-1}) and of Pt(4,6-dFppy)(acac) in CH_2Cl_2 (T=4.2 K, electronic 0–0 transition II/III → 0 at 21,867 cm^{-1}) [107] and in *n*-octane (T=4.2 K, electronic 0–0 transition II/III → 0 at 21,461 cm^{-1}), respectively (compare Sect. 3.3). Corresponding vibrational energies of the free (4,6-dFppy) ligand, determined from a Raman spectrum (T=298 K, neat ligand), are also given [53]

Vibrational satellites in emission (cm^{-1})			Raman (cm^{-1})
Ir(4,6-dFppy)$_2$(acac) in CH_2Cl_2[a]	Pt(4,6-dFppy)(acac) in CH_2Cl_2[b]	Pt(4,6-dFppy)(acac) in *n*-octane[c]	4,6-dFppy[d]
737	739	743	740
788			785
996	994	990	994
1,046	1,054	1,056	1,056
1,170	1,165	1,168	
1,301	1,304	1,310	1,305
1,487	1,488	1,497	
1,564	1,563	1,570	1,570

[a] This section
[b] [107]
[c] Sect. 3.3
[d] [53]

For Ir(4,6-dFppy)$_2$(acac) at 1.7 K, the electronic 0–0 transition I → 0 is the dominant line and much more intense than the resolved vibrational satellites, which sit on the inhomogeneously broadened background. When the temperature is increased to $T = 10$ K, the electronic 0–0 transition II → 0 grows in at 21,041 cm^{-1} (see also Fig. 7b). Independent from this effect, the spectrum becomes very broad and the narrow lines corresponding to vibrational satellites can be observed only weakly. The huge difference in the temperature dependence of the emission spectra of Ir(4,6-dFppy)$_2$(acac) compared to Pt(4,6-dFppy)(acac) can be related to significantly different homogeneous broadening processes due to electron–phonon coupling, involving low energy vibrations or librations[2] in the optical transition. (For details see for example [49, 96, 105, 106].) The temperature dependent coupling is significantly stronger for Ir(4,6-dFppy)$_2$(acac) in CH_2Cl_2 than for Pt(4,6-dFppy)(acac) in *n*-octane. Since highly resolved spectra – and thus, weak electron–phonon coupling – can be registered for Pt(4,6-dFppy)(acac) in CH_2Cl_2 even at 20 K [107], the observed differences do not solely depend on the host. Presumably, electron–phonon coupling is larger for compounds with emitting MLCT states, as in Ir(4,6-dFppy)$_2$(acac), than for dominantly LC states, as in Pt(4,6-dFppy)(acac). This is due to a more distinct redistribution of charges in the course of a MLCT, compared to a LC transition.

4.4 Matrix Dependence of T_1 State Properties

In contrast to the situation observed for Pt(4,6-dFppy)(acac), the photophysical properties of Ir(4,6-dFppy)$_2$(acac) depend distinctly on the individual site and on the host material [50]. A similar behavior has also been observed for other Ir(III) compounds [53, 72, 101, 106]. Table 3 summarizes characteristic data for Ir(4,6-dFppy)$_2$(acac). The spectroscopic discussion presented above refers to a prominent low energy site (site A). Another intense site of higher energy observed in CH_2Cl_2 (site B) exhibits distinctly smaller ZFS parameters than determined for site A (Sect. 4.1). For the host material THF, giving only broadband spectra at cryogenic temperatures, nonmonoexponential emission decay curves were observed in a wide

Table 3 Zero-field splitting values of two discrete sites of Ir(4,6-dFppy)$_2$(acac) in CH_2Cl_2 and ZFS ranges in THF [50]

Matrix	CH_2Cl_2		THF
	Site A	Site B	
0–0 transition 0 ↔ I (cm^{-1})	21,025	21,570	
ΔE_{II-I} (cm^{-1})	16	13	10–15
ΔE_{III-I} (cm^{-1})	109	92	80–125

[2] Librations are hindered rotational modes of the doped complex in its matrix cage.

temperature regime [50]. This behavior can be explained with a spread of ZFS values and individual decay times. Upper and lower limits for these spreads can be determined by approximating short and long components of the nonmonoexponential decay curves and by using these for the analysis of the temperature dependence of the emission decay time according to (2) [53]. The ranges determined for THF largely correspond to the values observed for the discrete sites in CH_2Cl_2. An interpretation of this unexpected behavior of matrix- and site-dependent T_1 state properties will be given below (Sect. 7).

5 Pt(4,6-dFppy)(acac) and Ir(4,6-dFppy)$_2$(acac): Energy Level Diagrams, Zero-Field Splittings, and Decay Times

The results presented in the previous sections allow us to derive energy level diagrams for the T_1 states of the main sites of Pt(4,6-dFppy)(acac) in *n*-octane and of Ir(4,6-dFppy)$_2$(acac) in CH_2Cl_2. They are depicted in Fig. 10.

As a most remarkable difference, the total zero-field splitting $\Delta E(\mathrm{ZFS}) = \Delta E_{\mathrm{III–I}}$ is more than one order of magnitude larger for the Ir(III) than for the Pt(II) compound. Further, the decay time τ_{III} is significantly shorter. Moreover, the ΔE(ZFS) values and individual emission decay times are found to exhibit distinct site- and matrix-dependences for Ir(4,6-dFppy)$_2$(acac), while these parameters are much less affected for Pt(4,6-dFppy)(acac).

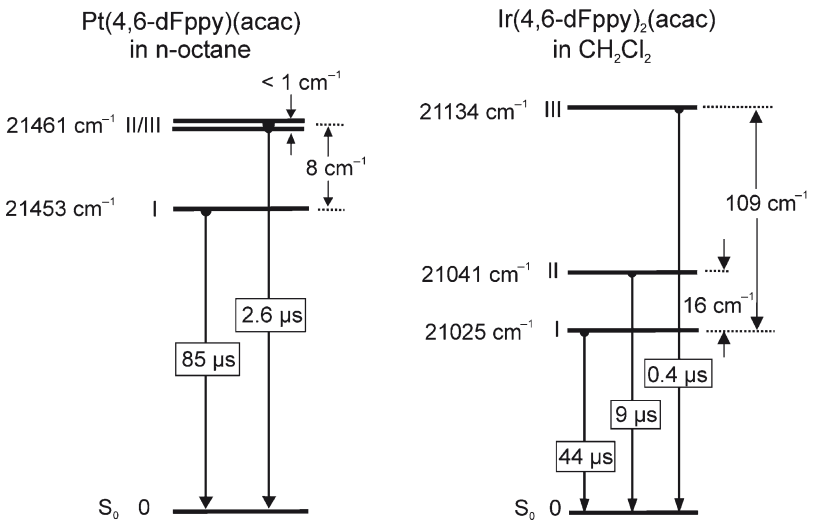

Fig. 10 Energy level diagrams for the T_1 states of Pt(4,6-dFppy)(acac) in *n*-octane and Ir(4,6-dFppy)$_2$(acac) in CH_2Cl_2. For both compounds, the data refer to the respective low energy sites (compare [50, 71])

In particular, the magnitude of ΔE(ZFS) represents an important ordering parameter. It is determined by SOC to higher lying singlet and triplet states and displays the amount of MLCT character in the emitting state. Thus, the metal involvement in the corresponding wave function can be assessed [12, 49, 63, 108]. Compounds with small ΔE(ZFS) values of, for example only several cm^{-1}, exhibit ligand centered ^{3}LC ($^3\pi\pi^*$) emitting states with only small or moderate MLCT contributions. Pt(4,6-dFppy)(acac) is a representative of this class of compounds. On the other hand, complexes with large splittings of the emitting triplet state of, for example several 10 cm^{-1}, are normally assigned as ^{3}MLCT emitters. Ir(4,6-dFppy)$_2$(acac) belongs to this group. TDDFT calculations [109] support this latter assignment. The extent of MLCT admixture or the contributions of the metal d-orbitals to the lowest triplet state govern the effectiveness of SOC, which determines ZFSs, radiative decay rates, and photoluminescence quantum yields. These properties are crucial for the performance of triplet emitters in OLEDs. Therefore, it is of high current interest to develop a deeper understanding of the impact of SOC in organo-transition metal compounds. This will be the focus of the next section.

6 Spin–Orbit Coupling: Theoretical Considerations

In this section, we will focus on SOC and its impact on the T_1 state properties of organo-transition metal compounds. By relatively simple theoretical models, it is illustrated, how SOC distinctly influences photophysical properties, such as zero-field splittings, radiative rates of the T_1 substates, and indirectly also the emission quantum yields. Quantitative calculations including SOC are still difficult, and only a few investigations are known [110–112]. Here, it is not attempted to provide any numerical data. Instead, trends will be derived and schemes are provided which are helpful for an understanding of the materials' properties. In particular, the discussed models will allow us to rationalize the drastic differences as observed for the photophysical properties of Pt(4,6-dFppy)(acac) and Ir(4,6-dFppy)$_2$(acac).

6.1 General Aspects

In general, the sublevels of triplet states do not represent pure triplet substates, since they contain contributions from higher lying singlets due to SOC. Thus, the photophysical properties of the substates of the lowest triplet state T_1 and of the corresponding transitions to the singlet ground states are strongly altered. For example, the ZFSs can become orders of magnitude larger than the splittings which originate from spin–spin couplings. The latter effects have been extensively investigated for purely organic molecules [113–115]. In transition metal compounds with heavy metal centers, spin–spin coupling effects are relatively small compared to SOC effects [113, 116–118]. Thus, spin–spin coupling will be disregarded in the present discussion.

In principle, all higher lying states can contribute to the T_1 substates via SOC, if the corresponding symmetries fit. However, many of these SOC routes contribute little and can be neglected relative to a few dominating spin–orbit interactions. We will describe fundamentals of the coupling routes from a theoretical point of view and discuss requirements for efficient SOC in organometallic compounds. To make this chapter understandable for the non-specialist, we will start with definitions, which are necessary to fix notations. This will be followed by some relations between orbitals and states.

6.2 Some Definitions

For many-electron states (energy states), the spin–orbit operator H_{SO} is given as a sum of one-particle operators, i.e., the sum of $h_{SO,i}$ operators for the single electron i:

$$H_{SO} = \sum_i h_{SO,i}. \tag{5}$$

Each $h_{SO,i}$ is essentially the same operator acting on the coordinates and spins of a single electron. Thus, the argument i can be dropped for clarity. Each h_{SO} operator in turn is given (approximately) as sum of contributions of the atoms A in the molecule:

$$h_{SO} = \sum_A h_{SO}(A). \tag{6}$$

Each atomic contribution is of the form [113]

$$h_{SO}(A) = \xi(r_A)\vec{l}(A)\cdot\vec{s}, \tag{7}$$

where $\vec{l}(A)$ is the angular momentum with respect to atom A, $\vec{s}$ is the spin of the electron, and $\xi(r_A)$ is a function of the distance r_A of the electron to the atom center A, describing the respective SOC strength [119]. The inner (scalar) product of the vectors $\vec{l}(A)$ and $\vec{s}$ can be written in the equivalent forms

$$\vec{l}(A)\cdot\vec{s} = l_x(A)s_x + l_y(A)s_y + l_z(A)s_z = l_z(A)s_z + \frac{1}{2}[l_+(A)s_- + l_-(A)s_+], \tag{8}$$

in terms of the Cartesian components $l_x(A)$, $l_y(A)$, $l_z(A)$, $s_x(A)$, $s_y(A)$, $s_z(A)$ and the complex components $l_+(A) = l_x(A) + il_y(A)$, $l_-(A) = l_x(A) - il_y(A)$, $s_+ = s_x + is_y$, $s_- = s_x - is_y$.

Spin–orbitals ϕ can be written as products of spatial orbitals χ times spin parts θ:

$$\phi = \chi\cdot\theta \text{ with } \theta = \uparrow, \downarrow. \tag{9}$$

The arrows ↑and ↓ are equivalent to the frequently used spin notations α and β, respectively. Each spatial orbital may be considered as a linear combination of basis functions $b_i(A)$ centered at the various atoms A of the molecule (linear combination of atomic orbitals, LCAO), i.e., as a sum:

$$\chi = \sum_{A,i} c_i(A,\chi)\cdot b_i(A), \tag{10}$$

where $c_i(A,\chi)$ denotes the coefficient of the i-th basis function at center A in the orbital χ.

Matrix elements of h_{SO} can thus be expressed by a spatial part and a spin part which may be written in terms of the SOC constant[3] $\zeta(A)$ for atom A and matrix elements of the angular momentum and of the spin:

$$\left\langle \phi_1 \left| h_{SO}(A) \right| \phi_2 \right\rangle = \zeta(A) \left\langle \chi_1 \left| \vec{l}(A) \right| \chi_2 \right\rangle \cdot \left\langle \theta_1 \left| \vec{s} \right| \theta_2 \right\rangle. \tag{11}$$

This relation is a consequence of the Wigner–Eckart theorem; for example see [120].

The matrix elements of the spin operators are given in any text book of quantum mechanics. For the convenience of the reader, we give the non-vanishing values in units of h: $\left\langle \uparrow \left| s_z \right| \uparrow \right\rangle = \frac{1}{2}, \left\langle \downarrow \left| s_z \right| \downarrow \right\rangle = -\frac{1}{2}, \left\langle \uparrow \left| s_+ \right| \downarrow \right\rangle = 1, \left\langle \downarrow \left| s_- \right| \uparrow \right\rangle = 1$. All other matrix elements of these three spin operators vanish. The matrix elements of s_x and of s_y are simple linear combinations of the above matrix elements. The matrix elements of the angular momentum operators display crucial photophysical properties and are discussed below in detail.

Inserting the LCAO expansions for χ_1 and χ_2 of the form of (10) in (11), the matrix element of the angular momentum operators, and hence the matrix element of h_{SO} on the left hand side of (11) is easily seen to be a linear combination of terms of the form

$$X = \left\langle b_i(B) \left| \vec{l}(A) \right| b_j(C) \right\rangle, \tag{12}$$

where A, B, and C denote the various atoms ("centers") of the molecule. According to the number of different centers in this expression, the matrix element X can be classified as one-, two-, or three-center contribution. Due to the exponential decay of the basis functions with increasing distance from the centers, the one-center matrix elements are usually much larger than corresponding two- and three-center matrix elements. These relations will be illustrated by examples later in this section.

[3] The radial average of the function $\xi(r_A)\hbar^2$ can be written as $hc\zeta(A)$ [119].

6.3 Orbitals and States

For an introduction to electronic states and their creation from atomic/molecular orbitals, we first discuss a simple 3-orbital model, which consists of a π- and a π*-orbital located at the ligands and a central metal d-orbital. First, from these orbitals many-electron states with pure spin will be constructed, i.e., pure singlets and triplets. This situation corresponds to the case of vanishing SOC. Later on, it will be explained, how SOC mixes the pure spin states.

In this model, three orbitals are occupied by four electrons. Thus, the ground state is given by a closed shell $d^2\pi^2$ electron configuration, which represents a singlet. In a first approximation, the lowest excited many-electron states are single excitations from the ground state: A single electron is taken from the doubly occupied d- or π- orbital and put into the unoccupied π* orbital, with or without spin-flip. The ground state and the excited states resulting from single excitations can be represented as Slater determinants [121]. Examples are given below. The spins of the electrons add up to the magnetic spin quantum number M_S. Spins of doubly occupied orbitals add up to zero. Thus, the value of M_S is determined by the spins of the unpaired electrons. In the case of single excitations, two unpaired electrons result and the possible values of M_S are +1, 0, and −1. The values $M_S = \pm 1$ correspond to substates of a triplet, while $M_S = 0$ describes either a singlet or a triplet substate. As will be seen, the correct substates are given by suitable sums or differences of the Slater determinants representing single excitations.

The resulting (sub)states are displayed in Fig. 11. The first state (Fig. 11a) is the triplet resulting from a $\pi \rightarrow \pi^*$ single excitation, i.e., a ligand-centered (LC) triplet denoted as $^3(\pi\pi^*)$. The upper left index corresponds to the spin multiplicity $(2S+1)$ which is three for a triplet with a total spin quantum number of $S = 1$. The state consists of three substates with the M_S values of +1, 0, and −1. These are depicted as lower right indices. While the substates $^3(\pi\pi^*)_{+1}$ and $^3(\pi\pi^*)_{-1}$ are represented by single Slater determinants, the substate $^3(\pi\pi^*)_0$ is described by a sum of two Slater determinants. Further important singly-excited states in the discussed 3-orbital model are the LC singlet $^1(\pi\pi^*)_0$ (Fig. 11b), the metal-to-ligand charge transfer triplet $^3(d\pi^*)_{M_S}$ ($M_S = -1, 0, +1$) (Fig. 11c), and the MLCT singlet $^1(d\pi^*)_0$ (Fig. 11d). For clarity, we drop the index $M_s = 0$ for singlet states from now on.

Later on it will be seen that at least one further metal d-orbital, denoted as d′, is needed in order to understand SOC routes. This orbital is assumed to be also doubly occupied in the ground state. Hence, further MLCT singlets and triplets can be formed, which are completely analogous to the ones displayed in Fig. 11.

The energies of the many-electron states can be obtained in a crude approximation as the sum of the energies $e(\chi)$ of the occupied molecular orbitals χ, taking into account the occupancy n ($n = 1, 2$). This implies that, for instance, the energy difference of $^1(\pi\pi^*)$ (Fig. 11b) to the closed shell ground state is approximately given by $\Delta E = e(\pi^*) - e(\pi)$. However, this crude approximation does not include the important singlet–triplet splitting, which stems from the exchange interaction (compare, for example, [119–121]).

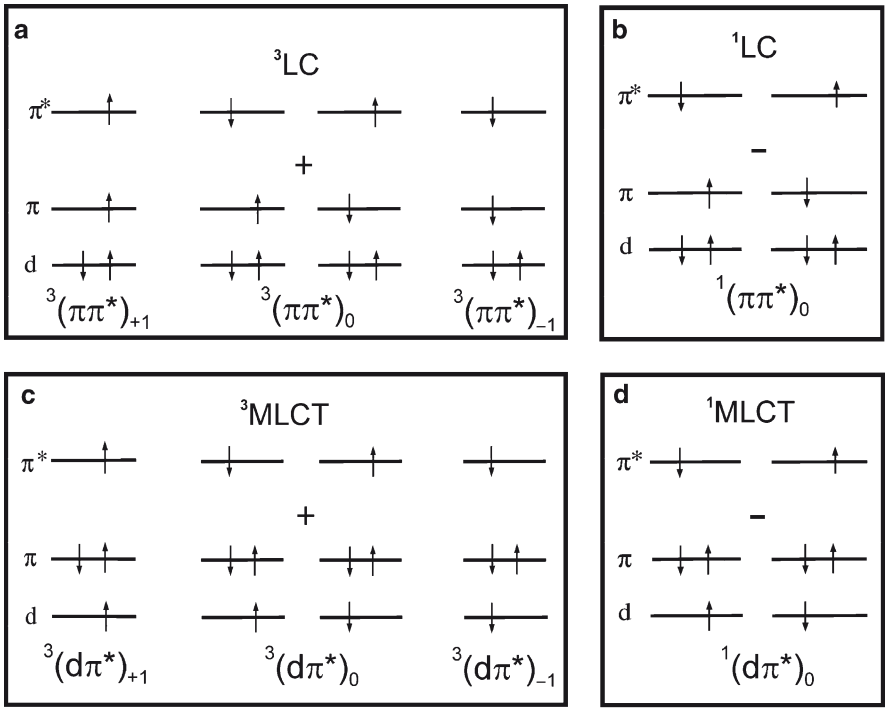

Fig. 11 Selected single excitations and orbital occupations. Displayed are the energy diagrams in the 3-orbital model and the electron occupations of (**a**) a ^{3}LC state, (**b**) a ^{1}LC state, (**c**) a ^{3}MLCT state, and (**d**) a ^{1}MLCT state

6.4 Spin–Orbit Coupling: General Aspects and Rules

In this section, SOC is discussed at first on the basis of the simplified orbital model as introduced above. In Fig. 12, examples of SOCs between different (sub)states are displayed. These couplings are effective in a different way. For a discussion of these examples, the following selection rules for SOC between singly-excited states are important:

Rule A: Only if two states differ in just one spin–orbital, the SOC matrix element describing the coupling of these states will not vanish. Furthermore, the allowed differences in the magnetic spin quantum numbers between the states are $\Delta M_S = 0, \pm 1$.

Rule B: Only if the two differing spin–orbitals couple via h_{SO}, there will be a coupling of the many-electron states.

These rules are a consequence of the fact that the spin–orbit operator for the many-electron states is a sum of one-particle operators according to (5) and the Slater–Condon rules for matrix elements between states of such operators [121].

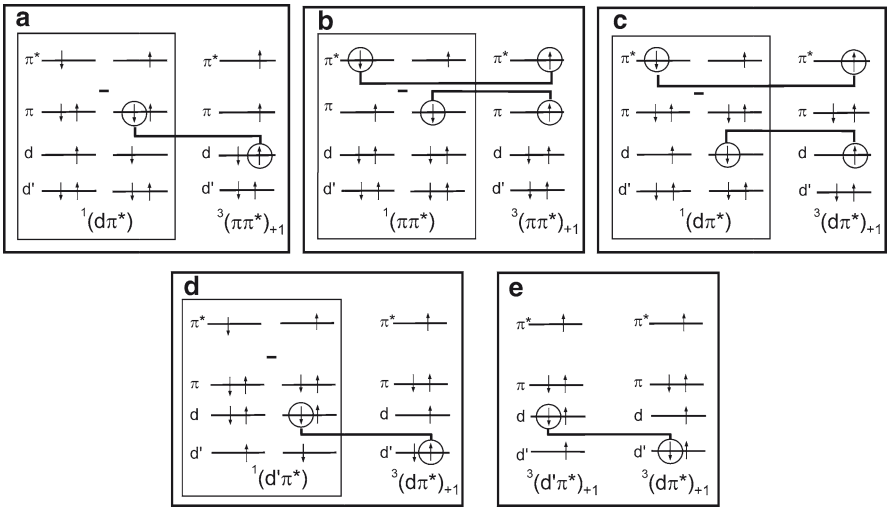

Fig. 12 Illustration of spin–orbit coupling (SOC) between various states. Differing orbitals in the coupling states are marked with *circles*. In the schemes (**a**) to (**c**) cases of vanishing SOC are depicted, while (**d**) and (**e**) display situations of strong SOC. For details see the descriptions in the text (compare [108])

Additionally, it has to be taken into account that the diagonal elements of h_{SO} vanish (compare Rule E below) in order to see that two states possessing identical spin–orbitals lead only to vanishing SOC matrix elements. By use of these rules the coupling between states can be greatly simplified and expressed by couplings of orbitals.

The resulting matrix elements of h_{SO} between orbitals can easily be evaluated by taking into account (11) and the fact that the SOC constants of the atoms at the ligands are much smaller than the SOC constant of the heavy metal ion [113]. Since each orbital decays exponentially with increasing distance from its center, the integrand of any matrix element of $\vec{l}(A)$ according to (12) is small if the two considered orbitals are located at different centers as has been discussed at the end of Sect. 6.2. This is expressed in the following selection rules:

Rule C: Significant SOC is only obtained if the corresponding spatial orbitals are located at the same center and if that center has a large SOC constant.

Rule D: Only if both spatial orbitals are coupled by the angular momentum operator at the central metal ion, there will be a significant spin-orbit coupling.

As a consequence of these rules, it is appropriate to approximate h_{SO} by $h_{SO}(M)$ for the central metal ion M in the following.

Further, the orbital angular momentum is a purely imaginary Hermitian operator (for details, see, e.g., [121, 122]). Thus – and as explained in detail in the Appendix – another rule results:

Rule E: The angular momentum operator never couples a real spatial orbital with itself.[4]

For an analysis of the different cases of SOC we now study several coupling situations as depicted in Fig. 12. In the first two examples, the emitting triplet state is regarded to be a ligand centered $^3(\pi\pi^*)$ state. In Fig. 12a, spin-orbit coupling between the $M_S=+1$ substate of the LC triplet $^3(\pi\pi^*)$ and the MLCT singlet $^1(d\pi^*)$ is depicted. Note that the singlet contains two configurations with $M_S=0$ (compare Fig. 11d). One of these two configurations (left hand side) differs in two orbitals from the $^3(\pi\pi^*)_{+1}$ substate. Thus, no SOC between this configuration and the $^3(\pi\pi^*)_{+1}$ substate occurs according to Rule A. The second $^1(d\pi^*)$ configuration (right hand side of Fig. 12a) differs in just one orbital from the $^3(\pi\pi^*)_{+1}$ substate. The corresponding configurations are related by moving an electron with spin-flip between the d- and the π-orbital (marked by circles). Using the rules for the matrix elements as outlined above and (7), (8), and (11), the SOC matrix element $\left\langle {}^1(d\pi^*)\middle|H_{SO}\middle|{}^3(\pi\pi^*)_{+1}\right\rangle$ can be expressed in terms of

$$\left\langle \pi\downarrow\middle|h_{SO}\middle|d\uparrow\right\rangle = \frac{\zeta(M)}{2}\left\langle \pi\middle|l_+(M)\middle|d\right\rangle\left\langle\downarrow\middle|s_-\middle|\uparrow\right\rangle. \tag{13}$$

The matrix element of $l_+(M)$ between the spatial orbitals d and π is small, since the two orbitals are located at different centers and each decays exponentially with increasing distance from its center (Rule C). As consequence, the SOC between these orbitals and, thus, also SOC between the $^1(d\pi^*)$ state and the $^3(\pi\pi^*)_{+1}$ substate is small. Analogously to the described procedure, one can derive that SOC between the $^1(d\pi^*)$ state and the $M_S=-1$, 0 substates of the $^3(\pi\pi^*)$ state is also insignificant. Similar conclusions for SOC between $^1(d\pi^*)$ and $^3(\pi\pi^*)$ states were drawn by explicit calculations of matrix elements [123].

In Fig. 12b, SOC between the LC singlet $^1(\pi\pi^*)$ and the $M_S=+1$ substate of the LC triplet $^3(\pi\pi^*)$ is displayed. Since both configurations of the $^1(\pi\pi^*)$ state differ in just one spin–orbital from the $^3(\pi\pi^*)_{+1}$ substate, the coupling to the triplet substate can – in principle – occur via two possibilities. Again, the differing spin–orbitals are marked with circles. The matrix element $\left\langle {}^1(\pi\pi^*)\middle|H_{SO}\middle|{}^3(\pi\pi^*)_{+1}\right\rangle$ can be expressed by a sum of

$$\left\langle \pi^*\downarrow\middle|h_{SO}\middle|\pi^*\uparrow\right\rangle = \frac{\zeta(M)}{2}\left\langle \pi^*\middle|l_+(M)\middle|\pi^*\right\rangle\left\langle\downarrow\middle|s_-\middle|\uparrow\right\rangle \tag{14}$$

and

[4] This rule is frequently addressed in the discussion of intersystem crossing (ISC) and SOC between $^1(\pi\pi^*)$ and $^3(\pi\pi^*)$ states of purely organic molecules (compare [113]). For these molecules, SOC is very weak. In this case, the matrix elements as expressed in (12) involve equal p-orbitals that are located on one C atom. The angular momentum operator acts on a p-orbital by rotating it by 90°. Thus, a matrix element of two orthogonal p-orbitals results, and this integral vanishes. A corresponding situation is discussed below by use of the example shown in Fig. 12b.

$$\left\langle \pi \downarrow \left| h_{\mathrm{SO}} \right| \pi \uparrow \right\rangle = \frac{\zeta(M)}{2} \left\langle \pi \left| l_{+}(M) \right| \pi \right\rangle \left\langle \downarrow \left| s_{-} \right| \uparrow \right\rangle. \tag{15}$$

The resulting SOC for the states is negligible, since both the π- and the π*-orbital are not centered at the metal (Rule D). Moreover, and even more strictly, these matrix elements of the angular momentum operator vanish according to Rule E.

Now we assume that the emitting state is a pure ^{3}(dπ*) state. Figure 12c shows the coupling between the ^{1}(dπ*) state and the M_S=+1 substate of the MLCT triplet ^{3}(dπ*). Analogous to the situation depicted in Fig. 12b, there are again two couplings possible. Thus, the matrix element $\left\langle {}^1(\mathrm{d}\pi^*) \left| H_{\mathrm{SO}} \right| {}^3(\mathrm{d}\pi^*)_{+1} \right\rangle$ can be expressed by a sum of

$$\left\langle \pi^* \downarrow \left| h_{\mathrm{SO}} \right| \pi^* \uparrow \right\rangle = \frac{\zeta(M)}{2} \left\langle \pi^* \left| l_{+}(M) \right| \pi^* \right\rangle \left\langle \downarrow \left| s_{-} \right| \uparrow \right\rangle \tag{16}$$

and

$$\left\langle \mathrm{d} \downarrow \left| h_{\mathrm{SO}} \right| \mathrm{d} \uparrow \right\rangle = \frac{\zeta(M)}{2} \left\langle \mathrm{d} \left| l_{+}(M) \right| \mathrm{d} \right\rangle \left\langle \downarrow \left| s_{-} \right| \uparrow \right\rangle. \tag{17}$$

Since the $l_+(M)$ operator cannot couple an orbital with itself, both matrix elements involved in the sum vanish according to Rule E. Thus, SOC between a ^{1}(dπ*) state and a ^{3}(dπ*) substate involving the same d-orbital can be neglected.

On the other hand, if another d-orbital denoted as d′ is involved, one obtains a different situation concerning SOC. Figure 12d depicts the coupling of the M_S=+1 substate of the MLCT triplet ^{3}(dπ*) with the singlet MLCT state ^{1}(d′π*). Now just one configuration of the ^{1}(d′π*) state differs in just one spin–orbital from the $^3(\mathrm{d}\pi^*)_{+1}$ substate. The matrix element $\left\langle {}^1(\mathrm{d}'\pi^*) \left| H_{\mathrm{SO}} \right| {}^3(d\pi^*)_{+1} \right\rangle$ can be expressed in terms of

$$\left\langle d \downarrow \left| h_{SO} \right| d' \uparrow \right\rangle = \frac{\zeta(M)}{2} \left\langle d \left| l_{+}(M) \right| d' \right\rangle \left\langle \downarrow \left| s_{-} \right| \uparrow \right\rangle \tag{18}$$

Since both orbitals d and d′ are situated at the central metal ion, their spin-orbit coupling is significant. Hence, the coupling between the corresponding (sub)states ^{1}(d′π*) and $^3(\mathrm{d}\pi^*)_{+1}$ can be large.

Another case of strong SOC is given by the coupling between $^3(\mathrm{d}\pi^*)_{+1}$ and a triplet MLCT substate involving the orbital d′, for example $^3(\mathrm{d}'\pi^*)_{+1}$. In this situation, which is depicted in Fig. 12e, an evaluation of $\left\langle {}^3(\mathrm{d}'\pi^*)_{+1} \left| H_{\mathrm{SO}} \right| {}^3(d\pi^*)_{+1} \right\rangle$ according to the Slater–Condon rules results in

$$\left\langle \mathrm{d} \downarrow \left| h_{\mathrm{SO}} \right| \mathrm{d}' \downarrow \right\rangle = \zeta(M) \left\langle \mathrm{d} \left| l_z(M) \right| \mathrm{d}' \right\rangle \left\langle \downarrow \left| s_z \right| \downarrow \right\rangle = -\frac{\zeta(M)}{2} \left\langle \mathrm{d} \left| l_z(M) \right| \mathrm{d}' \right\rangle. \tag{19}$$

Thus, a ^{3}MLCT substate can exhibit efficient SOC with another ^{3}MLCT substate involving a different d-orbital. However, the additional selection rule $\Delta M_S = 0, \pm 1$ has to be fulfilled.

For completeness, it is remarked that couplings between different substates of the *same* ^{3}MLCT state can be neglected according to Rule E. It is a good exercise for the interested reader to show that all nine matrix elements $\left\langle {}^3(\mathrm{d}\pi^*)_{M_S} \left| H_{\mathrm{SO}} \right|^3 (\mathrm{d}\pi^*)_{M_S'} \right\rangle$ with M_S, $M_S' = -1$, 0, 1 vanish. As consequence, the first-order energy corrections for the three degenerate substates of the $^3(\mathrm{d}\pi^*)$ state are zero when perturbation theory is applied with H_{SO} as perturbation operator. Thus, the well-known second-order expressions for the energy correction may be used. Consequences will be discussed in the next section.

Although only the couplings between particular substates were treated explicitly, it should now be plausible for the reader that direct SOCs of ligand-centered triplets (e.g., $^3(\pi\pi^*)$) to higher lying ^{1,3}MLCT and ^{1,3}LC states are small, while SOC between MLCT triplets and singlet or triplet MLCT states involving a different d-orbital can be significant.

6.5 Direct Spin–Orbit Coupling

The SOC paths explicitly treated above have important consequences on the photophysical properties of the substates of a ^{3}MLCT state. Perturbation theory can be used to illustrate the effects in the simple 4-orbital model as introduced above in Fig. 12. When taking into account significant SOC of the $^3(\mathrm{d}\pi^*)_{+1}$ substate with *only* the $^1(\mathrm{d}'\pi^*)$ state, as outlined above, the first-order corrected wave function $\left| {}^3(\mathrm{d}\pi^*)_{+1} \right\rangle^{\mathrm{SOC}}$ can be written as (compare also [113])

$$\left| {}^3(\mathrm{d}\pi^*)_{+1} \right\rangle^{\mathrm{SOC}} = \left| {}^3(\mathrm{d}\pi^*)_{+1} \right\rangle + a \left| {}^1(\mathrm{d}'\pi^*) \right\rangle \tag{20}$$

where in $\left| {}^3(\mathrm{d}\pi^*)_{+1} \right\rangle$ and $\left| {}^1(\mathrm{d}'\pi^*) \right\rangle$ are the unperturbed wave functions. a represents the mixing coefficient and is expressed as

$$a = \frac{\left\langle {}^1(\mathrm{d}'\pi^*) \left| H_{SO} \right| {}^3(\mathrm{d}\pi^*)_{+1} \right\rangle}{E\left[{}^3(d\pi^*)_{+1} \right] - E\left[{}^1(d'\pi^*) \right]} \tag{21}$$

$E\left[{}^3(d\pi^*)_{+1} \right]$ and $E\left[{}^1(\mathrm{d}'\pi^*) \right]$ are the energies of the unperturbed states. The effects of SOC on the energy stabilization of the $^3(\mathrm{d}\pi^*)_{+1}$ substate can also be illustrated by perturbation theory. The first-order correction energy is zero [121]. In second-order, the corrected energy of $^3(\mathrm{d}\pi^*)_{+1}$ is given as

$$E\left[{}^3(d\pi^*)_{+1} \right]^{SOC} = E\left[{}^3(d\pi^*)_{+1} \right] + \frac{\left| \left\langle {}^1(\mathrm{d}'\pi^*) \left| H_{SO} \right| {}^3(\mathrm{d}\pi^*)_{+1} \right\rangle \right|^2}{E\left[{}^3(d\pi^*)_{+1} \right] - E\left[{}^1(d'\pi^*) \right]} \tag{22}$$

For clarity, we constrained our model on SOC with a single higher lying state, i.e., the $^1(\mathrm{d}'\pi^*)$ state. Since the SOC matrix elements (and thus the mixing coefficients

according to (21)) are usually of different magnitude for the coupling of the other substates of the $^3(d\pi^*)$ state and the $^1(d'\pi^*)$ state, different energy stabilizations result. As a consequence, a SOC-induced zero-field splitting is obtained. Of course, taking – in a more realistic model – the coupling to further states into account, for example to the substates of the $^3(d'\pi^*)$ state, leads to further terms on the right hand side of (22) involving further mixing coefficients similar to (21), and to further contributions to the ZFS (see also below, (33)).

The radiative rate for the transition from the $^3(d\pi^*)_{+1}$ substate to the singlet ground state is distinctly affected by SOC to higher lying singlet MLCT states. For the case of coupling with only the $^1(d'\pi^*)$ state, the radiative rate constant for substate $^3(d\pi^*)_{+1}$ may be expressed as (compare also [113])

$$k^r\left(^3(d\pi^*)_{+1}{}^{SOC}\right)=\frac{64\pi^4\bar{\nu}^3}{3hc^3}\cdot\left|\frac{\left\langle {}^1(d'\pi^*)\middle|H_{SO}\middle|{}^3(d\pi^*)_{+1}\right\rangle}{E\left[{}^3(d\pi^*)_{+1}\right]-E\left[{}^1(d'\pi^*)\right]}\cdot\left\langle S_0\middle|e\vec{r}\middle|{}^1(d'\pi^*)\right\rangle\right|^2 \quad (23)$$

with $\bar{\nu}$ and $e\vec{r}$ representing the transition energy in cm^{-1} and the electric dipole operator, respectively. The matrix element $\left\langle S_0 \middle| e\vec{r} \middle| {}^1(d'\pi^*)\right\rangle$ represents the transition dipole moment between the electronic singlet ground state S_0 and the $^1(d'\pi^*)$ state. Note that the mixing coefficient a, as given by (21), multiplies the transition dipole moment in (23).

It is noted that the other substates of the $^3(d\pi^*)$ state experience different admixtures due to different mixing coefficients a and, thus, will get different radiative rates. If the coupling to further states is included, for example to other MLCT states, the corresponding mixing coefficients and transition dipole moments have to be included in the expression for the radiative rate constant.

6.6 *Indirect Spin–Orbit Coupling*

From the considerations in Sect. 6.4, it is obvious that, for the substates of a ligand-centered triplet, i.e., for substates of a $^3(\pi\pi^*)$ state, direct SOC with higher lying singlet and triplet MLCT (sub)states is too weak to obtain significant radiative rates or zero-field splittings. However, for transition metal compounds with ligand-centered T_1 states, much higher radiative rates than typical for organic molecules have been observed [60–65, 77, 123–127]. These results could be rationalized by taking into account configuration interaction (CI) of the LC T_1 substates with higher lying MLCT and MC (metal centered) triplets [115, 116, 123, 124].

In the following description, we consider a very simplified 3-state model, consisting of the purely LC T_1 substate $^3(\pi\pi^*)_{+1}$, the triplet MLCT substate $^3(d\pi^*)_{+1}$, and the singlet MLCT state $^1(d'\pi^*)$. This model is chosen to illustrate the perturbational approach and certainly does not contain all relevant physics. The situation is schematically depicted in Fig. 13.

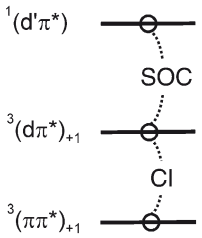

Fig. 13 Illustration of indirect spin-orbit coupling in a 3-state model. The ^{3}LC substate $^3(\pi\pi^*)_{+1}$ can mix via configuration interaction (CI) with the ^{3}MLCT substate $^3(d\pi^*)_{+1}$, which contains admixtures of the higher lying ^{1}MLCT state $^1(d'\pi^*)$ via SOC

Both SOC and the coupling by CI in this 3-state model are described by the following model Hamiltonian matrix:

$$\begin{pmatrix} E\left[{}^3(\pi\pi^*)_{+1}\right] & C_{\mathrm{CI}} & 0 \\ C_{\mathrm{CI}} & E\left[{}^3(\mathrm{d}\pi^*)_{+1}\right] & C_{\mathrm{SO}} \\ 0 & C_{\mathrm{SO}} & E\left[{}^1(\mathrm{d}'\pi^*)\right] \end{pmatrix} \tag{24}$$

with the matrix elements

$$C_{\mathrm{CI}} = \left\langle {}^3(\mathrm{d}\pi^*)_{+1} \middle| H_{\mathrm{CI}} \middle| {}^3(\pi\pi^*)_{+1} \right\rangle \tag{25}$$

and

$$C_{\mathrm{SO}} = \left\langle {}^1(\mathrm{d}'\pi^*) \middle| H_{\mathrm{SO}} \middle| {}^3(\mathrm{d}\pi^*)_{+1} \right\rangle \tag{26}$$

The energies of the unperturbed (sub)states have been defined above. H_{CI} is the configuration interaction Hamiltonian, which describes essentially the electron–electron interaction [128]. The off-diagonal terms are taken as the perturbation. The aim of this discussion is, at least for this simple model, to present the structure of the corresponding perturbational formulas. For example, it will be shown that different energy denominators occur, which are connected to the different states involved. In this model, we neglect any diagonal contributions to the model Hamilton operator and treat the matrix elements as real for simplicity.

In order to ease the discussion, we explain the effects of the CI perturbation first. Note that the selection rules $\Delta S=0$ and $\Delta M_S=0$ have to be fulfilled for CI. Thus, a triplet substate can configurationally mix only with the substates of higher lying triplets with the same M_S value. Thus, $^3(\pi\pi^*)_{+1}$ may configurationally mix with $^3(d\pi^*)_{+1}$. Treating CI as the only perturbation, the wave function of the ^{3}LC substate can be expressed as [115, 116, 123]

$$\left|{}^3(\pi\pi^*)_{+1}\right\rangle^{\mathrm{CI}} = \left|{}^3(\pi\pi^*)_{+1}\right\rangle + b\left|{}^3(\mathrm{d}\pi^*)_{+1}\right\rangle, \tag{27}$$

with the CI mixing coefficient

$$b = \frac{\left\langle {}^3(\mathrm{d}\pi^*)_{+1}\left|H_{CI}\right|{}^3(\pi\pi^*)_{+1}\right\rangle}{E\left[{}^3(\pi\pi^*)_{+1}\right] - E\left[{}^3(d\pi^*)_{+1}\right]} \tag{28}$$

The linear combination in (27) corresponds to an eigenvector of the 2×2 submatrix of the matrix (24) in the upper left corner.

A large mixing coefficient b leads to a significant ^{3}MLCT perturbation in the ^{3}LC substate. It is stressed that CI is equally efficient for the three substates of a triplet. This means that the introduction of CI as perturbation leads neither to different energy stabilizations of the substates and thus, to any zero-field splitting when acting alone, nor to changes of the individual radiative rates. However, the admixed $^3(\mathrm{d}\pi^*)_{+1}$ substate in turn contains admixtures of the $^1(\mathrm{d}'\pi^*)$ state via SOC as discussed in Sect. 6.5. Thus, one has to deal with a combination of both CI and SOC as perturbation as described by the full matrix (24). To lowest order in the simultaneous perturbation, the wave function of the doubly perturbed ^{3}LC substate can be expressed as

$$\left|{}^3(\pi\pi^*)_{+1}\right\rangle^{\mathrm{CI/SOC}} = \left|{}^3(\pi\pi^*)_{+1}\right\rangle + b\left|{}^3(\mathrm{d}\pi^*)_{+1}\right\rangle + a'b\left|{}^1(\mathrm{d}'\pi^*)\right\rangle \tag{29}$$

The coefficient b is defined in (28), and a' is given by

$$a' = \frac{\left\langle {}^1(\mathrm{d}'\pi^*)\left|H_{SO}\right|{}^3(\mathrm{d}\pi^*)_{+1}\right\rangle}{E\left[{}^3(\pi\pi^*)_{+1}\right] - E\left[{}^1(d'\pi^*)\right]} \tag{30}$$

Using the wave function given by (29), one obtains the following perturbational approximation for the energy shift of the $^3(\pi\pi^*)_{+1}$ substate:

$$\begin{aligned} E\left[{}^3(\pi\pi^*)_{+1}\right]^{CI/SOC} = {} & E\left[{}^3(\pi\pi^*)_{+1}\right] \\ & + \frac{\left\langle {}^3(\mathrm{d}\pi^*)_{+1}\left|H_{CI}\right|{}^3(\pi\pi^*)_{+1}\right\rangle^2}{E\left[{}^3(\pi\pi^*)_{+1}\right] - E\left[{}^3(d\pi^*)_{+1}\right]} \\ & - \frac{\left\langle {}^3(\mathrm{d}\pi^*)_{+1}\left|H_{CI}\right|{}^3(\pi\pi^*)_{+1}\right\rangle^4}{\left(E\left[{}^3(\pi\pi^*)_{+1}\right] - E\left[{}^3(d\pi^*)_{+1}\right]\right)^3} \\ & + \frac{\left\langle {}^3(\mathrm{d}\pi^*)_{+1}\left|H_{CI}\right|{}^3(\pi\pi^*)_{+1}\right\rangle^2 \cdot \left\langle {}^1(\mathrm{d}'\pi^*)\left|H_{SO}\right|{}^3(\mathrm{d}\pi^*)_{+1}\right\rangle^2}{\left(E\left[{}^3(\pi\pi^*)_{+1}\right] - E\left[{}^1(d'\pi^*)\right]\right) \cdot \left(E\left[{}^3(\pi\pi^*)_{+1}\right] - E\left[{}^3(d\pi^*)_{+1}\right]\right)^2} \end{aligned} \tag{31}$$

The radiative rate for the electronic transition to the singlet ground state can be expressed as

$$k^r\left({}^3(\pi\pi^*)_{+1}{}^{CI/SOC}\right) = \frac{64\pi^4\overline{\nu}^3}{3hc^3}\cdot\left|\frac{\left\langle {}^3(\mathrm{d}\pi^*)_{+1}\middle|H_{CI}\middle|{}^3(\pi\pi^*)_{+1}\right\rangle}{E\left[{}^3(\pi\pi^*)_{+1}\right]-E\left[{}^3(d\pi^*)_{+1}\right]}\cdot\right. \tag{32}$$
$$\left.\frac{\left\langle {}^1(\mathrm{d}'\pi^*)\middle|H_{SO}\middle|{}^3(\mathrm{d}\pi^*)_{+1}\right\rangle}{E\left[{}^3(\pi\pi^*)_{+1}\right]-E\left[{}^1(d'\pi^*)\right]}\cdot\left\langle S_0\middle|e\vec{r}\middle|{}^1(\mathrm{d}'\pi^*)\right\rangle\right|^2$$

Note that the combined mixing coefficient $a'b$ determines the radiative rate given by (32) (compare (28), (29), and (30)). According to (31) and (32), *two* matrix elements, one for CI and one for SOC, and *two* energy denominators determine the photophysical properties of the lowest triplet substate. As consequence, these indirect SOC paths to the substates of a ^{3}LC state have less influence on the ZFS and the radiative decay rates than direct SOC to the substates of a ^{3}MLCT.

6.7 Trends in Realistic Systems

In a more realistic treatment of spin-orbit coupling in organo-transition metal compounds, the simple 3-state or 4-state models, as presented above, do not hold, since there is a (large) number of higher lying singlet and triplet states which also have to be taken into account. As described above, many of these states can mix into the emitting triplet substates via direct or indirect SOC, if the symmetries of the corresponding wave functions fit and the selection rules for efficient SOC are fulfilled. In a more realistic description of direct SOC, the energies and radiative rates can be expressed by (33) and (34) as given below. Here, we apply the nomenclature as introduced in Sect. 3. This means that the lowest triplet state T_1 is composed of the substates I, II, and III. If only direct SOC is considered, the energy E(i) of the triplet MLCT substate i (with i=I, II, III) is given as [49, 53, 108, 129]

$$E(i) = E_{T_1} + \sum_{n,j}\frac{\left|\langle T_n(j)\,|\,H_{SO}\,|\,T_1(i)\rangle\right|^2}{E[T_1]-E[T_n]} + \sum_{m}\frac{\left|\langle S_m\,|\,H_{SO}\,|\,T_1(i)\rangle\right|^2}{E[T_1]-E[S_m]}, \tag{33}$$

while the radiative rate can be expressed by [49, 53, 108, 113, 130]

$$k^r(i) = \frac{64\pi^4\overline{\nu}^3}{3hc^3}\cdot\left|\sum_m\frac{\langle S_m\,|\,H_{SO}\,|\,T_1(i)\rangle}{E[T_1]-E[S_m]}\cdot\langle S_0\,|\,e\vec{r}\,|\,S_m\rangle\right|^2. \tag{34}$$

$E[S_m]$ and $E[T_n]$ are the unperturbed energies of higher lying singlet states S_m and triplet states T_n. $T_n(j)$ characterizes a substate j of T_n. (33) and (34) are the generalizations of (22) and (23), respectively. (34) shows that the expression for the radiative rate involves dipole matrix elements of the structure $\langle S_0\,|\,e\vec{r}\,|\,S_m\rangle$. Thus, the rate also depends on the allowedness of the singlet–singlet transitions between the mixing-in singlets and the electronic ground state, i.e., on their oscillator strengths.

On the other hand, SOC with the next higher lying ^{3}MLCT state(s) presumably dominates the individual energy stabilization of the T_1 substates due to the smaller energy denominators ($E[T_1] - E[T_n]$) as compared to ($E[T_1] - E[S_m]$).

The situation is different if the lowest triplet state represents a ^{3}LC state. As outlined in Sect. 6.6, SOC becomes effective via CI. Thus, (33) and (34) have to be modified according to the procedure described in Sect. 6.6. This leads to complicated formulas, since a huge manifold of possible paths of CI and SOC to higher lying states/substates has to be considered. This is illustrated schematically in a simplified example as shown in Fig. 14. The relevant coupling paths of a substate of ^{3}LC character to two higher lying singlet MLCT states and substates of two triplet MLCT states are depicted. According to the considerations of the previous sections, even in this simplified model two coupling paths of CI and three paths of SOC have to be included. The parameters α, β, γ, δ, and ε in Fig. 14 represent mixing coefficients and display the contributions of the respective (sub)states in the emitting substate $T_1(i)$. It is noted that for these coupling paths different selection rules apply. For the CI paths, only couplings of substates with the same M_S value are possible, while for the SOC paths the rule $\Delta M_S = 0, \pm 1$ applies. Moreover, the symmetries of the mixing states/substates have to be equal.

It is remarked that a perturbational approach, such as that carried out above, becomes rather complex. However, the radiative rate can generally be expressed by

$$k^r(i) = \frac{64\pi^4 \bar{\nu}^3}{3hc^3} \cdot \left| \sum_m c\left(S_m, T_1(i)\right) \cdot \langle S_0 \mid e\vec{r} \mid S_m \rangle \right|^2 , \tag{35}$$

where $c\left(S_m, T_1(i)\right)$ denotes the overall mixing coefficient of the singlet state S_m into the perturbed state $T_1(i)$, taking both SOC and CI into account. These mixing coefficients may be computed by perturbation theory or by other means. It is noted that this expression for the radiative rate is a generalization of (32) and that the overall structure is formally still rather simple.

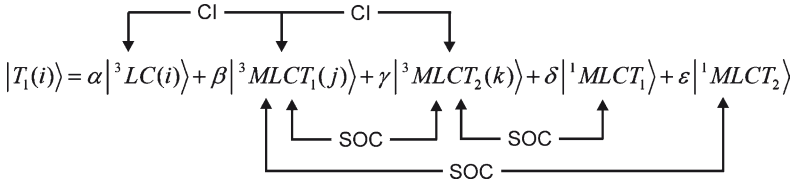

Fig. 14 Schematic illustration of SOC and configuration interaction (CI) routes being relevant for substate *i* of the lowest triplet state T_1 of ^{3}LC character in a five (sub)state model. *i* stands for one of the substates I, II, or III, while *j* and *k* represent substates of higher lying ^{3}MLCT states that can couple according to the selection rules as given in the text. Note that the ^{1,3}MLCT$_1$ and ^{1,3}MLCT$_2$ states involve different d-orbitals, but the same π^* orbital

6.8 Spin–Orbit Coupling and Coordination Geometry

The relations presented in the previous sections demonstrate that, both for direct and the indirect coupling paths, spin–orbit interactions are necessary to obtain a (distinct) zero-field splitting and a nonzero radiative rate. Moreover, (31) to (34) show that energy denominators, i.e., the energy differences between the unperturbed substate and the mixing states, also play an important role. The larger the energy denominator between two states, the smaller is their mixing via SOC or CI. Due to the necessary involvement of the central metal d-orbitals for SOC, one has to focus on the energy separations between the different d-orbitals. These separations depend significantly on the geometry of a compound, i.e., on the coordination geometry of the ligands around the central metal ion and on the ligand field splittings. This holds, since changes of the d-orbital energies lead to changes of the respective singlet and triplet MLCT state energies.

Figure 15 depicts the splittings of the central metal d-orbitals for (a) an octahedral and a distorted octahedral compound and for (b) a square planar and a distorted square planar compound. For this model discussion, one π*-orbital is introduced to represent the lowest unoccupied molecular orbital (LUMO). In these simplified schemes, other unoccupied π*-orbitals and occupied π-orbitals are neglected for clarity. Thus, all considered electronic states are MLCT states with a central metal d-orbital as highest occupied molecular orbital (HOMO).

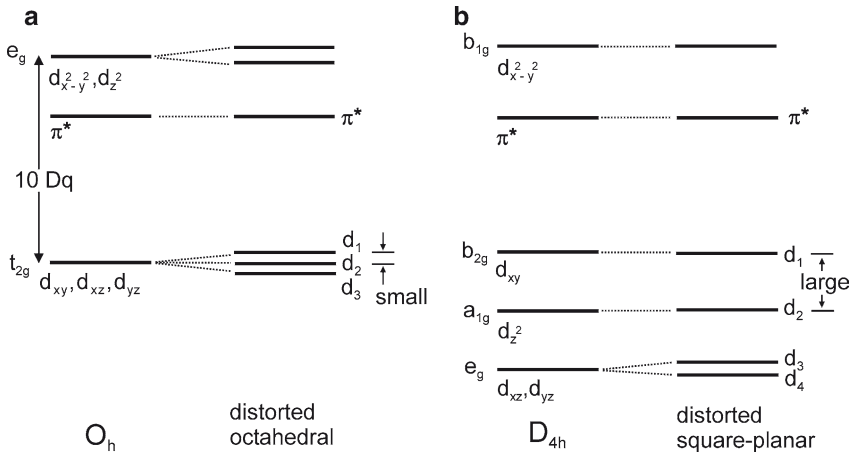

Fig. 15 Schematic splitting of the d-orbitals in an octahedral and a distorted octahedral compound (**a**) and in a square-planar and a distorted square planar compound (**b**). In all cases a π*-orbital, representing the LUMO, is displayed in addition (compare [49, 108, 128])

In the case of O_h symmetry, the d-orbitals split into sets of t_{2g} and e_g-orbitals, separated by 10 Dq with Dq being the ligand field parameter [128, 131]. For metal ions with a d^6 configuration, such as Ir(III), Os(II), and Ru(II), the t_{2g}-shell is fully occupied, while for systems of relevance for OLED applications, the unoccupied e_g-orbitals have to have energies high above the LUMO to prevent quenching induced by dd* states. For complexes with cyclometallating ligands, the O_h symmetry is not maintained. As a consequence, the orbitals of the t_{2g}-manifold are no longer degenerate and split into the three orbitals d_1, d_2, and d_3, according to the relevant symmetry and the distortion. However, they will still be rather proximate in energy [49, 108]. For $[Ru(bpy)_3]^{2+}$, for example, t_{2g}-splittings of several hundred wavenumbers were determined [81, 132–134]. Due to the SOC routes discussed above and the not very large energy denominators, the substates of the lowest ^{3}MLCT state $^3(d_1\pi^*)$ can experience efficient SOC with the close-lying singlet states $^1(d_2\pi^*)$ and $^1(d_3\pi^*)$ and the substates of the triplets $^3(d_2\pi^*)$ and $^3(d_3\pi^*)$. As a consequence, large ZFSs and relatively high radiative rates for the transitions between the substates of the lowest triplet and the ground state can occur.

For distorted square-planar compounds a different situation is found. For central metal ions exhibiting a d^8 electron configuration, such as Pt(II), the four lower lying d-orbitals are fully occupied. The ordering of these orbitals depends strongly on the nature and the bonding abilities of the coordinating ligands [128, 131, 135]. The depicted order, as shown in Fig. 15, is obtained from ligand field-theory without considering additional (back)bonding effects. The splittings between the occupied orbitals are relatively large, the unoccupied and antibonding $d_{x^2-y^2}$ orbital being strongly destabilized and shifted to high energy. In analogy to the situation described above for distorted octahedral compounds, the substates of the lowest ^{3}MLCT state $^3(d_1\pi^*)$ can exhibit efficient SOC with the singlet states $^1(d_2\pi^*)$, $^1(d_3\pi^*)$ and $^1(d_4\pi^*)$, as well as with the substates of the triplets $^3(d_2\pi^*)$, $^3(d_3\pi^*)$, and $^3(d_4\pi^*)$. However, the energy differences between d_1 and the other occupied d-orbitals d_2, d_3, and d_4 are for most compounds distinctly larger than for quasi-octahedrally coordinated compounds. For $[Pt(CN)_4]^{2-}$, for example, the energy difference between the highest occupied d-orbitals (HOMO and HOMO-1) is as high as about 4,000 cm^{-1} (0.5 eV) [135]. Consequently, the energy denominators between the MLCT states are significantly larger. Thus, spin-orbit coupling is much smaller in the situation depicted in Fig. 15b.

Similar arguments also hold for ^{3}LC states. In this case, indirect SOCs via CI are active. Note that the energetic positions of the d-orbitals are important for the size of both CI and SOC. Thus, smaller ZFSs and lower radiative rates are found for (distorted) square-planar compounds than for comparable (distorted) octahedral compounds.

In conclusion, under comparable conditions, SOC can become significantly larger for (distorted) octahedral compounds than for (distorted) square planar compounds. This has pronounced consequences on the magnitudes of zero-field splitting and radiative rates of the materials and thus is important for applications of the compounds as emitters in OLEDs.

7 Spin–Orbit Coupling and Photophysical Trends: Conclusion

For Ir(4,6-dFppy)$_2$(acac), the experimental results reveal a very large energy splitting of the emitting triplet state into substates, amounting to $\Delta E(\mathrm{ZFS}) = 109\ \mathrm{cm}^{-1}$ (in CH_2Cl_2, site A). This splitting is induced by very efficient SOC. According to the discussions in Sect. 6, this means that mixings of MLCT states stemming from *different* d-orbitals are very efficient. The involved d-orbitals are the splitting components of the t_{2g}-manifold of the coordinated Ir(III) center (compare Fig. 15a). Due to the very large amount of $\Delta E(\mathrm{ZFS})$ and the well-established ordering systematics [12, 49, 63, 108] (compare also Fig. 16), we classify the emitting triplet as being dominantly[5] of ^{3}MLCT character. In this approach, we describe the states' properties on the basis of the "direct SOC" model as introduced in Sect. 6.5 and extended to more realistic systems in (33) and (34). In particular, the ZFS is given by different energy shifts of the triplet substates I, II, and III according to differently effective SOCs. Very probably, the largest contributions are induced by higher lying triplet MLCT states, according to (33). Obviously, the ^{1}MLCT states will also induce shifts. However, the energy denominators are larger for the couplings to singlets than for the couplings to the ^{3}MLCT states.

On the other hand, the radiative rates are only determined by SOC induced admixtures of ^{1}MLCT states to the lowest ^{3}MLCT substates, according to (34). For applications as emitters in OLEDs, the rates k^r should be as large as possible. Thus, short emission decay times and in suitable cases also high photoluminescence quantum yields result. Large rates are induced by large SOC matrix elements, but also by small energy differences between the emitting triplet state and higher lying ^{1}MLCT

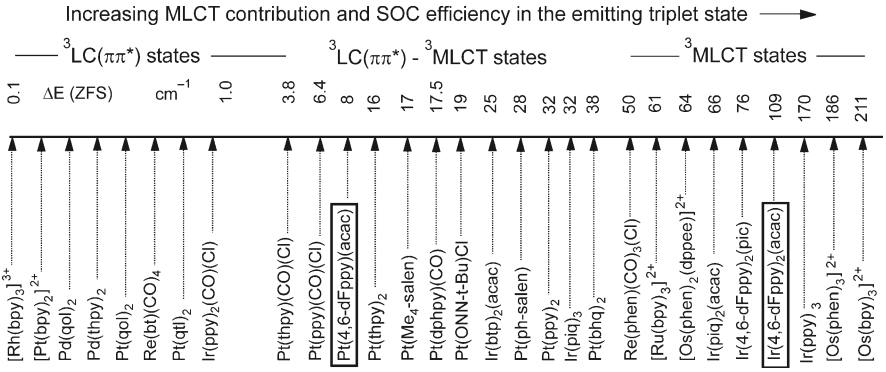

Fig. 16 Ordering scheme for triplet emitters [12, 49, 63, 108]. The diagram illustrates the relation of MLCT character of the emitting state to the magnitude of zero-field splitting $\Delta E(\mathrm{ZFS})$ of the T_1 state. The positions of compounds with $\Delta E(\mathrm{ZFS}) \leq 1\ \mathrm{cm}^{-1}$ are for most emitters only roughly estimated. The molecular structures are summarized in [49]. The diagram is adapted from [49]. Properties of the compounds in frames are discussed in detail in Sects. 2–5

[5]It is remarked that for a quantitative description, a significant LC (ππ*) contribution cannot be ignored (e.g., compare [110]).

states involving a different d-orbital. Moreover, the transition probability for the transition between these mixing-in singlet states and the electronic ground state should be as large as possible (high ε values). Obviously, the situation is very favorable for substate III of the emitting state of Ir(4,6-dFppy)$_2$(acac). In CH_2Cl_2 (site A), its decay time could be determined to $\tau(III) = 0.4\,\mu s$ from emission decay time measurements below 40 K (Fig. 8). At such low temperatures, nonradiative processes can often be neglected. Thus, a very large radiative decay rate of $k^r(III \rightarrow 0) \approx 2.5 \times 10^6\,s^{-1}$ can be estimated. On the other hand, the substates II and I experience distinctly smaller singlet admixtures. Hence, the radiative rates (obtained from the respective decay times, see Fig. 8) are distinctly smaller with $k^r(II \rightarrow 0) \approx 1.1 \times 10^5\,s^{-1}$ and $k^r(I \rightarrow 0) \approx 2.3 \times 10^4\,s^{-1}$.

Pt(4,6-dFppy)(acac) contains the same chromophoric as well as ancillary ligands as Ir(4,6-dFppy)$_2$(acac). Further, the SOC constants of Pt(II) and Ir(III) are very similar [136, 137]. Nevertheless, the properties of the emitting triplet state are very different. The ZFS amounts only to ≈8 cm^{-1} and the radiative decay rates were determined to $k^r(II/III \rightarrow 0) \approx 3.8 \times 10^5\,s^{-1}$ and $k^r(I \rightarrow 0) \approx 1.2 \times 10^4\,s^{-1}$. It is stressed that the values of $k^r(I \rightarrow 0)$ found for Ir(4,6-dFppy)$_2$(acac) and Pt(4,6-dFppy)(acac) cannot be compared directly due to different vibrational deactivation mechanisms (see the explanations given in the Sections 3.3 and 4.3). According to the ordering systematics, the emitting triplet of Pt(4,6-dFppy)(acac) is classified as ^{3}LC ($^3\pi\pi^*$) state, which is only moderately perturbed by ^{1,3}MLCT admixtures (compare Fig. 16 and [12, 49, 63, 108]). In the situation of an emitting state of ^{3}LC character, it is appropriate to describe the triplet state's properties by the model of "indirect SOC" as discussed in Sect. 6.6. This means that the required admixture of ^{1}MLCT character to the lowest ^{3}LC state is possible in a first step via CI between ^{3}LC and higher lying ^{3}MLCT states, and in a second step via SOC of these ^{3}MLCT states with higher lying ^{1}MLCT states involving different d-orbitals (compare Fig. 14). Obviously, these indirect SOC paths are less efficient than direct SOC as in the case of Ir(4,6-dFppy)$_2$(acac).

The observed essential differences of the (distorted) square-planar compared to the (distorted) octahedral compound can be related to the different coordination geometries. These lead to distinctly altered sequences and/or energy separations between the occupied d- and π-orbitals of the two compounds. For the square-planar situation, the energy difference between the highest occupied d-orbitals and thus, the separation of the lowest ^{3}MLCT state and the next ^{1}MLCT state involving a different d-orbital, is distinctly larger than in the case of an octahedral compound (compare Fig. 15). This has important consequences for the photophysical behavior. Independent of the relative ordering and the energy separations of the d- and π-orbitals, square planar complexes will not attain similarly high SOC efficiencies as it is possible for octahedral coordination. Hence, ZFSs and radiative decay rates are usually smaller for square planar compounds than for octahedral compounds with the same ligands.

Furthermore, the derived models also allow us to explain the different sensitivities of ZFSs and radiative rates on the host environment. Usually the sensitivity is less distinct for square planar Pt(II) than for octahedral Ir(III) compounds. Also for Ir(4,6-dFppy)$_2$(acac), the ZFSs and emission decay times strongly depend on the

environment, that is, for example, on the individual site of the dopant in its matrix cage, while for Pt(4,6-dFppy)(acac) a corresponding dependence is less distinct (see Sects. 3.4 and 4.4). This behavior can be related to SOC and its variation (compare also [49, 50, 53, 72, 101]). As discussed above, efficient SOCs occur if different d-orbitals are involved in the mixing paths. Consequently, changes of the compound's geometry, which, for example, are induced by different matrix cages, will result in changes of the energy separations between the relevant d-orbitals. Since these separations are displayed in the energy denominators of (33) and (34), the SOC efficiencies are altered. Hence, changes of zero-field splittings and decay times result. Specifically, the same amount of matrix-induced shifts of the relatively large energy separations between the occupied d-orbitals (or between the different resulting MLCT states) in Pt(II) compounds will have less impact on the SOC efficiencies than it is the case for the relatively small splittings in octahedral Ir(III) compounds. Further, it is a well-known fact that MLCT states usually are more sensitive to environmental effects than LC states [138–141]. This rationalizes that the emitting state of Pt(4,6-dFppy)(acac) – being largely of ^{3}LC character – depends only slightly on host effects, while the emitting ^{3}MLCT state of Ir(4,6-dFppy)$_2$(acac) exhibits a significant matrix dependence.

The detailed discussion presented above for Ir(4,6-dFppy)$_2$(acac) and Pt(4,6-dFppy)(acac) can be generalized to a large number of different organo-transition metal compounds. This leads to the mentioned ordering systematics as reproduced in Fig. 16. The compounds investigated in the scope of this contribution are marked by frames. Compounds with ΔE(ZFS) values of less than ≈1 cm^{-1} exhibit largely ligand centered ^{3}LC ($^3\pi\pi^*$) emitting states. The triplets of complexes with a ΔE(ZFS) value in the intermediate range, like Pt(4,6-dFppy)(acac), are moderately perturbed by ^{1,3}dπ^* admixtures. Those emitters with ΔE(ZFS) values larger than about 50 cm^{-1} are normally termed and assigned as ^{3}MLCT emitters (compare Footnote 5). Ir(4,6-dFppy)$_2$(acac) belongs to this group of complexes.

When considering the coordination numbers and molecular structures of the compounds listed in Fig. 16, one finds that all compounds which exhibit ΔE(ZFS) values of more than about 50 cm^{-1} have a quasi-octahedral structure, while the emitting triplet states of all quasi-square planar compounds investigated hitherto have splittings smaller than about 40 cm^{-1}. Interestingly, even the quasi-octahedral [Ru(bpy)$_3$]$^{2+}$ complex exhibits a larger ΔE(ZFS) value of the emitting T_1 state than found for Pt(II) complexes, although the SOC constant of Ru(II) is by a factor of about four smaller than the one of Pt(II) [136, 137]. This demonstrates that the MLCT character of the emitting triplet state does not simply depend on the central metal ion and the ligands. The coordination geometry, determined by the number of coordinating ligands, is also of high significance. This important trend is connected with specific SOC routes and has been explained above in detail.

Spin-orbit coupling not only governs the amount and pattern of ZFS of the emitting triplet state, but it is also of dominant importance for the radiative emission decay rates and thus for the photoluminescence quantum yields. These properties are crucial for the suitability of triplet emitters in OLEDs. In conclusion, detailed spectroscopic studies of compounds' triplet state properties in combination with

the analysis of SOC efficiencies is helpful to derive new guidelines for chemical engineering. These investigations may open new pathways to materials with improved photophysical properties than available up to now.

Acknowledgments The Bundesministerium für Bildung und Forschung (BMBF) is gratefully acknowledged for providing the funding of our research. We thank Prof. Dr. Mark E. Thompson (University of Southern California) for a fruitful cooperation with respect to the studied compounds.

8 Appendix

Here, we discuss how Rule E is related to the fact that angular momentum operators are purely imaginary. It further depends on the fact that, without magnetic field, the spatial orbitals are real. It is claimed that the diagonal matrix elements of the angular momentum operators vanish. For instance, in the case of l_z, we have for any real orbital $\chi = \chi(\vec{r})$

$$\langle \chi \,|\, l_z \,|\, \chi \rangle = \langle \chi \,|\, l_z \,|\, \chi \rangle^* ,$$

since l_z is Hermitian. On the other hand, performing the complex conjugation explicitly, we have

$$\langle \chi \,|\, l_z \,|\, \chi \rangle^* = \left(\iiint \chi(\vec{r}) \frac{1}{i} \frac{\partial}{\partial \varphi} \chi(\vec{r}) r^2 \mathrm{d}r \mathrm{d}\Omega \right)^* = -\langle \chi \,|\, l_z \,|\, \chi \rangle,$$

where $\mathrm{d}\Omega = \sin\vartheta \mathrm{d}\vartheta \mathrm{d}\varphi$ is the usual surface element in spherical coordinates r, ϑ, φ and the integration is over all space. Combining the two equations yields that the matrix element can only be zero.

This proves the assertion, since the other components of $\vec{l}$ can be treated similarly.

References

1. Yersin H (ed) (2008) Highly efficient OLEDs with phosphorescent materials. Wiley, Weinheim
2. Müllen K, Scherf U (eds) (2006) Organic light emitting devices – synthesis, properties and applications. Wiley, Weinheim
3. Kafafi ZH (ed) (2005) Organic electroluminescence. CRC Taylor & Francis, Boca Raton
4. Shinar J (ed) (2004) Organic light emitting devices. Springer, New York
5. Kalinowski J (2004) Organic light emitting diodes: principles, characteristics and processes. Marcel Dekker, New York
6. Hirani B, Li J, Djurovich PI, Yousufuddin M, Oxgaard J, Persson P, Wilson SR, Bau R, Goddard WA III, Thompson ME (2007) Inorg Chem 46:3865
7. Chou PT, Chi Y (2007) Chem Eur J 13:380

8. Borek C, Hanson K, Djurovich PI, Thompson ME, Aznavour K, Bau R, Sun Y, Forrest SR, Brooks J, Michalski L, Brown J (2007) Angew Chem Int Ed 46:1109
9. Evans RC, Douglas P, Winscom CJ (2006) Coord Chem Rev 250:2093
10. Adachi C, Baldo MA, Thompson ME, Forrest SR (2001) J Appl Phys 90:5048
11. Ikai M, Tokito S, Sakamoto Y, Suzuki T, Taga Y (2001) Appl Phys Lett 79:156
12. Yersin H (2004) Top Curr Chem 241:1
13. Baldo MA, O'Brien DF, Thompson ME, Forrest SR (1999) Phys Rev B 60:14422
14. Flamigni L, Barbieri A, Sabatini C, Ventura B, Barigelletti F (2007) Top Curr Chem 281:143
15. Tamayo AB, Garon S, Sajoto T, Djurovich PI, Tsyba IM, Bau R, Thompson ME (2005) Inorg Chem 44:8723
16. Yang CH, Cheng YM, Chi Y, Hsu CJ, Fang FC, Wong KT, Chou PT, Chang CH, Tsai MH, Wu CC (2007) Angew Chem Int Ed 46:2418
17. Su SJ, Gonmori E, Sasabe H, Kido J (2008) Adv Mater 20:4189
18. Sasabe H, Gonmori E, Chiba T, Li YJ, Tanaka D, Su SJ, Takeda T, Pu YJ, Nakayama KI, Kido J (2008) Chem Mater 20:5951
19. You Y, Park SY (2009) Dalton Trans 8:1267
20. Kawamura Y, Sasabe H, Adachi C (2004) Jpn J Appl Phys 43:7729
21. Kawamura Y, Goushi K, Brooks J, Brown JJ, Sasabe H, Adachi C (2005) Appl Phys Lett 86:071104
22. a) Hofbeck T, Yersin H (2009) submitted; b) Hofbeck T, Yersin H (2008) 3rd International Symposium on Molecular Materials - MOLMAT, Book of Abstracts. Toulouse, France, p.157
23. Williams JAG, Beeby A, Davies ES, Weinstein JA, Wilson C (2003) Inorg Chem 42:8609
24. Farley SJ, Rochester DL, Thompson AL, Howard JAK, Williams JAG (2005) Inorg Chem 44:9690
25. Kui SCF, Sham IHT, Cheung CCC, Ma CW, Yan B, Zhu N, Che CM, Fu WF (2007) Chem Eur J 13:417
26. Williams JAG (2007) Top Curr Chem 281:205
27. Yang X, Wang Z, Madakuni S, Li J, Jabbour GE (2008) Adv Mater 20:2405
28. Lin YY, Chan SC, Chan MCW, Hou YJ, Zhu N, Che CM, Liu Y, Wang Y (2003) Chem Eur J 9:1263
29. Connick WB, Geiger D, Eisenberg R (1999) Inorg Chem 38:3264
30. Pettijohn CN, Jochnovitz EB, Chuong B, Nagle JK, Vogler A (1998) Coord Chem Rev 171:85
31. Adamovich V, Brooks J, Tamayo A, Alexander AM, Djurovich PI, D'Andrade BW, Adachi C, Forrest SR, Thompson ME (2002) New J Chem 26:1171
32. Yersin H, Donges D, Humbs W, Strasser J, Sitters R, Glasbeek M (2002) Inorg Chem 41:4915
33. Lu W, Chan MCW, Zhu N, Che CM, Li C, Hui Z (2004) J Am Chem Soc 126:7639
34. Mdleleni MM, Bridgewater JS, Watts RJ, Ford PC (1995) Inorg Chem 34:2334
35. Yersin H, Monkowius U, Fischer T, Finkenzeller WJ, Czerwieniec R (2008) WO 2008/003464 A1
36. Yersin H, Monkowius U, Czerwieniec R (2007) WO2007/118671 A1
37. D'Andrade BW, Brooks J, Adamovich V, Thompson ME, Forrest SR (2002) Adv Mater 14:1032
38. D'Andrade BW, Forrest SR (2003) J Appl Phys 94:3101
39. Adamovich VI, Cordero SR, Djurovich PI, Tamayo A, Thompson ME, D'Andrade BW, Forrest SR (2003) Org Electron 4:77
40. Williams EL, Haavisto K, Li J, Jabbour GE (2007) Adv Mater 19:197
41. Cocchi M, Kalinowski J, Virgili D, Fattori V, Develay S, Williams JAG (2007) Appl Phys Lett 90:163508
42. Kalinowski J, Cocchi M, Virgili D, Fattori V, Williams JAG (2007) Adv Mater 19:4000
43. Cocchi M, Kalinowski J, Fattori V, Williams JAG, Murphy L (2009) Appl Phys Lett 94:073309
44. Brooks J, Babayan Y, Lamansky S, Djurovich PI, Tsyba I, Bau R, Thompson ME (2002) Inorg Chem 41:3055

45. Li J, Djurovich PI, Alleyne BD, Tsyba I, Ho NN, Bau R, Thompson ME (2004) Polyhedron 23:419
46. Yersin H, Huber P, Wiedenhofer H (1994) Coord Chem Rev 132:35
47. Colombo MG, Brunold TC, Riedener T, Güdel H, Förtsch M, Bürgi HB (1994) Inorg Chem 33:545
48. Finkenzeller WJ, Yersin H (2003) Chem Phys Lett 377:299
49. Yersin H, Finkenzeller WJ (2008) In: Yersin H (ed) Highly efficient OLEDs with phosphorescent materials. Wiley, Weinheim, p 1
50. Rausch AF, Thompson ME, Yersin H (2009) J Phys Chem A 113:5927
51. Ma B, Djurovich PI, Thompson ME (2005) Coord Chem Rev 249:1501
52. D'Andrade B, Forrest SR (2003) Chem Phys 286:321
53. Rausch AF, Thompson ME, Yersin H (2009) Inorg Chem 48:1928
54. Adachi C, Kwong RC, Djurovich PI, Adamovich V, Baldo MA, Thompson ME, Forrest SR (2001) Appl Phys Lett 79:2082
55. Su SJ, Sasabe H, Takeda T, Kido J (2008) Chem Mater 20:1691
56. Vecchi PA, Padmaperuma AB, Qiao H, Sapochak LS, Burrows PE (2006) Org Lett 8:4211
57. Li J, Djurovich PI, Alleyne BD, Yousufuddin M, Ho NN, Thomas JC, Peters JC, Bau R, Thompson ME (2005) Inorg Chem 44:1713
58. Coppo P, Plummer EA, De Cola L (2004) Chem Commun 15:1774
59. Yersin H, Schützenmeier S, Wiedenhofer H, von Zelewsky A (1993) J Phys Chem 97:13496
60. Yersin H, Donges D, Nagle JK, Sitters R, Glasbeek M (2000) Inorg Chem 39:770
61. Schmidt J, Wiedenhofer H, von Zelewsky A, Yersin H (1995) J Phys Chem 99:226
62. Becker D, Yersin H, von Zelewsky A (1995) Chem Phys Lett 235:490
63. Yersin H, Donges D (2001) Top Curr Chem 214:81
64. Donges D, Nagle JK, Yersin H (1997) Inorg Chem 36:3040
65. Kozhevnikov DM, Kozhevnikov VN, Ustinova MM, Santoro A, Bruce DW, König B, Czerwieniec R, Fischer T, Zabel M, Yersin H (2009) Inorg Chem 48:4179
66. Shpol'skii EV (1960) Sov Phys Usp 3:372 Engl Transl
67. Murao T, Azumi T (1979) J Chem Phys 70:4460
68. Jansen G, Noort M, van Dijk N, van der Waals JH (1980) Mol Phys 39:865
69. Komada Y, Yamauchi S, Hirota N (1985) J Chem Phys 82:1651
70. Dick B, Nickel B (1986) Chem Phys 110:131
71. Rausch AF, Thompson ME, Yersin H (2009) Chem Phys Lett 468:46
72. Finkenzeller WJ, Hofbeck T, Thompson ME, Yersin H (2007) Inorg Chem 46:5076
73. Van Dijk N, Noort M, Voelker S, Canters GW, van der Waals JH (1980) Chem Phys Lett 71:415
74. Chen WH, Rieckhoff KE, Voigt EM (1985) Chem Phys 95:123
75. Huang SC, Chen WH (1996) J Chem Phys 104:8210
76. Gliemann G (1986) Comments Inorg Chem 5:263
77. Czerwieniec R, Finkenzeller WJ, Hofbeck T, Starukhin A, Wedel A, Yersin H (2009) Chem Phys Lett 468:205
78. Baker DC, Crosby GA (1974) Chem Phys 4:428
79. Gallhuber E, Hensler G, Yersin H (1987) J Am Chem Soc 109:4818
80. Yersin H, Kratzer C (2002) Chem Phys Lett 362:365
81. Yersin H, Humbs W, Strasser J (1997) Top Curr Chem 191:153
82. Yersin H, Kratzer C (2002) Coord Chem Rev 229:75
83. Carrigan RW, Crosby GA (1973) J Chem Phys 59:3468
84. Azumi T, O'Donnell CM, McGlynn SP (1966) J Chem Phys 45:2735
85. Pentlehner D, Grau I, Yersin H (2008) Chem Phys Lett 455:72
86. Yersin H, Strasser J (2000) Coord Chem Rev 208:331
87. Strasser J, Homeier HHH, Yersin H (2000) Chem Phys 255:301
88. Wiedenhofer H, Schützenmeier S, von Zelewsky A, Yersin H (1995) J Phys Chem 99:13385
89. Albrecht AC (1963) J Chem Phys 38:354

90. Fischer G (1984) Vibronic coupling. Academic Press, London
91. Flint CD (ed) (1989) Vibronic processes in inorganic chemistry. NATO ASI Series C, vol 288. Kluwer Academic, Dordrecht
92. Hochstrasser RM (1966) Molecular aspects of symmetry. Benjamin Inc WA, New York
93. Braun D, Hensler G, Gallhuber E, Yersin H (1991) J Phys Chem 95:1067
94. Ballhausen CJ (1979) Molecular electronic structures of transition metal complexes. McGraw-Hill, New York
95. Wilson RB, Solomon EI (1980) J Am Chem Soc 102:4085
96. Henderson B, Imbusch GF (1989) Optical spectroscopy of inorganic solids. Clarendon, Oxford
97. Solomon EI (1984) Comments Inorg Chem 3:225
98. Seiler R, Kensy U, Dick B (2001) Phys Chem Chem Phys 3:5373
99. Humbs W, Yersin H (1997) Inorg Chim Acta 265:139
100. Humbs W, Yersin H (1996) Inorg Chem 35:2220
101. Finkenzeller WJ, Thompson ME, Yersin H (2007) Chem Phys Lett 444:273
102. Marchetti AP, Deaton JC, Young RH (2006) J Phys Chem A 110:9828
103. Wang X, Li J, Thompson ME, Zink JI (2007) J Phys Chem A 111:3256
104. Liu T, Xia BH, Zhou Y, Zheng QC, Pan QJ, Zhang HX (2008) Theor Chem Account 121:155
105. Rebane KK (1988) In: Sild O, Haller K (eds) Zero-phonon lines and spectral hole burning in spectroscopy and photochemistry. Springer, Berlin
106. Bauer R, Finkenzeller WJ, Bogner U, Thompson ME, Yersin H (2008) Org Electron 9:641
107. Rausch AF, Phd thesis, in preparation
108. Rausch AF, Homeier HHH, Djurovich PI, Thompson ME, Yersin H (2007) In: Kafafi Z, So F (eds) Proceedings of SPIE optics and photonics – organic light emitting materials and devices XI, vol 6655. San Diego, USA, p 66550F
109. Gu X, Fei T, Zhang H, Xu H, Yang B, Ma Y, Liu X (2008) J Phys Chem A 112:8387
110. Nozaki K (2006) J Chin Chem Soc 53:101
111. Jansson E, Minaev B, Schrader S, Ågren H (2007) Chem Phys 333:157
112. Minaev B, Minaeva V, Ågren H (2009) J Phys Chem A 113:726
113. Mc Glynn SP, Kinoshita M, Azumi T (1969) Molecular spectroscopy of the triplet state. Prentice Hall, Englewood Cliffs
114. Yagi M, Schlyer D, Maki AH (1991) Chem Phys 157:209
115. Miki H, Azumi T (1994) J Phys Chem 98:6059
116. Azumi T, Miki H (1997) Top Curr Chem 191:1
117. Vanhelmont FWM, Güdel HU, Förtsch M, Bürgi HB (1997) Inorg Chem 36:5512
118. Funayama T, Kato M, Kosugi H, Yagi M, Higuchi J, Yamauchi S (2000) Bull Chem Soc Jpn 73:1541
119. Atkins PW (1997) Molecular quantum mechanics. Oxford University Press, Oxford, p 208
120. Sakurai JJ (1994) Modern quantum mechanics. Addison-Wesley, Reading, p 239
121. Szabo A, Ostlund NS (1989) Modern quantum chemistry: introduction to advanced electronic structure theory. McGraw-Hill, New York
122. Roos BO (ed) (1992) Lecture notes in quantum chemistry (Lecture notes in chemistry), vol 58. Springer, Berlin
123. Miki H, Shimada M, Azumi T, Brozik JA, Crosby GA (1993) J Phys Chem 97:11175
124. Giesbergen C, Glasbeek M (1993) J Phys Chem 97:9942
125. Komada Y, Yamauchi S, Hirota N (1986) J Phys Chem 90:6425
126. Glasbeek M, Sitters R, van Veldhoven E, von Zelewsky A, Humbs W, Yersin H (1998) Inorg Chem 37:5159
127. Finkenzeller WJ, Stößel P, Yersin H (2004) Chem Phys Lett 397:289
128. Schläfer HL, Gliemann G (1967) Einführung in die Ligandenfeldtheorie. AkadVerlagsgesellschaft, Wiesbaden
129. Ikeela S, Yamamto S, Nozaki K, Ikeyama T, Azumi T, Burt JA, Crosley GA (1991) J Phys Chem 95:8583
130. Abedin-Siddique Z, Ohno T, Nozaki K, Tsubomura T (2004) Inorg Chem 43:663

131. Figgis BN (1987) Ligand field theory. Comprehensive coordination chemistry. Pergamon, Oxford, p 213
132. Ceulemans A, Vanquickenborne LG (1981) J Am Chem Soc 103:2238
133. Kober EM, Meyer TJ (1982) Inorg Chem 21:3967
134. Daul C, Baerends EJ, Vernooijs P (1994) Inorg Chem 33:3538
135. Ziegler T, Nagle JK, Snijders JG, Baerends EJ (1989) J Am Chem Soc 111:5631
136. Murov SL, Carmichael J, Hug GL (1993) Handbook of photochemistry, 2nd edn. Marcel Dekker, New York
137. Griffith JS (1964) The theory of transition metal ions. Cambridge University Press, London
138. Chen P, Meyer TJ (1998) Chem Rev 98:1439
139. Ulstrup J (1979) Processes in condensed media (Lecture notes in chemistry), vol 10. Springer, New York
140. Colombo MG, Hauser A, Güdel HU (1993) Inorg Chem 32:3088
141. Colombo MG, Hauser A, Güdel HU (1994) Top Curr Chem 171:143

Index

A
Acetylide, 162
Anthracen-9-yl, 136
Arylacetylide, 162
Avidin, rhenium(I) tricarbonyl diimine-biotin, 28
Avidin–biotin, 129, 148
Azurin, 125

B
Bathophenanthroline sulfate, 137
Benzenetriyl-tris(1-phenyl-1H-benzimidazole) (TBPI), 30
3-Benzoylpyridine, 77
Bipyridyl acetylides, 172
Bis(alkynyl)platinate, 182
Bis(cyclometallated)iridium(III), 144
BODIPY, 174
bpy-diarylethene, 77
BSA, 135

C
Calix[4]arene{$Re(CO)_3Cl$}, 25
Carbonyl, 37, 73
Cells, 115
Character mixing, lowest excited states, 90
Charge transfer, 73, 161
Chromium, 37
Chromophores, 1, 159
Complete active space (CAS), 40
Crown ethers, 27

D
Decarbonylation, photoinduced, 37
Decay times, 211
DFT, 73
2,3-Di(2-pyridyl)pyrazine, 76
2,3-Di(2-pyridyl)quinoxaline, 76
Diarylethenes, 17
4,4-Dicarbazolylbiphenyl (CBP), 30
Digoxin, 145
Diimine, 73
Diimine rhenium(I) tricarbonyl, 1
5,6-Dimethyl-1,10-phenanthroline, 5
2,6-Dimethylphenylisocyanide, 4, 77,
DNA, 115
  binding/photocleavage, diimine rhenium(I) tricarbonyl, 3

E
El Sayed's rules, 83
Electroluminescence (EL), 29, 194
Electron transfer, 73, 105, 159
Electronic 0–0 transitions, 198, 206
Electronic structure, 37
Emission quantum yields, 193
Energy gap law, 5, 7
Energy level diagrams, 211
Energy transfer, 159
Energy-gap law maps, 85
Equations-of-motion coupled cluster methods (EOM–CC), 40
Estradiol, 135, 150
2-(1-Ethylbenzimidzol-2-yl)pyridine, 30
Excited state, 73
  chemistry, 159
  dynamics, 37
  DFT, 86
  infrared spectra, 87

G
Glutathione, 129

H
Haem, 126
Halide-to-ligand charge transfer, 9
Herzberg–Teller (HT) coupling, 203
High-resolution spectroscopy, 193

I
Indole compounds, 133
Intersystem crossing, 73, 81
Intramolecular energy transfer, 103
IR spectroscopy, time-resolved, 73
$Ir(4,6\text{-dFppy})_2(acac)$, 195, 211
Iridium, 115
Iridium(III) systems, 140, 193
  arylbenzothiazole biotin, 147
  cellular probes, 153
  DNA probes, 140
  estradiol, 150
  polypyridine, DNA probes, 140
  protein probes, 143
Iron, 37
cis-trans-Isomerization reactions, photoinduced, 13
Isothiocyanate, 124

L
Ligand substitution reactions, photochemical, 11
Ligand-to-ligand charge transfer (LLCT), 3
Light-controlled photoswitch, 14
Light-emitting devices (LEDs), 29
  rhenium(I) tricarbonyl diimine, 30
Luminescence, 1, 115
  rigidochromism, diimine rhenium(I) tricarbonyl, 3
Luminescent heterometallasquare, 22

M
Mass selective detection, 37
Metal-ligand-to-ligand charge transfer transition (MLLCT), 4
Metallonucleosides, 123
Metal–organic chromophores, 159
Metal-to-ligand charge transfer (MLCT), 3
5-Methyl-1,10-phenanthroline, 5
Mitochondria-specificity, 139

N
Nickel, 37
Nitric oxide synthase, 126
5-Nitro-1,10-phenanthroline, 5
Nitropolypyridine Re, 102

O
Oligonucleotides, 125, 140
Optical excitation, 78
Orbitals, 215
Organic light-emitting diodes (OLEDs), 29, 160, 194
  emitters, 193
Organometallics, 1, 193

P
pH sensor ligands
Phenanthroline, 4, 167
1,10-Phenanthrolinopyrrole, 5
Phenothiazine, 162
t-Phenylazopyridine, 77
Phosphorescence, 193
Phosphorescent organic light-emitting diodes (PhOLEDs), 29
Photochemical ligand substitution (PLS), 11
Photochemistry, 102
Photochromism, 1
Photocyclization, 17
Photodecarbonylation, $Cr(CO)_6$, 39
  $Fe(CO)5$, 52
  $Ni(CO)4$, 63
Photoinduced transformations, 11
Photoluminescence, 159
Photophysics, 1, 37, 73, 159, 193
Platinum, 159, 193
Poly(N-vinylcarbazole) (PVK), 29
Polypyridyl ligands, 175
Proteins, 115
Pt(4,6-dFppy)(acac), 195, 197, 211
Pt^{II} acetylides, bidentate polypyridyl ligands, 161
  electronic structures, 181
  phosphine chromophores, photophysics, 177
  phosphine-containing ligands, 167, 177
  tridentate polypyridyl ligands, 175
py-azacrown, 77
py-catecholate, 77
Pyrenylacetylide, 163
2-Pyridinecarboxaldehyde, 122

Q
2-Quinolinecarboxaldehyde, 122

R
Radiative rates, 193
Radiopharmaceuticals, diimine rhenium(I) tricarbonyl, 3
Realistic systems, 224
Relaxation, 73
Rhenium anthracene, DNA intercalation, 120
Rhenium carbonyl diimine, 3, 84
Rhenium-ligand bond splitting, 102
Rhenium tricarbonyl, 18
Rhenium(I) systems, 1, 73, 115, 119
  bipyridine 9-ethylguanine, 121
  cellular probes, 136
  DNA probes, 119
  iodoacetamide, 127
  perfluorobiphenyl diimine, 126
  polypyridine estradiol, 136
  polypyridine isothiocyanate, 124
  protein probes, 125
  tricarbonyl diimine-biotin, avidin, 28
Rigidochromic effect, 5

S
Self-assembly, 1
Sensitization axial ligand isomerization, 103
Sensors, 1, 25
Sigma bond-to-ligand charge transfer, 13
Singlet excited states, 81
SOC, 193
  geometry, 193
  paths, 193
Spin–orbit coupling, 193, 194, 212, 216
  coordination geometry, 226
  direct, 220
  indirect, 221
  photophysical trends, 228
Spironucleus vortens, 137
Spirooxazine, 17
States, 215
t-Styrylpyridine, 77
Sulfhydryl-containing biomolecules, 128
Supramolecular chemistry 1

T
T1 state properties, matrix dependence, 210
TD-DFT, 3, 86, 160, 182
Terpyridylacetylide, 172
Thermalized emission decay, 200, 207
4'-Tolylterpyridyl arylacetylide, 171
Triplet emitters, 193
Triplet excited states, 84
  relaxation, 94

U
Ultrafast electron diffraction, 37
Ultrafast multiphoton excitation, $Fe(CO)_5$, 53

V
Vibrational energy relaxation (VER), 96
Vibrational satellite structure, 202, 208

W
White electroluminescence in single dopant organic light emitting diodes (WOLEDs), 195

Z
Zero-field splittings (ZFS), 85, 193, 205, 211